Université de Montréal

Plastic Flow and Brittle Fractures of Rocks from the Earth's Upper Mantle and Crust

par

SARUWATARI Kazuko
Département de géologie
Faculté des art et des sciences

Thèse présentée à la Faculté des études supérieures
en vue de l'obtention du grade de
Philosophiae Doctor (Ph.D.)
en géologie

Mars 2000

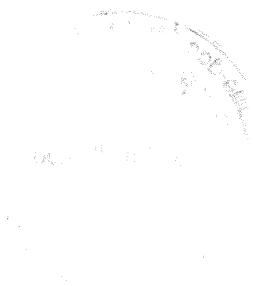

Université de Montréal

Faculté des études supérieures

Cette thèse intitulée:

Plastic Flow and Brittle Fractures of Rocks from the Earth's Upper Mantle and Crust

présentée par:

Kazuko SARUWATARI

a été évaluée par un jury composé des personnes suivantes:

Dr Jacques Martignole	Président rapporteur
Dr Shaocheng Ji	Directeur de recherche
Dr Andrew J. Hynes	Membre du jury
Dr Matthew Salisbury	Examinateur externe
Dr Michel Chouteau	Représentant du doyen

RÉSUMÉ

Les travaux de cette thèse sont réalisées sur des xénolithes mantelliques, sur des roches métamorphiques du faciès des granulites et enfin sur des roches sédimentaires que l'on considére respectivement représentatives du manteau supérieur, de la croûte continentale inférieure et supérieure. Les travaux sont concentrés sur le fluage plastique, la fracturation, les microstructures, les mécanismes de déformation et les propriétés pétrophysiques de ces roches.

Le chapitre 1 aborde des notions théoriques (élasticité, anisotropie sismique, déphasage des ondes S, modèle de "shear-lag") et méthodologiques (inclusions fluides) utilisées dans les chapitres suivants. Le chapitre 2 est consacré à l'étude des déformations plastiques, des orientations préférentielles de réseaux et des propriétés sismiques des xénolithes mantelliques de la Cordillère sud canadienne. Sur la base des propriétés sismiques modélisées, les analyses de vitesse des ondes P_n et de déphasage des ondes SKS et SKKS obtenues pour cette région suggèrent que la foliation et la linéation d'étirement soient horizontales dans le manteau supérieur situé au-dessous de la Cordillère sud canadienne. Ces données indiquent que ces anisotropies sismiques se prolongent jusqu'à 350-400 km de profondeur. Le chapitre 3 présente nos résultats de l'étude des fractures de tensions dans les grenats de roches granulitiques situées dans la zone de cisaillement ductile de Morin (Province du Grenville). Les conséquences géodynamiques de ces observations microstructurales sont discutées. Un nouveau modèle de "shear-lag" est développé pour expliquer la localisation des fractures de tension dans les grenats ainsi que leur répartition géométrique préférentielle. Enfin le dernier chapitre caractérise la relation entre l'espacement des diaclases (joints) et l'épaisseur des couches dans les roches sédimentaires Cambriennes des Appalaches québecoises. En considérant à la fois une décroissance non-linéaire de la contrainte de cisaillement et des épaisseurs variables des couches compétentes et incompétentes, une amélioration importante du modèle de "shear-

lag" est apportée. Un tel modèle permet de prédire les variations d'espacement des diaclases à l'état de saturation en fonction des épaisseurs des couches compétentes et incompétentes. Ce modèle pourrait être important pour des applications pratiques dans le domaine de la géotechnique et du génie civil.

Mots clés:

Xénolites mantelliques, mylonites de haut grade, diaclases, fractures, orientations préférentielles, anisotropie sismique, déphasage des ondes S, modèle de "shear-lag", Cordillèra canadienne, Province du grenville, Appalaches.

ABSTRACT

This thesis encompasses ultramafic xenoliths, granulite-facies metamorphic rocks and sedimentary rocks, which are representative of the Earth's upper mantle, lower crust and upper crust, respectively. The accent is on plastic flow, brittle fracturing, microstructures, mechanical processes, and petrophysical properties of these rocks. Chapter 1 gives the indispensable background on elasticity, seismic anisotropy, shear-wave splitting, the shear-lag model and fluid inclusions; these will be crucial to understand the next chapters of the thesis. Chapter 2 is devoted to plastic deformation, lattice preferred orientations, and seismic properties of ultramafic xenoliths from the southern Canadian Cordillera. Analyses of the P_n and SKS splitting data obtained from the region, based on the calculated seismic properties of the mantle xenoliths, suggest that both the foliation and stretching lineation are horizontal in the upper mantle beneath the southern Canadian Cordillera and the seismic anisotropy extends to about 400 km depth. Chapter 3 deals with pervasive, closely spaced, relatively straight, tensile fractures in garnet crystals from granulite facies metamorphic rocks from the Morin shear zone in the Grenville province and explores the possible implications of these fractures for the uplift process of high grade metamorphic terranes. A modified shear-lag model is developed to explain why tensile fracturing took place preferentially in stiff garnet rather than in felsic material, and why the fractures are unequally spaced in the garnet grains. The final chapter is concerned with the relationship between joint spacing and layer thickness in Cambrian sedimentary rocks from the Quebec Appalachians. Taking into account a non-linear decay of the shear-stresses and various thicknesses of bounding non-jointing beds, an improved shear-lag model has been developed in order to better predict observed variations of saturated joint spacing as functions of both jointing and non-jointing layer thicknesses. The model may have important potential significance for the solution of a number of very practical problems in the design and

stability of engineering and mining projects.

Key Words:

Mantle xenoliths, high-grade mylonites, joints, fracture, lattice preferred orientation, seismic anisotropy, shear-wave splitting, shear-lag theory, Canadian Cordillera, Grenville Province, Appalachians.

Contents

List of Tables

List of Figures

Acknowledgment

I would like to express my great gratitude to my supervisor, Prof. Shaocheng Ji, for his wise guidance and support throughout my Ph.D. period. He has given me great opportunities to progress in my Ph.D. research and invaluable help from the inception to the present form of this thesis. I also would like to thank Professor J. Martignole for critical reading of my manuscript during my Ph.D. studies. Many thanks to Dr. Z. Wang for his discussion and his research support, to Katie St-Amand for her field and research assistance, to Dr. P. Zhao for his modeling calculation, to Dr. X. Zhao for his helpful discussion, and to Dr. J.-E. Martelat for his help with translating of French resume of this thesis. Biiig thanks to all my friends in Montreal, in Canada, and in Japan. Notable thanks to Uda-chan and Ha-chan for always giving me heartfelt encouragement and for having marvelous discussion together. Groß danke zum Jürgen. Special thanks to Prof. D. Mainprice (Université Montpellier) for enormous help and patience with the EBSD analyses and for providing EBSD and seismic computer programs, to Prof. A.-M. Boullier (CNRS, Grenoble) for critical suggestions of my fluid inclusion study, and to Prof. A. William-Jones (McGill) for a permission of the usage of a fluid inclusion stage at McGill University. Immeasurable thanks to Dr. K. Michibayashi for giving me an idea to study abroad and also for his help and encouragement. I also would like to acknowledge the help I received from the staff of Département de géologie, Université de Montréal. Especial gratitude to Lucie Charbonneau for her invaluable help and her French lesson in the secretary .

I gratefully acknowledge the Faculté des études supérieure of Université de Montréal for the exemption of the foreign student tuition fees and for the Bourses de doctorat de l'Université de Montréal during my Ph.D. studies.

Finally, inexpressible and invisible thanks to my parents.

父と母へ

人生、我が道を行く

和子

Chapter 1

Introduction

Je sais bien que de deux choses l'une:
ou tu vis, ou tu écris.
Moi je veux "vécrire".
J. Godbout (1967)

1.1. Objective and organization of this thesis

This thesis is devoted to microstructural analyses of deformed rocks from the Earth's upper mantle to the upper crust. The analyses have been performed under microscopes and at outcrops, measuring different types of deformation structures such as lattice preferred orientations (LPOs) of upper mantle minerals and tensile fractures in garnet crystals and sedimentary rocks.

In order to investigate upper mantle structure and its lateral variation beneath the Canadian Cordillera region, the LITHOPROBE project has performed deep seismic reflection profiling, teleseismic shear wave splitting, gravity and geotherm measurements along various transects. In order to provide basic constraints for realistic interpretation of these geophysical data, I investigated the seismic properties of ultramafic xenoliths from alkaline basalts in the southern Canadian Cordillera (Chapter 2). The main methods used in this study include geothermobarometry based on microprobe analyses, petrofabric measurements using a U-stage, numerical calculations of P-wave and S-wave velocities, analysis of deformation mechanisms, and geothermal, rheological and seismic modeling. My study has mainly focused on: (i) P-wave anisotropy and variation in the horizontal plane, (ii) Orientation and magnitude of S-

wave anisotropy, (iii) Thickness of the anisotropic layer as a function of dominant deformation mechanism in the upper mantle, and (iv) reasonable interpretation for the deep tectonics of the Canadian Cordillera. Both P_n and teleseismic shear-wave splitting data measured from the Southern Canadian Cordillera can be well explained by assuming a horizontal, NE-oriented, plastic flow in the asthenospheric mantle above about 400 km.

Pervasive, closely spaced, foliation-perpendicular, brittle extension fractures of garnet crystals are very common in high grade, foliated and lineated metamorphic rocks. The garnet fractures may be observed both in the field and under the microscope. However, to our knowledge, the garnet fractures have not been studied explicitly and in detail in the literature, and no mechanical model has been proposed for their origin(s). In chapter 3, I choose high grade mylonites and gneisses from the Morin shear zone (MSZ) of the Grenville Province (Quebec) as an example to demonstrate characteristics of garnet fractures and to analyze the origin of the fractures.

Knowledge of joint spacing is important for the solution of a number of very practical problems in the design and stability of engineering and mining projects, such as major roads cuts, open pits, large mines and other underground openings and chambers. It is also important in the development of models for underground flow of water and hydrocarbons in fractured rocks where a high permeability is so desirable that fractures need to be artificially induced. Knowledge of rock mass behavior and permeability is also extremely important for nuclear waste disposal and reservoir construction where it is desirable to prevent leakage. However, it is very difficult for geologists to measure directly the joint spacing in subsurface strata. If a relationship between joint spacing and bed thickness is known, it is possible to determine the joint spacing from the bed thickness data obtained from boreholes. In chapter 4, I will investigate the relationship between the joint spacing and bed thickness in Cambrian flysch sediments at Plage Victor in the Saint-Jean-Port-Joli area of the Quebec Appalachians.

In order to facilitate the reading of this thesis, a brief review of basic principles is provided below.

1.2. Seismic anisotropy

An elastic solid is said to be 'homogeneous' if the characteristics of the solid are independent of position, and it is regarded to be 'isotropic' if the properties of the solid are independent of direction. Conversely the word 'anisotropic' is used for a material whose properties vary with direction. Seismic anisotropy is revealed as velocity variations both as a function of propagation and polarization direction of seismic wave (Silver, 1996). The propagation anisotropies commonly studied are azimuthal variations in the body-wave phase Pn velocity for the mantle below the Moho (see Smith and Ekstrom, 1999 for review). On the other hand, another important manifestation of the polarization anisotropy is shear-wave splitting that is often revealed when one component of a shear wave travels faster than the orthogonal component in anisotropic media (Fig. 1.1) and that is a seismological analog of optical birefringence. The anisotropic parameters of the shear-wave splitting are obtained as the polarization direction (ϕ) of the fast arrived split S-wave and the delay time (δt) between the fast and slow S-wave arrivals.

The origin of the shear-wave splitting is geologically interpreted in terms of mineral lattice preferred orientation (LPO), which develops in deformed rocks when the deformation mechanism is dominated by recovery-accommodated dislocation creep. In general, LPOs are correlated with tectonic processes based on their structural frameworks such as foliation and lineation. According to laboratory measurements, the fast splitting direction is dependent on the propagation direction of the seismic ray path relative to the structural framework (Fig. 1.2) (e.g., Ji and Salisbury, 1993). If seismic rays propagate parallel to the Y-direction or the Z-direction, the fast polarization directions are parallel to the lineation direction (X-direction). If S-wave rays propagate

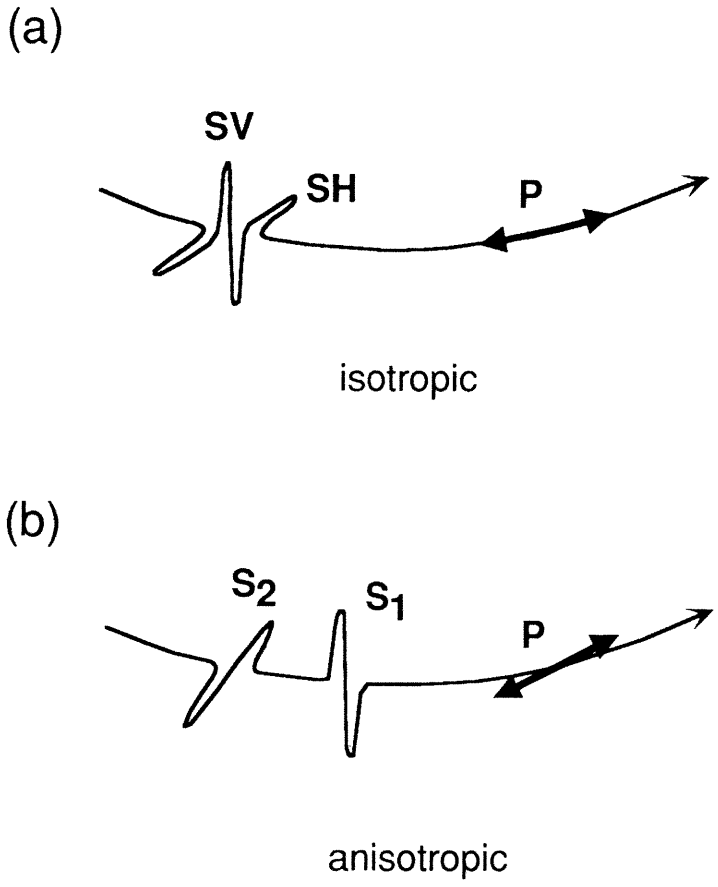

Figure 1.1. Schematic figures of seismic wave propagation in isotropic (a) and anisotropic (b) media, modified from Savage (1999). In isotropic media, P-wave vibrates parallel to the propagation direction. Horizontal (SH) and vertical (SV) components of the S-wave follow the P-wave at the same velocity. In anisotropic media, the P-wave vibrates oblique to the propagation direction, while the S-wave is split into fast (S_1) and slow (S_2) components.

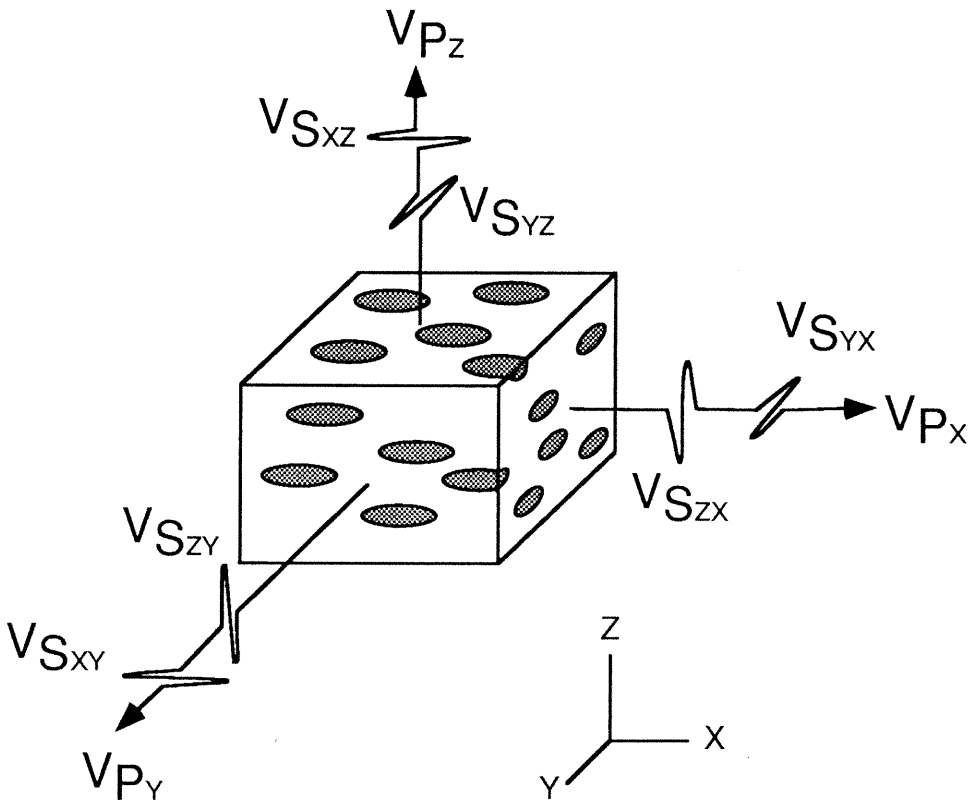

Figure 1.2. Schematic diagram showing the orientations of P and S wave velocities relative to the structural framework (X, Y, and Z directions). X: direction parallel to the stretching lineation; Y: direction normal to the lineation in the foliation plane; Z: direction normal to the foliation plane.

parallel to the X-direction, the fast polarization directions are parallel to the Y-direction. Thus, if we know the structural framework beneath a seismic station, and if the seismic wave is a vertically-propagating SKS phase, it becomes possible to infer the structural and tectonic implications of shear-wave splitting. If the framework is unknown, the direction of ϕ can coincide with any orientation in the rocks, making it difficult to interpret the shear-wave anisotropy in terms of any geologic/tectonic features (Ji et al., 1994).

Shear-wave splitting has been observed in different tectonic settings (e.g., continents, subduction zones, rift zones, and mid-oceanic ridges), and from different original depths of earthquakes (see reviews by Silver, 1996; Savage, 1999). The average SKS δt value for the whole world is estimated to be about 1.0 s by Silver (1996). According to a variety of studies focused on crustal anisotropy (see Silver, 1996; Savage, 1999), the majority of the crust displays splitting delay times of 0.1 to 0.3 s regardless of the crustal thickness, with occasional values up to 0.5 s. The possible sources of the crustal anisotropy are (1) stress-aligned fluid-filled fractures; (2) fractures in the vicinity of active faults; and (3) intrinsic lithological layering or structural anisotropy resulting from deformation, metamorphism or sedimentation (Kaneshima, 1990). Thus the average delay time of 1.0 sec is too large to be confined to the crust, and it is considered to originate mainly in the upper mantle (Silver and Chan, 1988, 1991). Such in-situ measurements are also in good agreement with laboratory shear-wave splitting measurements, which show that the splitting delay times in crustal rocks are less than 0.2 s for a thickness of 10 km (Ji and Salisbury, 1993), while those in mantle rocks are 1.0 s for a thickness of 200 km (e.g., Long and Christensen, in press). Furthermore, mantle xenolith studies yield S-wave anisotropy values of up to 7% according to the LPO of mantle minerals, primarily olivine, and they also indicate that the fast polarization direction ϕ tends to align parallel to the olivine a axes (Mainprice and Silver, 1993; Ji et al., 1994, Kern et al., 1996). Although it is still uncertain whether

anisotropy continues through to the 400-600 km transition zone from the upper parts of the mantle, in general, anisotropy in the upper mantle is confined to above the Lehmann discontinuity at about 200 km depth, which may be a transition from dislocation creep and anisotropic material in the upper mantle to diffusion creep and isotropic material below (e.g. Karato, 1992; Zhang and Karato, 1995). In the mantle below the transition zone from 400-600 km, most studies suggest little or no anisotropy (e.g. Vinnik et al., 1992; Silver et al., 1999), indicating that lower mantle minerals such perovskite do not develop a strong LPO. This is consistent with experimental studies that imply deformation occurs by diffusion creep over most of the lower mantle (e.g. Karato and Li, 1992; Meade et al., 1995).

1.3. Theoretical calculations of seismic properties

Theoretical calculations of elastic wave propagation are based on the elastic theory. Elasticity, which is an end-member of the type of rheological behavior of rocks, describes the linear relation between stress and strain when the strain is fully recoverable. The elastic behavior of a material is described by Hooke's law:

$$\sigma_{ij} = C_{ijkl}\varepsilon_{kl} \qquad (1.3.1)$$

or

$$\varepsilon_{kl} = S_{ijkl}\sigma_{ij} \qquad (1.3.2)$$

where σ_{ij} and ε_{ij} are stress and strain tensors, respectively, and C_{ijkl} and S_{ijkl} are the elastic coefficients and the elastic stiffnesses, respectively, which consist of a set of 81 (3^4) elements (each i, j, k, and l takes one of the three directions, 1, 2, or 3). However, since σ_{ij} and ε_{ij} are symmetric tensors and have only six components, the both elastic coefficient and stiffness parameters can be reduced to 36 independent elements. For example, the elastic coefficients are:

$$c_{ij} = \begin{pmatrix} c_{11} & c_{12} & c_{13} & c_{14} & c_{15} & c_{16} \\ c_{21} & c_{22} & c_{23} & c_{24} & c_{25} & c_{26} \\ c_{31} & c_{32} & c_{33} & c_{34} & c_{35} & c_{36} \\ c_{41} & c_{42} & c_{43} & c_{44} & c_{45} & c_{46} \\ c_{51} & c_{52} & c_{53} & c_{54} & c_{55} & c_{56} \\ c_{61} & c_{62} & c_{63} & c_{64} & c_{65} & c_{66} \end{pmatrix} \qquad (1.3.3)$$

Furthermore, when the relations can be proved on the basis of the existence of the strain energy function, the elastic coefficients are reduced to 21 independent elements because of the following relation:

$$c_{ij} = c_{ji} \qquad (1.3.4).$$

Since crystals generally exhibit crystallographic symmetries, the number of independent coefficients is reduced depending on the different crystallographic symmetries (Fig. 1.3).

Table 1.1. Number of independent elastic coefficients for selected symmetry systems.

Symmetry	Number of independent elastic coefficients	Example
Triclinic	21	plagioclase
monoclinic	13	clinopyroxene
orthorhombic	9	orthopyroxene
tetragonal	6	stishovite
trigonal I	7	ilmenite
trigonal II	6	quartz
hexagonal	5	ice
cubic	3	garnet
isotropic solid	2	volcanic glass

For homogeneous isotropic elastic materials, compressional (V_P) and shear (V_S)

Stiffness tensor components (*) of the major crustal and upper mantle minerals. Units are in GPa.

A - Major crustal minerals

Quartz [1]

$$(C_{ij}) = \begin{pmatrix} 86.6 & 6.7 & 12.6 & -17.8 & 0 & 0 \\ 6.7 & 86.6 & 12.6 & 17.8 & 0 & 0 \\ 12.6 & 12.6 & 106.6 & 0 & 0 & 0 \\ -17.8 & 17.8 & 0 & 57.8 & 0 & 0 \\ 0 & 0 & 0 & 0 & 57.8 & -17.8 \\ 0 & 0 & 0 & 0 & -17.8 & 39.9 \end{pmatrix}$$

density = 2.65 g/cm³
symmetry: trigonal

Calcite [1]

$$(C_{ij}) = \begin{pmatrix} 144 & 53.9 & 51.1 & -20.5 & 0 & 0 \\ 53.9 & 144 & 51.1 & 20.5 & 0 & 0 \\ 51.1 & 51.1 & 84.0 & 0 & 0 & 0 \\ -20.5 & 20.5 & 0 & 33.5 & 0 & 0 \\ 0 & 0 & 0 & 0 & 33.5 & -20.5 \\ 0 & 0 & 0 & 0 & -20.5 & 45.1 \end{pmatrix}$$

density = 2.712 g/cm³
symmetry:trigonal

Feldspar (microcline) [2]
$(Or_{78.5}Ab_{19.4}An_{2.1})$

$$(C_{ij}) = \begin{pmatrix} 62.5 & 42.8 & 3.8 & 0 & -15.4 & 0 \\ 42.8 & 172 & 24.1 & 0 & -14.3 & 0 \\ 3.8 & 24.1 & 124 & 0 & -11.5 & 0 \\ 0 & 0 & 0 & 14.3 & 0 & -2.8 \\ -15.4 & -14.3 & -11.5 & 0 & 22.3 & 0 \\ 0 & 0 & 0 & -2.8 & 0 & 37.4 \end{pmatrix}$$

density = 2.56 g/cm³
symmetry: triclinic (quasi monoclinic)

Feldspar (oligoclase) [3]
(An_{24})

$$(C_{ij}) = \begin{pmatrix} 81.8 & 39.3 & 40.7 & 0 & -9.0 & 0 \\ 39.3 & 145 & 34.1 & 0 & -7.9 & 0 \\ 40.7 & 34.1 & 133 & 0 & -18.5 & 0 \\ 0 & 0 & 0 & 17.7 & 0 & -0.8 \\ -9.0 & -7.9 & -18.5 & 0 & 31.2 & 0 \\ 0 & 0 & 0 & -0.8 & 0 & 33.3 \end{pmatrix}$$

density = 2.64 g/cm³
symmetry: triclinic (quasi monoclinic)

Diopside [4]

$$(C_{ij}) = \begin{pmatrix} 204 & 84.4 & 88.3 & 0 & -19.3 & 0 \\ 84.4 & 175 & 48.2 & 0 & -19.6 & 0 \\ 88.3 & 48.2 & 238 & 0 & -33.6 & 0 \\ 0 & 0 & 0 & 67.5 & 0 & 11.3 \\ 19.3 & 19.6 & 33.6 & 0 & 58.8 & 0 \\ 0 & 0 & 0 & 11.3 & 0 & 70.5 \end{pmatrix}$$

density = 3.31 g/cm³
symmetry: monoclinic

Hornblende [5]

$$(C_{ij}) = \begin{pmatrix} 116 & 45 & 61 & 0 & 4 & 0 \\ 45 & 160 & 66 & 0 & -2 & 0 \\ 61 & 66 & 192 & 0 & 10 & 0 \\ 0 & 0 & 0 & 57.4 & 0 & -6 \\ 4 & -2 & -10 & 0 & 31.8 & 0 \\ 0 & 0 & 0 & -6 & 0 & 36.8 \end{pmatrix}$$

density = 3.124 g/cm³
symmetry: monoclinic

Mica (muscovite) [6]

$$(C_{ij}) = \begin{pmatrix} 178 & 42.4 & 14.5 & 0 & 0 & 0 \\ 42.4 & 178 & 14.5 & 0 & 0 & 0 \\ 14.5 & 14.5 & 54.9 & 0 & 0 & 0 \\ 0 & 0 & 0 & 12.2 & 0 & 0 \\ 0 & 0 & 0 & 0 & 12.2 & 0 \\ 0 & 0 & 0 & 0 & 0 & 67.8 \end{pmatrix}$$

density = 2.790 g/cm³
symmetry: monoclinic (quasi hexagonal)

B - Major upper-mantle minerals

Olivine [7]
$(Mg_{92.7}Fe_{7.2})_2SiO_4$

$$(C_{ij}) = \begin{pmatrix} 323.7 & 66.4 & 71.6 & 0 & 0 & 0 \\ 66.4 & 197.6 & 75.6 & 0 & 0 & 0 \\ 71.6 & 75.6 & 235.1 & 0 & 0 & 0 \\ 0 & 0 & 0 & 64.6 & 0 & 0 \\ 0 & 0 & 0 & 0 & 78.7 & 0 \\ 0 & 0 & 0 & 0 & 0 & 79.0 \end{pmatrix}$$

density = 3.311 g/cm³
symmetry: orthorombic

Orthopyroxene [8]
(bronzite)

$$(C_{ij}) = \begin{pmatrix} 230 & 70 & 57.3 & 0 & 0 & 0 \\ 70 & 165 & 50 & 0 & 0 & 0 \\ 57.3 & 50 & 206 & 0 & 0 & 0 \\ 0 & 0 & 0 & 83.1 & 0 & 0 \\ 0 & 0 & 0 & 0 & 76.4 & 0 \\ 0 & 0 & 0 & 0 & 0 & 78.5 \end{pmatrix}$$

density = 3.335 g/cm³
symmetry: orthorombic

Garnet (pyrope) [5]

$$(C_{ij}) = \begin{pmatrix} 287.4 & 105.0 & 105.0 & 0 & 0 & 0 \\ 105.0 & 287.4 & 105.0 & 0 & 0 & 0 \\ 105.0 & 105.0 & 287.4 & 0 & 0 & 0 \\ 0 & 0 & 0 & 91.6 & 0 & 0 \\ 0 & 0 & 0 & 0 & 91.6 & 0 \\ 0 & 0 & 0 & 0 & 0 & 91.6 \end{pmatrix}$$

density = 3.582 g/cm³; symmetry: cubic

(*) The direct set of mutually perpendicular axes (x_1, x_2, x_3) is oriented as follows:
- symmetry around axis x_3 for hexagonal crystals
- $(x_1, x_2, x_3) \Leftrightarrow$ ([100], [010], perpendicular to (001)) for monoclinic crystals.

(for other symmetry systems see the caption of table 3-2).

[1] Hearmon (1956); [2] Ryzhova and Aleksandrov (1965); [3] Ryzhova (1964); [4] Aleksandrov et al. (1963); [5] Hearmon (1979); [6] Aleksandrov and Ryzhova (1961c); [7] Kumazawa and Anderson (1969); [8] Kumazawa (1969).

Figure 1.3. Elastic constants in GPa for typical rock-forming minerals.

wave velocities, density (ρ), and the elastic moduli are related by the following equations:

Bulk Modulus: $$K = \rho(V_p^{\,2} - \frac{4}{3}V_s^{\,2}) \qquad (1.3.5)$$

Shear Modulus: $$\mu = \rho V_S^{\,2} \qquad (1.3.6)$$

Poisson's Ratio: $$\upsilon = \frac{\left[(Vp/Vs)^2 - 2\right]}{2\left[(Vp/Vs)^2 - 1\right]} \qquad (1.3.7)$$

Young's Modulus: $$E = 2\mu(1+\upsilon) \qquad (1.3.8)$$

Compressional Wave Velocity:

$$V_p = \sqrt{(K + (4/3)\mu)/\rho} \qquad (1.3.9)$$

Shear Wave Velocity: $$V_S = \sqrt{\mu/\rho} \qquad (1.3.10).$$

The elastic constants of an isotropic, monomineralic aggregate containing a large number of randomly oriented, highly anisotropic crystals can be calculated from the single crystal data according to the following equations:

$$C_{11} = \lambda + 2\mu \qquad (1.3.11)$$

$$\mu = C_{44} \qquad (1.3.12)$$

$$C_{12} = \lambda = C_{11} - 2C_{44} \qquad (1.3.13)$$

$$K = \frac{3\lambda + 2\mu}{3} \qquad (1.3.14)$$

$$\lambda = \frac{3K - 2\mu}{3} \qquad (1.3.15)$$

where λ is called Lame's constant.

For a homogeneous, anisotropic medium, the velocities (V) and displacement directions of the three waves (P, S_1, S_2) are given by the eigenvalues and eigenvectors of the second order tensor velocity matrix T_{il} defined by the Christoffel equation:

$$\det|T_{il} - \rho V^2 \delta_{ik}| = 0 \qquad (1.3.16)$$

and

$$T_{il} = C_{ijkl} n_j n_k \qquad (1.3.17)$$

where ρ is density, δ_{ik} is the Kronecker delta (δ_{ik} =1 if i=j; δ_{ik} =0 if $i \neq j$), C_{ijkl} is the elasticity tensor for the media, and n is a unit vector that defines the propagation direction. If a density ρ and an elasticity C_{ijkl} are assigned and a propagation direction (wave normal) vector is given, the solution of Eq. (1.3.17) as an eigenvalue problem gives the three velocities for plane waves propagating in the direction of the wave normal.

The shear wave splitting parameter, δt, is estimated from the following equation as the approximate expression:

$$\delta t = L \delta V_s / V_s \qquad (1.3.18)$$

where L is the path length, δV_S is the dimensionless intrinsic anisotropy, which is a function of n, and V_s is the isotropically averaged shear wave velocity (Silver and Chan, 1991). Another parameter ϕ is determined by the crystallographic orientation of minerals. The anisotropies of V_P and V_S are calculated from the following equations:

$$A(V_P) = 2(V_p{}^{max} - V_p{}^{min}) / (V_p{}^{max} + V_p{}^{min}) \qquad (1.3.19)$$

$$A(V_S) = 2(V_{S_1} - V_{S_2}) / (V_{S_1} + V_{S_2}) \qquad (1.3.20).$$

Thus, in order to calculate the seismic velocities and their anisotropies of a single crystal, we need to know the density (ρ), elastic constants (C_{ij}) and a crystallographic orientation of the single crystal (Fig. 1.4). To calculate the properties of a polycrystalline rock, we need similar information of the rock. Regarding rocks as mineral aggregates, the density and elastic constants of rocks can be predicted from single crystal data by considering the volume fraction and the LPOs of the constituent minerals (Fig. 1.4).

The average density ($\overline{\rho}$) of aggregates is estimated as

$$\overline{\rho} = \sum_{i=1}^{N} f_i \rho_i \qquad (1.3.21)$$

where N is the number of mineral phases, and f_i and ρ_i are the volume fraction and density, respectively, of the mineral phase i. Rock densities depend on the temperature and pressure,

$$\rho(P,T) = \rho_0 + (\rho_0/K)(P - P_0) - \alpha\rho_0(T - T_0) \qquad (1.3.22)$$

where ρ_0, K, and α are the density at the ambient condition, the bulk modulus, and the thermal expansion, respectively. Values of these terms for mantle minerals such olivine, Opx, Cpx, and spinel are given in Appendix 1.

The elastic coefficients of aggregates predicted from single crystal data vary depending on the assumptions embedded in the equations of state used for determining the behavior of material under high pressure and temperature. There are three hypotheses: Voigt (Voigt, 1928), Reuss (Reuss, 1929) and Hill (or Voigt-Reuss-Hill)

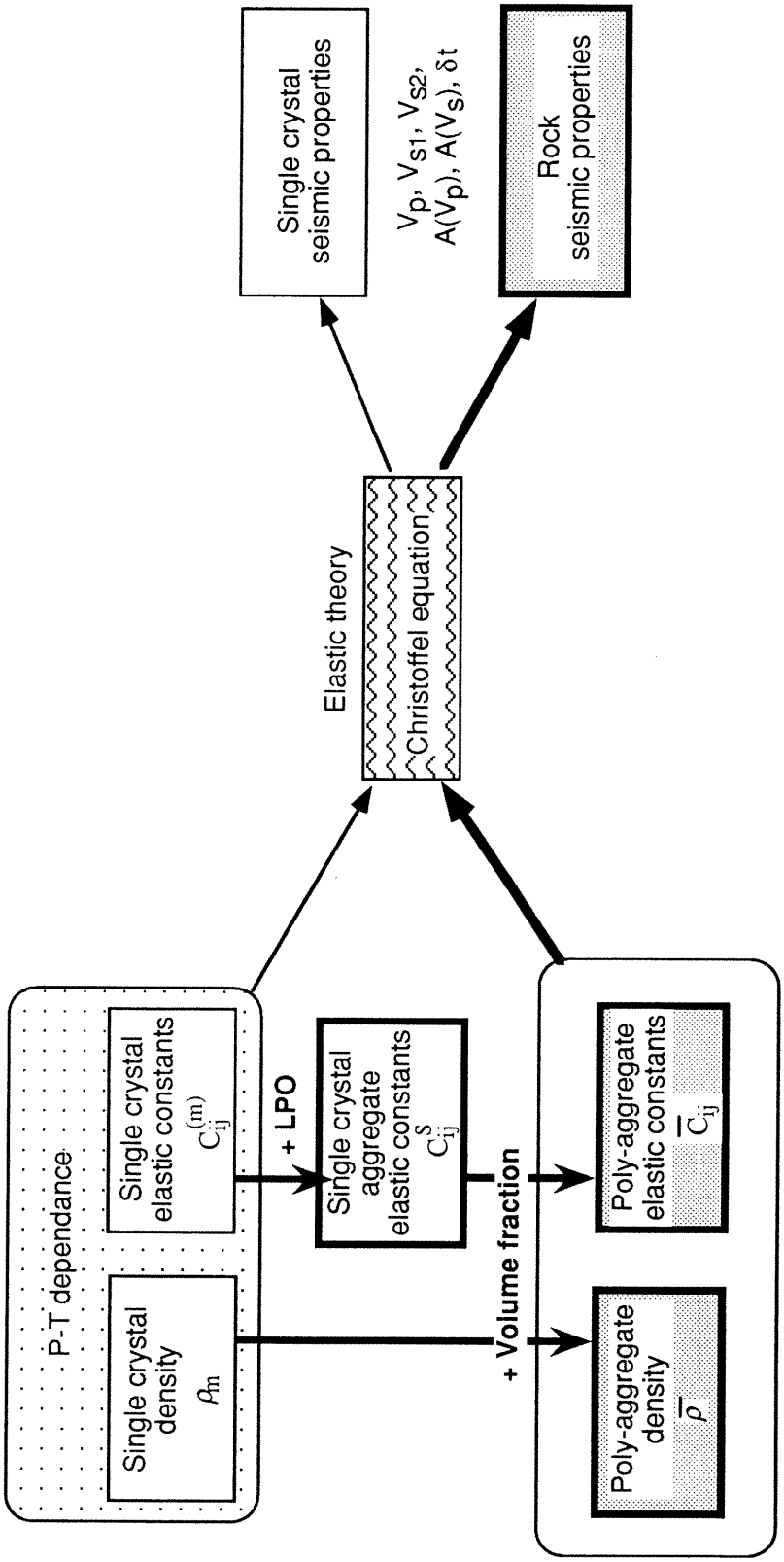

Figure 1.4. Flow chart used for calculating seismic properties of rocks.

(Hill, 1952). In the Voigt scheme, it is assumed that the strain ε_{ij} induced in an aggregate is uniform throughout the aggregate. The average stress (σ_{ij}) in the aggregate as a whole is defined as the space average of the uniform stress fields in each grain

$$\sigma_{ij} = (\sum_{1}^{N} C_{ij}^{(m)} / N)\varepsilon_{ij} = C_{ij}\varepsilon_{ij} \qquad (1.3.23)$$

where N is the total number of grains in the sample, and C_{ij} is the Voigt average elastic stiffness tensor.

In the Reuss scheme, it is assumed that stress is uniform throughout the aggregate, and thus the Reuss average compliance tensor S_{ij} is calculated as:

$$\varepsilon_{ij} = (\sum_{1}^{N} S_{ij}^{(m)} / N)\sigma_{ij} = S_{ij}\sigma_{ij} \qquad (1.3.24)$$

$$C_{ij} = 1 / S_{ij} \qquad (1.3.25).$$

The Hill approximation is the arithmetic mean of the elastic constants calculated according to the Voigt and Reuss schemes. Since the Voigt average yields the closest agreement between the calculated value of seismic velocities and those of laboratory measurements for natural rocks (e.g., Crosson and Lin, 1971; Kern and Wenk, 1985; Ji and Salisbury, 1993; Ji et al., 1993), it is generally used for velocity calculations. The Voigt average elastic coefficient is calculated for an aggregate with several mineral phases from the following equation (Peselnick et al., 1974):

$$C_{ij} = \sum_{1}^{S} f_S C_{ij}^{S} \qquad (1.3.26)$$

where S is the number of constituent mineral phases, f_S is the volume fraction of one of the mineral phases S, and C_{ij}^{S} are the elastic constants of the one of the mineral phases S.

C_{ij}^{S} is calculated as the arithmetic average of all of the mineral phases S from the following equation:

$$C_{ij}^{S} = \sum_{1}^{Ns} C_{ij}^{(m)} / Ns \qquad (1.3.27)$$

where Ns is the total number of grains of mineral phase S. $C_{ij}^{(m)}$ is the elastic coefficient in the mth grain of mineral phase S, and is affected by the crystallographic orientation of each grain m. As for ρ_S , $C_{ij}^{(m)}$ depends on the temperature and pressure according to an equation

$$C_{ij}(P,T) = C_{ij}(P_0,T_0) + (dC_{ij}/dP)(P - P_0) - (dC_{ij}/dT)(T - T_0) \qquad (1.3.28)$$

where $C_{ij}(P_0,T_0)$, dC_{ij}/dP, and dC_{ij}/dT are elastic constants at the ambient condition, pressure derivatives, and temperature derivatives of elastic constants, respectively. Values of these coefficients are given for mantle minerals in Appendix 1.

1.4. Shear-lag theory

Shear-lag theory or fiber-loading theory, originally proposed by Cox (1952), is the most widely used model in material science to describe the effect of loading for a two-phase composite material (Clyne and Withers, 1993) and has been developed and improved in terms of mechanical equilibrium and boundary conditions by Holister and Thomas (1966), Kelly and Macmillan (1986) and Zhao and Ji (1997). The concept of this theory can be briefly described as: the harder phase carries a comparatively greater part of the stress, while the soft phase tends to take the greater part of the strain (with reference to the volume fraction ratio) (Ji and Zhao, 1994). The theory considers a composite material, consisting of a single fiber embedded in an isotropic incompetent matrix, with extension stress parallel to the fiber direction (Fig. 1.5). Because of the

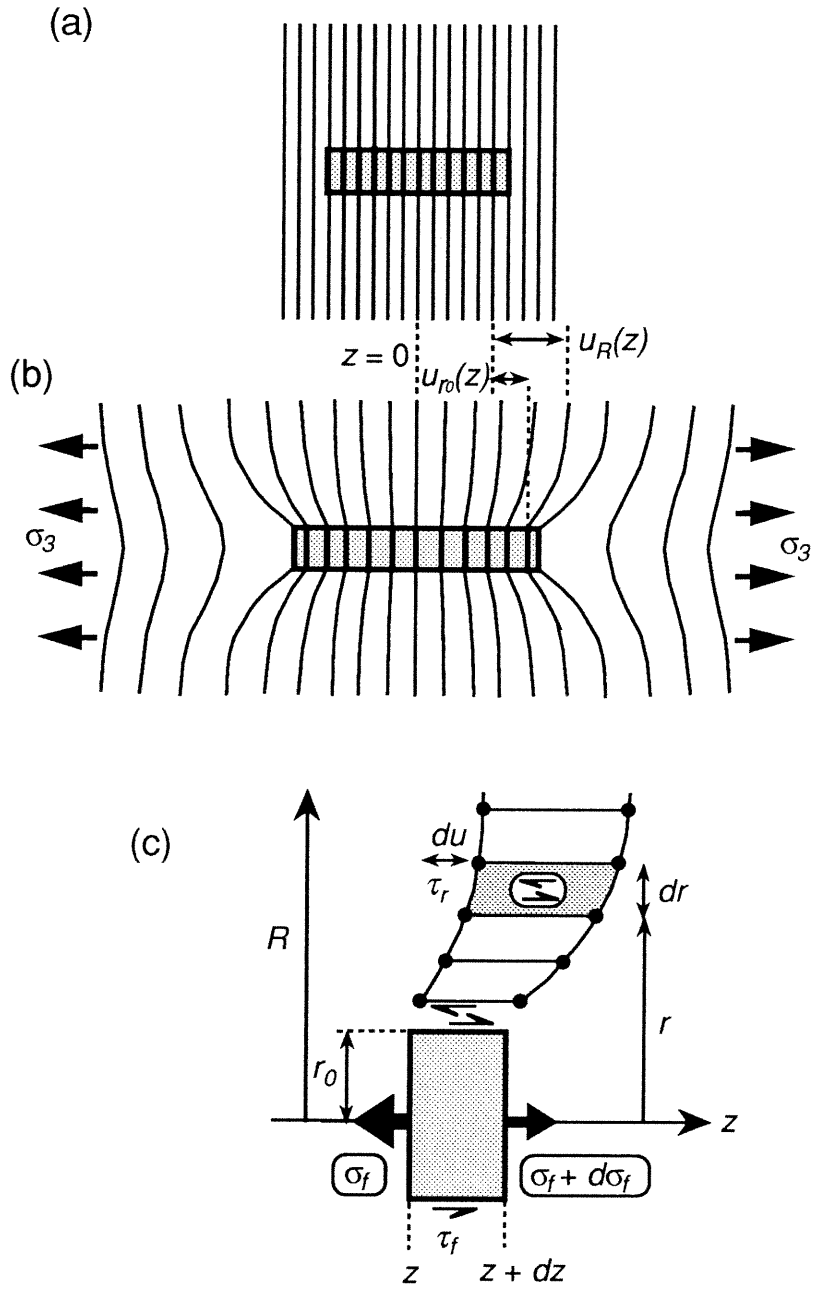

Figure 1.5. Schematic illustrations of the basic principles of the shear-lag theory modified from Clyne and Withers (1993). (a) Unstressed composite material composed of a fiber embedded in an isotropic matrix. (b) The composite under extensional stress with axial displacements parallel to the fiber. (c) Variation of the stress and strain with radial location in the composite.

difference in elastic moduli of the two phases, the elastic displacement at the boundary between the fiber and the matrix will be different, producing radial shear stress in the matrix (τ_r) and at the interface between the fiber and the matrix (τ_i) towards the z direction parallel to the fiber direction (Fig. 1.5c). The shear stress τ_r at any particular radius r can be related to the shear stress τ_i at the interface by the relation

$$\tau_r = \tau_i\left(\frac{r_0}{r}\right) \tag{1.4.1}$$

where r_0 is the radius of the fiber.

The increment of the displacement, *du*, on moving out from the fiber axis by *dr* is determined by the shear strain γ and the shear modulus of matrix G_m,

$$\frac{du}{dr} = \gamma = \frac{\tau_r}{G_m} = \frac{\tau_i}{G_m}\left(\frac{r_0}{r}\right) \tag{1.4.2}$$

For a given z, the difference between the displacement of the matrix at a radius R and that of the interface is given by a simple integration

$$\int_{u_{r_0}}^{u_R} du = \frac{\tau_i r_0}{G_m}\int_{r_0}^{R}\frac{dr}{r} \tag{1.4.3}$$

or

$$\left(u_R - u_{r_0}\right) = \frac{\tau_i r_0}{G_m}\ln\left(R/r_0\right) \tag{1.4.4}$$

assuming that the matrix strain is uniform remote from the immediate vicinity of the fiber. Thus the tensile stress in the fiber $\sigma_f(z)$ is built up from the interfacial shear stress τ_i, which results from the shear strain on the interface. The force balance is

$$2\pi r_0 \tau_i dz = -\pi r_0^2 d\sigma_f \tag{1.4.5}$$

or

$$\left(u_R - u_{r_0}\right) = \frac{\tau_i r_0}{G_m}\ln\left(R/r_0\right) \qquad (1.4.6)$$

Now, the variation of τ_i with z is unknown a priori, but equation (1.4.4) can be used to relate it to displacement and hence to axial strains. The equation (1.4.6) becomes

$$\frac{d\sigma_f}{dz} = -\frac{2G_m}{r_0^2\ln\left(R/r_0\right)}\left(u_R(z) - u_{r_0}(z)\right) \qquad (1.4.7)$$

The displacements themselves are unknown, but their differentials are related to identifiable strains.

$$\frac{du_{r_0}(z)}{dz} = \varepsilon_f = \frac{\sigma_f}{E_f} \qquad (1.4.8)$$

and

$$\left.\frac{du_R(z)}{dz}\right|_{r=R} \approx \varepsilon_m \sim \varepsilon_c \qquad (1.4.9)$$

where ε_f, ε_m , and ε_c are the fiber strain, the matrix strain and the overall composite strain, respectively. Thus, the differentiation of Eq. (1.4.5) and the substitutions of Eqs. (1.4.6) and (1.4.7) leads to

$$\frac{d^2\sigma_f}{dz^2} = \frac{2G_m}{r_0^2\ln\left(R/r_0\right)}\left(\frac{\sigma_f}{E_f} - \varepsilon_c\right) \qquad (1.4.10)$$

Eq. (1.4.10) is a standard second order linear differential equation, with the solution

$$\sigma_f = E_f\varepsilon_c + A\sinh\beta z + B\cosh\beta z \qquad (1.4.11)$$

where A and B are constants and

$$\beta = \left(\frac{2G_{\mathrm{m}}}{E_f r_0^2 \ln(R_0/r)} \right)^{1/2} \qquad (1.4.12).$$

The boundary conditions are

$$\sigma_f = 0 \quad \text{at} \quad z = \pm L \qquad (1.4.13)$$

where L is the half-length of the fiber. The solution for Eq. (1.4.11) is thus

$$\sigma_f(z) = E_f \varepsilon_c \left[1 - \frac{\cosh(\beta z)}{\cosh(\beta L)} \right] \qquad (1.4.14)$$

The shear-lag model has been applied to explain extension boudinage structures of brittle minerals or compositional layers in a ductilely flowing matrix. For example, mesoscopic layer boudinage and belemnites in schists, and microscopic mineral boudinage such tourmaline and piedmontite in a quartz matrix. White et al. (1980) considered the shear-lag model as one of the possible mechanisms for the fracturing process of boudinaged tourmaline in mylonite. Ferguson and Lloyd (1981) and Lloyd et al. (1981) applied the shear-lag model described in Kelly and Macmillan (1986) to explain mesoscopic layered boudin structures. Ferguson (1987) and Masuda and Kuriyama, (1988) used the principle of the shear-lag model to explain the mid-point fracturing of belemnites and piedmontite in deformed metamorphic rocks, respectively. Ji and Zhao (1993) developed a modified shear-lag model to explain microboudins of circular, truncated, conical minerals such as tourmaline.

The shear-lag model has also been widely used to interpret extensional joints or mode I fractures in sedimentary rocks. Hobbs (1967) revised the shear-lag model to

explain the formation of joints and the linear relationship between joint spacing and layer thickness, observed by Bogdonov (1947) and Price (1966), in layered sedimentary rocks. Since then, the revised Hobbs' model has been widely used as a theoretical basis for the linear relationship between joint spacing and layer thickness in various sedimentary rocks (e.g., McQuillan, 1973; Ladeira and Price, 1983; Huang and Angelier, 1989; Narr and Suppe, 1991; Gross, 1993; Gross et al., 1995; Wu and Pollard, 1995). However, as pointed out recently by Zhao and Ji, (1997) and Ji and Saruwatari (1998), Hobbs' model was based on an unrealistic assumption that the shear stress in the matrix (bounding non-jointing beds) decreases *linearly* from the maximum value at the layer-matrix interface to zero *at a distance exactly equal to the jointing layer thickness* from the interface [equation (9) in Hobbs, 1967]. In order to exclude this assumption, Ji and Saruwatari (1998) revised Hobbs' model by taking into account the non-linear decay of the shear-stresses and the various thicknesses of bounding non-jointing beds. In Chapter 3 of this thesis, I applied the shear-lag theory to explain why tensile fractures occurred preferentially in stiff garnet crystals rather than in the matrix of felsic minerals such as quartz and feldspar in the high grade mylonites and metamorphic rocks from the Morin Shear zone (Grenville Province, Quebec). In Chapter 4, the shear-lag model is modified in order to explain the relationship between joint spacing and bed thickness in sedimentary rocks.

1.5. Fluid inclusion planes as tectonic indicators

Fluid inclusions have been considered as paleo-fluids which can provide evidence of fluid-rock interactions. Most previous studies have focused on chemical aspects in order to understand fluid compositions and the thermobarometric histories of rocks (e.g., Roedder, 1984). Physical aspects of fluid inclusions such as shape change and volume change have also been investigated in conjunction with the thermobarometric estimations using fluid densities (e.g., Roedder, 1984). Fluid inclusion

planes are recognized as secondary fluid inclusions which are aligned along pre-existing fractures (Fig. 1.6). These fractures are partially healed due to the so-called dissolution-precipitation process and are marked by aligned fluid inclusions with equant shapes (Tuttle, 1949). Tuttle (1949) has found that fluid inclusion planes are uniformly oriented over large area (24 x 32 hectares of granite), intimating the use of fluid inclusion planes as a microstructural indicator. Wise (1964) used fluid inclusion planes as microscopic fractures correlating with mesoscopic joints in Precambrian basement rocks. However, structural studies of fluid inclusion planes did not advance further until the late 1980s when many experimental results (e.g., Brace and Bombolakis, 1963; Fiedman and Logan, 1970; Peng and Johnson, 1972; Tapponnier and Brace, 1976; Krantz, 1979, 1983) suggested that most cracks are actually extensional fractures which propagated nearly parallel to the local maximum stress direction. Thus, being parallel to the σ_1-σ_2 plane, fluid inclusion planes were extensively studied by measuring their preferred orientations in granites and sandstones (e.g., Pecher et al., 1985; Lespinasse and Pecher, 1986; Kowallis et al., 1987; Jang et al., 1989; Laubach, 1989; Ren et al., 1989; Vollbrecht et al., 1991) as well as in drill cores (Wang and Sun, 1990; Vollbrecht et al., 1994, 1999). Those studies indicate that the orientations of fluid inclusion planes generally coincide with paleo- and present-regional σ_1-σ_2 planes. Furthermore, fluid inclusion planes are often developed in more than two sets with different fluid compositions or fluid densities (Fig. 9.1 in Passchier and Trouw, 1995; Fig. 2 in Lespinasse, 1999). Since the intersection relationship can be established from the cutting relationship, the sequence of fracturing and the associated fluid compositions and densities can be linked to deformation history and evolution of metamorphic conditions (Boullier et al., 1991, 1997; Passchier and Trouw, 1995).

Another important feature of fluid inclusion planes is shapes of their inclusions. When fluid inclusion planes are formed from fractures by healing, each fluid inclusion acquires a negative crystal shape, which corresponds to their lowest possible energy

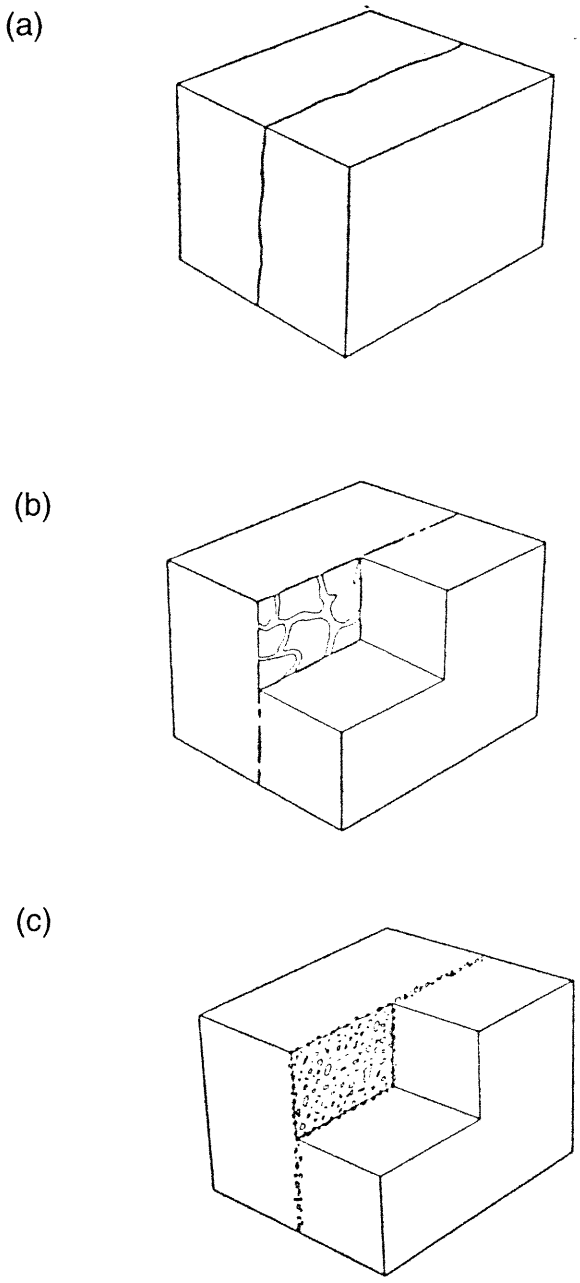

Figure 1.6. Schematic block diagrams illustrating the origin and development of a fluid inclusion plane, according to Tuttle (1949). (a) The first stage in the development of a fluid inclusion plane indicating a fracture. (b) Individual, thin, sheet-like inclusions formed by differential solution and deposition of silica. (c) More advanced stage of fluid inclusions with equant shapes.

(Tuttle, 1949). However, this low-energy configuration may be destroyed if the fluid inclusions are not in equilibrium with their physical environment, i.e., if the pressure and temperature do not correspond to the isochoric line of the inclusions (Boullier, 1999). According to experimental studies (Pecher, 1981; Gratier and Jenatton, 1984; Pecher and Boullier, 1984; Boullier et al., 1989, Sterner and Bodnar, 1989; Vityk and Bodnar, 1995), there are two types of changes in shape which correspond to slow and rapid loading rates (Boullier, 1999). For slow loading rates, though it is almost impossible to simulate slow natural loading rates in the laboratory, Vityk and Bodnar (1995) provides two types of fluid inclusion microstructure depending on the internal pressure in the inclusion with relatively slow loading rates (0.7-1 kb par week). When the internal pressure (P_i) becomes less than the confining pressure (P_C) (internal underpressure), as in the case of nearly isobaric cooling or nearly isothermal compression (Fig. 1.7), their experiment shows annular textures or implosion halos. This microstructure is remarkably similar to that found in the so-called Higher Himalaya metamorphic rocks (Boullier et al., 1991). When P_i exceeds P_C (internal overpressure), as in the case of nearly isothermal decompression or nearly isobaric heating (Fig. 1.7), many large inclusions tend to make smaller clusters and most of the medium and small-sized inclusions show a regular morphology and no decrepitation clusters. In the case of the rapid loading rate, however, fluid inclusions under internal overpressure lead to radial microcracks around previous larger inclusions (Pecher, 1981; Pecher and Boullier, 1984) or so-called 'decrepitation clusters' (Swanenberg, 1980; Boullier, 1999), while fluid inclusions under internal underpressure lead to a star-like texture (Sterner and Bodnar, 1989; Vityk et al., 1994). Such decrepitation structures are frequently observed in naturally deformed rocks (Swanenberg, 1980; Roedder, 1984; Hurai and Horn, 1992). Thus, investigating different shapes of inclusions can provide information about the evolution of P-T conditions. In Chapter 3 of the present thesis, I will use the microstructural characteristics of fluid inclusions together with their thermobarometric data to investigate the formation of fluid

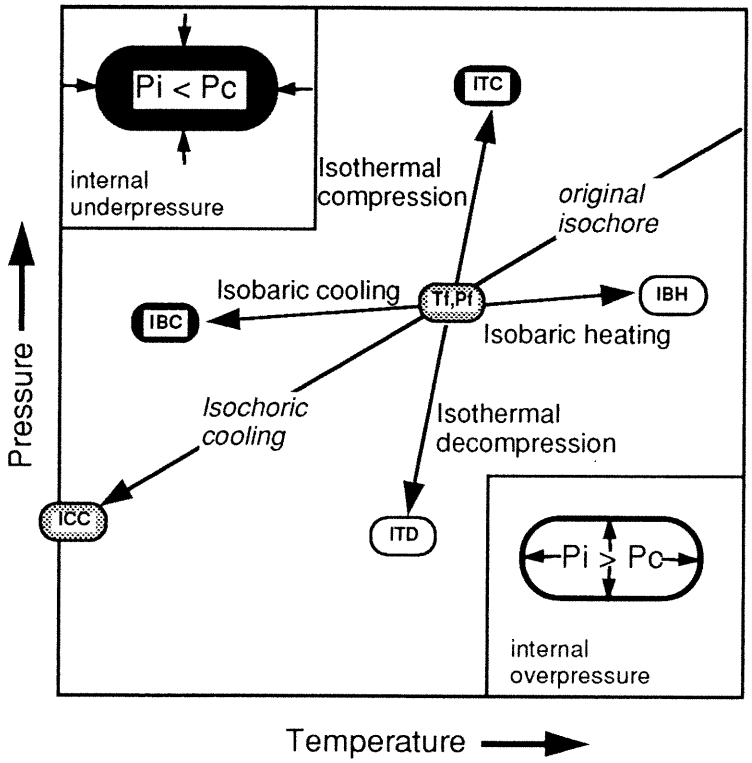

Figure 1.7. Schematic representation of P-T paths which a fluid inclusion might follow after entrapment at T_f and P_f, modified from Vityk and Bodnar (1995). The internal pressure in the inclusion (P_i) becomes less than the confining pressure (P_c) at P-T conditions above the original isochore line (internal underpressure), where P-T paths become isobaric cooling (IBC) and isothermal compression (ITC). Conversely, the P_i exceeds P_c at P-T condition under the isochore line (internal overpressure), where P-T paths include isothermal decompression (ITD) and isobaric heating (IBH). When the path approximates the fluid inclusion isochore, and so-called isochoric cooling (ICC) occurs, the effective pressure becomes zero ($P_i = P_c$).

inclusions and the role of fluids in fracturing of garnets from the high grade metamorphic rocks in the Morin Shear zone (Grenville Province, Quebec).

Chapter 2

Seismic properties of mantle xenoliths from the southern Canadian Cordillera: implications for upper mantle deformation

Man is learning to harness for his enquiring use the very wrath of the earth; the tremblings of our vibrant globe are used to 'X-ray' the deep interior.

Reginald A. Daly

(A. Holmes, 1965)

2.1. Introduction

One of the most powerful methods to understand the interior of the Earth is to study the passage of elastic seismic waves through the Earth and to inspect the generated anisotropy. While seismic refraction surveys provide Pn velocities and anisotropy information for the uppermost part of the upper mantle, shear wave splitting may provide information through the entire upper mantle (see Silver, 1996; and Savage, 1999 for reviews). Since Nur and Simons (1969) and Christensen (1971) experimentally observed shear wave splitting in naturally deformed rocks, the relationship between the shear wave anisotropy and lattice preferred orientation (LPO) in mineral has been extensively studied by both theoretical modeling (e.g., Ribe, 1989, 1992; Ribe and Yu, 1991; Tommasi, 1998) and laboratory experiments (e.g., Kern and Wenk, 1990; Ji and Salisbury, 1993; Long and Christensen, in press). Many natural mantle xenoliths from kimberlites and basalts have petrofabric patterns similar to those of peridotites from ophiolites: the olivine a-axes concentrate within the foliation plane and are aligned parallel to the stretching lineation (e.g., Christensen and Salisbury, 1979; Toriumi, 1984; Mainprice and Silver, 1993; Kern,

1993; Ji et al., 1994). Since numerical modeling shows that the polarization direction (ϕ) of the fast split shear wave is parallel to the olivine a-axes concentration, the observed mantle anisotropy is interpreted to be due to strain-induced LPO of olivine (e.g., Mainprice and Silver, 1993, Ji et al., 1994; Kern, 1996; Savage, 1999).

Since the first observation of shear-wave splitting beneath Honsu, Japan, (Ando et al., 1980) and especially during the last decade, measurements of shear wave splitting have accumulated from different tectonic settings around the world, providing important information on seismic anisotropy in the mantle (see Savage, 1999 for review). Of particular interest, the subduction zones yield more opportunities to comprehend the origin of seismic anisotropy because both direct S and ScS waves are frequently generated by earthquakes at various depths along the subducting slab (Table 2.1). Previous studies measuring direct S and ScS waves as well as teleseismic SKS and SKKS waves suggest that the anisotropy exists mantle portions both above and beneath the subducting slabs and that the anisotropic layer seems to be extended to the 400 km transition zone (e.g., Fischer and Wiens, 1996; Fouch and Fischer, 1996). It is still unclear, however, how the anisotropy is distributed (continuously or homogeneously?) in the upper mantle above 400 km. These studies reveal also that the ϕ directions of S and SKS waves are parallel either to the trend of the subduction or the plate margin (e.g., Japan, New Zealand, Caribbean, southern Kuriles) or to the absolute plate motion (APM) (e.g., Tonga, Izu-Bonin). Assuming the anisotropy is controlled by olivine LPO, the ϕ directions parallel to APM can be explained by two-dimensional corner flow associated with entrainment of lithosphere due to a subducting slab (Chastel et al., 1993; Dawson and Wenk, In press). In contrast, the trench-parallel anisotropy can be due to deformation by strike-parallel movement and compression in the upper mantle wedge (Saruwatari et al., 1998; Savage, 1999).

The Canadian Cordillera (Fig. 2.1) is one of the major mantle-xenolith-bearing provinces in the world, and has been the main target of LITHOPROBE

Table 2.1. Shear wave splitting measurements from different subduction zones in the world.

Region	Area	Phase	ϕ	Delay time (s)	ϕ parallel to:	Sources
North America	northern Cordillera	SKS	EW~NS	~1.55	Strike-slip fault zones	1,2
	southern Cordillera	SKS	NE-SW	~1.7	Relative plate motion	1,2
		S(i)	NW-SE	0.32	Trench	3
		S(s)	NW-SE	0.2	Trench	3
Central America	Caribbean	SKS	E-W	~2.1	Trench	4
South America	Colombia	SKS	N20°E	1.2	Trench	5
		S(i)	N6°E	~0.5	Trench	6
	Peru	SKS	N110°E	~1.1	30-40° wrt APM	7,8,9
		ScS	N110°E	~0.85	30-40° wrt APM	8
		S(d)	N110°E	~1.66	30-40° wrt APM	8,9
		S(i)	N110°E	~0.23	30-40° with APM	8
Pacific	NewZealand	SKS	N28°E	~1.5	Trench	10
		S(i)	NE	0.3-1.0	Trench	11
		S(s)	NE	~0.4	Trench	11
	Tonga	SKS	N60°W	~1.45	APM	12
		S(d)	N60°W	~1.8	APM	12
	Guam, Mariana	S(i)	E-W	~0.3	APM	13
Eurasia	Izu-Bonin	S(d)	WNW	~0.75	APM	14
	Japan	SKS	NNE	1.05-1.85	Trench	14
		ScS	NNW	~2.36	Trench	9,15,16
		S(d)	NW	~0.65	Trench	14,17,18
		S(i)	NS+EW	~1.15	Trench	9,15,16,17,18
		S(s)	NE~NW	~0.25	Trench	14,18
	southern Kuril	SKS	N	0.9-0.95	Trench	14
		S(d)	N	~1.35	Trench	14
		S(i)	N	0.4-0.6	Trench	14
	Aleutian	S(i)	N60°E	0.1-0.35	Trench	19

S(d), S(i) and S(s) indicate direct S waves from the earthquakes deeper than 400 km, between 400 km and 50 km, and shallower than 50 km, respectively. wrt APM: with respect to absolute plate motion. 1: Silver and Chan (1991); 2: Bostock and Cassidy (1995); 3: Cassidy and Bostock (1996); 4: Russo et al. (1996); 5: Vinnik et al. (1992); 6: Shih et al. (1991); 7: Russo and Silver (1994); 8: Kaneshima and Silver (1995); 9: Meade et al. (1995); 10: Gledhill and Gubbins (1996); 11: Gledhill and Stuart (1996); 12: Fischer and Wiens (1996); 13: Xie (1992); 14: Fouch and Fischer (1996); 15: Iidaka and Obara (1995); 16: Hiramatsu and Ando (1996); 17: Ando et al. (1983); 18: Okada et al. (1995); 19: Yang and Fischer (1995).

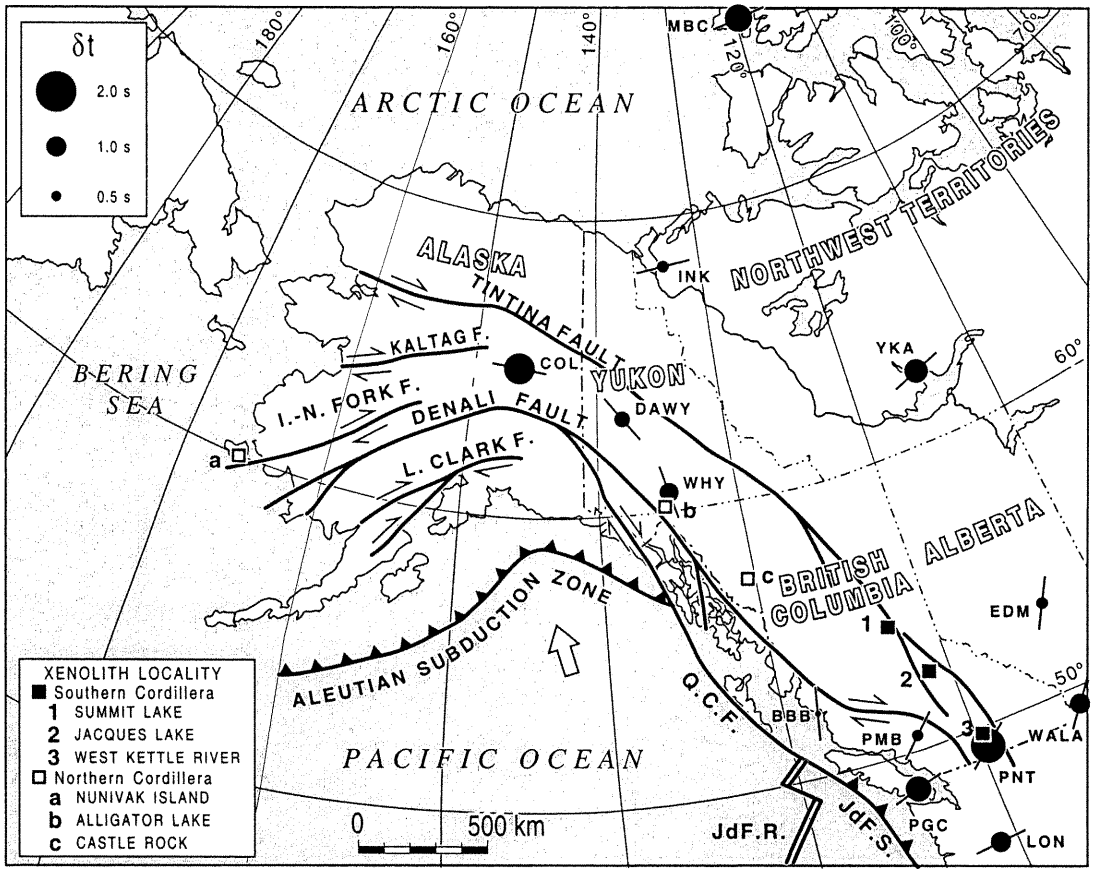

Figure 2.1. Simplified tectonic map of Northwestern America showing locations of mantle xenoliths. Shear-wave splitting parameters (ϕ and δt) have been measured at stations COL and LON by Silver and Chan (1991) and at other stations by Bostock and Cassidy (1994). Q.C.F.: Queen Charlotte Fault; JdF.R.: Juan de Fuca Ridge; JdF.S.: Juan de Fuca Subduction.

seismic reflection and teleseismic SKS splitting studies. The SKS splitting measurements in the northern Canadian Cordillera and Alaska show the fast polarization direction parallel to the major transcurrent fault systems (Bostock and Cassidy, 1995). This indicates coherent strike-slip deformation between the continental crust and upper mantle. The calibration of seismic properties using mantle xenoliths from these regions by Ji et al. (1994) suggests that the shear wave splitting in these active orogenic regions is controlled by modern tectonic deformation in the lithosphere and plastic flow in the asthenosphere. In the southern Canadian Cordillera, the ϕ directions of SKS and SKKS waves are nearly orthogonal to the regional tectonic trend with the delay time δt = 0.3-1.7 s (Silver and Chan, 1991; Bostock and Cassidy, 1995). On the other hand, the fast polarization directions of the direct S-waves measured near southern Vancouver Island are parallel to the continental margin with δt = 0.2-0.32 s.

In order to constrain the tectonic interpretation(s) of both Pn and teleseismic SKS splitting data obtained from the southern Canadian Cordillera, we investigated the microstructures, petrofabrics and seismic properties of ultramafic xenoliths collected from the region.

2.2. Mantle xenoliths from the southern Canadian Cordillera

The Canadian Cordillera located along the western continental margin of the North America plate has been tectonically active since the Early Proterozoic (Monger et al., 1994). The most parts were formed between the Middle Jurassic and the Paleocene (170-60 Ma) through successive accretion of tectonic terranes (mainly arc-related) to the western margin of the stable Canadian Shield (e.g., Gabrielse et al., 1991). Large dextral strike-slip movement began during Mesozoic compression and continues today along the Tintina, Denali and Queen Charlotte Fault zones. Calc-alkaline and alkaline basalts, which contain ultramafic xenoliths as samples of the

upper mantle, erupted in pull-apart zones within these strike-slip fault since the beginning of the Cenozoic (Clowes et al., 1992). These xenoliths provide an excellent opportunity to investigate the lithology and seismic properties of the upper mantle beneath the southern Canadian Cordillera.

The Canadian Cordillera is divided into five morphogeological belts whose present configuration resulted from the tectonic process responsible for the continental growth from east to west (Clowes et al., 1995). The xenoliths studied here are from sites located in the Omineca belt which is the southeasternmost of these belts. Seismic refraction profiling shows that the Moho beneath this belt is at a depth of 35-38 km (Clowes et al., 1995) and that the subducted Pacific lithosphere exists below about 300-400 km depth (Bostock and VanDecar, 1995). According to petrological analyses performed recently by Peslier (1999), the mantle xenoliths from the southern Cordillera are dominated by spinel lherzolite that evidently represents the dominant lithology of the lithospheric mantle beneath the southern Canadian Cordillera. A similar lithology has been established for the uppermost portion of the mantle beneath the northern Canadian Cordillera (Francis, 1987; Ji et al., 1994; Shi et al., 1998). The average volume fractions of olivine, orthopyroxene, clinopyroxene and spinel in the upper mantle beneath the southern Canadian Cordillera are: 60.9%, 24.8%, 11.8% and 2.5%, respectively. This modal composition was calculated from the weight percentages of the minerals estimated by D. Francis (McGill University, personal communication) based on C.I.P.W. norm calculations from whole rock analyses of more than 200 representative mantle xenolith samples. Microstructures of the xenoliths can be classified into 4 types: protogranular (Fig. 2.2a), equigranular (Fig. 2.2b), foliated (Fig. 2.2c) and porphyroclastic (Fig. 2.2d) textures. However, the protogranular texture is dominant.

The mantle xenoliths studied in this paper were collected from Summit Lake, Jacques Lake and West Kettle River (Fig. 2.1 and Table 2.2).

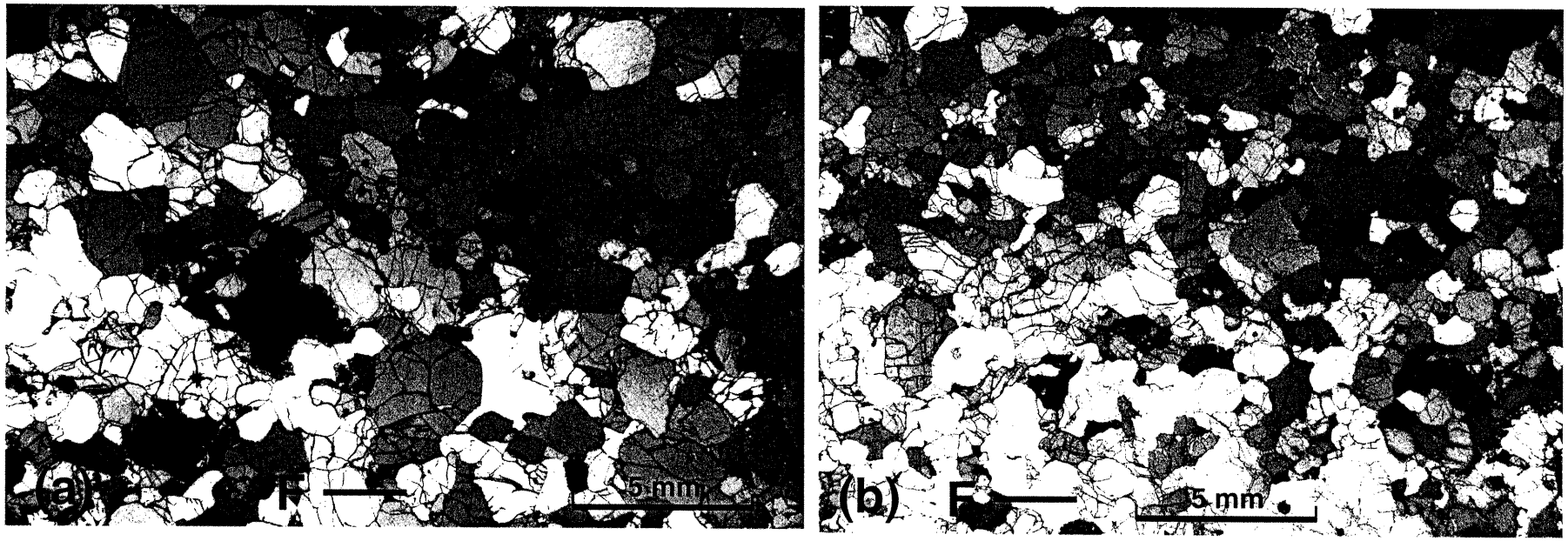

Figure 2.2. Photomicrographs of mantle xenoliths with protogranular (a), equigranular (b), foliated (c) and porphyroclastic (d) textures from the southern Canadian Cordillera. The foliation plane is indicated by F.

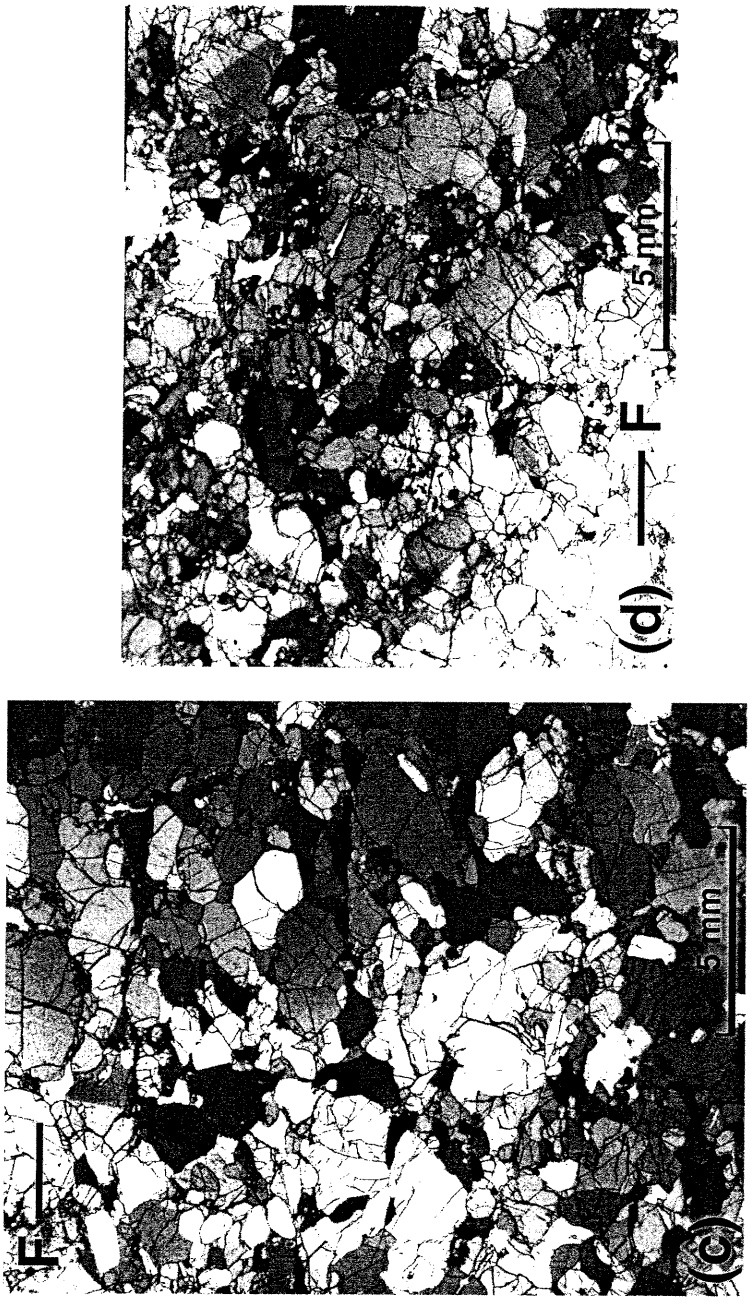

Figure 2.2. (Continued).

2.2.1. Summit Lake

Summit Lake (122°45' W, 54°25' N) is located 40 km north of Prince George, British Columbia (Fig. 2.1). The host rock of the xenoliths is a basanitoid flow of Late Cenozoic (possibly post-glacial) age (Brearley et al., 1984). The ultramafic xenoliths are composed of chrome diopside-bearing and aluminous augite-bearing series (Wilshire and Shervais, 1975). The most abundant xenoliths are spinel lherzolite (55%), with subordinate wehrlite (22%), clinopyroxenite (10%), olivine websterite (10%), websterite (2%) and dunite (1%) (Brearley et al., 1984). This site is characterized as a lherzolite-wehrlite site when comparing it to other sites in the Cordillera. Furthermore, the lherzolite is divided into two groups, normal lherzolite and orthopyroxene-poor lherzolite (Peslier, 1999). The average volumetric composition of the dominant normal lherzolite, extrapolated from weight percentages by whole rock analyses (Canadian Cordillera petrological database of D. Francis), is: 60.9% olivine, 25.3% orthopyroxene, 11.4% clinopyroxene, and 2.4% spinel.

Using the two pyroxene geothermometer of Wells (1977), equilibrium temperatures are calculated to be 1080-1100 °C (Brearley et al., 1984). The more recent and reliable geothermometer of Brey and Köhler (1990), which is based on the Ca exchange between Opx and Cpx and on its dependence on pressure, yields similar equilibrium temperatures (1000-1100 °C at 1.0 GPa, Peslier, 1999). Brearley et al. (1984) estimated the pressure to be between 1.8 and 2.0 GPa using Ranalli's (1980) geotherm for the Canadian Cordillera. Both of the estimated pressures are consistent with the spinel stability field from 1.0 to 2.0 GPa (Green and Hibberson, 1970; O'Neil, 1981).

Five representative samples were selected for detailed LPO measurements. Samples SLL6, SLL7 and SLL19 show protogranular texture (Fig. 2.2a) as defined by Mercier and Nicolas (1975). Sample SLL28 is weakly foliated with compositional

Table 2.2. Characteristics of mantle xenoliths from three sites in the southern Canadian Cordillera.

Site	Number	Ol (%)	Opx (%)	Cpx (%)	Sp (%)	Lithology	microstructure
Summit Lake	SLL6	81.8	0.1	17.5	0.6	Weh	protogranular
T=1000-1100 °C (1)	SLL7	77.5	18.2	4.0	0.3	Hrz	protogranular
P=1.0-2.0 GPa (1)	SLL19	60.1	16.9	20.0	3.0	Lhz	protogranular
	SLL28	83.3	9.6	6.2	0.9	Opx-poor Lhz	w. foliated g.
	SLL29	59.4	24.4	13.5	2.7	Lhz	foliated granular
	Average Lhz	60.9	25.3	11.4	2.4		
Jacques Lake	JLL1	19.5	42.0	35.5	2.9	Ol-web	protogranular
T=1000-1130 °C (2)	JLL6	58.2	23.7	17.5	0.6	Lhz	protogranular
P=1.5-2.0 GPa	JLL9	52.7	35.3	9.0	3.0	Lhz	w. foliated g.
West Kettle	KL1	65.2	22.8	8.3	3.7	Lhz	equigranular
River	KL3	53.6	22.7	17.3	6.4	Lhz	w. foliated g.
T=900-1040 °C (3)	KL9	67.1	20.8	10.5	1.6	Lhz	w. foliated g.
P=1.2-1.6 GPa	KL10	56.7	29.5	11.5	2.3	Lhz	equigranular
	Average Lhz	54.3	27.9	14.9	2.9		
southern Cordillera	Average Lhz	60.9	24.8	11.8	2.5		

Ol: olivine; Opx: orthopyroxene; Cpx: Clinopyroxene; Sp: spinel; Weh: wehrlite; Hrz: Harzburgite; Lhz: lherzolite; web: websterite. w. foliated g.: weakly foliated, granular texture. (1) Brearly et al. (1982) and Peslier (1999); (2) Littlejohn and Greenwood (1974); (3) Fujii and Scarf (1982) and Peslier (1999).

bands with varying amounts of pyroxenes and spinel (Fig. 2.2c). Sample SLL29 shows well-developed foliation and porphyroclastic texture (Fig. 2.2d) with elongated olivine grains aligned parallel to the stretching lineation. Olivine grain sizes are similar for all the studied samples with the average grain size being 2 mm. Opx average grain sizes are similar to those of olivine except in the Opx-poor samples (SLL6 and SLL28 where the average grain size is 1.3 mm), while Cpx average grain sizes are 1.5 mm for all of the studied samples. Spinel grains are generally interstitial and have an average grain size of ~1 mm. Subgrain boundaries and/or kink bands are often observed in olivine, indicating operation of crystalline plasticity.

2.2.2. Jacques Lake

This locality (121°14'E, 52°30'N) is a small cone of alkali basalt tuff, believed to be Pleistocene is age (Campbell, 1978), 25 km north-west of Housefly in central British Columbia (Fig. 2.1). The ultramafic rocks belong to the Cr-diopside and the Al-augite series as at Summit Lake (Ross, 1983). Spinel lherzolites are mainly found with secondary wehrlites and websterites (Littlejohn and Greenwood, 1974; Ross, 1983). The spinel-olivine geothermometer of Jackson (1969), which uses the partitioning of iron and magnesium between spinel and olivine, yields a temperature range from 1000 to 1130 °C (Littlejohn and Greenwood, 1983). This temperature range corresponds to a pressure range of 1.5 to 2.0 GPa (about 54-67 km) using Ranalli's estimated geotherm for the Canadian Cordillera (see Fig. 8a in Ji et al., 1994).

Three representative samples were chosen for petrofabric study. Samples JLL1 (websterite) and JLL6 (lherzolite) show protogranular textures with interstitial spinel grains, while JLL9 (lherzolite) is weakly foliated with alignments of holly-leaf shaped spinels (Mercier and Nicolas, 1975) with an average grain size of 1 mm. The olivine grains in the websterite (average 2 mm), sample JLL1, are smaller than those

in the lherzolite samples (average 3 mm). The Opx grains have similar average grain sizes (~3 mm) for all of the studied samples, whereas the Cpx grains in weakly foliated JLL9 have smaller grain sizes (average 1.3 mm) than the Cpx grains in the protogranular samples (average 2.5 mm). Subgrain boundaries and/or kink bands occur frequently in large grains of olivine and Opx.

2.2.3. West Kettle River

Ultramafic xenoliths from this site (119°04'E, 49°47'N) are contained in a basanitoid flow of Miocene age (Fujii and Scarfe, 1982). As in the other localities, both Al-augite and Cr-diopside series ultramafic xenoliths were observed at this site. The mantle xenolith population is dominated by spinel lherzolite (68%), olivine websterite (11%), websterite (8%), dunite (2%), and harzburgite (1%) of the Cr-diopside series and clinopyroxenite (5%) and wehrlite (5%) of the Al-augite series (Mitchell, 1987; Fujii and Scarfe, 1982). The average volumetric composition is: 54.3% olivine, 27.9% orthopyroxene, 14.9% clinopyroxene, and 2.9% spinel, calculated on the basis of the weight percentage data from Francis's Canadian Cordillera petrological database.

Equilibrium temperatures for the mantle xenoliths from West Kettle River of 900-1040 °C were obtained by Fujii and Scarfe (1982) using the two-pyroxene geothermometer of Wells (1977). This is consistent with the temperatures of 900-1000 °C estimated by Peslier (1999) using the Ca-exchange geothermometer of Brey and Köhler (1990). The pressure obtained from the Ca-exchange geothermometer is only 1.0 GPa (Peslier, 1999). According to Ranalli's (1980) Cordilleran geotherm, however, the corresponding pressures range from 1.2 to 1.6 GPa.

Four representative samples were selected for petrofabric measurements. KL1 and KL10 show equigranular textures (Fig. 2.2b) with straight grain boundaries which commonly converge at 120° in triple-junctions (Mercier and Nicolas, 1975). KL3 and

KL9 are weakly foliated. Olivine and Opx grain sizes are quite similar for these samples and the both average grain sizes are 2.5 mm. Clinopyroxene and spinel grains are generally smaller than olivine and orthopyroxene grains and the average grain sizes are 2 mm and 1 mm, respectively. Spinel grains in KL3 have holly-leaf shapes aligned parallel to the foliation defined by flattened and elongated olivine grains. Subgrain boundaries and/or kink bands are frequently seen in olivine grains from all of the samples.

2.2.4. Discussion: Can the xenoliths be representative of the upper mantle?

One important question is whether the xenoliths are representative of the present-day upper mantle in terms of seismic properties and modal composition. We consider that they reflect the present-day upper mantle beneath the southern Cordillera based on the following points:

(1) According to the equilibration temperature of the ultramafic xenoliths (e.g., Peslier, 1999) and the geotherm under the southern Canadian Cordillera (Ranalli, 1980; Hyndman and Lewis, 1999), the original depth of the xenoliths is estimated to have been between 50-60 km. This estimate is consistent with that for the northern Canadian Cordillera (Ji et al., 1994). Accordingly, the xenoliths are thought to be derived from in-situ upper mantle at a depth of 50-60 km when they were caught within upwelling basaltic melt.

(2) Based on the rapid ascent velocities (about 5-10 km/h) of basaltic magma estimated by Kushiro et al. (1976) and Fujii and Scarf (1982), the xenoliths did not suffer any significant changes in petrological composition and they could survive without dissolving completely during their rapid ascent.

(3) Since the volume fraction of xenoliths in ascending magma is very low (e.g., 0.5 % at West Kettle River, Fujii and Scarf, 1982), strain is largely localized in the melt and any stress prevailing in the surrounding melt is too low to deform the

solid xenoliths. Thus the xenoliths preserved their original microstructures without regaining any deformation features.

(4) The basaltic eruptions transporting the xenoliths occurred during the Quaternary and the late Tertiary. Consequently, it is conceivable to regard that the xenoliths reflect the present state of underlying upper mantle.

2.3. Petrofabrics

Petrofabric measurements were performed with a five-axis universal stage. Olivine, orthopyroxene and clinopyroxene fabrics were measured for each sample, but the measurable numbers of grains, especially pyroxenes, are limited for each thin-section due to coarse grain sizes. Olivine fabrics for all of the samples, except JLL1 which is a websterite, are shown in Fig. 2.3. Pyroxene fabrics (Figs. 2.4 and 2.5) are demonstrated for those samples in which more than 50 grains could be measured from a single thin section. The LPO diagrams, which were prepared using a computer program written by D. Mainprice (1990), were projected in equal-area and lower hemisphere with respect to the X, Y, and Z directions of the tectonic framework (X is parallel to the stretching lineation, Y is perpendicular to lineation and parallel to foliation, and Z is normal to the foliation).

2.3.1. Olivine

Samples from all the localities show well-developed olivine petrofabrics (Fig. 2.3). Through all of the samples, the olivine [100] axis shows a high concentration parallel or subparallel to the lineation (X). Two patterns of olivine LPO are observed:

(i) The olivine [100], [010], and [001] axes are, respectively, oriented parallel to the X, Z and Y directions (e.g., SLL28, SLL29, JLL9). This indicates that the olivine was deformed by dislocation creep at high temperature (>1000°C) with (010)[100] as the dominant slip system (Carter and AvéLallemant, 1970).

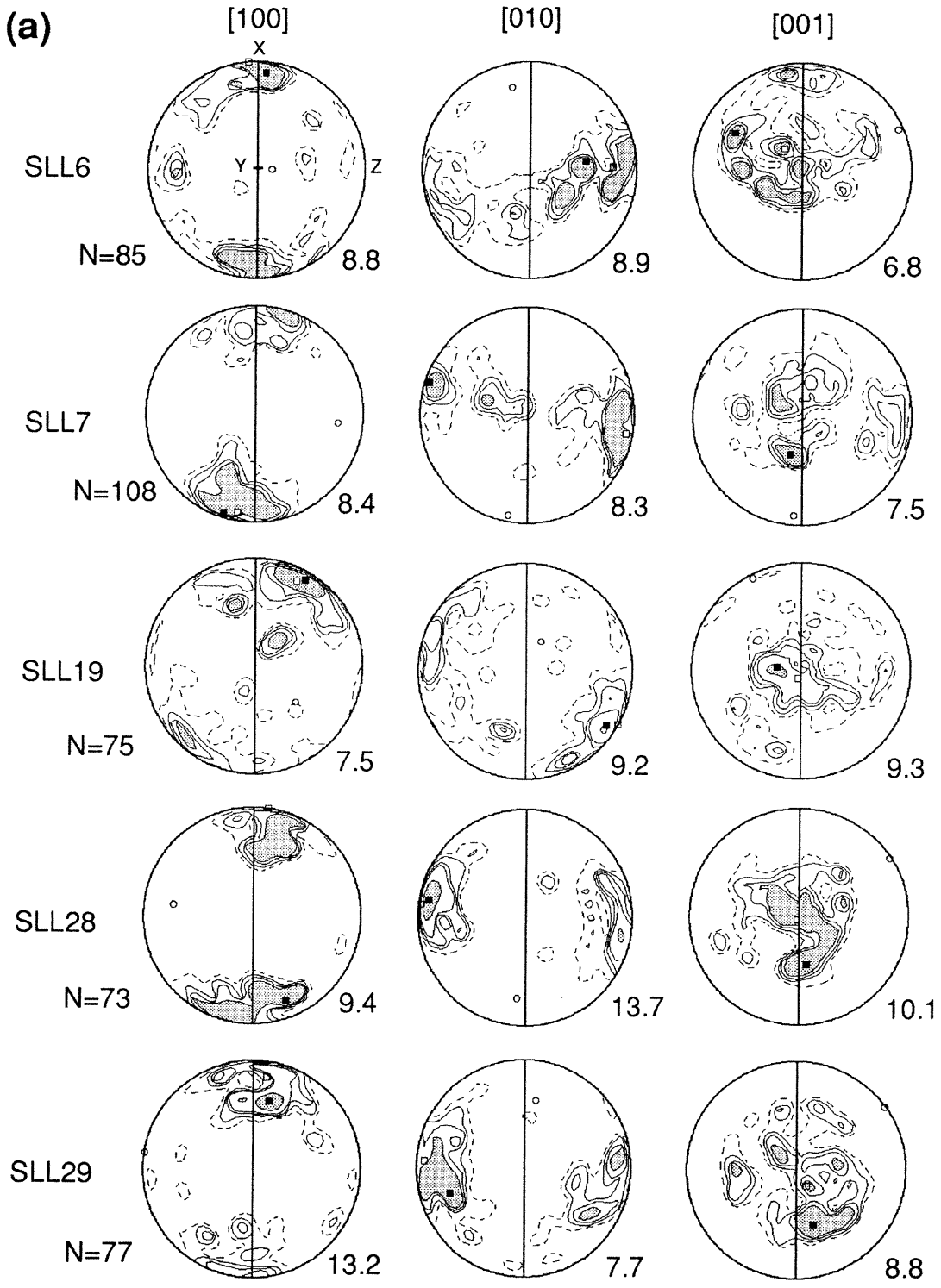

Figure 2.3. Olivine LPO diagrams shown as equal area and lower hemisphere projections from (a) SLL: Summit Lake, (b) JLL: Jacques Lake, (c) KL: West Kettle River. (d) Composite olivine LPO of all lherzolite samples from the three xenoliths sites. N: the number of measured grains for each sample. The number located at the lower right corner of the stereonet is the maximum concentration per 1% of the hemispherical area. The solid line is the foliation (XY-plane) and the N-S direction is the X-direction (stretching lineation). The black and white squares and white circle indicate the maximum density, the calculated best fabric axis, and the pole of the best fabric plane, respectively.

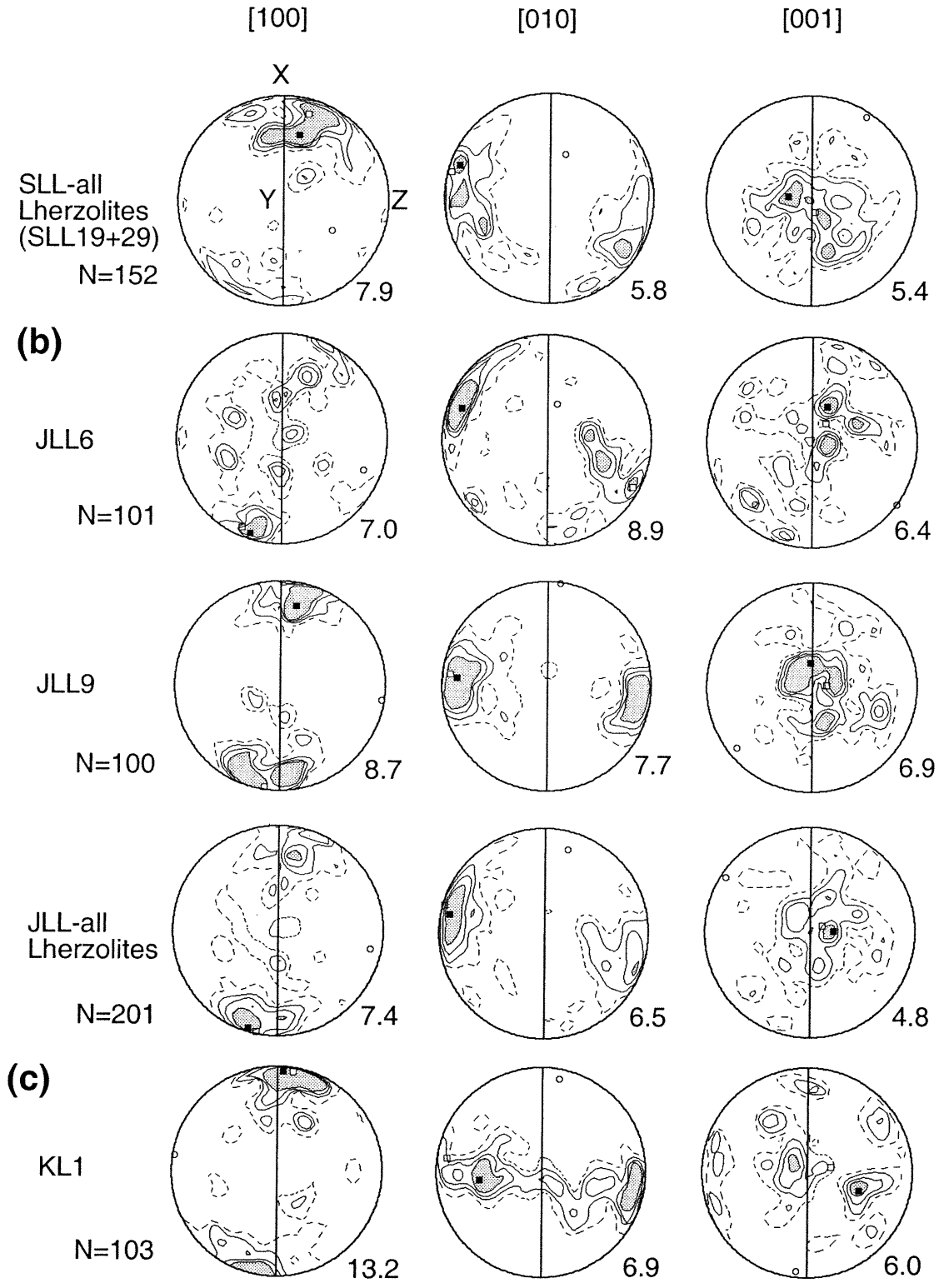

Figure 2.3. (continued)

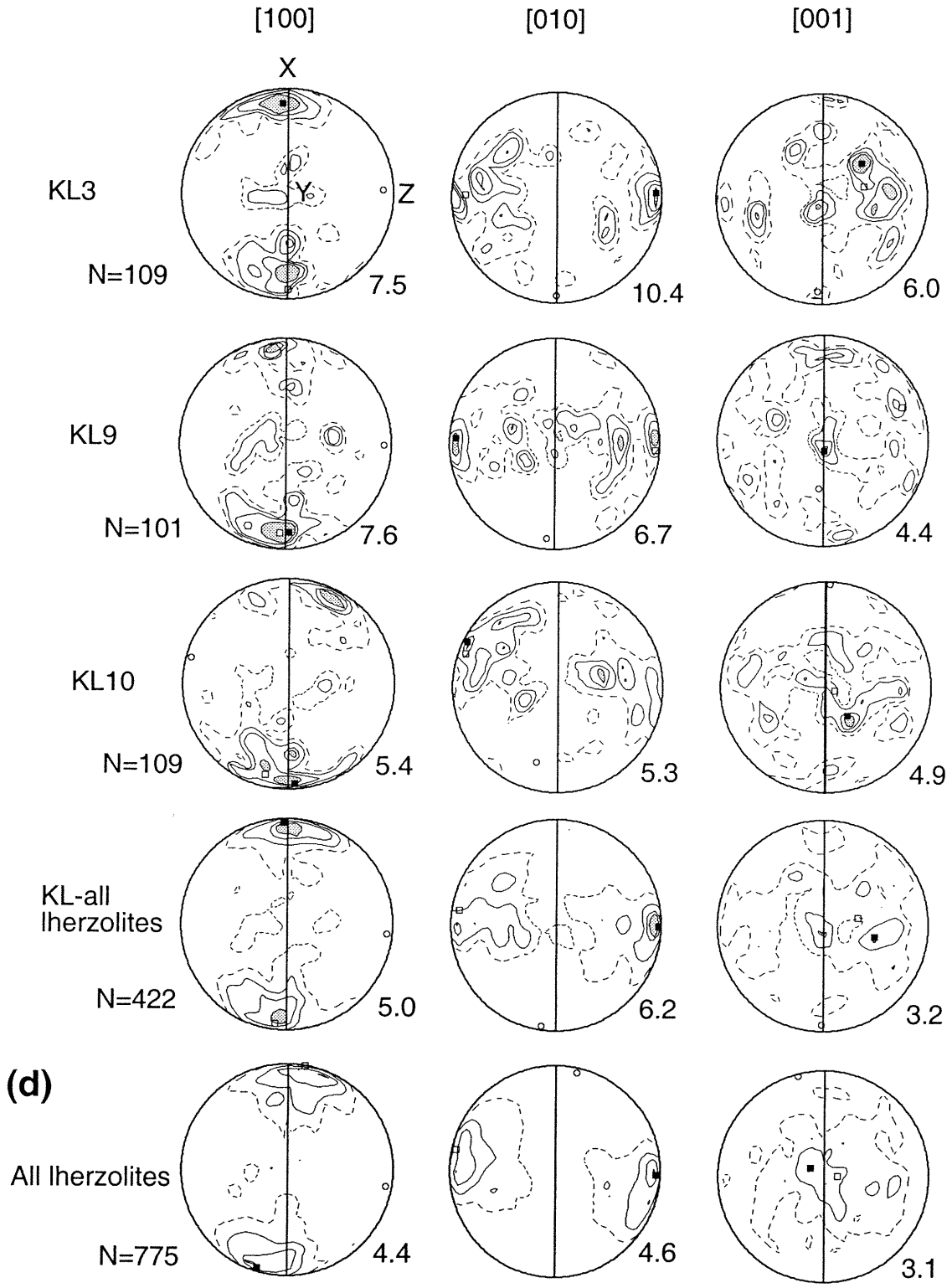

Figure 2.3. (continued)

(ii) The olivine [100] axis is oriented parallel to the X-direction, whereas both the [010] and [001] directions form girdles perpendicular to the lineation (e.g., SLL7, KL1, KL9, KL10). This LPO pattern is formed by dislocation creep at relatively lower temperature (<1000°C) with {0kl}[100] as the dominant slip system (Carter and AvéLallemant, 1970).

Both LPO patterns have been found at all localities in the region, regardless of the lithologic compositions (e.g., dunite, harzburgite, wehrlite) and microstructures (e.g., protogranular, porphyroclastic) of the xenoliths. Fabric pattern (i) has been documented in deformed garnet lherzolites from African kimberlite xenoliths (Boullier and Nicolas, 1975; Mainprice and Silver, 1993), in spinel-garnet lherzolite xenoliths from Russia (Kern et al., 1996), and in protogranular spinel lherzolites from Alpine Corsica (Jackson and Ohnenstetter, 1981). Fabric pattern (ii) has been found in mylonitic spinel lherzolites from the Bay of Island ophiolites (Suhr, 1993). Both patterns were found in the spinel lherzolite xenoliths from the northern Canadian Cordillera and Alaska (Ji et al., 1994).

2.3.2. Pyroxene

Both orthopyroxene (Opx) and clinopyroxene (Cpx) show weaker fabrics than olivine (Fig. 2.4, 2.5) in individual samples. Orthopyroxene crystals in SLL7 and KL1 show [100] maximum concentrations normal to the foliation, and [001] subparallel to the Y-direction. This fabric pattern is similar to the enstatite fabrics in kimberlite xenoliths from South Africa (Mainprice and Silver, 1993). However, the total composite fabrics of orthopyroxene for the lherzolites are almost random and are similar to those of xenoliths from Castle Rock and Alligator Lake in the northern Canadian Cordillera (Ji et al., 1994). Although the clinopyroxene in a wehrlite (clinopyroxene-rich) sample (SLL6) shows a [010] maximum perpendicular to the foliation and [001] parallel to the Y-direction (Fig. 2.5a), the composite

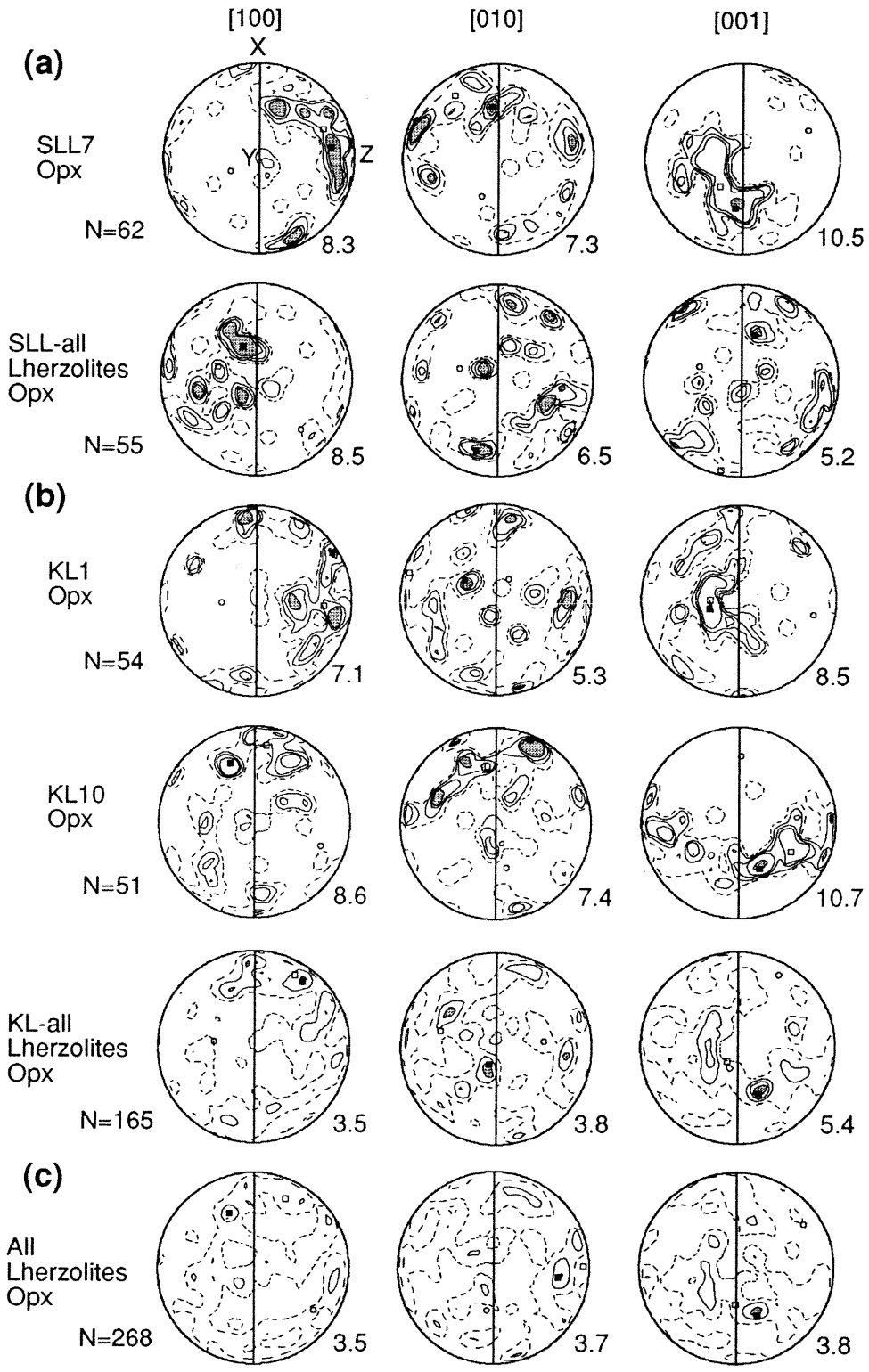

Figure 2.4. Orthopyroxene LPO diagrams shown as equal area and lower hemisphere projections from (a) SLL: Summit Lake, (b) KL: West Kettle River. (c) Composite Opx LPO of all lherzolite samples from the three xenoliths sites. Symbols as Fig. 2.3.

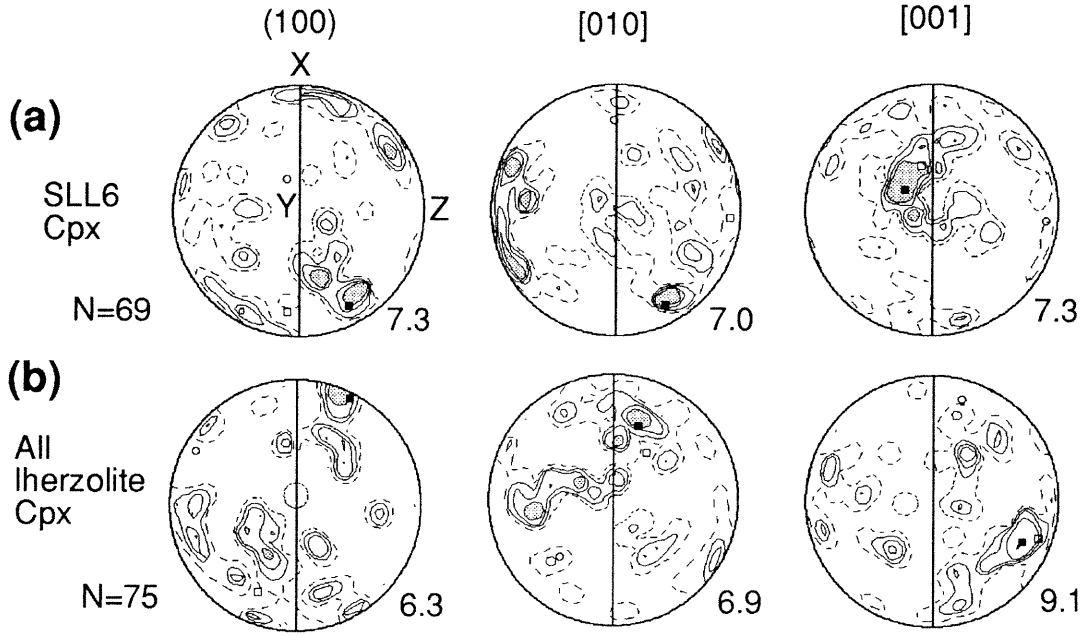

Figure 2.5. Clinopyroxene LPO diagrams shown as equal area and lower hemisphere projections from (a) SLL: Summit Lake. (b) Composite Cpx LPO of all lherzolite samples from the three xenolith sites. Symbols as Fig. 2.3.

clinopyroxene fabric for the lherzolite samples shows a more or less random LPO (Fig. 2.5b). Both the Opx and Cpx fabrics in the mantle xenoliths from the northern (Ji et al., 1994) and southern Canadian Cordillera are significantly weaker than those from peridotite massifs and ophiolites (AvéLallement, 1967; Möckel, 1969; Christensen and Lundquist, 1982; Nicolas and Prinzhofer, 1983). As pointed out by Ji et al. (1994), the difference in fabric intensity may reflect the different magnitude in flow stress: the peridotite massifs were tectonically emplaced under a much higher flow stress (100-300 MPa) than in-situ subcontinental upper mantle flowing under less stress (< 50 MPa).

2.4. Seismic properties of ultramafic xenoliths

The compressional wave velocity (V_p), the velocities of first (V_{s1}) and second (V_{s2}) split shear waves, the shear-wave anisotropy [$A(V_s)$], and the fast polarization direction (ϕ) were calculated from the LPO, density, volume fraction and elastic stiffness coefficients (C_{ij}) of each constituent mineral. To calculate the elastic stiffness coefficients for each mineral at a given temperature and pressure (e.g., 1000 °C and 1.5 GPa), several experimental coefficients were needed including the average thermal expansion coefficient (α), the adiabatic bulk modulus (K_s), the density [$\rho(P_0,T_0)$] and elastic constants [$C_{ij}(P_0,T_0)$] at ambient conditions (0.1 MPa, 25 °C), and the first-order pressure (dC_{ij}/dP) and temperature (dC_{ij}/dT) derivatives of the elastic constants.

The elastic stiffnesses of olivine were derived from Kumazawa and Anderson (1969). For orthopyroxene, K_s, $\rho(P_0,T_0)$ and $C_{ij}(P_0,T_0)$ were taken from Duffy and Vaughan (1988) because the examined enstatite composition is close to those in the southern Cordillera. The pressure and temperature derivatives are quoted from Frisillo and Barsch (1972), and the average thermal expansion coefficient is from Frisillo and Buljan (1972). Ks, $\rho(P_0,T_0)$ and $C_{ij}(P_0,T_0)$ for clinopyroxene (diopside) are those

measured by Levien et al. (1979) and the thermal expansion is that determined by Cameron et al. (1973). Pressure derivatives for diopside are those calculated by Matsui and Busing (1984) but the values of dC_{ij}/dT are not available at present. The temperature derivatives of orthopyroxene were thus used to represent those of clinopyroxene as done by Estey and Douglas (1986) and Ji et al. (1994). The coefficients of spinel are derived from Yoneda (1990) except for dC_{ij}/dT which is taken from Askarpour et al. (1993).

The calculated results including velocities, anisotropy, fast polarization direction, delay time, and elastic constants are shown in Figure 2.6 and Table 2.3, respectively. V_p has a unique maximum in most samples (except in samples JLL1 and JLL6). The maximum Vp corresponds to the olivine a-axis maximum concentration parallel to the lineation (X) and the minimum Vp generally coincides with the olivine b-axis concentration normal to the foliation plane. This V_p pattern has been ubiquitously found from seismic calculations (e.g., Mainprice and Silver, 1993; Ji et al., 1994; Kern et al., 1996) and laboratory measurements (Kern, 1993; Kern et al., 1996). The calculated V_p maximum anisotropy ranges from 12.9 % to 5 % and increases with increasing olivine content (Fig. 2.7a). Such a correlation between A(Vp) and olivine volume fraction has also been observed for ophiolites (Christensen and Lundquist, 1982) and kimberlite nodules (Mainprice and Silver, 1993).

V_S shows various and more complicated anisotropy patterns (Fig. 2.6). There are two V_S anisotropy patterns: (i) a point maximum occurs nearly parallel to the Y-direction (e.g., samples SLL7, SLL28, JLL9) and (ii) a complete or partial girdle occurs along the YZ-plane, in which two point maxima are symmetrically distributed with respect to the foliation (XY) plane (e.g., samples SLL19, SLL29, composite lherzolite for Summit Lake, KL1, KL3, KL9, KL10, and composite lherzolite for West Kettle River). These two patterns were also observed in mantle xenoliths from

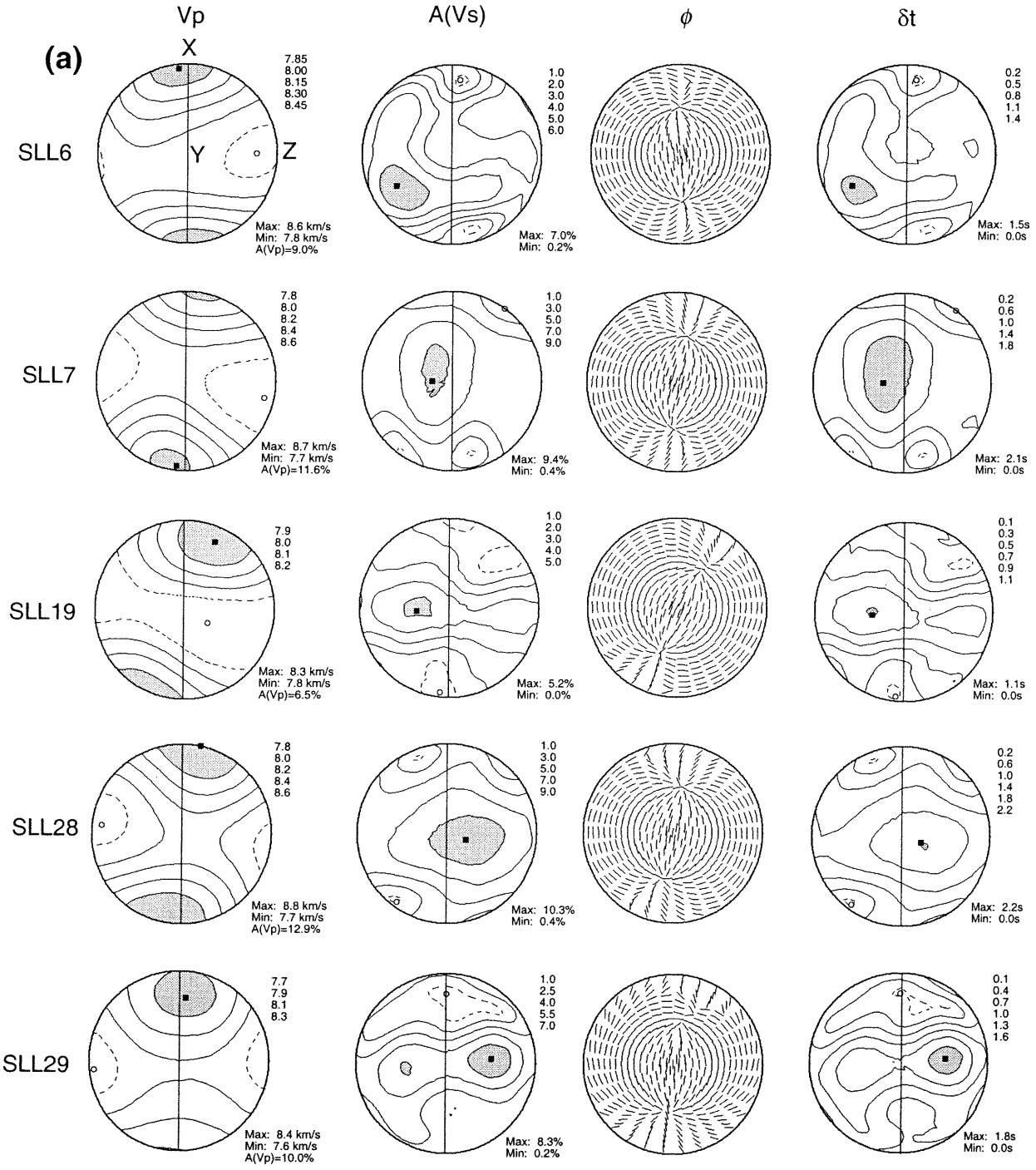

Figure 2.6. Seismic properties of each mantle xenolith sample from (a) SLL: Summit Lake, (b) JLL: Jacques Lake, (c) KL: West Kettle River. (d) Average seismic properties of lherzolite mantle under the southern Cordillera. All the properties were calculated for 1000 °C and 1.5 GPa (corresponding to about 50 km depth). Vp, A(Vs) and ϕ are P-wave velocity, S-wave anisotropy, and the fast S-wave polarization direction, respectively. δt, which is the delay time between the two split S-wave arrivals, was calculated for a path length of 100 km.

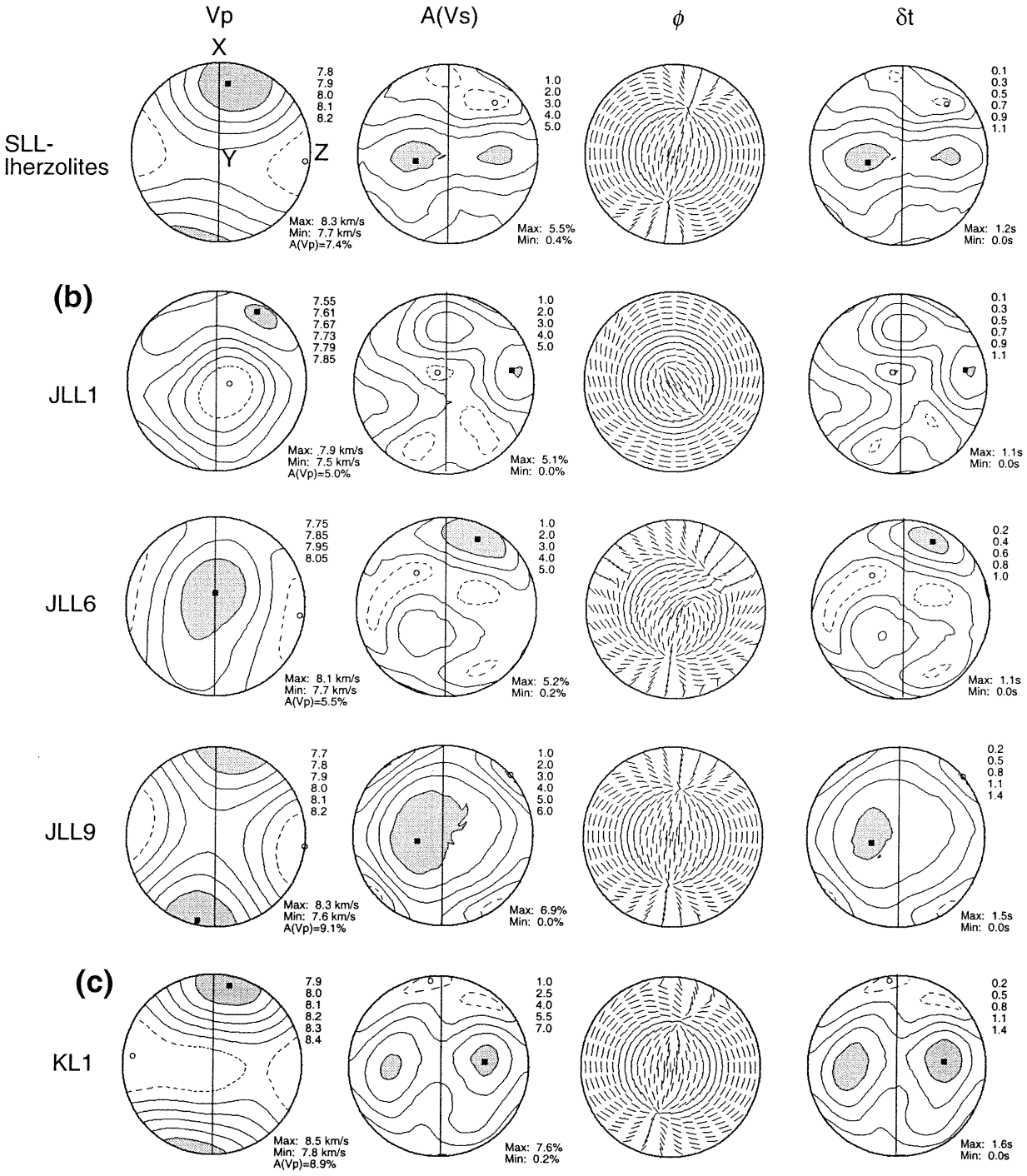

Figure 2.6. (continued)

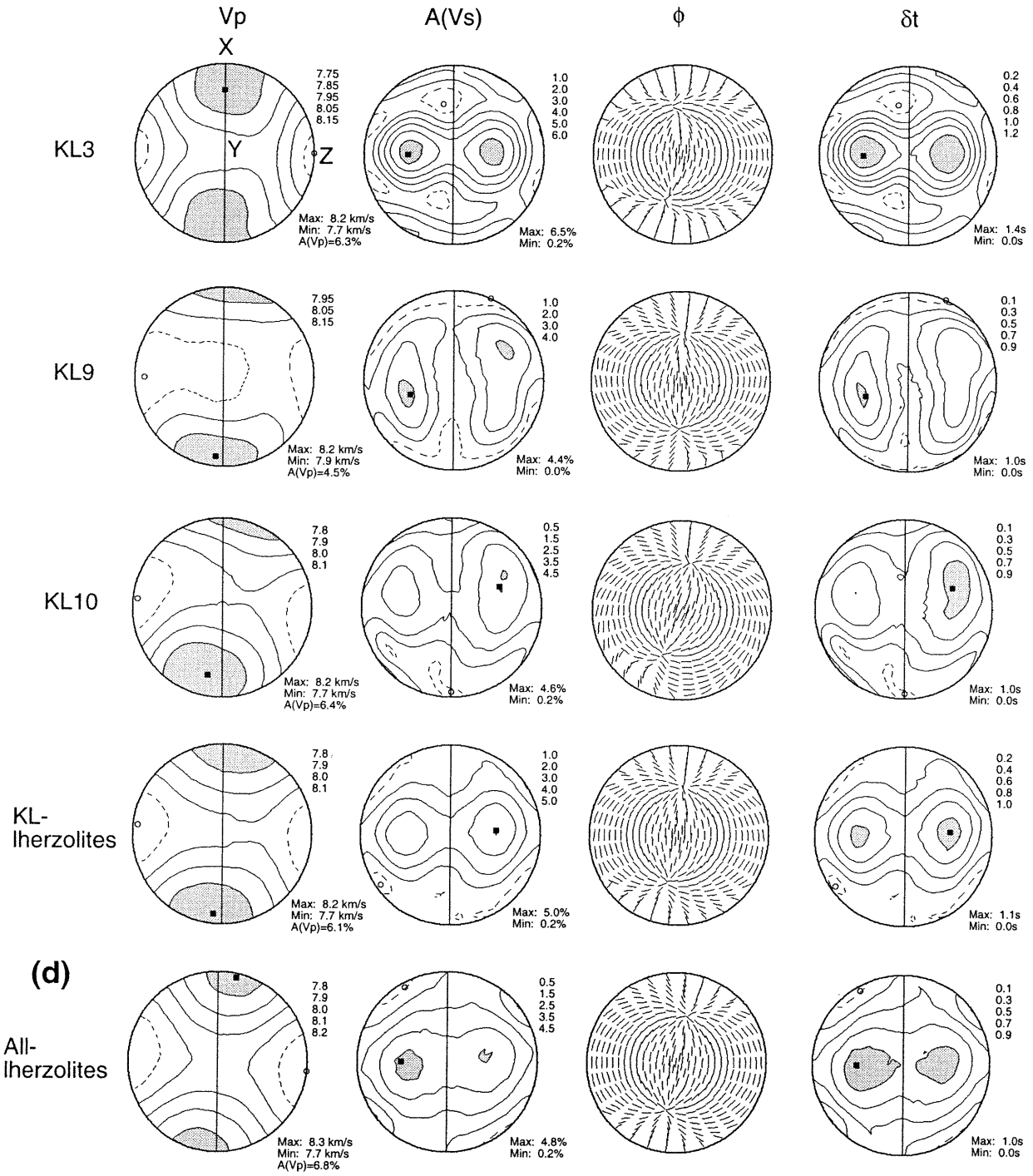

Figure 2.6. (continued)

Table 2.3. Elastic constants in GPa of the upper mantle beneath the xenolith sites at Summit Lake (SLL), West Kettle River (KL), and the southern Cordillera (SC). Values calculated from average data of ultramafic xenoliths.

Cij	SLL	KL	SC
C11	219.85	217.24	220.09
C22	193.10	192.37	192.68
C33	201.69	200.98	203.71
C44	65.93	67.35	66.54
C55	72.45	71.92	72.06
C66	70.96	70.14	69.82
C12	67.58	67.38	67.63
C13	70.60	68.01	69.05
C14	0.29	-0.06	0.08
C15	-3.98	0.85	-0.16
C16	-3.31	-1.69	-2.75
C23	67.62	67.53	68.19
C24	0.28	0.53	0.21
C25	-0.01	0.22	0.11
C26	-1.47	-0.91	-1.29
C34	-0.09	0.63	0.13
C35	-2.75	0.59	-0.30
C36	-0.24	-0.14	-0.20
C45	-1.12	-0.30	-0.67
C46	-1.26	0.57	0.14
C56	0.35	0.00	-0.09

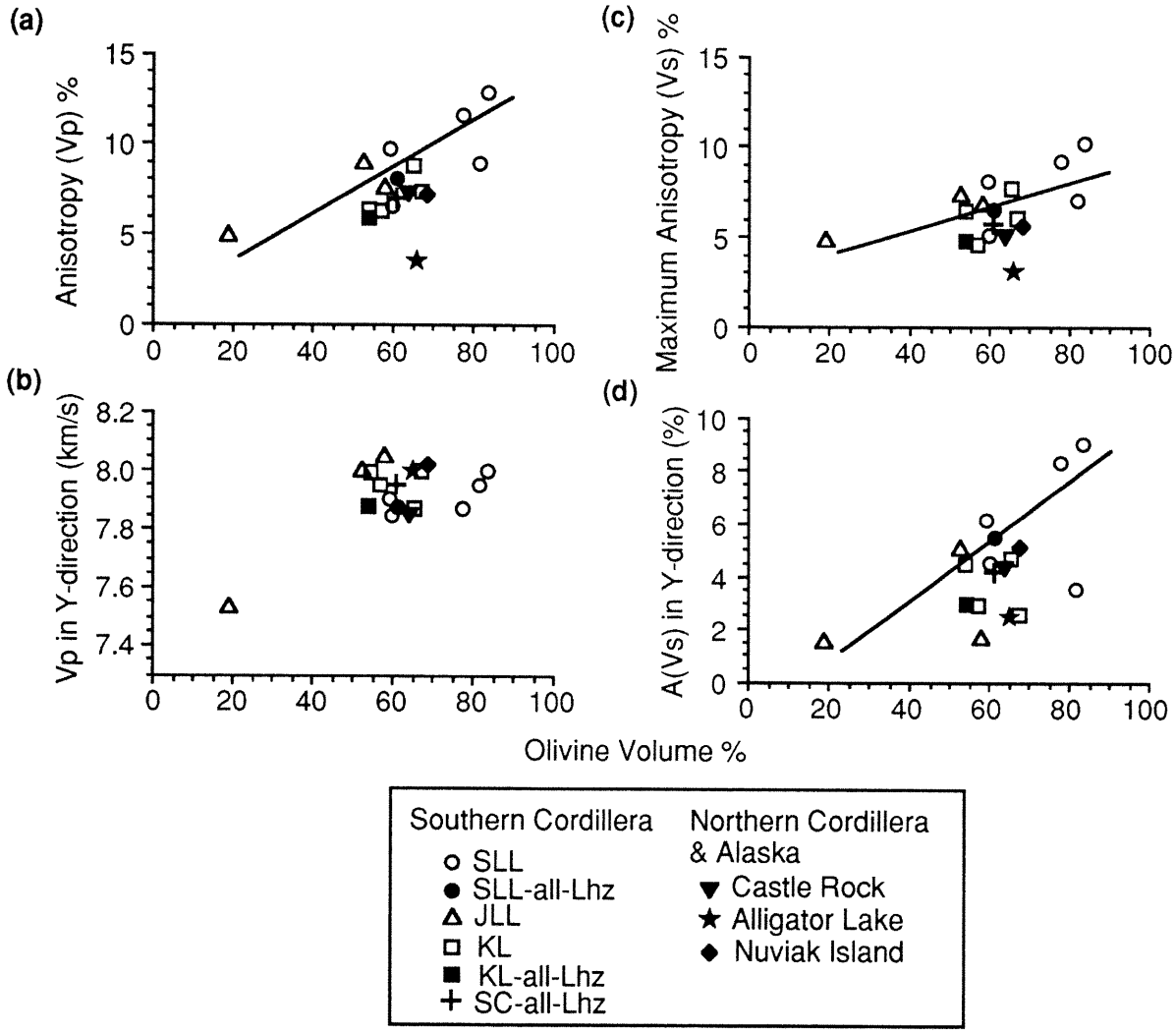

Figure 2.7. Relationship between the olivine volume fraction (%) and seismic properties in each xenolith sample. The data from Northern Cordillera and Alaska are from Ji et al. (1994).

the northern Canadian Cordillera and Alaska (Ji et al., 1994) and from African kimberlites (Mainprice and Silver, 1993). Ji et al. (1994) explained the first pattern and the second pattern of $A(V_S)$ in terms of the different olivine LPO pattern caused by the dominant slip system on (010)[100] and on {0kl}[100], respectively. Recently Ismail and Mainprice (1998) also observed a correlation between [100] and [001] axis concentrations and $A(V_S)$ maxima based on calculated seismic anisotropy patterns in pure olivine aggregates. However, this correlation is not clearly observed for most xenolith samples from the southern Canadian Cordillera. The reason for this difference is that the modeling of Ismail and Mainprice (1998) did not take into consideration the contribution of other minerals such orthopyroxene, clinopyroxene and spinel.

The magnitude of Vs anisotropy varies from 10.3% to 4.4 %, and shows a marked correlation with the olivine volume fraction (Fig. 2.7c) although this correlation is less clear than that for the V_p anisotropy (Fig. 2.7a). Mainprice and Silver (1993) attributed the relatively poor compositional sensitivity of A(Vs) to constructive interference caused by the similar orientations of the polarization planes produced by the petrofabrics of olivine and orthopyroxene and to the low strength of the orthopyroxene petrofabrics. The other reason for the relatively poor compositional sensitivity of A(Vs) is also due to different definitions of the anisotropy. $A(V_p)$ is defined as $(Vp_{max} - Vp_{min})/Vp_{mean}$ while $A(V_S)$ is defined as $(V_{S_1} - V_{S_2})/V_{S_{means}}$. Thus, for a given rock, $A(V_p)$ is a unique value while $A(V_S)$ depends on the propagation direction.

The calculated seismic properties of the mantle xenoliths from the southern Cordillera are fundamentally similar to those from the northern Cordillera and Alaska (Ji et al., 1994).

2.5. Discussion

The Canadian Cordillera is a collage of disparate geological terranes grouped into superterranes associated with the area's characteristic morphogeological belts (Gabrielse and Yorath, 1989; Wheeler et al., 1991). LITHOPROBE performed a set of multi-disciplinary transects in the southern Canadian Cordillera to study the origin and present-day structure of the lithosphere on the western edge of North America. The main results of these seismic transects have been reported in Kanasewich et al. (1994), Clowes et al. (1995), Burianyk and Kanasewich (1995, 1997), Bostock and Cassidy (1995), and Cassidy and Bostock (1996). In the following paragraphs, we will first summarize the seismic results measured in the region (also see Table 2.4, Fig. 2.1 and Fig. 2.8), and then use the seismic properties of the mantle xenoliths to interpret the in-situ measured seismic velocities and anisotropies.

2.5.1. P-wave velocities

Line 7 of the LITHOPROBE 1990 Southern Cordillera Refraction Experiment (SCoRE '90) is comprised of a set of east-west seismic refraction/wide angle reflection profiles perpendicular to the regional geological strike across the entire width of the Omineca and Intermontane Belts of the southeast Canadian Cordillera at about 50°N latitude (Fig. 2.8a). This line is a 410 km long profile from the Fraser River to Radium Hot Springs near the Rocky Mountain Trench. Seismic data (Burianyk and Kanasewich, 1995) obtained from line 7 show: (i) The Moho dips from 31 km depth at the west end to 40 km depth at the east end of the profile; (ii) The crust is laminated with the upper crust having an average thickness of 15.3 km and a Vp increasing from 5.9 km/s at the top to 6.2 km/s at the bottom, the middle crust having an average thickness of 9.2 km and an average Vp of 6.1 km/s, and the lower crust having an average thickness of 10 km and an average Vp of 6.6 km/s; (iii) The upper mantle has P-wave velocities increasing from 7.9 km/s at the Moho (31 km) to 8.2 km/s at 48 km.

Table 2.4. In-situ P_n velocities measured from the southern Canadian Cordillera using different techniques.

Locality	depth	Vp	Technique	Reference
Greenbush (NE)	35 km	8.03	refraction	Berry and Forsyth (1974)
SCoRE'90 Line 7 (EW)	35 km	7.90	refraction/	Burianyk and Kanasewich (1995)
	40 km	8.03	wide-angle reflection	
	45 km	8.10		
	48 km	8.20		
Nearly Line 9 (EW)	31-40 km	7.80	wide-angle	Cumming et al. (1979)
SCoRE'90 Line 9 (EW)	35 km	7.90	wide-angle	Zelt and White (1995)
SCoRE'90 Line 8 (NS)	35 km	7.90	refraction/	Kanasewich et al. (1994)
	40 km	7.96	wide-angle reflection	
	45 km	8.02		
	48 km	8.10		
SCoRE'90 Line 6 (NS)	50-62 km	7.8-8.0	broadside wide-angle	Burianyk and Kanasewich (1997)

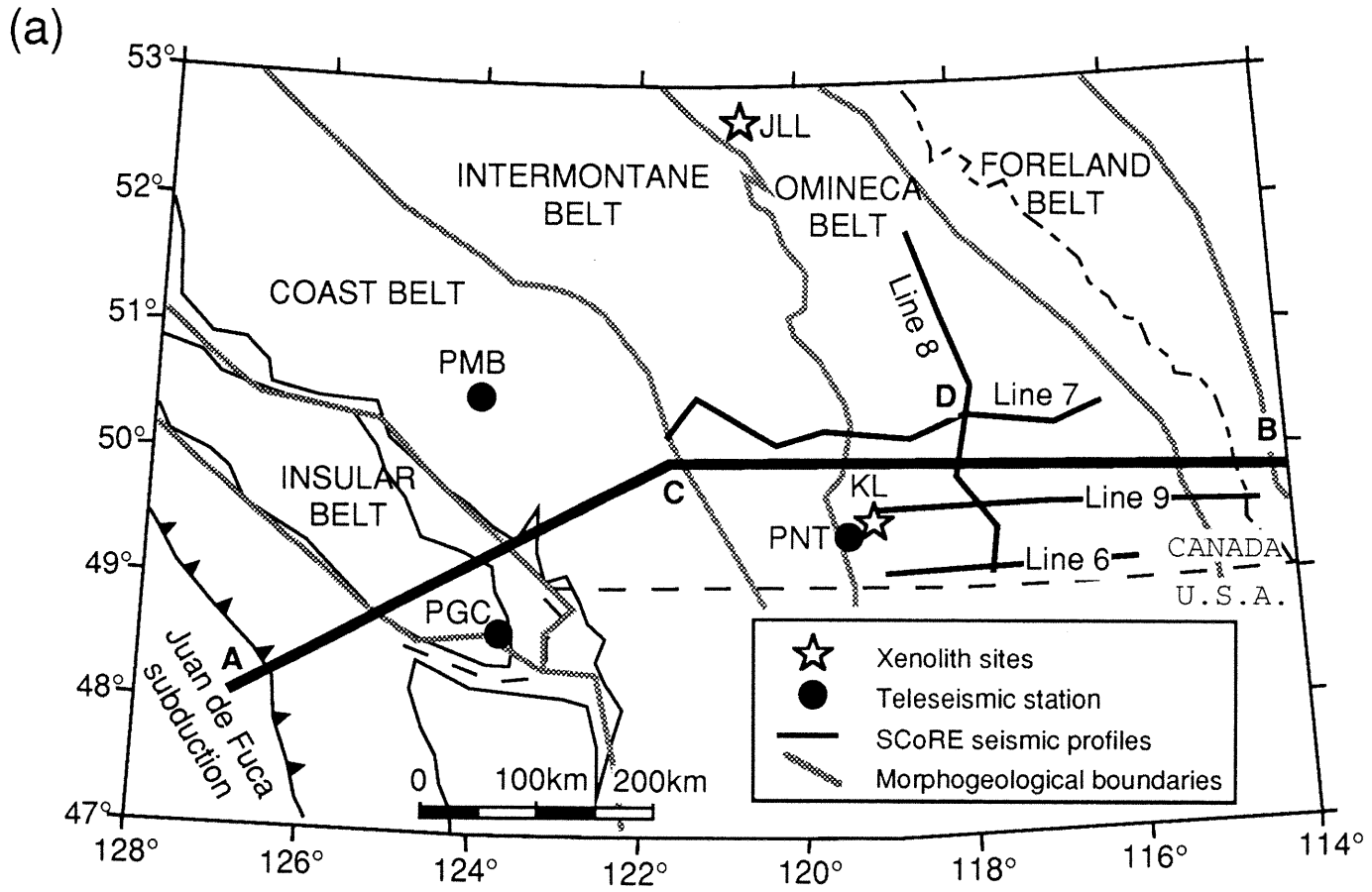

Figure 2.8. (a) Simplified tectonic map of the southern Cordillera modified from Clowes (1997). KL: West Kettle River, JLL: Jacques Lake. Lithoprobe transect lines are indicated. (b) Cross section along line A-C-B in (a), modified from Clowes (1997) and Hyndman and Lewis (1999). FF: Fraser fault.

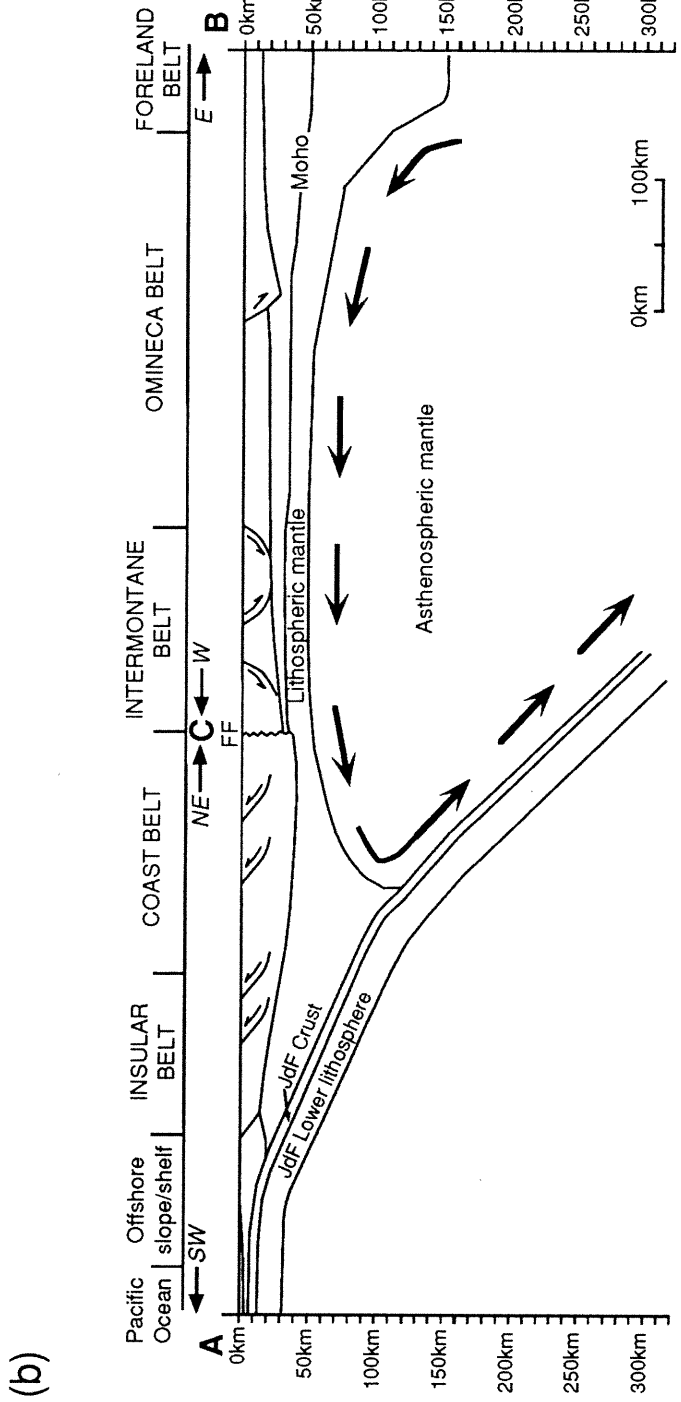

Figure 2.8. (Continued)

Line 8 (Fig. 2.8a) is a 350-km LITHOPROBE seismic refraction/wide-angle reflection profile along the regional tectonic strike (NS or NNW-SSE) in the Omineca Belt of the Canadian Cordillera. Seismic data obtained from this profile (Kanasewich et al., 1994) show that the crust is relatively thin and has an average thickness of about 36 km. The upper crust, with a thickness of 12-18 km, has average P-wave velocities from 5.6 km/s near the surface to 6.2 km/s to the top of the middle crust. The middle crust has an average thickness of about 10 km and an average velocity of less than 6.1 km/s. The low velocity middle crust, together with high conductivities and high heat flow (Lewis et al., 1992), is most likely due to an elevated geothermal gradient. The lower crust has P-wave velocities ranging from 6.4 km/s at the top to 6.8 km/s at the base. Immediately beneath the Moho, the upper mantle has P-wave velocities of 7.9 km/s and the velocities increase from the Moho to 8.1 km/s at about 46-49 km depth. An intramantle reflector is found at about 46-49 km depth and has been interpreted as the base of the lithosphere (Kanasewich et al., 1994).

While shooting of the north-south refraction/wide-angle reflection profile (Line 8) through the Omineca Belt, 79 seismographs were deployed along an east-west line perpendicular to line 8, just north of the U.S. border and centered on Castlegar (Line 6, Fig. 2.8a). The seismographs recorded the north-south line of shots in a broadside, or fan, geometry, creating east-west lines of common-mid-points (Burianyk and Kanasewich, 1997). Beneath LITHOPROBE line 8, Vp ranges from 6.5-6.8 km/s in the lower crust and the Moho lies at a depth of 35-36 km depth. The uppermost or lithospheric mantle is only about 15 km thick and has a compressional wave velocity 7.9-8.0 km/s at the top and 8.1 km/s at the bottom. A P_m reflector occurs at 50±2 km depth, beneath which a low velocity (Vp ~7.9 km/s) zone is detected. This low velocity zone continues to at least 58-62 km (Burianyk and Kanasewich, 1997). This is consistent with the results of surface wave studies by Wickens (1977) who found a substantial S-wave low velocity zone in the mantle

beginning at 50 km depth in the Omineca Belt. Burianyk and Kanasewich (1997) interprets the observed reflector at 50 km as the lithosphere/asthenosphere boundary. The thin lithosphere may also explain the high heat flow (Lewis et al., 1992) observed in the region of the southeastern Canadian Cordillera.

Geophysical data including seismic velocities (Kanasewich et al., 1994; Clowes et al., 1995; Burianyk and Kanasewich, 1995, 1997), heat flow (Lewis et al., 1988; Hyndman and Lewis, 1999), gravity and magnetotelluric data (Clowes et al., 1995) suggest that the thickness of the continental lithosphere is only about 50 km for the Omineca and Intermontane belts. It is widely accepted that there is a westward, horizontal asthenospheric flow (Fig. 2.8b) from the Cordillera-craton boundary on the east toward the subduction zone to the west (Hyndman and Lewis, 1999; Clowes et al., 1995). The mantle material with lateral flow loses heat near the subduction zone and is then driven downward by the motion of the subducting Juan de Fuca oceanic slab (Fig. 2.8b). Deep asthenospheric upwelling occurs near the Cordillera-craton boundary (Hyndman and Lewis, 1999), east of which the North America craton has a thickness of ~150 km. Therefore, it is reasonable to consider that foliation in the upper mantle below the Omineca and Intermontane belts is horizontal, and the stretching lineation (olivine a-axis) is oriented NE (Fig. 2.8b), which coincides with the relative plate motion and the maximum horizontal compressive stresses measured at the Earth's surface in the region.

Thermobarometrical analyses of the mantle xenoliths from Summit Lake, West Kettle River and Jacques Lake (this study) and from Lassie Lake and Lightening Peak (Ross, 1983) yield equilibrium temperatures ranging from 900 to 1250 °C. If the lithosphere/asthenosphere boundary has a temperature of 1250 °C (Turcotte and Schubert, 1982), most of the studied mantle xenoliths would be derived from subcrustal lithospheric mantle. As we know, thermobarometry methods have substantial uncertainty although they often show relative consistency. If we accept the

temperature gradient of about 20 °C/km proposed by Lewis (1991) for the southeastern Cordillera lithosphere, the xenoliths having equilibrium temperatures higher than 1000 °C would be derived from the uppermost part of the asthenosphere (i.e., the low velocity zone, >50 km depth). If this is the case, the seismic velocities and anisotropies of the mantle xenoliths are representative of both the lithospheric mantle and the asthenospheric mantle.

The in-situ Pn velocities are observed to range from 7.8 to 8.1 km/s along the N-S direction (Line 8, Kanasewich et al., 1994) and from 7.9 to 8.2 km/s along the E-W direction (Line 7, Burianyk and Kanasewich, 1995). As shown in Fig. 2.6, P-wave velocities calculated for the mantle at 1000 °C and 1.5 GPa (corresponding to a depth of about 45-50 km) are remarkedly anisotropic in the foliation plane and increase gradually from ~7.9 km/s along the Y-direction (normal to the stretching lineation) to ~8.2 km/s along the X-direction (parallel to the stretching lineation). The calculated results thus provide quite good constraints on the interpretation of the in-situ Pn velocities measured along LITHOPROBE transects in the region. These results also suggest that the foliation in the upper mantle is most likely horizontal, and the stretching lineation is most likely perpendicular to the tectonic strike of the region. The observed variation in Pn velocity with transect orientation can be explained by taking account of the seismic anisotropy in the foliation plane. The small difference in Pn velocities along lines 7 (EW) and 8 (NS) may be due to the fact that these lines are not exactly parallel to the X and Y directions. It is likely that the Pn anisotropy would be more significant if the resolution of the seismic studies had been enhanced and if more transects aligned in different orientations with respect to the tectonic strike had been performed. Finally, the present study, in spite of the above limitations, provides an additional constraint on the tectonic model proposed for the region by Clowes et al. (their Fig. 10, 1995) and Hyndman and Lewis (their Fig. 18, 1999).

2.5.2. Shear-wave velocities and splitting

Teleseismic SKS or SKKS splitting in the southern Canadian Cordillera has been measured at 6 stations (PGC, LON, PNT, BBB, WALA and PMB) near the west coast by Bostock and Cassidy (1995) and Silver and Chan (1991) (Table 2.5, Fig. 2.1). The fast polarization directions (ϕ) for SKS or SKKS are aligned NE-SW at PMB, PNT, WALA and PGC to nearly EW at LON. These measured ϕ directions are almost parallel to the relative plate motion of the Juan de Fuca oceanic plate (DeMets et al., 1990; Bostock and Cassidy, 1995) or the maximum horizontal compressive stresses in the region (Zoback and Zoback, 1991; Adams and Bell, 1991). It is important to note that the ϕ directions measured at stations WHY and DAWY in the northern Canadian Cordillera and COL in Alaska are nearly parallel to the regional strike-slip shear zones (e.g. Tintina fault and Denali fault) and perpendicular or subperpendicular to the relative plate motion of the Pacific Ocean plate (DeMets et al., 1990; Bostock and Cassidy, 1995) and the maximum horizontal compressive stresses in the region (Zoback and Zoback, 1991; Adams and Bell, 1991). The transition from strike-parallel to strike-perpendicular ϕ directions appears to occur in central British Columbia (i.e., near station BBB, Fig. 2.1).

The calculated results (Fig. 2.6) show clearly that the fast S-wave polarization (ϕ) depends on the propagation direction with respect to the tectonic framework (i.e., foliation and lineation). This is consistent with the previous findings of Ji et al. (1994). As indicated in the previous paragraphs, the foliation in the upper mantle is most-likely horizontal, thus the propagation direction of the vertical SKS or SKKS rays is along the Z-direction, that is, normal to the foliation plane. In this case, the ϕ direction is systematically aligned parallel to the stretching lineation (X), that is, the maximum concentration of olivine [100] directions or the plastic flow line in the upper mantle.

As shown in Fig. 2.1, the ϕ directions of SKS and SKKS are aligned NE-SW

Table 2.5. Shear wave splitting measurements in the southern and northern Canadian Cordillera.

Region	Station	Lat (°N)	Lon (°W)	Phase	δt (s)	ϕ (°)	Ref.	σ	ϕ vs σ	Ref.
Southern Cordillera	BBB	52.18	128.11	SKS	0.30	9	1	NE comp.	//	4, 5
JF going under NA:	PMB	50.51	123.06	SKS	0.65	45	1	-		
41 mm/yr, NE	PNT	49.31	119.61	SKS	1.70	51	1	-		
	PGC	48.65	123.45	SKS	1.15	74	1	NE comp.	//	4, 5
				S (15-30km)	0.20±0.50	312±19	2		⊥	
				S (40-60km)	0.32±0.07	293±27	2		⊥	
	LON	46.75	121.81	SKS	1.00	84	3	NS comp.	⊥	4, 5
	WALA	49.05	113.91	SKS	0.90	37	1	NE comp.	//	4, 5
Northern Cordillera	WHY	60.65	134.88	SKS	0.95	166	1	NE comp.	⊥	4, 5, 6
PA going under NA:	DAWY	64.06	139.31	SKS	1.35	116	1	-		
52 mm/yr, NNW	COL	64.89	147.79	SKS	1.55	98	3	NNW comp.	⊥	4, 6
	INK	68.30	133.52	SKS	0.60	81	1	NE comp.	⊥	4
	YKA	62.49	114.60	SKS	1.55	53	1	-		

1: Bostock and Cassidy (1995); 2: Cassidy and Bostock (1996); 3: Silver and Chan (1991); 4: Zoback and Zoback (1991); 5: Adams and Bell (1991); 6: Estabrook and Jacob (1991). JF: Juan de Fuca Plate; NA: North America Plate; PA: Pacific plate; σ : Crustal stress field; comp.: compression; //: parallel; ⊥ : oblique.

at stations PMB, PNT, WALA and PGC and nearly EW at LON. The ϕ directions may reflect local orientation of the tectonic lineation in the upper mantle beneath the stations. If the tectonic model proposed by Clowes et al. (1995) and Hyndman and Lewis (1999) is accepted, it is easy to understand why the measured ϕ directions in the southern Canadian Cordillera are almost parallel to the relative plate motion of the Juan de Fuca oceanic plate (DeMets et al., 1990; Bostock and Cassidy, 1995) or the maximum horizontal compressive stresses in the region (Zoback and Zoback, 1991; Adams and Bell, 1991). The coincidence of the ϕ directions and the relative plate motion of the Juan de Fuca oceanic plate with respect to the North American plate implies that the seismic anisotropy detected by SKS splitting mainly originates in the asthenosphere (Vinnik et al., 1992; Vinnik et al., 1995) rather than the subcontinental lithospheric mantle (Silver and Chan, 1988; 1991; Silver, 1996) in the region of the southern Cordillera where the geotherm gradient is very high and the lithosphere is very thin (~50 km). Thus, the measured ϕ directions appear to reflect the average, present-day, plastic flow directions in a column of upper mantle rocks which is about 50 km wide (the lateral resolution of the SKS splitting method). The coincidence of the ϕ directions with the maximum horizontal compressive stresses in the upper crust implies that the tectonic stresses in the crust may be derived from the plastic flow in the asthenosphere which, according to plate tectonic theory, provides one of the main forces that drive plates motion (Zoback and Zoback, 1980; Gough, 1984).

The ϕ directions measured at stations DAWY (64.06°N, 139.31°W) in the northern Canadian Cordillera and COL (64.89°N, 147.79°W) in Alaska (Fig. 2.1) are nearly parallel to the regional strike-slip shear zones (e.g., the Tintina and Denali faults) and perpendicular to the relative plate motion of the Pacific Ocean plate with respect to the continent (DeMets et al., 1990; Bostock and Cassidy, 1995). The ϕ directions measured at these two stations are also perpendicular to the maximum horizontal compressive stresses in the region (Zoback and Zoback, 1991; Adams and

Bell, 1991). The ϕ direction measured at station WHY (60.65°N, 134.88°W) is at about 15-20° to the strike-slip shear zones (e.g., Denali fault). The geometrical relationship between the ϕ and plate motion directions cannot be interpreted by assuming that the foliation is horizontal in the upper mantle beneath the northern Canadian Cordillera and Alaska. Ji et al. (1994) suggest that the foliation is nearly vertical while the stretching lineation is nearly horizontal in the upper mantle beneath the northern Canadian Cordillera and Alaska, since the subcontinental mantle deformation is dominated by lateral movement. In other words, the SKS and SKKS rays are parallel to the Y-directions in the upper mantle beneath the northern Canadian Cordillera and Alaska so that the measured ϕ directions are still parallel to the stretching lineation or the maximum concentration of olivine [100] directions. The above analysis implies that the subcontinental upper mantle beneath the northern Canadian Cordillera and the southern Canadian Cordilleras deforms predominantly by strike-slip shear and horizontal convection, respectively. It is even possible to speculate that a transition from strike-slip shear in the north to horizontal layered flow in the south takes place in the upper mantle beneath central British Columbia. Such a change in deformation mode may cause complex variations in the orientation of foliation and lineation in the upper mantle (Fig. 2.9), and consequently complex variations in the ϕ directions with respect to surface structures and smaller delay times between the first and second split SKS arrivals in central British Columbia. Station BBB (52.18°N, 128.11°W) shows an intermediate ϕ direction between those of the southern and the northern Canadian Cordillera and a very small δt value (0.30 s), implying that this station is located in such a transitional region.

The measured SKS and SKKS splitting in the southern Cordillera ranges from 0.65 s to 1.7 s with an average value of 1.21 s. The maximum splitting occurs at PNT and the minimum splitting occurs at PMB. The average SKS splitting is not significantly different between the southern (1.21 s) and northern (1.28 s) Cordilleras.

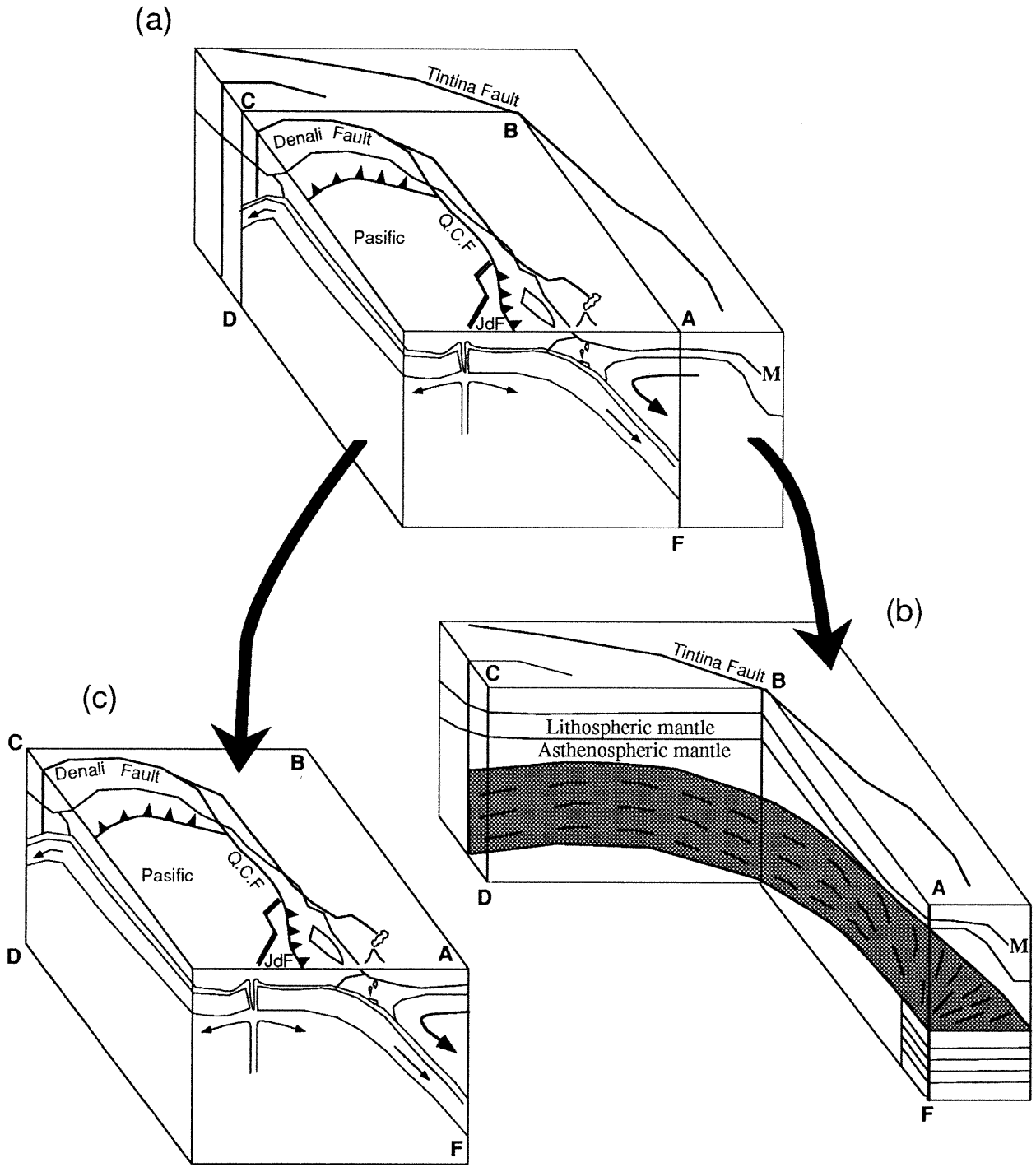

Figure 2.9. Schematic block diagrams (a, b, and c) of the Canadian Cordillera. M - Moho. Model (b) shows proposed mantle structure below the Canadian Cordillera. The northern Cordillera develops vertical foliation and horizontal lineation in the upper mantle due to dominant strike-slip movement in the region, while the southern Cordillera shows horizontal foliation and lineation in the upper mantle due to horizontal asthenospheric flow in the region.

The results calculated on the basis of LPO data from mantle xenoliths show that the average S-wave anisotropy is only about 2% when the SKS and SKKS rays travel parallel to the Z-directions in the upper mantle (i.e., a horizontal foliation). This magnitude of S-wave anisotropy gives a delay time of about 0.5 s for a 100 km thick anisotropic layer (Table 2.6, Fig. 2.6d). In the case where foliation is horizontal in the crust, the contribution of the crust to SKS splitting may be negligible (Ji and Salisbury, 1993), and thus it may be reasonable to assume that all the delay time is due to the seismic anisotropy hosted in the upper mantle. As a first approximation, a delay time of 1.7 sec implies a 340 km thick anisotropic layer in the upper mantle beneath Station PNT. The smaller δt values detected at other stations can be simply caused either by a thinner anisotropic layer or by possible deviations of the foliation and lineation from their horizontal orientation.

Previous theoretical analyses (e.g., Karato and Wu, 1993) and experiments (Karato et al., 1986; Zhang and Karato, 1993; Zhang et al., 2000) show that LPO development in polycrystalline aggregates is controlled by the deformation mechanism. LPO develops where the deformation mechanism is dominated by recovery-accommodated dislocation creep. But no LPO develops when grain-size-sensitive diffusion creep prevails, resulting in an isotropic seismic structure. Based on this idea, Ji et al. (1994) considered the lower boundary of the anisotropic layer to coincide with the transition from dislocation creep to diffusion creep in the upper mantle. They used the following power-law flow law to evaluate the deformation mechanism fields for olivine:

$$\dot{\varepsilon} = A\left(\frac{\sigma}{\mu}\right)^n \left(\frac{b}{d}\right)^m \exp\left(-\frac{E+PV}{RT}\right) \qquad (2.1)$$

where $\dot{\varepsilon}$ is the strain rate, A is a pre-exponential coefficient, σ is the differential

Table 2.6. Delay time between two split shear-wave arrivals for different mantle layer thickness, calculated based on average xenolith data.

Thickness	δt (s)			
(km)	**X-direction**	**Y-direction**	**Z-direction**	**maximum**
100	0.3	0.9	0.5	1.0
150	0.5	1.4	0.7	1.6
200	0.7	1.7	1.0	2.1
250	0.9	2.2	1.2	2.6
300	1.0	2.6	1.5	3.1
350	1.3	3.0	1.8	3.7

stress, μ is the shear modulus (81 GPa), n is the stress exponent, m is the grain-size exponent, b is the length of the Burgers vector (0.5 nm for [100] slip), d is the grain size, E is the activation energy, P is the pressure, V is the activation volume, T is the temperature in K, and R is the gas constant. For olivine in the dislocation creep regime, $A=3.5x10^{22}$ s^{-1}, n=3.5, m=0, E= 540 kJ/mol, and V=15 cm^3/mol (Karato et al., 1986). For olivine in the diffusion creep regime, $A=8.7x10^{15}$ s^{-1}, n=1.0, m=2.5, E=300 kJ/mol, and V=6 cm^3/mol (Karato and Wu, 1993). Based on the assumption that at a given T, P, grain size, and strain rate, the mechanism which gives the lowest flow stress is the dominant deformation mechanism, the critical grain size for the transition between dislocation creep and diffusion creep was calculated as a function of temperature in the upper mantle (Fig. 2.10). As shown in Fig. 2.10b, line ab separates two domains; at lower T and P, higher stress, and larger grain size, dislocation creep dominates, whereas at higher T and P, lower stress and smaller grain size, deformation occurs by diffusion creep.

The mantle xenoliths from both the southern and northern Canadian Cordilleras have average olivine grain sizes of at least 1-2 mm and have been equilibrated at temperatures between 900 and 1250 °C. The commonly observed occurrences of strong olivine LPOs (Fig. 2.3) and dislocation recovery structures such as subgrain boundaries (Fig. 2.2) suggest that dislocation creep is important in the mantle from which they were sampled by magma. Thus these mantle xenoliths are located well within the dislocation creep field (above line ab) predicted by extrapolating the laboratory flow laws of Karato et al. (1986) to natural strain rates (e.g. 10^{-13}/s for active orogenic zones). There is thus a good correspondence between theoretical models and the features observed in mantle peridotites.

As shown in Fig. 2.10, the geothermal profile and particularly the olivine grain size are critical factors in determining the thickness of the mantle anisotropic layer. In the Canadian Cordillera, where the geothermal gradient is high (Fig. 2.10a)

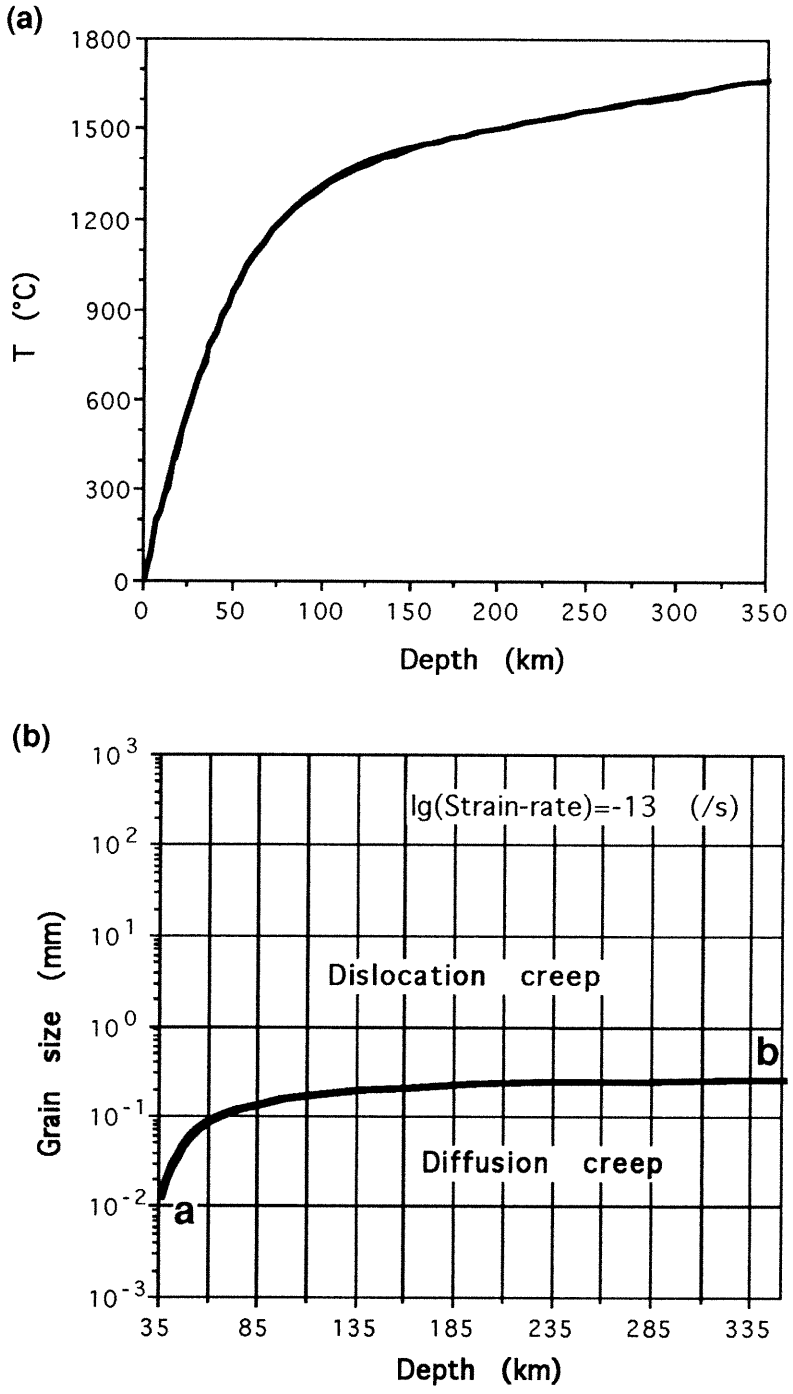

Figure 2.10. (a) Temperature variation with depth for the Canadian Cordillera. (b) Transition between dislocation creep and grain-size-sensitive diffusion creep in olivine aggregates as a function of depth and grain-size in the mantle beneath the Canadian Cordillera.

and the strain-rate is rapid (e.g. 10^{-13}/s), as long as the average olivine grain size exceeds 0.5 mm, all of the upper mantle above the olivine-spinel transition zone at about 350-400 km will be dominated by dislocation creep, and consequently be seismically anisotropic (Fig. 2.10b). But the olivine fabric intensity and hence bulk seismic anisotropy may vary with depth as the differential flow stress attenuates first with increasing temperature from the Moho to about 150 km depth and then increases slowly with increasing pressure due to the effects of activation volume (Fig. 2.11). This agrees with the results of surface-wave tomography (Montagner and Tanimoto, 1991) and S-wave splitting (Russo and Silver, 1993).

The thickness of the anisotropic layer (~350 km) in the upper mantle estimated from the point view of olivine rheology coincides with the S-wave splitting measurements in the southern Canadian Cordillera (Bostock and Cassidy, 1995). This is consistent with the shear-wave splitting results obtained from other subduction zones. For example, Fouch and Fischer (1996) investigated the anisotropic structure of the upper mantle beneath Sakhaline Island (Russia) and Japan arc by analyzing both local subduction zone earthquakes and teleseismic SKS phases. They found that the delay time between the two split shear waves coming directly from the subducting slab increases with source depth, reaching the SKS values at depths between 400 and 600 km. Similar results have been obtained by Gledhill and Stuart (1996) from studies of the Hikurangi subduction zone (New Zealand). The study of Alsina and Snieder (1994) suggests that the anisotropy recorded by SKS and SKKS splitting is partly located in the asthenosphere at about 400 km depth. Other evidence for the presence of anisotropy throughout the upper mantle is found in a comparison of the results of Vinnik et al. (1992) with those of Shih et al. (1991). At the same station (BOCO: 4.6°N, 74°W), Vinnik et al. (1992) and Shih et al. (1991) respectively measured S-wave splitting in SKS phases and shear-waves from intermediate-depth earthquakes in the neighboring Bucaramanga nest. The fast polarization directions

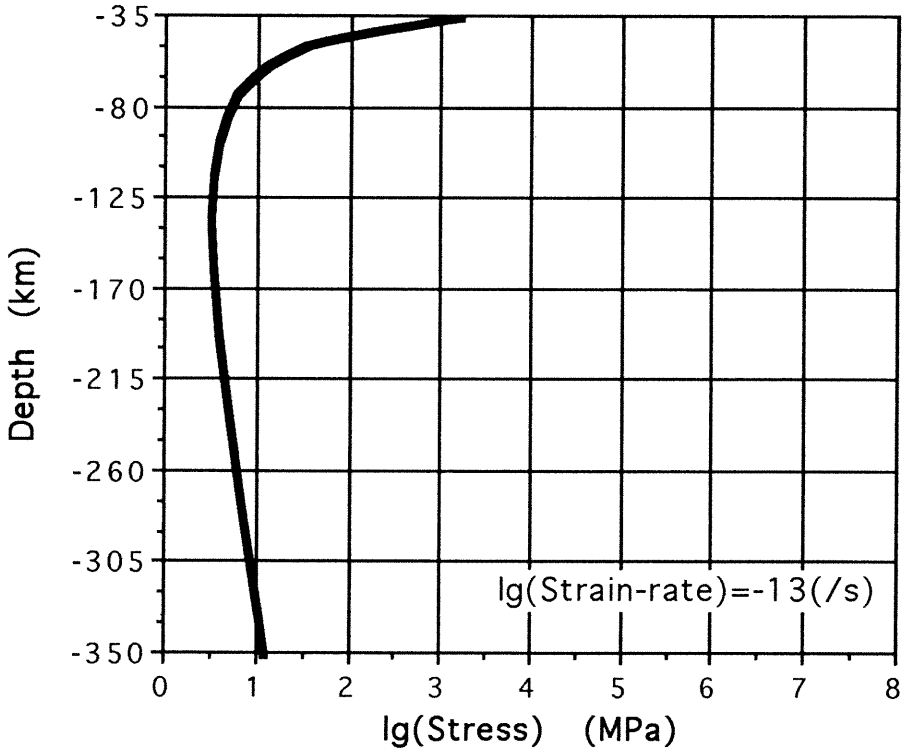

Figure 2.11. Variation of upper mantle flow strength with depth in the dislocation creep field beneath the Canadian Cordillera. The strain rate is assumed to be 10^{-13} /s.

determined using these two methods are very similar (~16°± 4°). The largest delays reported by Shih et al. (1991) for events at depths near 160 km, however, are only about 0.4 s, which is only one third of the value obtained by Vinnik et al.. This discrepancy implies that a larger thickness (300-400 km) of anisotropic mantle was sampled by the SKS waves. Finally measurements of direct S-waves from events deeper than 400 km and measurements of SKS phases at the same station display the same δt values (e.g., Peru: Kaneshima and Silver, 1995; Meade et al., 1995; the western Pacific margin: Fouch and Fischer, 1996; New Zealand: Gledhill and Stuart, 1996. Tonga: Fischer and Wien, 1996) implying that the entire upper mantle above the olivine/spinel transition zone at 400 km is anisotropic.

In the northern Canadian Cordillera and Alaska, mountain-parallel movement results in intensive ductile deformation with displacements of hundreds to thousands of kilometers and produces strong olivine LPO, steeply dipping foliation and horizontal stretching lineation in the upper mantle (Ji et al., 1994). Under these circumstances, the SKS waves propagate nearly parallel to the Y-direction of the structural frame. As a result, δt may be as high as 1.7 s for a S-wave propagating vertically through a 200 km thick section of upper mantle and the ϕ direction is nearly parallel to the strike of the shear zones (Figs. 2.1 and 2.6). The parallelism between the ϕ directions and the fault zones (Tintina fault, Denali fault, Kaltag fault) indicates a horizontal stretching lineation in the upper mantle beneath the northern Canadian Cordillera and Alaska. The maximum delay time (δt = 1.6 s) observed at station COL suggests that an anisotropic layer about 200 km thick underlies in the region. However, it is difficult to conclude, based simply on the measured δt values, that the total thickness of the anisotropic layer(s) in the upper mantle is smaller beneath the northern Cordillera than the southern Cordillera. The reason is that there is no way, at present, to know how uniform seismic anisotropy is in the subcontinental upper mantle. If the seismic anisotropy is concentrated in distinct layers rather than

distributed continuously throughout the upper mantle, one might expect multiple splitting of the SKS phase (Ji et al., 1994). Each split shear wave rising out of a deeper anisotropic layer could split again when it enters a shallower anisotropic layer. Multiple splitting will complicate the waveform (Savage and Silver, 1993) and make the measurement and interpretation of S-wave splitting difficult. Hence shear-wave splitting in a single, thick anisotropic layer may be much easier to detect than in multiple, thin anisotropic layers.

In terms of crustal structure and deformation style, the northern and southern Canadian Cordillera differ markedly (Sweeney et al., 1991; Gabrielse, 1991). Fault motions in the northern Cordillera are dominated by large dextral offsets while such offsets are much less prevalent in the southern Cordillera. As pointed out by Gabrielse (1991), there is no evidence of strike-slip faulting at the surface in southern British Columbia. Seismic reflection profiles show that the crust is thicker in the northern (~37-40 km, Creaser and Spence, 1999; Lowe and Cassidy, 1995) than in the southern (33-38 km) Canadian Cordillera. In the southern Canadian Cordillera, crustal deformation between the Fraser Fault and the Rocky Mountain Trench is dominated by extension and normal faulting (Fig. 2.8b). The Fraser Fault and Rocky Mountain Trench are the continuation of the Denali Fault and the Tintina Fault, respectively. Moreover, the southern Canadian Cordillera is characterized by high heat flow (Hyndman and Lewis, 1999). The above crustal deformation characteristics are believed to reflect different deformation styles in the upper mantle: mountain-parallel movement beneath the northern Canadian Cordillera and mountain-perpendicular extension beneath the southern Canadian Cordillera.

A tectonic model is schematically shown in Fig. 2.9. From north to south, the strike slip faults evolve progressively into listric normal faults. In the subcrustal upper mantle, the foliation is vertical in the north and turns gradually into sub-horizontal in the south (Fig. 2.9). The large dextral strike slip in the northern Canadian Cordillera

and Alaska is accommodated by extensional deformation in the southern Canadian Cordillera. This model may provide a good explanation for the variation of the ϕ directions in the region.

2.6. Conclusions

(1) Two olivine LPO patterns are recognized for the peridotite xenoliths from the upper mantle beneath the southern Canadian Cordillera: one formed by (010)[100] slip, the other by {0kl}[100] slip. The dominant deformation mechanism in the upper mantle above the olivine/spinel transition zone at about 400 km is dislocation creep.

(2) Seismic properties of representative peridotite xenoliths from the southern Canadian Cordillera have been calculated from LPO data and the volume fractions of each constituent mineral. Extrapolation to in-situ P-T conditions (~1000 °C, 1.5 GPa, corresponding to approximately 50 km) gives an average P-wave anisotropy of 7.5 % with the maximum Vp parallel to the stretching lineation (X), the minimum Vp parallel to the normal to foliation (Z), and an average S-wave anisotropy of 4.8 % (Fig. 2.5d). Both the V_p and the V_s anisotropy of the peridotite xenoliths increase with the volume fraction of olivine, and decrease with the volume fraction of pyroxenes and spinel. The average S-wave splitting (Fig. 2.6d) shows a complicated pattern with maximum values mid-way between the Y- and Z-directions and minimum values mid-way between the X- and Z-directions. The fast split S-wave polarization depends on the propagation direction with respect to the tectonic framework (X-Y-Z) and is parallel to the stretching lineation when the propagation direction is parallel to either the Y- or Z-direction. The maximum delay time between the split S-wave arrivals can be as high as 1.0 s for a 100-km thick anisotropic mantle layer.

(3) Calculated Vp patterns for peridotite xenoliths from the southern Canadian Cordillera show a single maximum parallel to the olivine a-axis concentration, while

A(Vs) patterns are divided into two types: (i) a point maximum nearly parallel to the Y-direction and (ii) a complete or partial girdle along the YZ-plane, in which two point maxima are symmetrically distributed with respect to the foliation (XY) plane.

(4) Comparison of in-situ P_n velocities in the upper part of the upper mantle with calculated V_p values for peridotite xenoliths suggests that both the foliation and stretching lineation are horizontal in the upper mantle beneath the Intermontane and Omineca Belts. The presence of a weak Pn anisotropy between the NS and EW transects suggests that the stretching lineation is oriented NE. This conclusion is consistent with the ϕ directions of teleseismic SKS waves, the relative plate motion, and the maximum horizontal stresses measured in the crust.

(5) The maximum measured SKS delay time in the region is about 1.7 s (Bostock and Cassidy, 1995). Such a value corresponds to a continuous 350 km thick anisotropic layer with horizontal foliation. A similar thickness is also supported by the olivine rheology and geotherm gradient. These results suggest that the entire upper mantle above the olivine/spinel transition zone contributes to the seismic anisotropy observed using SKS splitting. The observed SKS splitting probably results from the present-day asthenospheric flow under the Canadian Cordillera, which is an active orogenic belt, rather than ancient tectonic deformation frozen within the lithospheric mantle.

(7) A tectonic model has been proposed for the Canadian Cordillera based on regional geological and geophysical data. From north to south, the strike slip faults evolve progressively into listric normal faults. In the subcrustal upper mantle, the foliation is vertical in the north and turns gradually into sub-horizontal in the south. The upper mantle is dominated by dextral strike slip beneath the northern Canadian Cordillera and Alaska (Ji et al., 1994) and by horizontal extension beneath the southern Canadian Cordillera. This model provides a good explanation for observed variations of ϕ in the region.

Chapter 3

Fractures in garnet crystals in granulite-facies metamorphic rocks of the Morin shear zone, Grenville Province, Canada*

Can you hear me?
I'm trying to say something.
Jayamya Guha
(E. Roedder, 1984)

3.1. Introduction

Pervasive, closely spaced, foliation-perpendicular or quasi-perpendicular, brittle extension fractures of garnet crystals are very common in high grade, foliated and lineated metamorphic rocks (e.g. Martignole, 1975; Petrakakis, 1986; Prior, 1993; Hames and Menard, 1993; Ji et al., 1993; Ji and Martignole, 1994; Elvevold et al., 1994; Moecher and Wintsch, 1994; Indares, 1995; Whitney, 1996; Azor et al., 1997; Pennacchioni and Cesare, 1997; Kraus and Williams, 1998; Bell et al., 1998; Raith and Harley, 1998; Hannula et al., 1999). The garnet fractures may be observed both in the field and under the microscope. However they have not been studied explicitly and in detail in the literature. In this chapter, high grade mylonites and gneisses from the Morin Shear Zone (MSZ) of the Grenville Province (Quebec) were chosen as an example to demonstrate the characteristics of garnet fractures and to analyze the origin of the fractures.

---

* A part of the study is published in the Journal of Structural Geology, 19, (1997) 603-620.

3.2. Geological setting

The MSZ constitutes the eastern limit of the Morin terrane which belongs to the southern part of the Canadian Grenville Province (Rivers et al., 1989) (Figs. 3.1 and 3.2). The central part of this terrane is occupied by the Morin anorthosite which consists of a dome emplaced as a diapir during the Grenville orogenic cycle (1154 Ma, U/Pb on zircon, Doig 1991) and an eastern lobe that was considered to be a nappe thrust towards the east (Martignole and Schrijver 1970), but is now interpreted as a portion of the MSZ based on seismic reflection profiles along LITHOPROBE lines 53 and 54 (Martignole et al., 1995; Martignole and Calvert, 1996; Ji et al., 1997). The Morin anorthosite is surrounded by charnockites intruded between 1135 Ma and 1160 Ma (Friedman and Martignole, 1995) and recrystallized under granulite facies conditions (750-900 °C and 700-900 MPa; Zhao, 1997). The transition between the weakly deformed anorthosite protolith and the MSZ is quite sharp in the studied area (Figs. 3.1 and 3.2). The high grade metamorphic rocks of the MSZ had been uplifted to the Earth's surface before 544 Ma since they are covered by horizontal Cambrian and Ordovician sedimentary strata.

The MSZ consists of highly strained (γ can be as high as 10) rocks of both metasedimentary and metaplutonic origin. Most of these rocks can be classified as straight gneisses (Hanmer and Ciesielski, 1984), protomylonites, mylonites and ultramylonites. Generally, they show a W-dipping (20-40°) mylonitic foliation defined by quartz ribbons, flattened feldspar and pyroxene grains and a predominantly subhorizontal stretching lineation defined by elongated pyroxene, quartz ribbons, feldspar porphyroclasts or sillimanite crystals. The direction of these lineations varies slightly from NNW to NS. Outcrop-scale isoclinal folds have their axial planes parallel to the mylonitic foliation and their axes parallel to the stretching lineation (Fig. 3.2). The mineral assemblages of these rocks were equilibrated at granulite-facies conditions and have suffered very little retrograde metamorphism, indicating rapid uplift and cooling with no inflow of water. Kinematic indicators such as winged porphyroclasts, C/S

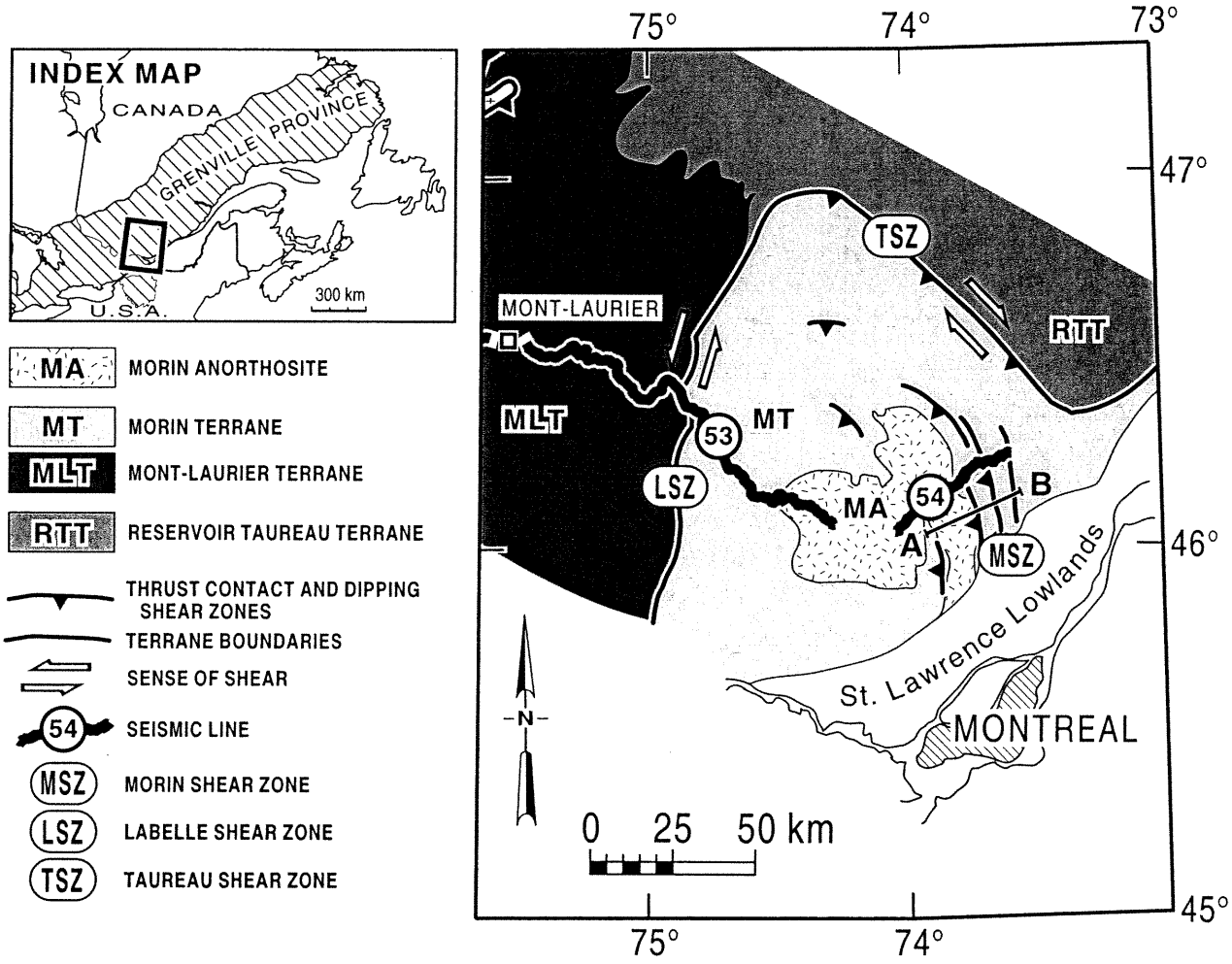

Figure 3.1. Geological map showing the location of the Morin shear zone (MSZ), seismic reflection lines 53 and 54, and major structural features in the study region. The inset map shows the location within the Grenville Province in Canada. According to Ji et al. (1997).

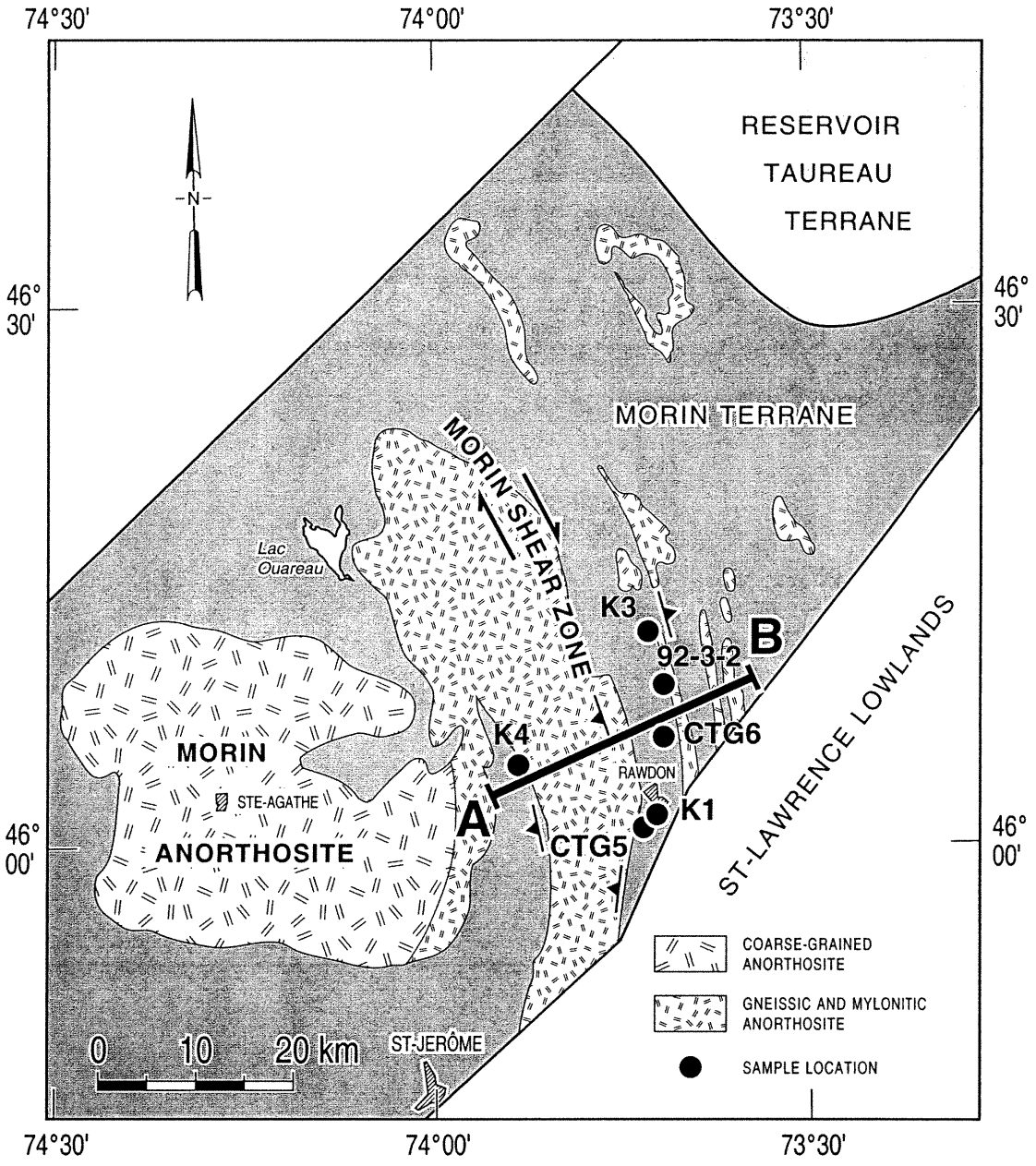

Figure 3.2. Geological map showing the location of the Morin shear zone and the locations of samples examined in this study.

structures, asymmetric boudins and extensional shear bands indicate that the MSZ was a dextral transcurrent fault and that it represents a lateral ramp along which the Morin terrane was displaced towards the north during the period between 1155 and 1030 Ma (Martignole et al., 1995). Detailed structural data for the MSZ are also given in Zhao et al. (1997) and Ji et al. (1997).

Starting from the SW along profile AB (see Fig. 3.1), the MSZ includes five major lithological units (Ji et al., 1997):

(1) annealed mylonitic charnockite (~1000 m);

(2) mylonitic anorthosite (~5000 m);

(3) granitic mylonites with repeated meter-scale clusters of quartzite, mafic granulite and granitic mylonite (~1300 m);

(4) charnockitic mylonites with repeated meter-scale clusters of granitic mylonite, mafic granulite and charnockitic mylonite (~1800 m), and

(5) thick (several hundred meter), moderately deformed garnet-sillimanite paragneisses (see Fig. 2 in Ji et al., 1997).

Units 3 and 4, which outcrop almost continuously along the eastern boundary of the Morin anorthosite, constitute a highly-strained and well-laminated horizon and represent a major strain boundary in the study area since there is a considerable rheological contrast between homogeneous anorthosite and quartz-rich supracrustal rocks. The rocks are usually separated by sharp contacts which are parallel to the foliation. This indicates that the lithologic laminations are tectonically-transposed layers and/or metamorphically-differentiated layers.

The garnet-bearing metamorphic rocks in the MSZ are mainly pelitic, charnockitic, quartzitic, granitic and mafic mylonites and gneisses. Strong ribbon and streaky shape-preferred orientation are manifested by these rocks. The quartzitic and granitic mylonites are characterized by highly strained quartz grains with scalloped or amoeboid grain boundaries preserving evidence of grain boundary migration. The

charnockitic gneisses are characterized by an annealed quartz microstructure including strain-free polygonal grains with straight grain boundaries. Garnet represents about 2-10 vol. % of the quartzitic, granitic and charnockitic mylonites and gneisses, and 10-40 vol. % of the pelitic and mafic gneisses. Outcrop-scale mode I joints (Price and Cosgrove, 1990) are preferentially oriented subnormal to the subhorizontal mylonitic lineation (Fig. 3.3). As shown in this figure, although the EW-oriented joints are dominant, NE-SE and NW-SE oriented joints are also recognized.

3.3. Characteristics of fractured garnets

Garnet is commonly isolated in a ductilely deformed matrix of feldspars and particularly quartz (Fig. 3.4). Electron microprobe data show that the garnets have almost identical composition (Alm 61-65 Prp 20-30 Grs 3-10 Sps 1-5) and that there is no significant compositional variation from core to rim. The garnet composition close to a fracture wall is the same as the bulk of the garnet crystal. The absence of compositional variation in the garnets can be attributed to homogenization by effective diffusion at high temperature (Yardley, 1977), to the absence of exchange reactions between garnet and adjacent minerals (quartz and feldspar) during cooling (Ji and Martignole, 1994), and likely to the low temperature environment during the fracturing of garnets.

Two large orthogonal thin sections (7x5 cm), one parallel to the mylonitic lineation (X) and perpendicular to the foliation (Z), and another one parallel to the foliation (XY plane) were cut from each sample for microstructural characterization. As demonstrated in Ji and Martignole (1994), the garnet crystals in granulite-facies mylonites and gneisses from the MSZ are approximated as oblate ellipsoids with their major axes in the XY plane and minor axes parallel to the Z direction. Every section parallel to the XZ plane through such an oblate ellipsoid, produces an elliptical profile with a constant axial ratio or aspect ratio (X/Z). For this reason, any section parallel to

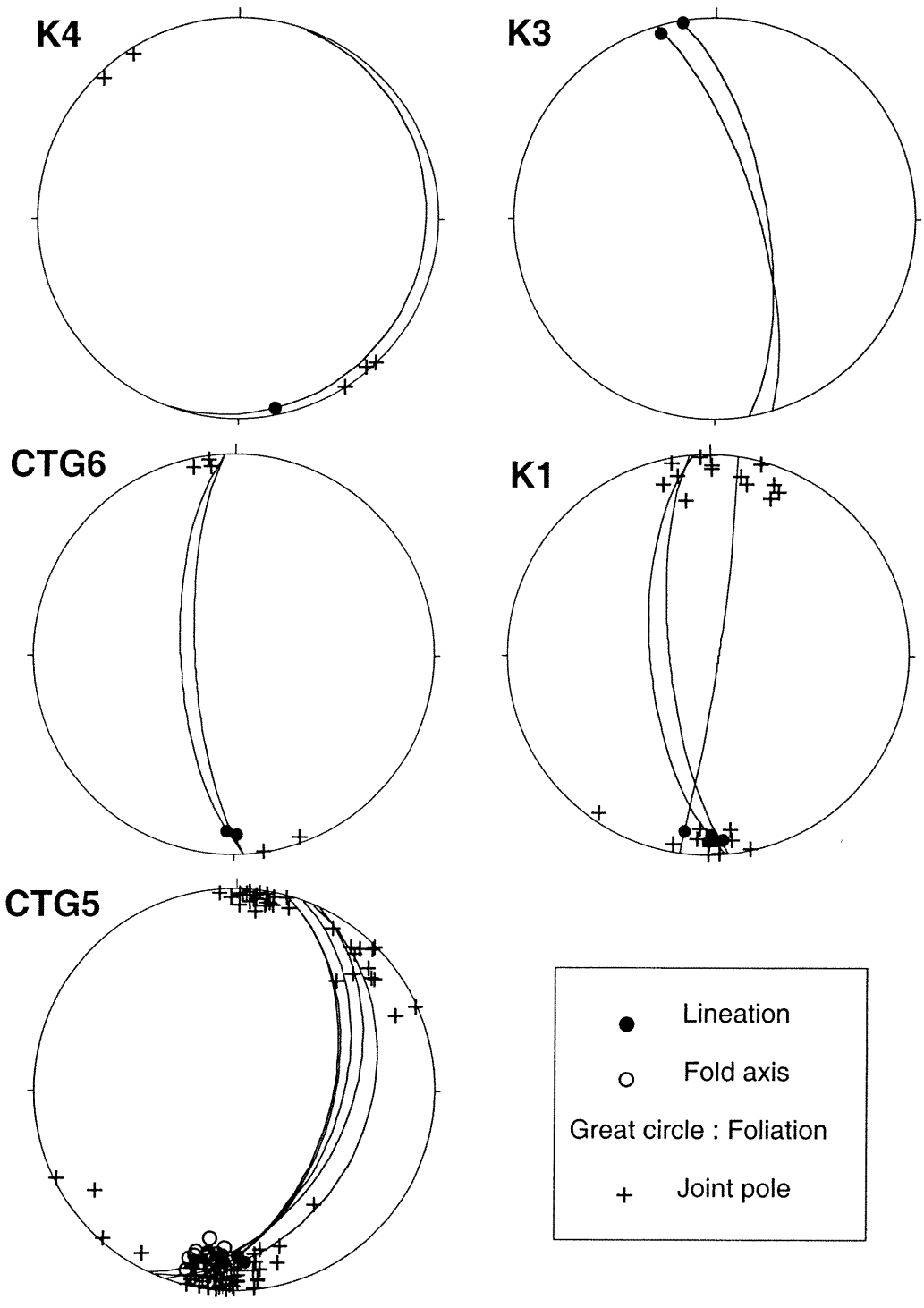

Figure 3.3. Stereographical plots of structural data measured at five localities within the MSZ.

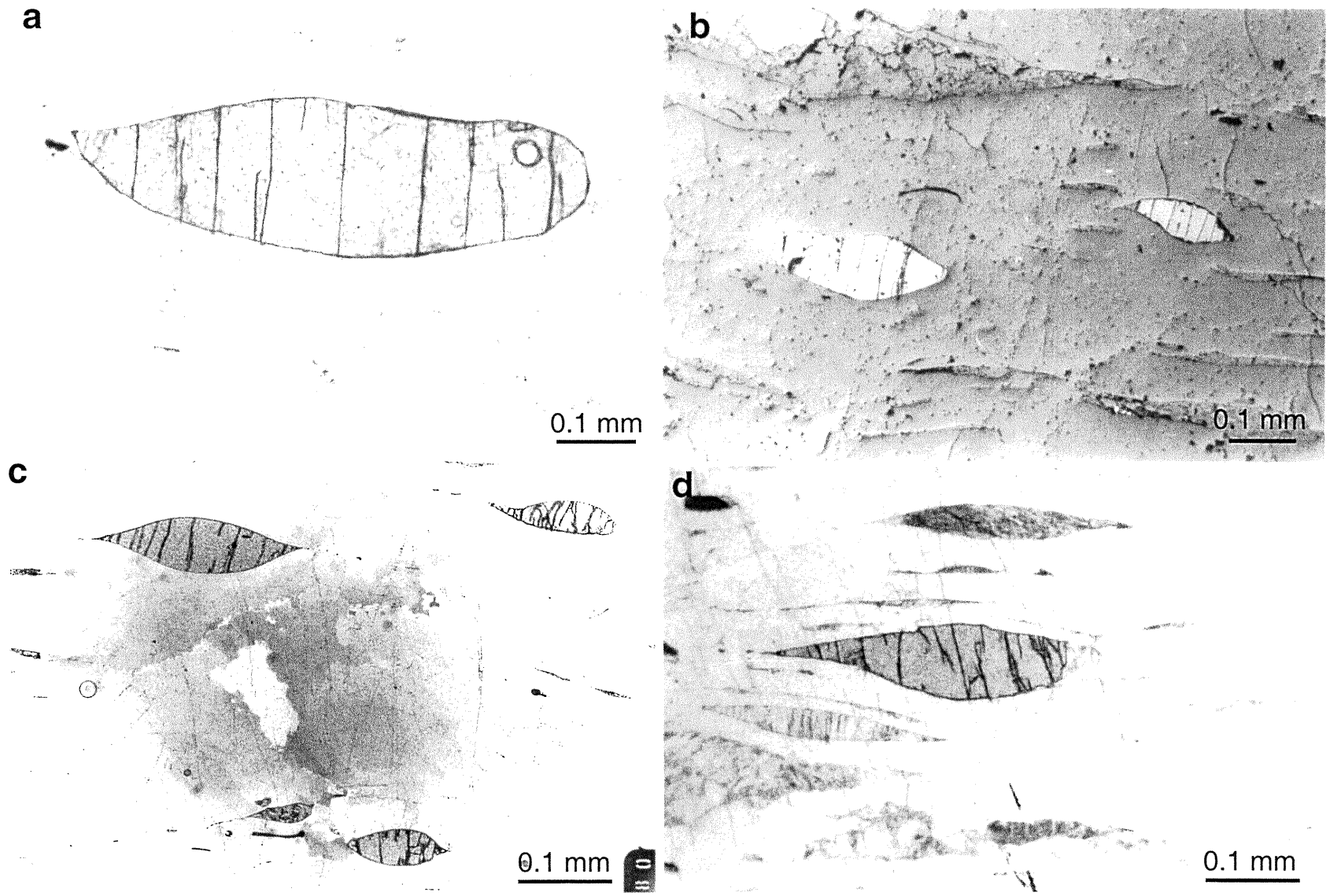

Figure 3.4. Photomicrographs of X-Z thin sections of fractured garnet crystals in quartzitic layers (a-i) and in paragneissic mylonites (j-l). All are transmitted light except (b). In (j-l), both lineation-perpendicular and foliation-parallel fractures developed. Lineation-perpendicular fractures are predominant and more planar and regular than subordinate foliation-parallel fractures. In (c-h), fluid inclusion trails in the quartz matrix are observed parallel to the fractures in the garnets.

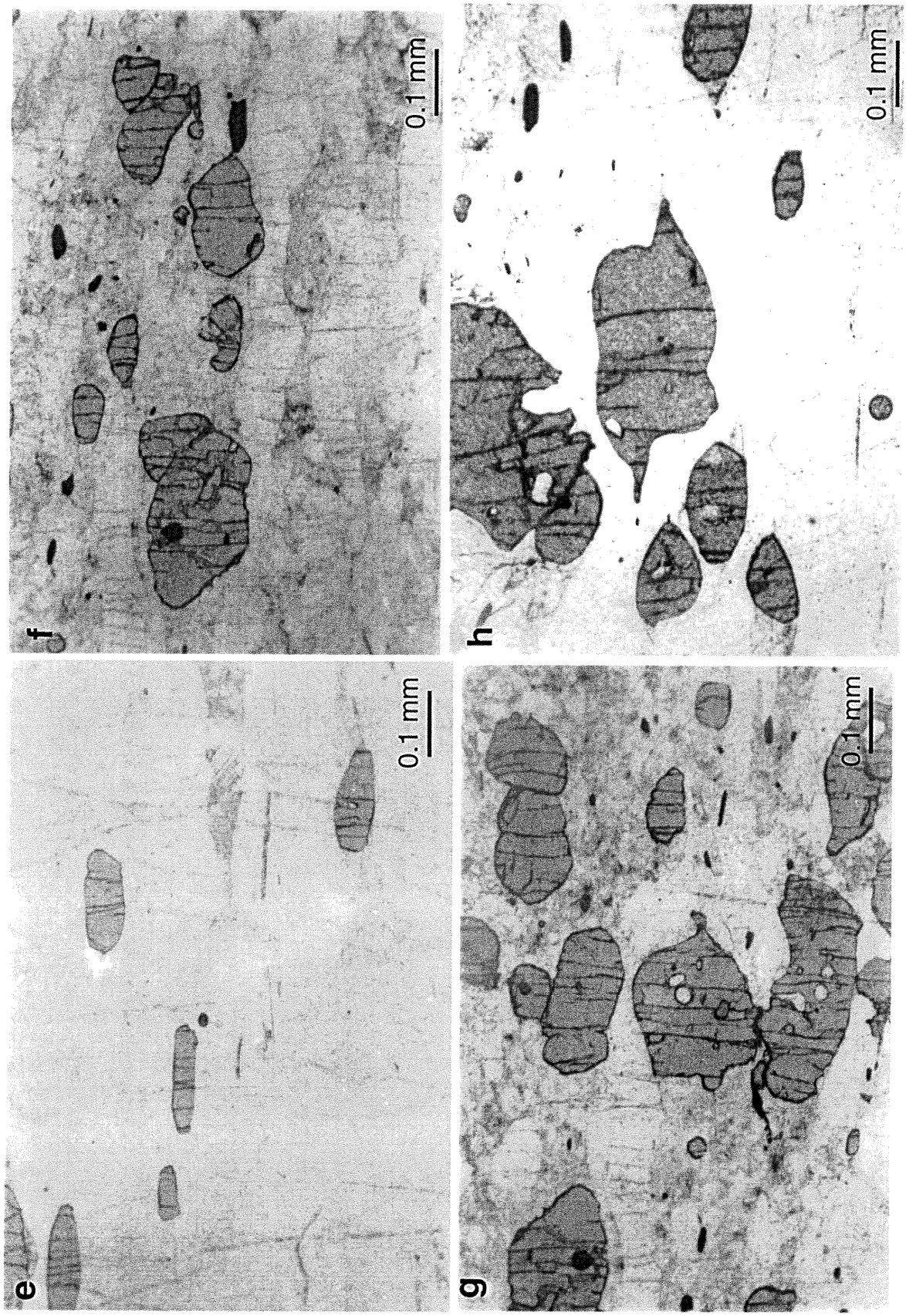

Figure 3.4. (Continued)

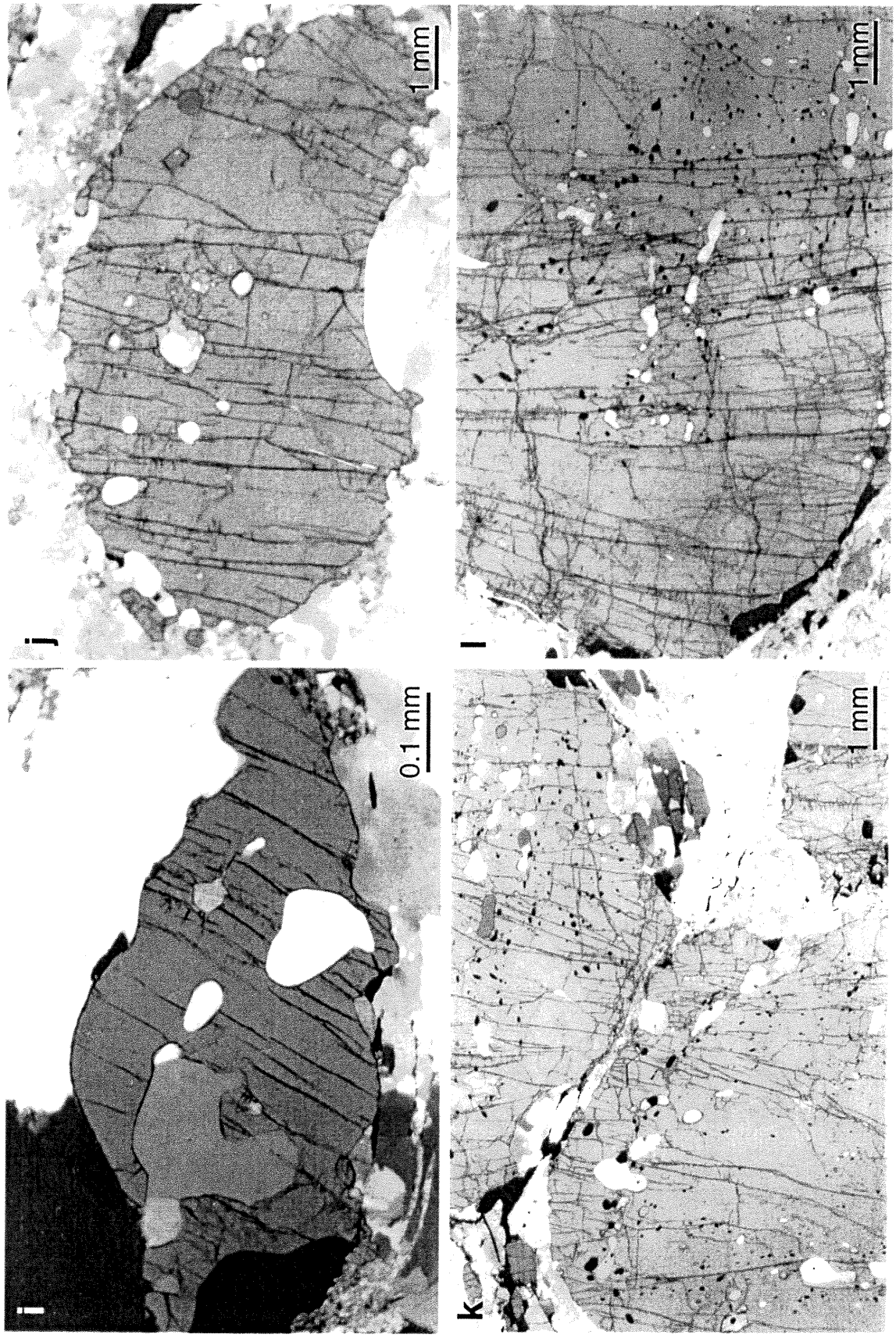

Figure 3.4. (Continued)

the Z direction (e.g. the XZ sections) is almost sufficient to determine the characteristic parameters for garnet size. Moreover, both field and laboratory observations demonstrate that the fractures in the studied garnet crystals are dominantly perpendicular to the XZ plane. It is thus best to measure fracture spacing and orientation on the XZ sections.

Whether it is possible to determine the true 3-D size distribution from 1-D or 2-D size data depends largely on the variations in shape and volume of the grains. If all grains approximate equi-sized spheres or cubes, the relationship between the 3-D size and the mean linear intercept is simple (Underwood, 1970). For ellipsoidal grains with varying volumes and axial ratios, however, it has not been possible to determine the 3-D volume distribution from the measured cross sectional area (Underwood, 1970).

The X-ray CT (Carlson and Denison, 1992) was not used to characterize the microstructure of the mylonites from the Morin shear zone for the following reasons: (1) The technique is complicated, expensive and inaccessible to many geologists. (2) As shown by Denison et al. (1997), the practical limit of resolution for the X-ray CT is on the order of 0.1-0.2 mm. Thus, grains smaller than this limit cannot be measured. (3) The 3-D data needed to determine the size and shape of individual crystals can only be obtained by stacking a series of two-dimensional CT images of slabs through the specimen. The thickness of each such slab is as large as 0.25-0.50 mm (Carlson and Denison, 1992). Each slab is then idealized as a flat cylinder. A sufficient numbers of slabs is needed through an individual grain in order to allow reconstruction of the true grain shape. Thus, the shapes of garnet crystals smaller than 3.0 mm cannot be determined precisely using the technique and most of the garnet grains from the MSZ are smaller than 2 mm. Finally it is difficult to separate overlapping grains within a slab along the transmission direction.

Under the optical microscope, the following parameters were measured for all of the garnet grains in each thin section cut parallel to the XZ plane (Fig. 3.5):

(1) the maximum length ($2L$);

(2) the maximum width ($2r_0$);

(3) the angle between each fracture and the mylonitic foliation (ϖ);

(4) the width of a grain in the direction of each given fracture (w);

(5) the actual length of each fracture (b), $b = w$ for transgranular fractures, and $b < w$ for intragranular fractures; and

(6) the normal distances between a fracture and its two nearest neighbors (f_1 and f_2). In addition, special attention was paid to determining whether the fractures in garnet grains extend into their surrounding matrix minerals such quartz, feldspar and sillimanite.

The grain size (d) and aspect ratio (s) of each garnet grain were calculated respectively by

$$d = 2\sqrt{Lr_0} \qquad (3.1)$$

and

$$s = L/r_0 \qquad (3.2).$$

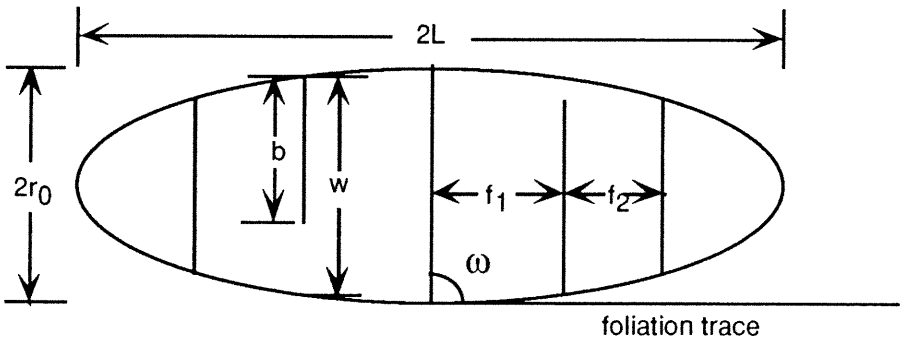

Figure 3.5. Schematic diagram illustrating the parameters measured for statistical analysis.

Figures 3.6a and c are linear histograms showing frequency distributions of d and s of

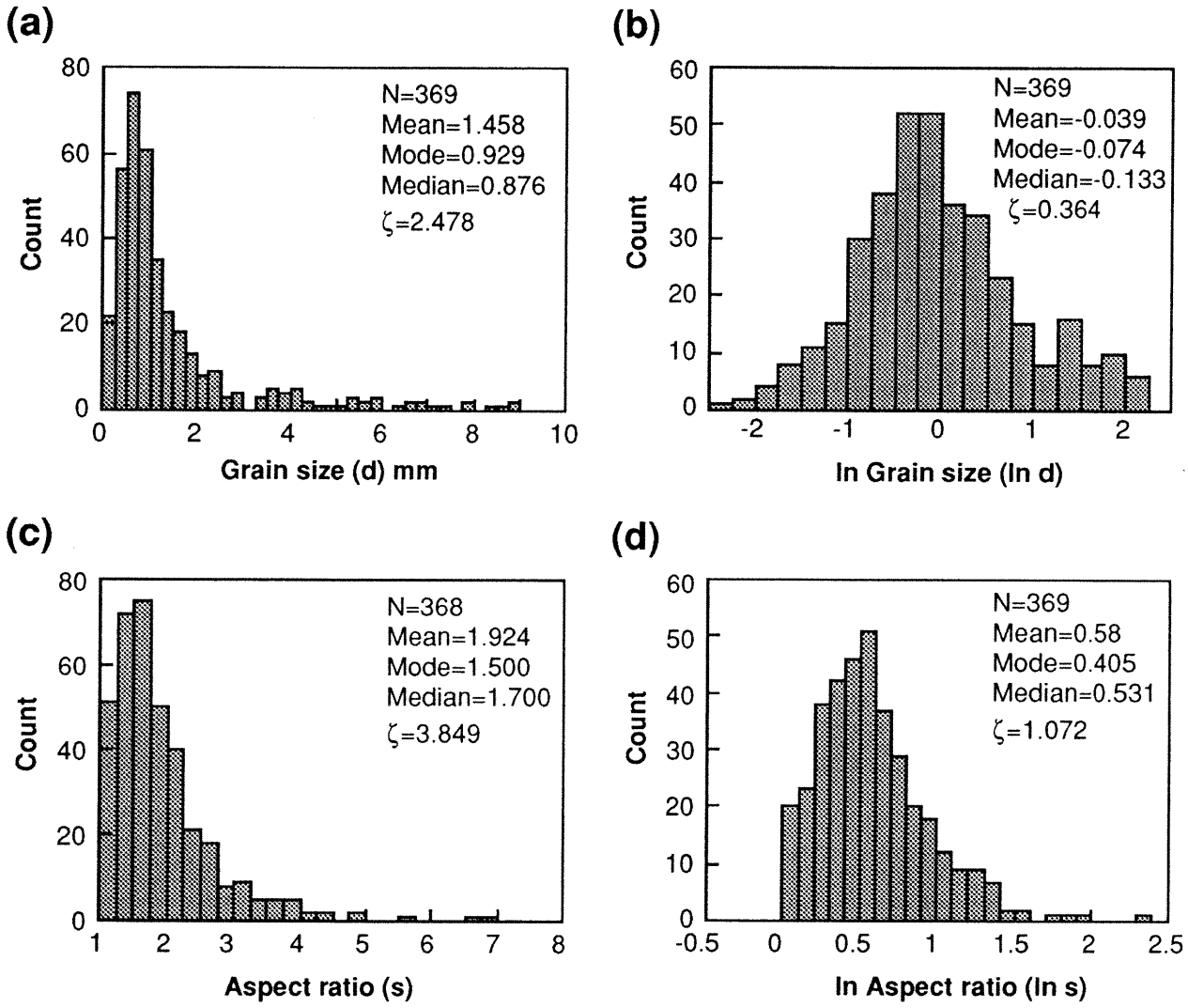

Figure 3.6. Frequency distributions of garnet grain size (a and b) and aspect ratio (c and d) in the studied mylonites; (a) and (c) linear scale; (b) and (d) natural log scale. ξ: skewness; N: number of measurements.

garnet, respectively. The mean d and s values are greater than the mode and median values, which indicates that the distributions of grain size and aspect ratio are skewed with the right tail of the distributions being longer than the left tail (Figs. 3.6a and c). The distribution of s is truncated at values less than 1 because the aspect ratio is defined as the ratio of the maximum length to the maximum width. Figures 3.6b and d are histograms of the natural logarithms of d and s for the same data and show that the grain size and aspect ratio of the garnets may be approximately described by log-normal distributions. It is noted that 34% of the garnet grains have an aspect ratio larger than 2 while only 33% have an aspect ratio less than 1.5. Garnet crystals from quartzitic, granitic and charnockitic mylonites are more elongate than those from paragneiss and mafic granulite. The elongate garnet crystals are oriented with their longer axis parallel to the mylonitic foliation. The origin of these flattened garnets has been discussed in Ji and Martignole (1994, 1996).

The mean fracture spacing (m) of a given grain is calculated according to

$$m = \frac{2L}{n+1} \qquad (3.3)$$

where n is the total number of fractures across the garnet elongation direction.

The aspect ratio of fractured segments (s_f) can be calculated from w and f_1 or f_2 data,

$$s_f = f_1/w \qquad (3.4).$$

Principal characteristics of the fractured garnets are as follows:

(1) In a garnet crystal, the fractures can either cut across the entire grain (transgranular) or terminate inside the grains (intragranular) (Figs. 3.4 and 3.7a). Statistical studies (Fig. 3.7a) show that 51% of the garnet microfractures are

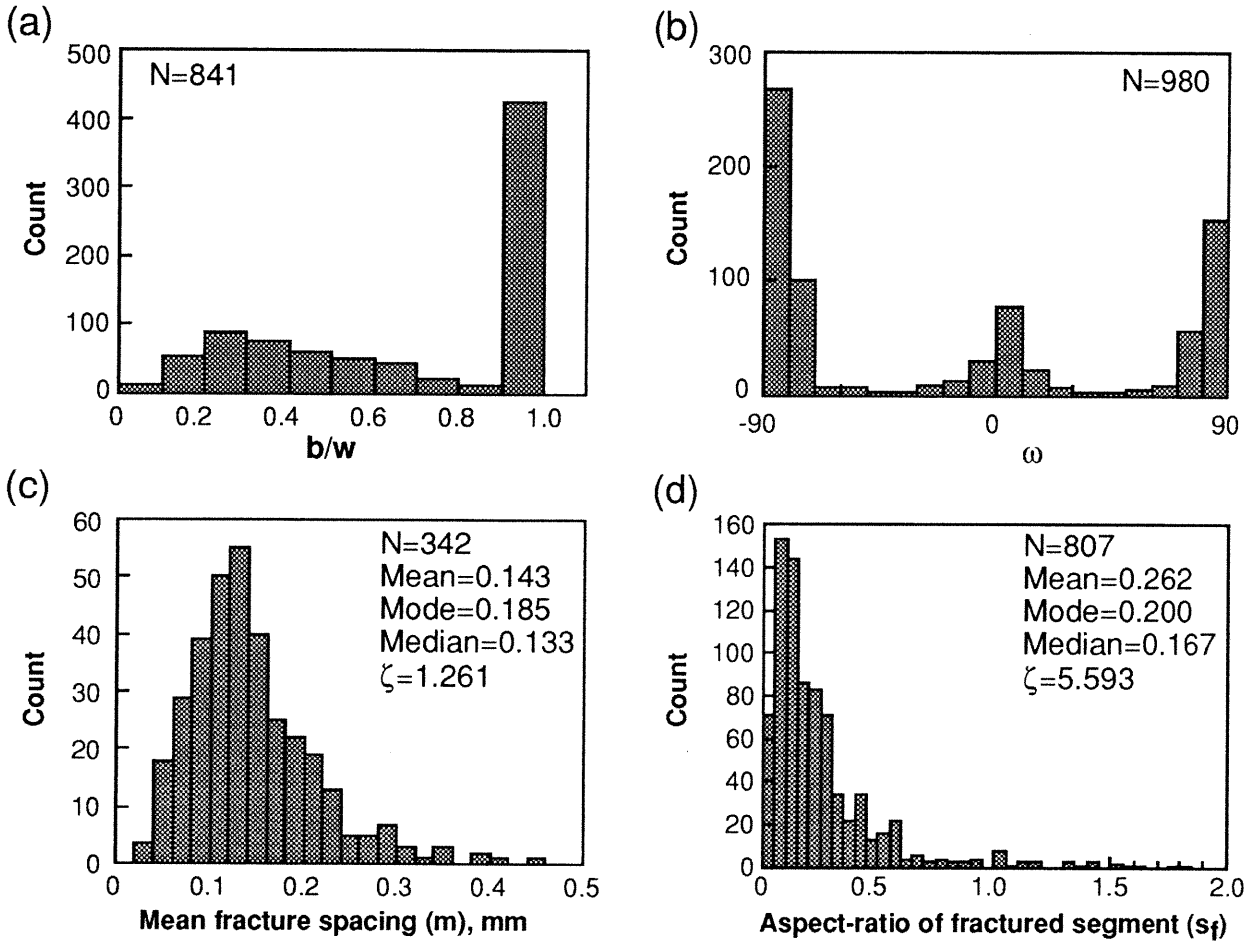

Figure 3.7. (a) Frequency distribution of b/w ratio; (b) preferred orientation of the garnet fractures with respect to the foliation and lineation (0° position); (c) mean fracture spacing; (d) aspect ratios of fractured segments, ξ, skewness; N, number of measurements.

transgranular and 49% are intragranular. Both types of fractures are generally straight rather than curvilinear (Figs. 3.4) and form quasi-parallel arrays. The intragranular microfractures commonly taper from the grain boundary towards the core, indicating that these microcracks initiated at flaws along grain boundaries and then propagated inward for different distances toward the grain centers. Our measurements show that about 36% of the microfractures propagated inward for a distance less than half the width of a grain (Fig. 3.7a). Some fractures appear to have started and propagated from the boundaries of inclusions (mainly quartz) within the garnets since few inclusions are cut through by fractures (Figs. 3.4a, 4i-l). These observations indicate that the interfaces between different phases are mechanical and structural heterogeneities that control the initiation of fractures. Cracks might originate independently at each side boundary of a garnet crystal and propagate inward, forming a single transgranular crack or two overlapping cracks (Figs. 3.4i-l). Single intragranular fractures that have their two ends terminating in the interior of a garnet are also observed locally (Fig. 3.4). Some cracks have a curving-perpendicular geometry (Rawnsley et al., 1992) at abutments with nearby fractures (e.g. Fig. 3.4b).

(2) About 70% of individual fractures are confined to the host garnet, including both transgranular and intragranular fractures (Figs. 3.4), while about 30% of fractures appear to extend into the surrounding matrix minerals (e.g., mainly quartz and sillimanite) (Figs. 3.4). The fractures in quartz grains are healed and recognized by the alignment of bubbles which are either fluid inclusions or mineral precipitates deposited when the microfractures were open to pore fluids during or after fracturing. No grain boundary fractures are observed, indicating a high interfacial strength in the rocks (Lloyd and Knipe, 1992).

(3) Fractures within garnet crystals are pervasively developed and are relatively straight, single strand cracks (Figs. 3.4). There is no evidence showing that the crack surfaces in garnet grains have been eroded or modified by dissolution.

(4) Elongate and/or small garnet grains generally develop only a set of tensile fractures perpendicular to foliation and lineation (Figs. 3.4a-d) while large and/or equant garnet grains usually develop two sets of tensile fractures (Figs. 3.4j-l). Figure 3.7b shows that about 80% of the fractures are perpendicular and 20% are parallel to the foliation and lineation. Both sets are best observed in the XZ sections cut perpendicular to the foliation and parallel to the lineation (Figs. 3.4j-l). The lineation-perpendicular (LP) fractures are more planar and regular than the foliation-parallel (FP) cracks. Within a variance of $\pm 15^{\circ}$, the LP fractures are mutually parallel, and parallel to those in all other garnets in the same sample and even in the same outcrop. The FP cracks usually abut against the nearest LP fractures, forming a ladder-like pattern. Some FP cracks cross-cut one or several LP fractures before abutting (Fig. 3.4i-l). The frequent abutments of FP cracks against LP fractures suggest that the FP cracks are younger than the LP fractures. The occurrence of two perpendicular sets of tensile fractures in garnet crystals from a gabbro-derived amphibolite at Gore Mountain (Adirondacks, New York) was reported by Valentino and Sclar (1981). The FP cracks in garnet crystals are similar to the cross joints observed in sedimentary rocks (Gross, 1993).

(5) Based on our observations of thousands of microfractures, no microfractures were seen to offset grain boundaries or any other features such as inclusions within garnet grains, even down to the microscopic scale. For any given fracture, the two fracture walls are almost always parallel to each other rather than converging in a V-shape (Hippertt, 1993; Michibayashi, 1996), suggesting that neither rotation of the fractured segments nor displacement oblique to the fracture normal occurred after microfracturing. Moreover, no *en echelon* arrays of fractures are found in the garnet grains. Thus, the fractures are extensional mode I (opening mode) fractures which formed perpendicular to the least principal stress (Engelder, 1993).

(6) The crack planes are very sharp, and no ductile deformation is visible at their edges, suggesting that the garnet was brittle when cracking took place. The fractures are

generally only several micrometers wide and appear as hairline fractures under the optical microscope. In addition, the fractures are generally very clean, with no marked retrograde materials (e.g. biotite, muscovite and chlorite). The fractured parts of each garnet grain have not been separated or filled with matrix minerals such as quartz and feldspar. This indicates that the mylonitic matrix did not flow plastically during and after the fracturing of the garnets. A stiff crystal such as garnet which fractured while located in a still active ductile shear zone would be rapidly disrupted by continued plastic deformation of its quartzo-feldspathic matrix (Lloyd et al., 1982, Ji and Zhao, 1993). One possible interpretation is that the fracturing took place at a low temperature or a high strain rate below which the quartzo-feldspathic matrix would not be capable of plastic flow. The upper limit of the quasi-plastic zone in quartzo-feldspathic crust generally corresponds to the critical temperature (300-350°C) for thermal activation of intracrystalline creep in quartz at a typical natural strain rate of 10^{-14} /s (Scholz, 1990). However, at higher strain rates, the quartz matrix may be elastic-brittle at higher temperatures.

(7) The total fracture length (y) within a garnet grain increases with increasing grain size (d) or the length of the longer axis ($2L$) and appears to follow a power law (Fig. 3.8): $y = Ad^i$ or $y = B(2L)^j$, where A, B, i and j are constants. The distribution of fracture spacing is generally single-peaked, although skewed to some extent (Fig. 3.7c). Variations in fracture spacing with respect to grain size, aspect-ratio and garnet spacing are complex. Generally speaking, the larger grains have a larger mean fracture spacing and the grains with larger aspect-ratios have a smaller mean fracture spacing. For an individual grain, the fracture spacing generally decreases with decreasing diameter from the center to the two ends (Figs. 3.4 and 3.9). In addition, fracturing becomes intensive in regions where garnet crystals are spaced very close together in a cluster (Figs. 3.4g, k-l). Though the garnet grains generally are not in contact with each other, mechanical interactions between them result in local stress concentrations in the garnet clusters.

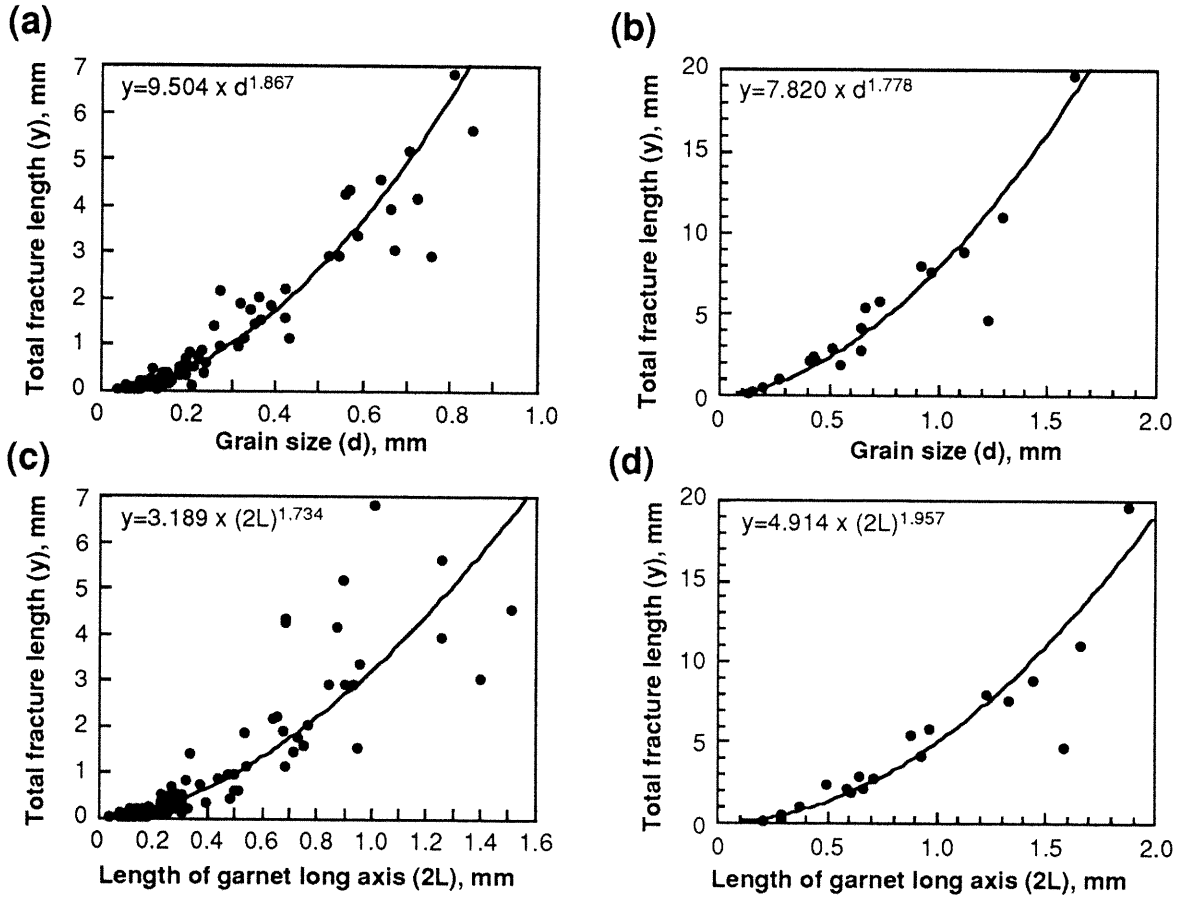

Figure 3.8. Variation in the total fracture length within a given garnet grain in two samples as a function of grain size (a and b) and long axis length (c and d).

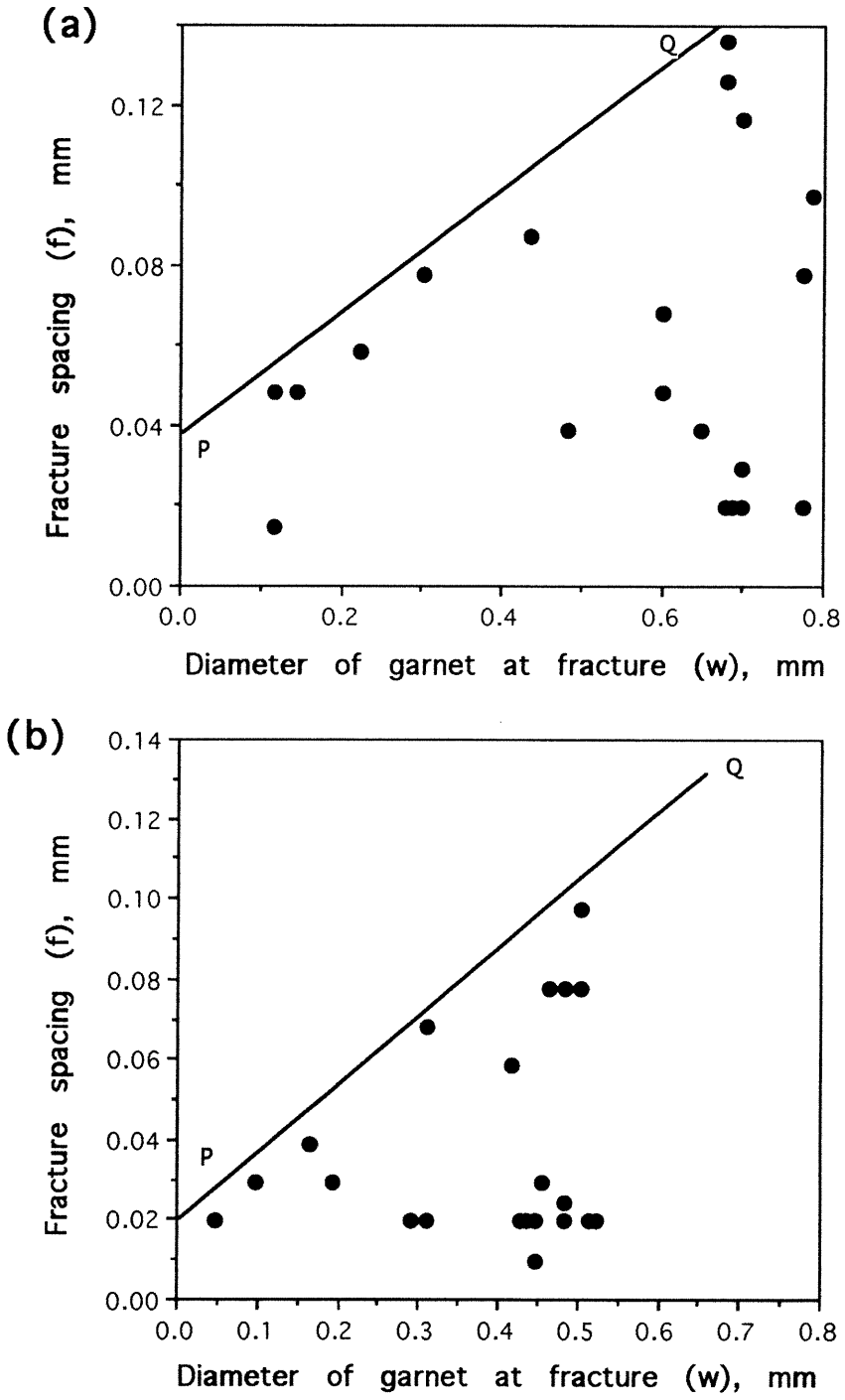

Figure 3.9. Variation in fracture spacing as a function of garnet diameter at positions of fractures for two garnet grains (a and b). No points plot above line PQ, indicating a non-random distribution of fracture spacing.

Drucker (1965) noted that in particle-reinforced metal-matrix composites, matrix deformation between closely spaced strong particles is highly constrained, resulting in local stress levels several times higher than the far-field matrix stress. This behavior has recently been confirmed by finite-element modeling (Watt et al. 1996).

(8) Grains with a larger grain size and/or a large aspect ratio are favorable for tensile fracturing (Figs. 3.4. and 3.10). Fractures in grains smaller than 0.2 mm with an aspect ratio of less than 2 are rare. A similar effect of particle size on particle cracking has been well documented for two-phase industrial composites such as the Al-SiC system. (Lloyd, 1991; Li and Ellyin, 1995) and for granitic mylonites (Ji and Zhao 1993; Michibayashi, 1996). These authors found that in populations with a large range in size, it is the largest particles which tend to fracture. Since the internal tensile stress in a stiff grain such as garnet is approximately independent of size, this effect can be attributed to a size dependency for fracture toughness. A large grain contains more and larger flaws than a small grain (Lloyd, 1991).

3.4. Lattice preferred orientation (LPO) of garnet

As shown above, fractures in garnet are preferentially aligned at high angles to the foliation and lineation. In order to know if the fractures are controlled by lattice preferred orientation (LPO), we measured the LPO of garnet from two samples, CTG5 and CTG6, using the electron back-scatter diffraction (EBSD) technique and a JEOL JSM 5600 SEM at the Université Montpellier II, France. The thin sections were polished on a polyurethane lap for 3-5 hours using a suspension of 0.05 μm silicon in water. No coating was used in the SEM which operated at 15-20 kV with a beam current around 0.5 nA.

EBSD patterns are generated by inelastic interaction of the incident electron beam with the sample, which scatters the electrons in a pear-shaped volume. Some of these electrons will have the correct angular relationship with the planes of the

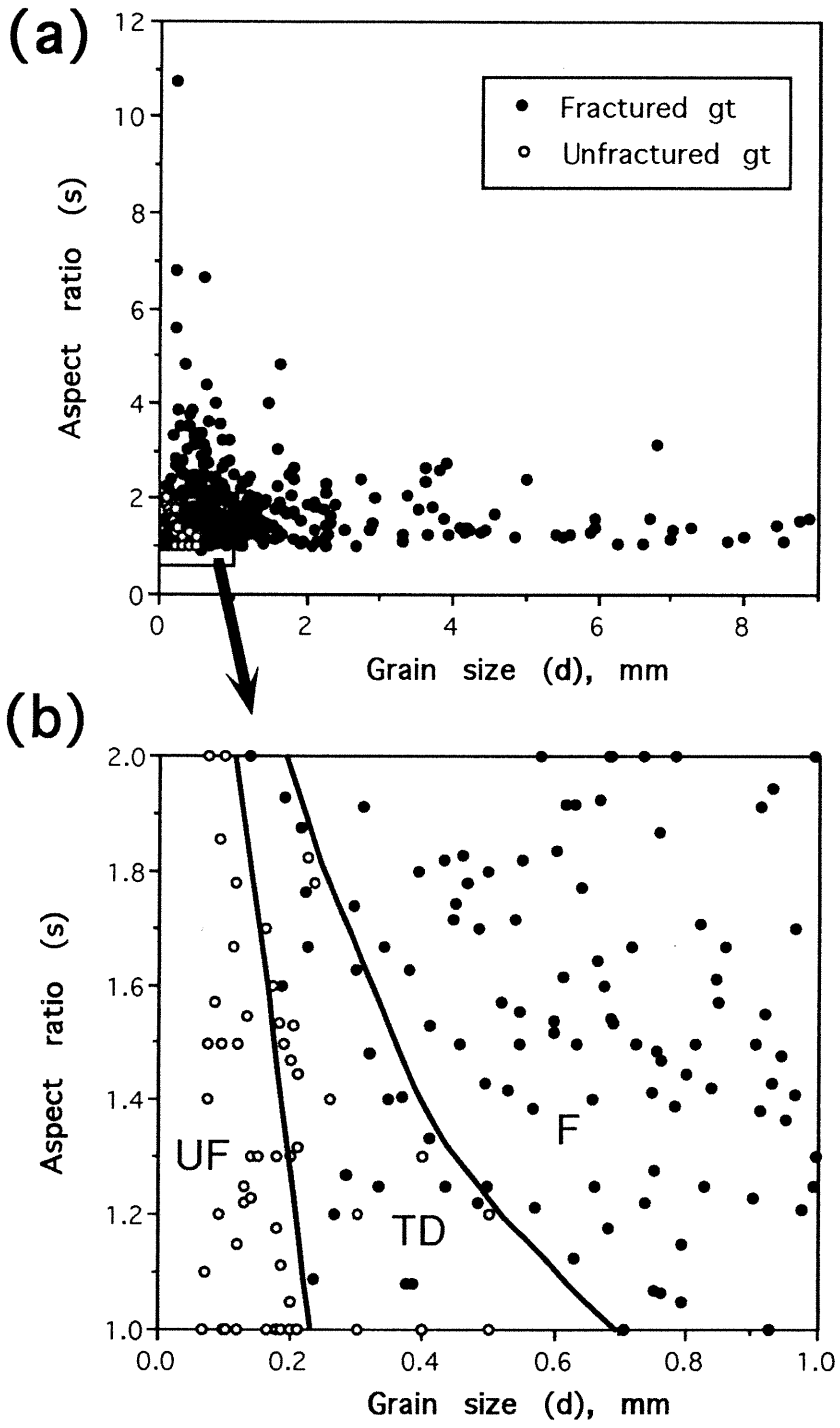

Figure 3.10. Data showing the influence of grain size and aspect ratio on tensile fractures in garnet (gt). Almost no fractures are found in the grains smaller than 0.2 mm with an aspect ratio of less than 2. F, UF and TD stand for fractured, unfractured and transition domains of garnet, respectively.

surrounding crystalline material (garnet in the present case) for coherent scattering (Bragg diffraction). Because the initial inelastic scattering generates electrons with a continuous range of directions, a number of planes will fulfill the Bragg condition; each plane generates a band of diffracted electron intensity. Together, these bands form a pattern which reflects the relationships of the planes in the crystal structure. These patterns can be used to determine the orientation of the crystal relative to the incident beam. To allow most of the electrons to leave the sample, the sample is inclined 70° from the usual horizontal position. The EBSD patterns were indexed using the Channel^{+} package from HKL software (Schmidt and Olesen, 1989). The error in the orientation determination is estimated to be less than 1° (Randle, 1992 and 1993).

As shown in Fig. 3.11, pole figures of the [100], [111] and [110] axes of 107 and 55 individual garnet grains from samples CTG5 and CTG6, respectively, show complicated and weak LPO patterns. To assess the randomness of the orientation data, a texture index (pfJ) was calculated using the 1/n law method, where n gives the number of individual orientations (D. Mainprice, personal communication). pfJ at 1/n=0 corresponds to an extrapolation to an infinite number of measurements. For a random distribution, pfJ=1. The pfJ values for these three crystallographic directions in samples CTG5 and CTG6 range from 1.04 to 1.20. This indicates that the LPOs are very weak. Therefore, it is concluded that the tensile fractures in the garnets are not controlled by the garnet crystallographic orientation.

As is common knowledge in materials science, the development of LPO in a mineral or metal depends not only on the prevailing deformation mechanism, but also on many other factors such as the crystalline nature and volume fraction of the materials in polyphase aggregates as well as the deformation conditions (e.g., temperature, pressure and strain-rate). For a given finite strain produced by dislocation slip, crystals with more active independent slip systems generally develop weaker LPOs than those with fewer active slip systems, even though the critical shear strengths of the different slip systems

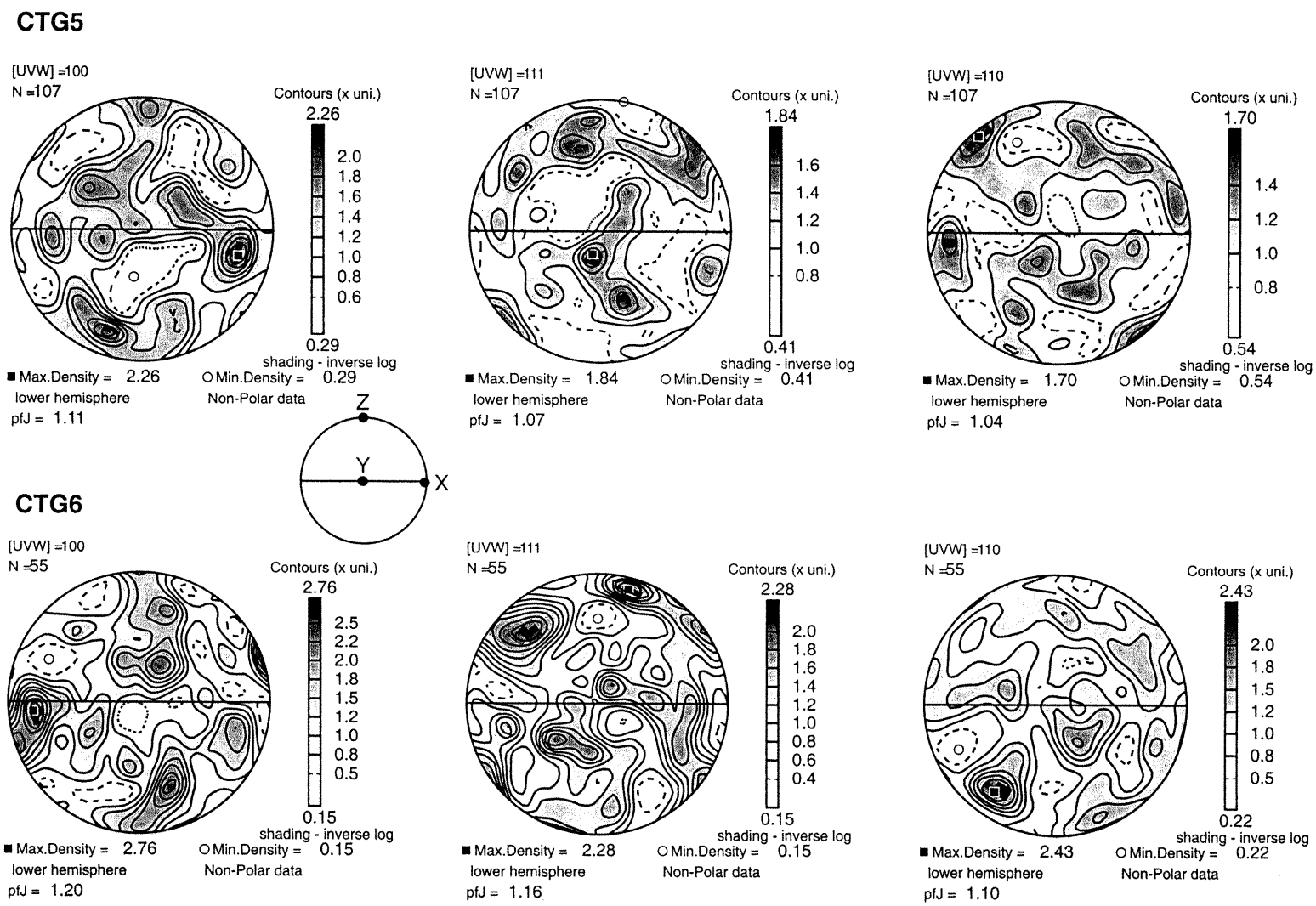

Figure 3.11. Stereograph (lower hemisphere, equal area) plots of garnet crystallographic orientations determined by EBSD. Note that the garnet [100], [111] and [110] axes show weak and complicated patterns.

are almost equal (e.g. Nicolas and Poirier, 1976). During slip, an unconstrained crystal with five or more independent slip systems changes its shape but its lattice is subject to little rotation with respect to the instantaneous stretching axes of bulk flow. Hence it is not surprising that the garnets in the mylonites show a weak LPO even though each garnet appears to have been deformed by plastic processes (e.g., dislocation creep). The likely reasons for this are: (i) Garnet displays cubic symmetry and has more than 5 independent slip systems. (ii) The garnets from the MSZ are volumetrically minor and isolated in a matrix of quartz and feldspar. (iii) As interpreted by Ji and Martignole (1994), the garnet crystals were flattened during an early high-temperature deformation (~900 °C) and were subsequently rotated as rigid inclusions in the flowing quartz matrix during a later low temperature (550-750 °C) non-coaxial deformation. Thus, the absence of strong garnet LPO in the MSZ mylonites does not provide unequivocal evidence that dislocation glide did not occur during the early stage of high temperature deformation.

3.5. Fluid inclusions in quartz

3.5.1. Characteristics of fluid inclusions

Microthermometric measurements of fluid inclusions in quartz were performed for four different samples (K3, 92-3-2, 31H/13, and CTG5-K) using a Fluid Inc. adapted U.S.G.S. gas-flow heating/freezing system at McGill university. All of the studied samples contain both CO_2 and H_2O-rich fluid inclusion trails.

The CO_2 fluid inclusions are spherical or ellipsoidal in shape, and the average inclusion size is 5-7 μm. The final melting temperatures (T_mCO_2) are settled around -56.7 °C, but the homogenization temperatures (T_hCO_2) are different from sample to sample. For samples CTG5-K and 92-3-2, T_hCO_2 ranges from -30 °C (homogenization to liquid) to +30 °C (homogenization to vapor), giving multi-peak histograms (Touret, 1981) (Fig. 3.12). However, most inclusions in any one trail homogenize at similar

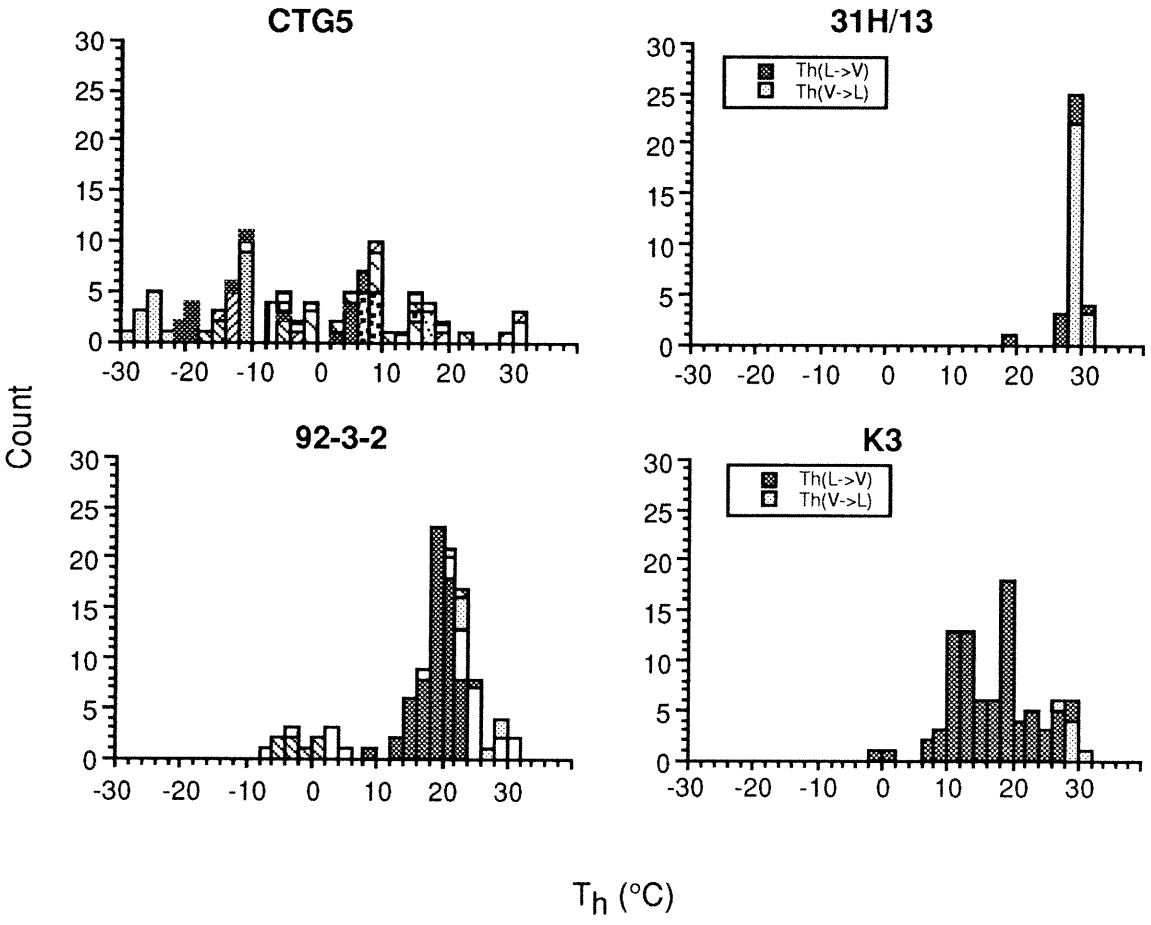

Figure 3.12. Homogenization temperature distribution for CO_2 fluid inclusions in the quartz matrix surrounding garnet crystals. L->V: homogenizing from liquid to vapor; V->L: homogenizing from vapor to liquid. CTG5 and 92-3-2 samples show multi-histogram distributions without any V->L inclusions, while 31H/13 and K3 samples show one-peak histogram distributions with both L->V and V->L inclusions.

temperatures ± few degrees, indicating fast healing of the fractures (Touret, 1981) and the insignificance of necking-down phenomena. For the other two samples (31H/13 and K3), $Th CO_2$ is concentrated within a range from +10 °C (homogenization to liquid) to +25 °C (homogenization to vapor), giving one-peak histograms (Touret, 1981) (Fig. 3.12).

H_2O-rich fluid inclusions, which are more irregular in shape and are larger than CO_2 inclusions (<10 μm), are composed of two different types. In general, one type has T_m values around 0 °C with higher T_h temperatures, while the other has lower T_m temperatures (-20 to -15 °C) and lower T_h temperatures (Fig. 3.13). These inclusions are too small to measure the eutectic temperatures in order to determine the precise fluid compositions. Both types are similar to the aqueous inclusions in granulites from North Norway studied by Olsen (1978).

3.5.2. Implications for temperature and pressure

In order to constrain the likely cooling history of the MSZ mylonites and the P-T conditions during the fracturing of the garnets, we calculated CO_2 isochores using the equation of state of Kerrick and Jacobs (1981) (Fig. 3.14). The CO_2 isochores represented by dashed lines and by black lines were, respectively, estimated from the mean T_h value for each inclusion trail which shows a T_h multi-peak histogram and which shows a T_h single-peak histogram. Boxes of A and B are peak and retrograde metamorphic P-T conditions estimated by Indares and Martignole (1990) for plagioclase, pyroxene and garnet assemblages from the region. The highest density CO_2 fluid inclusions may form around 550-600°C immediately after the P-T conditions indicated by Box B. Then, continuous entrapment of CO_2 inclusions would take place with the decreasing pressure and temperature until finally the H_2O-rich fluid inclusion trails formed around 350-300°C. This result appears to be supported by observations of fluid inclusion microstructures. According to Vityk and Bodnar (1995), all fluid inclusions,

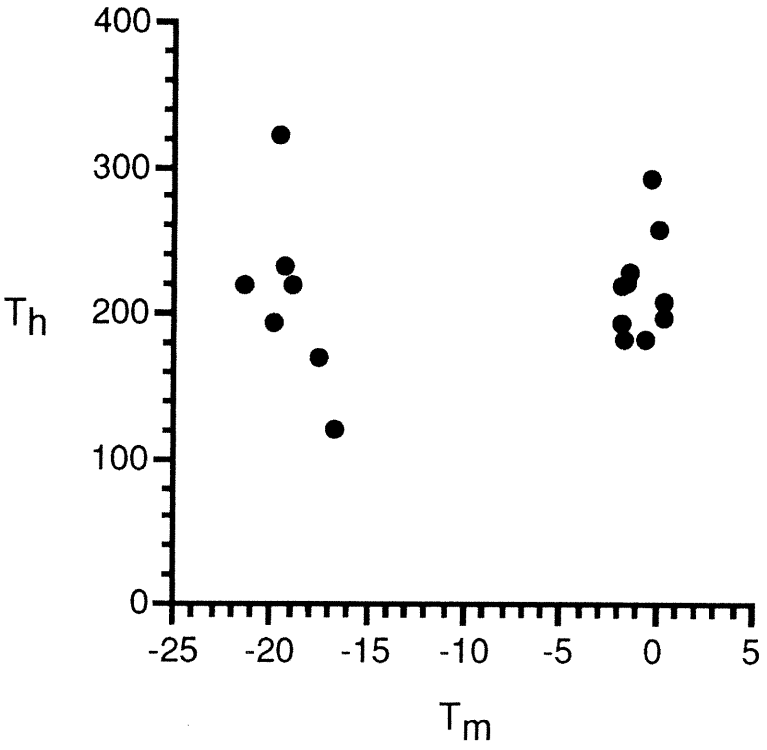

Figure 3.13. Plots of homogenezation temperature (T_h) as a function of melting temperature (T_m) for H_2O-rich fluid inclusions in the quartz matrix surrounding fractured garnet crystals.

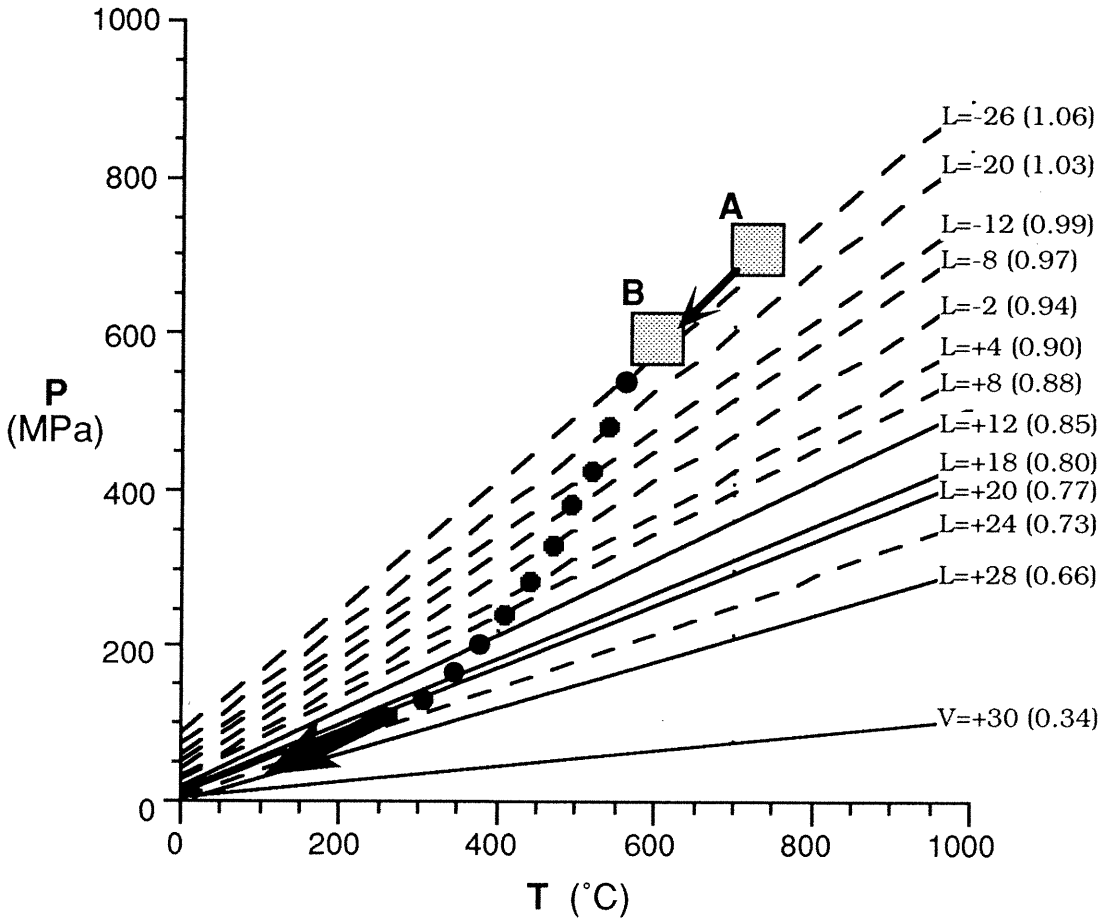

Figure 3.14. P-T path of the Morin shear zone based on fluid inclusion data. Boxes A and B are peak and retrograde P-T conditions, respectively, estimated by Indares and Martignole (1990). The dashed lines are isochores for samples which show multi-peak histograms, while the solid lines are isochores for samples which show one-peak-histograms. The homogenization temperature (°C) and the density (g/cm^3) of CO_2 liquid (L) or vapor phase (V) corresponding to each isochore are written at the right of each isochore.

regardless of their size, change their shapes and become highly irregular and dendritic during isobaric cooling. During isothermal decompression (uplift), however, many large inclusions become irregular shapes associated with small inclusion clusters, while medium and small-sized inclusions retain their regular morphology. The CO_2 fluid inclusions in the MSZ samples are very similar to the isothermal decompression microstructures described by Vityk and Bodnar (1995). The microthermometric results are also consistent with the data from the Adirondack mountains, in the south-eastern part of the Grenville Province (Lamb et al., 1987; Lamb et al., 1991). The fracturing in the garnets from the MSZ likely started at high temperature around 550-600 °C and continued during uplift-related cooling and decompression.

3.5.3. Possible origins of fluids

The presence of CO_2 fluid inclusions has been documented in many high-grade granulite facies metamorphic terranes (e.g., Roedder, 1984; Oliver, 1996). However, the origin of CO_2 fluids remains poorly understood. It is even debatable whether the granulite facies metamorphism occurs in the presence of fluids or in the absence of fluids. Many authors who have investigated CO_2 fluid inclusions in granulite-facies metamorphic rocks (e.g., Herms and Schenk, 1992; Boullier et al., 1991; Lamb et al., 1991; Rudnick et al., 1984) support metamorphism in the presence of fluids. Two origins have been proposed for the CO_2 fluids in granulite-facies rocks: (1) CO_2 is derived from an external source such as the mantle (Newton et al., 1980) or from surrounding rocks through decarbonization reactions (Glassley, 1983) or oxidation of graphite (Kreulen and Schuiling, 1982) during metamorphism. (2) CO_2 represents an internal residual fluid which is left behind after extraction of H_2O into the melt fraction during partial anatexis (Touret and Dietvort, 1983). The first model is applicable to the MSZ because metamorphosed marbles, which occur in the northern part of the MSZ, are likely external sources for the CO_2. The second model is also possible for the MSZ,

although the evidence would tend to be obliterated by ductile shearing.

It is impossible to reach any further conclusions about the origin of the CO_2 without further constraints such as carbon isotopic measurements. It is clear, however, that CO_2 fluids percolated though the rocks or existed in isolated pores along grain boundaries and triple junctions during and after the shear zone deformation as a free, pervasive and super-critical fluid phase. According to Watson and Brenan (1987), H_2O fluid has a low wetting angle (< 60°), achieving a complete interconnectivity of pores. On the other hand, CO_2 fluid has a high wetting angle (> 60°) precluding extensive interconnectivity of pores. Therefore, H_2O fluid is able to leave the system while CO_2 fluid remains in isolated pores and forms the fluid inclusions observed in quartz.

As was mentioned before, the aqueous-rich inclusions were formed at a later stage of uplift after the entrapment of CO_2 fluids. There are also two possibilities for the origin of the aqueous fluids: they could have either external or internal (metamorphic) sources. As for the CO_2 inclusions, however, we need to carry out more investigations to constrain the origin of the aqueous fluids.

3.5.4. Discussion about fluid inclusions

Secondary fluid inclusions are healed microcracks whose morphology changes from thin and sheet-like fractures to separated inclusion trails due to dissolution-precipitation mechanisms within the fluid (Tuttle, 1949). This interpretation of the origin of fluid inclusion planes has been confirmed by experiments on crack healing or on synthetic fluid isochore (Shelton and Orville, 1980; Smith and Evans, 1984; Brantley et al., 1990). Isochoric cooling experiments in which synthetic fluid inclusions are quenched along isochores show that changes in morphology of the inclusions do not effect the density of the inclusions when the host minerals are undeformed (Roedder and Skinner, 1968; Roedder and Kopp, 1975; Shelton and Orville, 1980; Pecher, 1981, Pecher and Boullier, 1984; Sterner and Bodnar, 1989; Vityk and Bodnar, 1995). In other

words, fluid inclusions undergo strong shape and density changes when they depart from their isochoric lines and re-equilibrates along P-T paths significantly different from their trapping isocores (Sabouraud, 1981; Pecher, 1981; Pecher and Boullier, 1984; Sterner and Bodnar, 1989; Vityk and Bodnar, 1995) and when the host minerals are deformed (Gratier and Jenatton, 1984; Boullier et al., 1989). According to experiments by Sterner and Bodnar (1989), the density modifications caused by P-T changes are divided into two opposite ways: fluid inclusions experiencing near-isothermal decompression may have considerably lower densities than those at entrapment, while fluid inclusions experiencing near-isobaric cooling may have much higher densities than those at entrapment. Furthermore, density changes occur with accompanying modifications in the shape of inclusions (Sterner and Bodnar, 1989). In isothermal experiments studied by Vityk and Bodnar (1995), many large inclusions change to irregular shapes associated with small inclusion clusters while most of medium to small-sized inclusions retain their regular morphology. On the other hand, in their isobaric experiments, all fluid inclusions regardless of their size become highly irregular and dendritic. Concerning the modification related with deformation, plastic deformation around fluid inclusions also causes them to change in shape to decrepitation and in density to values exceeding those at entrapment (Boullier et al., 1989). In addition, water diffusion around the inclusions facilitates leakage and makes the density changes possible (Bakker and Jansen, 1984; Boullier et al., 1989). The CO_2 fluid inclusions from the MSZ do not show any annular shapes due to isobaric P-T changes or the plastic deformation of quartz. Moreover, CO_2 is less soluble than H_2O in quartz (Walther and Orville, 1983), suggesting that CO_2 fluid inclusions are less likely to change in density because of diffusion process after the enclosure of inclusions than H_2O inclusions. Thus it is believed that the densities of the fluid inclusions from the MSZ have been modified very little during cooling and uplifting. Consequently, the P-T path appears to lie between the isochoric cooling path and the isothermal decompression path and probably lie closer to the isochoric cooling

path (Fig. 3.14).

3.6. Existing models related to garnet fractures

The microstructural observations presented earlier suggest that a model to explain the origin of the garnet fractures in the MSZ must account for: (i) restriction of the most of the fractures to the garnets (most fractures do not propagate into the adjacent quartz matrix), (ii) the pervasive, non-random spacing of the fractures, and (iii) the systematic orientation of the fractures with respect to the foliation and lineation of the rocks. The following discussion relates only to the origin of the garnet fractures in the MSZ, although there are obvious implications for tensile fractures of minerals in similar environments elsewhere.

3.6.1. Fractures induced by residual stresses

Rocks are polycrystalline aggregates in which different minerals generally have different thermal expansion coefficients and elastic stiffnesses. As a result of this thermoelastic heterogeneity, misfit (or residual) stresses are generated because each phase expands or contracts differently in response to changes in temperature and pressure, phase transformation, inelastic deformation and initial stress. For an isolated inclusion with an arbitrary shape embedded in an infinite elastic matrix, analysis of the stresses in the inclusion and the surrounding matrix can only be carried out numerically, but for the special case of an ellipsoid (Eshelby, 1957, 1959; Mura 1982) or a sphere (Holzhausen and Johnson, 1979; van der Molen, 1981; Gillet et al. 1984; Lee and Tromp, 1995; Zhang and Liou, 1998) an analytical solution can be found. The models predict that the stresses in a spherical inclusion are uniform and the stress field in the matrix is eccentrically symmetric if the stresses applied to the matrix at infinity are hydrostatic. Upon cooling, for example, an inclusion with a smaller thermal expansion than the matrix will generate circumferential tensile stresses and promote radial

cracking. In contrast, an inclusion with a greater thermal expansion than the matrix will generate radial tensile stresses and promote circumferential cracking. A volume increase due to a phase transformation of the inclusion during unloading and cooling (e.g. from coesite to α-quartz) will also generate circumferential tensile stresses resulting in radial cracking. This has been considered as the mechanical origin of radial tensile cracks around coesite or former coesite inclusions in garnet from ultra-high-pressure metamorphic terranes (e.g. Chopin, 1984; Zhang et al., 1995) and in metamict zircon (Lee and Tromp, 1995). Recently, Wendt et al. (1993) found that radial cracks around quartz inclusions in garnet from high-P metapelitic rocks (1.0-2.0 GPa, 450-600°C) in Oman formed during uplift entirely within the stability field of α-quartz. Their data demonstrate that quartz dilates more than its surrounding garnet during uplift. For the same reason, we would have observed either concentric fractures in garnet grains embedded in a matrix of quartz or radial cracks around quartz inclusions within garnet. Therefore, the existing spherical models cannot be used to interpret the origin of the fractures in the garnets from the MSZ because (i) they are neither radial nor concentric; (ii) they are not randomly spaced and thus cannot be explained by the assumption of uniform stress in the inclusion; and (iii) they occur in garnet grains both with and without inclusions.

Microcracking resulting from internal stresses between grains due to incompatible strains from either thermal expansion, decompression or elastic anisotropy has been well studied by materials scientists. Both experimental (Cleveland and Bradt, 1978; Rice and Pohanka, 1979) and theoretical (Evans, 1978; Tvergaard and Hutchinson, 1988) investigations demonstrate that such cracking occurs principally along grain boundaries and initiates primarily at triple points (locations where three grains come into contact) where the maximum tensile stress concentration is located. Fredrich and Wong's (1986) experiments on Westerly granite at room pressure and temperature between 250-620 °C show that after most of the grain boundaries have

already cracked, intragranular or transgranular cracking may occur in feldspar, but not in quartz. They attribute such a discrepancy to the fact that feldspar has well-developed cleavages while quartz does not. Obviously, the above model cannot explain our observations that cracks are intragranular and transgranular and restricted to stiff garnets lacking cleavage whereas the feldspars in the same rock are not cracked. In addition, no cracks are observed along grain boundaries in the studied rocks.

The release of residual stresses during natural or artificial excavation may generate the so-called rebound fractures such as sheet structure and exfoliation found in some rock masses (Nichols, 1980; Suppe, 1985). Rebound fractures are generally parallel to the topographic surface and independent of the foliation and lineation. In contrast to the sheet structure and exfoliation described by previous authors (Holzhausen and Johnson, 1979; Suppe, 1985; Prior and Behrmann, 1990), the fractures described in this paper are restricted to garnet crystals and preferentially perpendicular to the (subhorizontal) lineation (Figs. 3.4 and 3.7b). Thus, rebound fracture processes cannot be invoked to explain the garnet fractures.

3.6.2. Fluid-assisted dissolution-precipitation

Prior (1993) studied fractures in garnets from the Alpine Fault mylonites and suggested that the fractures were propagated by fluid-assisted dissolution-precipitation at high stress crack tips under greenschist-amphibolite facies conditions. However, the garnet fractures studied by Prior (1993) are irregularly distributed, highly variable in orientation, and filled either with new garnet grains or with retrogressive assemblages such as quartz-chlorite-plagioclase±biotite±muscovite. This microstructure differs substantially from that described here, so the fracture process proposed by Prior (1993) might take place only locally at the tips of cracks when propagating in the garnets within the MSZ.

3.6.3. Hydraulic fracture

Ladeira and Price (1981) proposed a hypothesis involving the pore fluid pressure to explain fractures in rocks. This hypothesis is described as follows: when a fracture forms, the pore fluid pressure in the neighborhood of the fracture decreases as the pore fluid flows into the open fracture. As the pore fluid pressure declines, the effective Mohr circle moves away from the failure criterion, so further fracture in the vicinity of the initial fracture is impossible. A second fracture can form in the rock only beyond the zone of reduced pore pressure, thereby defining the minimum spacing for the formation of hydrofractures. This hypothesis predicts that the fracture spacing depends on the permeability of the rock, so highly permeable rocks should have a larger fracture spacing than less permeable rocks. The permeability is almost zero in unfractured single crystals of garnet. The average fracture spacing in the garnet grains from the MSZ is only 0.14 mm (Fig. 3.7c) while the average fracture length is 3-5 times larger than this value (Fig. 3.7d). Moreover, the garnet fractures formed in the brittle upper crust when the permeability was large due to the high connectivity of fluid-migration pathways along foliation-parallel cracks. In such an environment, the fluid pressure should remain near-hydrostatic (Reynolds and Lister 1987). Furthermore, garnet fragments detached from fracture walls and floating in a retrogressive fracture filling, which would be considered diagnostic evidence of hydraulic fracturing in this setting (Prior, 1993), have not been observed in the rocks from the MSZ. Thus the closely-spaced fractures in the garnets from the MSZ cannot be readily interpreted in terms of hydraulic fracturing mechanism.

3.7. Proposed model for garnet fractures

3.7.1. Source of tensile stresses

It is necessary to analyze the source of the tensile stresses which caused the garnet fractures. As described before, the garnet fractures are preferentially oriented

normal to the subhorizontal stretching lineation irrespective of its trend. This suggests that the orientation of fracture arrays could be controlled by the anisotropic response of the mylonites to a far-field tensile stress in the horizontal plane. Because there is no geological evidence of any significant tectonic activity in the region after the granulite-facies metamorphism, the simplest and most widely acceptable geological event which might result in such a horizontal stress is unloading and cooling.

The horizontal stress (σ_H) at a given depth (H_f) within the brittle portion of the crust can be approximately estimated from the following equation (Haxby and Turcotte, 1976):

$$\sigma_H = \left(\frac{\upsilon}{1-\upsilon}\right)\rho_c g H_f + \left(\frac{E}{1-\upsilon}\right)\alpha\frac{dT}{dz}\Delta H + \frac{E}{(1-\upsilon)}\frac{\rho_c}{\rho_m}\frac{\Delta H}{(R-\Delta H)} \qquad (3.5)$$

where υ, ρ_c, E and α are the Poisson ratio, density, Young's modulus and coefficient of thermal expansion of crustal rock, respectively; g is the gravitational acceleration; dT / dz is the thermal gradient; R is the radius of the Earth, 6370 km; ρ_m is the density of mantle rock; and ΔH is the incremental change in depth due to uplift and erosion. Equation (3.5) is derived using a uniaxial strain model which assumes that the rock cannot freely extend or contract horizontally because to do so, it would have to separate from the adjacent rock (Haxby and Turcotte, 1976; Bruner, 1984). The first term of equation (3.5) describes the horizontal compressive stress induced by the vertical load ($\rho_c g H_f$) due to the Poisson effect. The second and third terms of equation (3.5) describe two horizontal tensile stresses which are related to the thermal contraction upon cooling and the change in radial distance from the Earth's center due to the vertical uplift, respectively. As the radial distance increases due to uplift, the arc length increases from deep to shallow depths.

Equation (3.5) predicts that as long as the absolute value of ΔH is large enough, the horizontal stress σ_H becomes tensile. Figure 3.15 shows variations of σ_H as

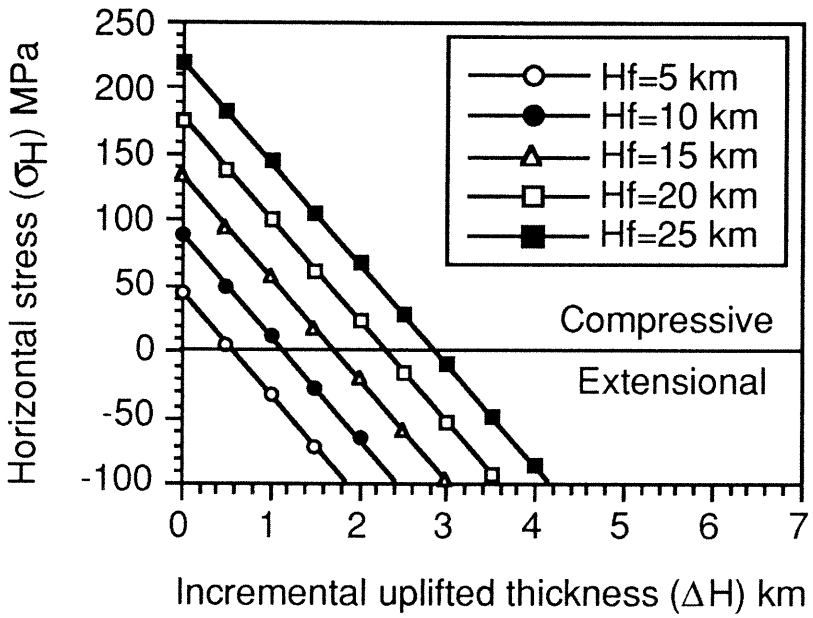

Figure 3.15. Variation in horizontal stress as a function of incremental uplifted thickness (ΔH) and the depth at which fractures are initiated (H_f). The horizontal stress can be switched from compressive to extensional as long as ΔH is large enough.

functions of ΔH and H_f, calculated using E=97000 MPa, υ=0.25, α=3x10^{-5} °C^{-1} (Turcotte and Schubert, 1982, P. 179) and dT/dz=20 °C/km. The critical value of ΔH for the switch from compressive to tensile stresses increases with increasing H_f. The tensile strength of minerals generally decreases with decreasing confining pressure as the overburden is removed (Price and Cosgrove, 1990). Thus, tensile fracturing can take place even at great depths. If the horizontal tensile stress (negative) is smaller than or equal to the tensile strength of the rock (e.g. 40 MPa, Price and Cosgrove, 1989), vertical fractures or joints will form normal to this stress. At a depth of 25 km, for example, an incremental uplift of 3.0 km can cause tensile fractures to form (Fig. 3.15).

3.7.2. Cause for the preferred orientation of garnet fractures

The fracture orientation appears to have been controlled by the elastic anisotropy of the mylonitic rocks. Ji et al. (1997) measured P-wave velocities of representative paragneissic mylonites and typical garnet-bearing quartzitic mylonites in the directions parallel to lineation and normal to foliation at room temperature and hydrostatic confining pressures ranging up to 600 MPa (equivalent to crustal depths of approximately 20 km). The mini-cores cut from the rock samples for velocity measurements were 2.5 cm in diameter and 5.0 cm in length. The velocity measurements were made on dry, jacketed samples using the pulse transmission technique (Birch, 1960). P-waves were generated and received by 1 MHz lead zirconate piezoelectric transducers. Errors in ultrasonic velocity measurements are generally regarded to be less than 1% (Christensen and Shaw, 1970). As shown in Fig. 3.16, there is a rapid increase in velocity up to about 100 MPa, which is related to the closing of cracks (Birch, 1960). From 100 MPa to 600 MPa, velocity increases almost linearly with increasing pressure, reflecting the intrinsic properties of the minerals in the rock. The P-wave velocities are significantly higher along the lineation (X) than normal to the foliation (Z). This indicates that the mylonites and gneisses are more compressible in the Z than in the X

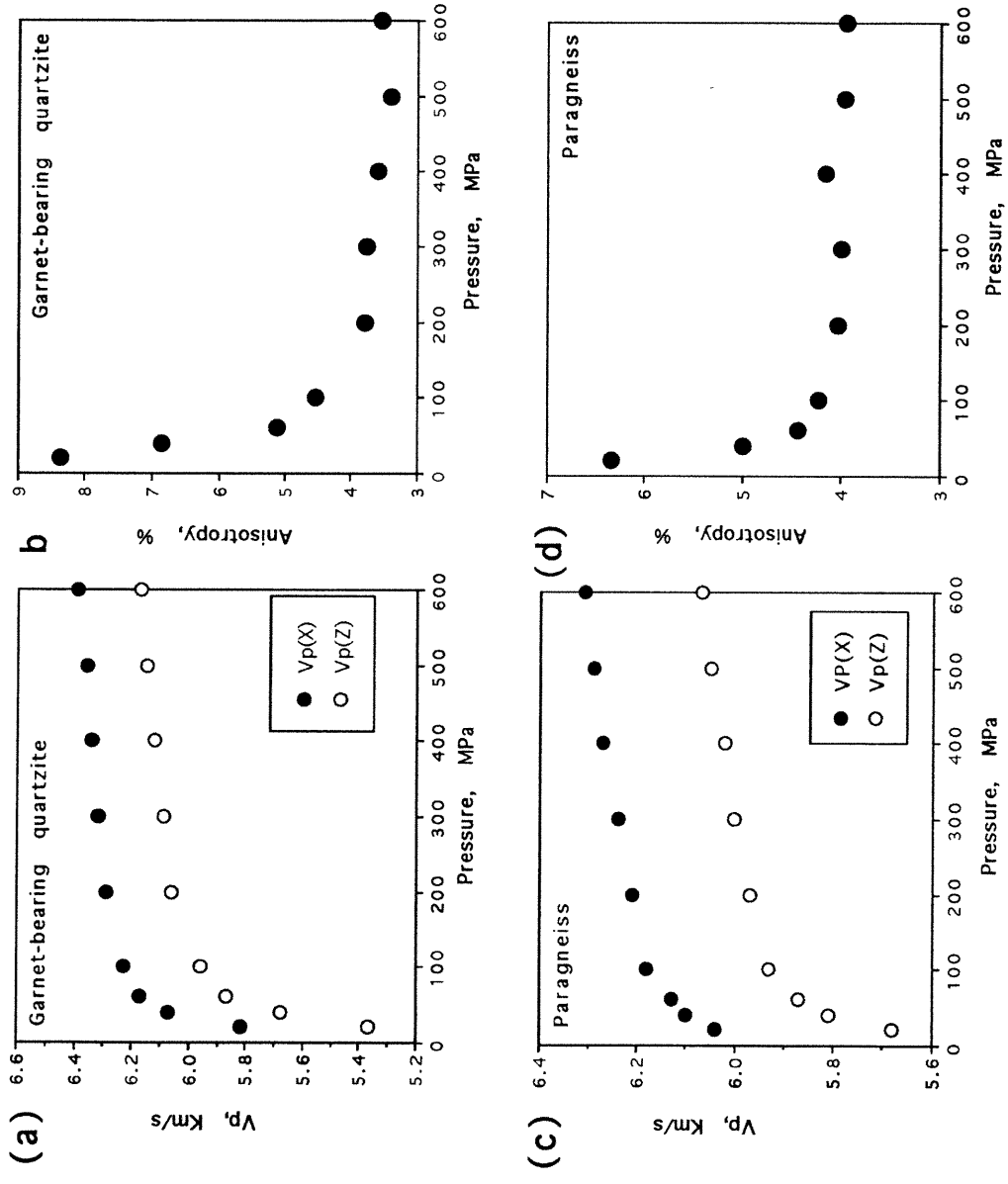

Figure 3.16. P-wave velocities as a function of confining pressure for the directions parallel to the extension lineation and perpendicular to foliation in a garnet-bearing quartzite (a) and a paragneiss (c). P-wave velocity anisotropy increases with decreasing confining pressure (b and d).

direction, i.e., E (Young's modulus) is larger in the X than in the Z direction. The seismic anisotropy (A) is defined as: $A=100\%(V_{max}-V_{min})/V_{mean}$ (Birch, 1960). As shown in Figs. 3.16b and d, the seismic anisotropy increases with decreasing confining pressure below 200 MPa (<~8 km) and is almost constant (A = 3-4%) at confining pressures higher than 200 MPa. At confining pressures below 200 MPa, the seismic anisotropy mainly reflects the behavior of foliation-parallel fractures in the rocks, but at higher confining pressures the cracks are closed and the seismic anisotropy mainly reflects the crystallographic preferred orientation of minerals in the rocks (Ji et al., 1993).

According to equation (3.5), the far-field tensile stress σ_H increases with increasing E. In the case of a strike-slip ductile shear zone (e.g. the MSZ) where lineation is subhorizontal, E and thus σ_H are larger along the lineation direction than normal to the foliation. The mylonites could readily accommodate the elastic stretching normal to the foliation, whereas within the plane of foliation, the mylonites would be less able to accommodate the imposed elastic extension. Consequently, the tensile stress in the direction parallel to foliation and lineation could be high enough to break brittle minerals such as garnet. Because the difference in E value between the X and Z directions decreases with increasing confining pressure, the dominance of fractures normal to the foliation should imply that the fractures formed at shallow depths. This conclusion agrees with that derived from our microstructural observations.

3.7.3. Shear-lag model

Since the tensile strength of garnet could be higher than that of quartz and feldspar, the fracturing should take place preferentially in quartz and feldspar. In the following, the reason why tensile fracturing took place preferentially in garnet will be analyzed using the shear-lag model.

The shear-lag or stress transfer model was originally developed by Cox (1952) and later refined by Holister and Thomas (1966) and Kelly and Macmillan (1986) to

predict the distribution of tensile stress along a cylindrical fiber and the shear stress at the interface between the fiber and matrix in a two-phase composite. This theory assumes that if no slip occurs on the phase interfaces, the presence of the fiber redistributes the stresses and strains within the composite material and the load is transferred from the matrix to the fiber. This process has two corollaries (Zhao and Ji, 1997): (i) A shear stress occurs at the fiber-matrix interface, and (ii) the harder phase carries a comparatively greater part of the stress, while the soft phase tends to take the greater part of the strain (with respect to the volume fraction ratio). This model has been widely used by materials scientists and structural geologists to analyze extension fracture boudins (Lloyd et al., 1982; Masuda and Kuriyama, 1988; Ji and Zhao, 1993), and to the predict flow strengths of two-phase rocks (Ji and Zhao, 1994) and industrial composites (e.g. Kelly and Street, 1972; McLean, 1972; Nardone and Prewo, 1986).

The classic shear-lag model considers a basic unit cell consisting of a long, cylindrical fiber embedded completely in a continuous incompetent matrix, which is subjected to a remotely applied tensile loading. According to Kelly and Macmillan (1986), the axial tensile stress [$\sigma(x)$] in the fiber is given by

$$\sigma(x) = E_f \varepsilon \left[1 - \frac{\cosh[\beta(l/2 - x)]}{\cosh(\beta l/2)} \right] \qquad (3.6)$$

where E_f and l are the Young's modulus and the length of the fiber, respectively; ε is the tensile strain of the unit cell along the fiber alignment direction (x); x is the distance along the fiber; and

$$\beta = \frac{2s}{l} \sqrt{\frac{-2E_m}{E_f(1+\upsilon)\ln(V_f)}} \qquad (3.7)$$

where s is the aspect-ratio of the fiber, E_m and υ are the Young's modulus and Poisson's

ratio of the matrix, and V_f is the volume fraction of fiber in the composite.

Equation (3.6) cannot be used for estimating the tensile stress in a short fiber (s<10) since the derivation of this equation is based on the assumption that no load transfer occurs from the matrix to the end faces of the fiber. For a short fiber, the load transfer at the ends cannot be ignored and should be equal to $\pi r^2 E_m \varepsilon$. The distribution of tensile stress in the short fiber as a function of distance (x) is then given by Ji and Zhao (1994) as

$$\sigma(x) = E_m \varepsilon \left\{ \frac{E_f}{E_m} + \left(1 - \frac{E_f}{E_m} \right) \frac{\cosh[\beta(l/2 - x)]}{\cosh(\beta l/2)} \right\} \qquad (3.8)$$

In Equations (3.6) and (3.8), $\varepsilon = \varepsilon_a + \varepsilon_t$, where ε_a is the strain due to the applied external tensile stress, and ε_t is the mismatch strain due to the differences in coefficients of thermal expansion between the fiber and matrix. Neglecting the radial strains, which are small compared to the axial strains for a slender body (Dunand and Mortensen, 1991), we have

$$\varepsilon_t = (\alpha_m - \alpha_f)\Delta T \qquad (3.9)$$

where α_m and α_f are, respectively, the matrix and the fiber coefficients of thermal expansion, and ΔT is the temperature change. In the present study, ε_t can be neglected since there is only a minor difference in the coefficients of thermal expansion between α-quartz (24.3×10^{-6}/°C) and garnet (20.6×10^{-6}/°C) in the range of temperature from 25 to 500°C (Fei, 1995). Hence, the tensile stresses resulting in the fracturing of garnet were derived from far-field tensile stresses rather than from the thermal mismatch stresses between garnet and the surrounding matrix (mainly quartz) upon cooling.

Equation (3.8) predicts that the tensile stress $\sigma(x)$ increases from $E_m \varepsilon$ (the

tensile stress of the matrix) at the ends of the fiber to a maximum at the center, so that fracture will occur at the mid-point of the fiber. However, most stiff minerals in deformed mylonites have a lenticular or ellipsoidal shape rather than a perfect cylindrical shape; their cross-sectional area is variable along their length (Ji and Zhao 1993). Thus, the tensile stress distribution and resulting fracture location in flattened garnets cannot be correctly predicted by Equation (3.8).

In order to do so, Ji et al. (1997) developed a new mechanical model (see Appendix for details) for an inclusion-matrix system based on the fundamental assumptions of the shear-lag model (Cox, 1952; Holister and Thomas, 1966; Kelly and Macmillan, 1986). They did not intend to obtain an exact numerical solution for the distributions of stress and strain in an actual garnet crystal and its surrounding anisotropic matrix. To do so, one should perform tedious numerical calculations. For simplicity, they approximated the system as a rotational body (e.g., a lens, ellipsoid or truncated ellipsoid) embedded in an elastically isotropic matrix. Either of these treatments results in underestimating the magnitude of the tensile stress to some extent within the garnet crystals in the XZ plane and particularly in the X direction, though the simplification does not change the fundamental conclusions.

The axial tensile stress in the inclusion as a function of distance along the long axis (the X direction in Fig. 3.17) can be obtained by numerically solving a differential equation (A14 in Appendix) if the material constants E_f, E_m and υ are known. In the present case, E_f=3.09x10^5 MPa for garnet. If the matrix is quartz, E_m=9.70x10^4 MPa and υ=0.08. If the matrix is plagioclase, E_m=1.16x10^5 MPa and υ=0.30. The calculated results for a lenticular garnet using these elastic constants and setting $\varepsilon = 0.5\%$, s=4 and $V_f = 7\%$, are shown in Fig. 3.18. The values of the elastic constants given above were obtained from laboratory measurements of acoustic velocities at room temperature (Bass, 1995). Under natural conditions, the elastic contrast (E_f/E_m) between garnet and quartz or feldspar may be larger than that in the laboratory. For

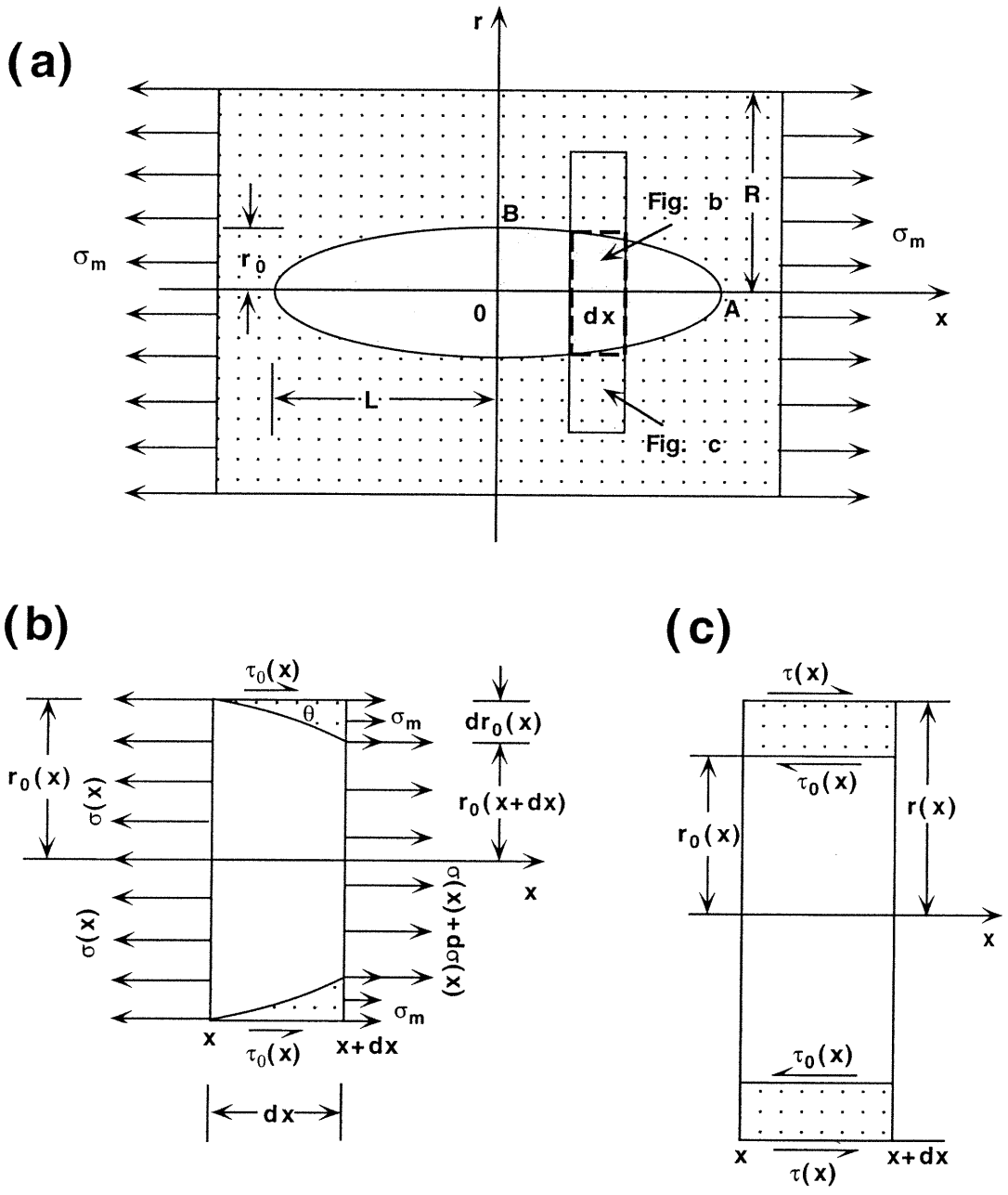

Figure 3.17. Schematic illustration of the mechanical equilibrium analysis in the shear-lag model. (a) Unit cell containing a stiff rotational body (e.g., ellipsoidal inclusion) embedded completely in an incompetent matrix. (b) Infinitesimal element of the inclusion. (c) Internal stress distribution in the matrix surrounding the infinitesimal element of the inclusion.

comparison, we also calculate the tensile stress distribution in a lenticular particle using E_f/E_m=10, $\upsilon = 0.08$ for quartz and $\upsilon = 0.30$ for feldspar, and the results are shown in Fig. 3.18. The following points can be highlighted:

(1) The tensile stress in a garnet grain is always larger than the far-field tensile stress applied on the composite rock (Fig. 3.18) because the E value of garnet is larger than that of the felsic matrix. This is the reason why tensile fracturing takes place preferentially in garnet rather than in the surrounding felsic matrix. Since the maximum ratio σ_f/σ_m increases with E_f/E_m, it is not surprising that the maximum tensile stress in a garnet embedded in a quartz matrix is larger than that in a plagioclase matrix. Moreover, the maximum ratio σ_f/σ_m also increases with the garnet aspect ratio. Thus, grains which are aligned parallel to the direction of the applied tensile stress and which have high aspect ratios break first. When a garnet crystal is broken during extension, the stress around it is relaxed, and the force carried by this crystal is transferred to the surrounding matrix and thus propagates the fracture from the garnet into the neighboring quartz. According to Smith and Evans (1984), microcracks in quartz have a geologically short lifetime at temperature higher than 200 °C because of rapid diffusional crack healing, which results in the formation of secondary fluid inclusion trails. In contrast, the fractures in garnet were healed so slowly that almost all of them remain open with no fluid inclusion trails along these fractures.

(2) In an intact, lens-shaped stiff particle, the tensile stress is a maximum at the center and decays to σ_m at the apexes (Fig. 3.18). Accordingly, the first fracture will occur at the mid-point of the particle. Then, the entire lens is divided into two half-lenses. The tensile stress distribution in the half-lenses is asymmetrical with respect to their mid-points (Fig. 3.18), and the location of the maximum tensile stress is closer to the end with smaller cross-sectional area. If fracturing occurs at the position of maximum tensile stress in a fractured segment of garnet, this segment will fragment into two sub-segments of unequal length, the longer of which has the larger diameter. It

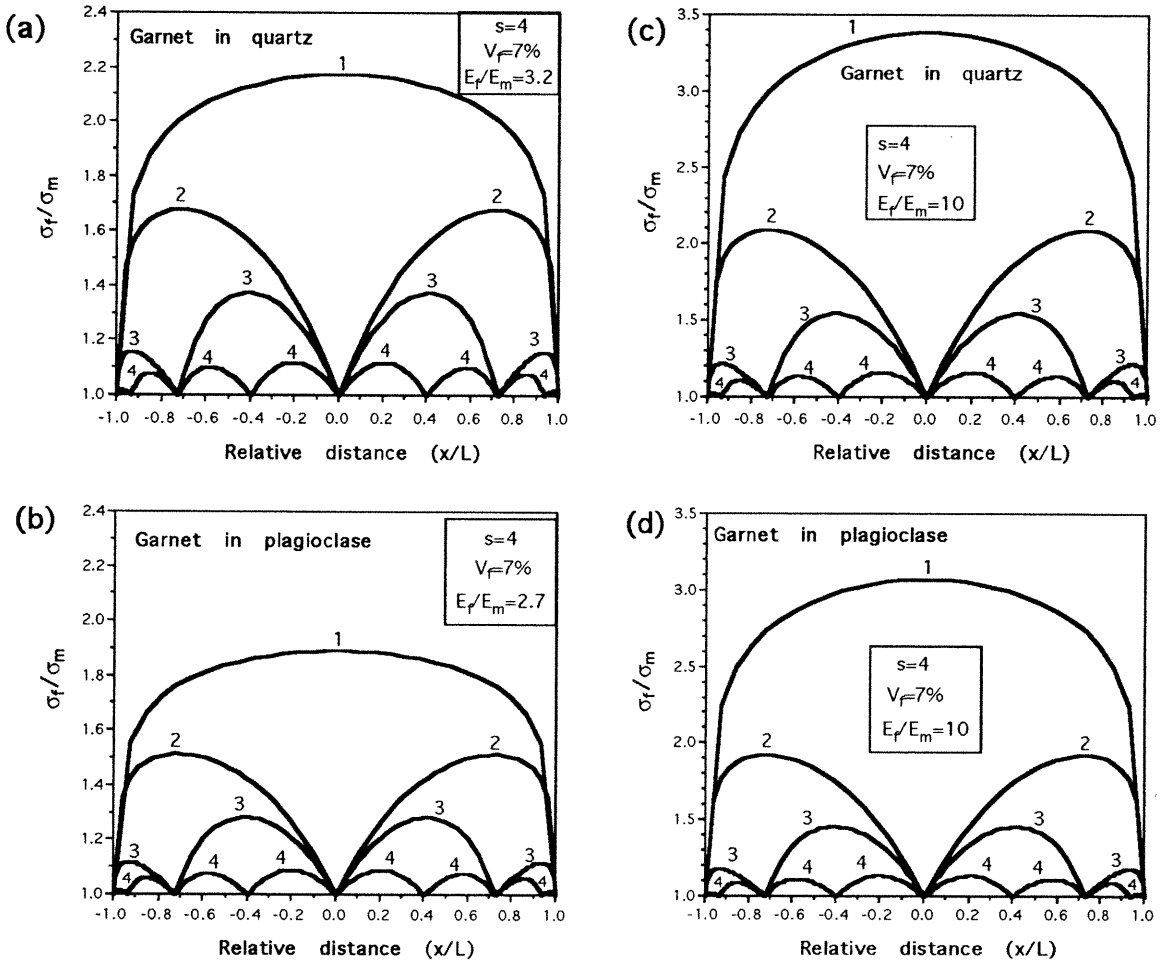

Figure 3.18. Predicted tensile stress along each fragment produced by sequential fracturing of a lenticular garnet grain with an aspect ratio of 4. (a) and (c) Garnet in a quartz matrix with Poisson ratio of 0.08. E_f/E_m equals of 3.2 and 10, respectively. (b) and (d) Garnet in a plagioclase matrix with Poisson ratio of 0.3. E_f/E_m equals of 2.7 and 10, respectively. Elastic constants for quartz, plagioclase and garnet were taken from Bass (1995). The numbers infer fracture generations.

should be pointed out that inhomogeneous distribution of microflaws may perturb the fracturing location predicted by the shear-lag model (Ferguson, 1987, Ji and Zhao, 1993).

(3) The fracturing process is sequential. After a break occurs, the segments are newly loaded in the course of extension and break again. Since each segment has one position of maximum tensile stress along the loading direction (Fig. 3.18), the fractured garnet segment should never break along more than one plane at the same time provided the segment is mechanically homogeneous (Prior, 1993). As described before, a number of parallel tensile fractures occur in each garnet grain. These fractures should belong to different generations which were formed by progressive uplift events. Alternatively, each generation of fractures may correspond to a given thickness (e.g., 1 km) of unroofing. If the matrix were ductile, it could have flowed into the gaps between the segments (boudins). The temporal sequence of fracturing in a brittle inclusion in response to flow in the plastic matrix could be established according to the different length of the gaps between the boudins; longer gaps would be associated with earlier fractures and shorter gaps with later fractures (Lloyd et al., 1982; Masuda and Kuriyama 1988; Ji and Zhao, 1993). In the present case, however, where both the matrix and the particle are elastic, fracturing of the brittle particle in response to elastic deformation in the surrounding matrix cannot be dilational although it is sequential. Hence, the time relationships of the fractures cannot be determined in any given garnet grain due to the lack of significant separation between the fractured segments.

(4) The magnitude of the tensile stress in a fractured segment of a given size decreases with decreasing length/diameter (aspect) ratio (Fig. 3.18). The sequential fracturing process will decrease the aspect ratio and in consequence, will reduce the tensile stress in the elastic-brittle segment. As shown in Fig. 3.7d, the aspect-ratios of most fractured garnet segments are much smaller than 1, with an average value of only about 0.26. This means that, in the fracture direction (i.e. the direction normal to

foliation), their aspect-ratios have a mean value of 3.8. The tensile stress within the garnet increases in the direction normal to foliation so that new fracturing in garnet segments may take place possibly along a plane parallel to the foliation. Thus, two orthogonal fracture sets may occur in the same grain due to the above switch of the aspect-ratio for fractured garnet segments (Fig. 3.19). In a plastic matrix, however, such a switch is almost impossible. Because the flow stress of the plastic matrix is much lower than the failure strength of the competent particle and because there may be slipping to some extent on the particle/matrix interface, the critical aspect ratio for fractured segments, below which the segments cannot undergo any further fracturing, is generally larger than 0.5-1.0. The interpretation of the ladder-like fracture sets may be applicable to the orthogonal joint sets described by Nickelsen and Hough (1967), Rawnsley et al. (1992), Gross (1993) and Caputo (1995). When the tensile strength of the rock is locally reached, fracturing (jointing) occurs perpendicular to the least principal stress (σ_3). Then, the stress along that direction locally and positively drops due to the stress release. For this reason, the stress field, though retaining the same principal directions, is locally distorted by a swap between the σ_3 and the σ_2 components in a volume of rock surrounding the fracture. As a consequence of the continued application of the far field stresses ($\sigma_1 / \sigma_2 / \sigma_3$), when elastic failure conditions are newly reached again, a second fracture forms and propagates perpendicular to the previous fracture set. Repeated fracture events, stress drops and stress swaps eventually generate orthogonal sets of extension fractures.

According to Smith and Evans (1984), microcracks in quartz will have geologically short lifetimes at temperature higher than 200 °C because of rapid diffusional crack healing, which results in the formation of secondary fluid inclusion trails. On the other hand, fractures in garnet are healed much more slowly so that many of them remain as fractures with a few fluid inclusion trails and half-healed fractures.

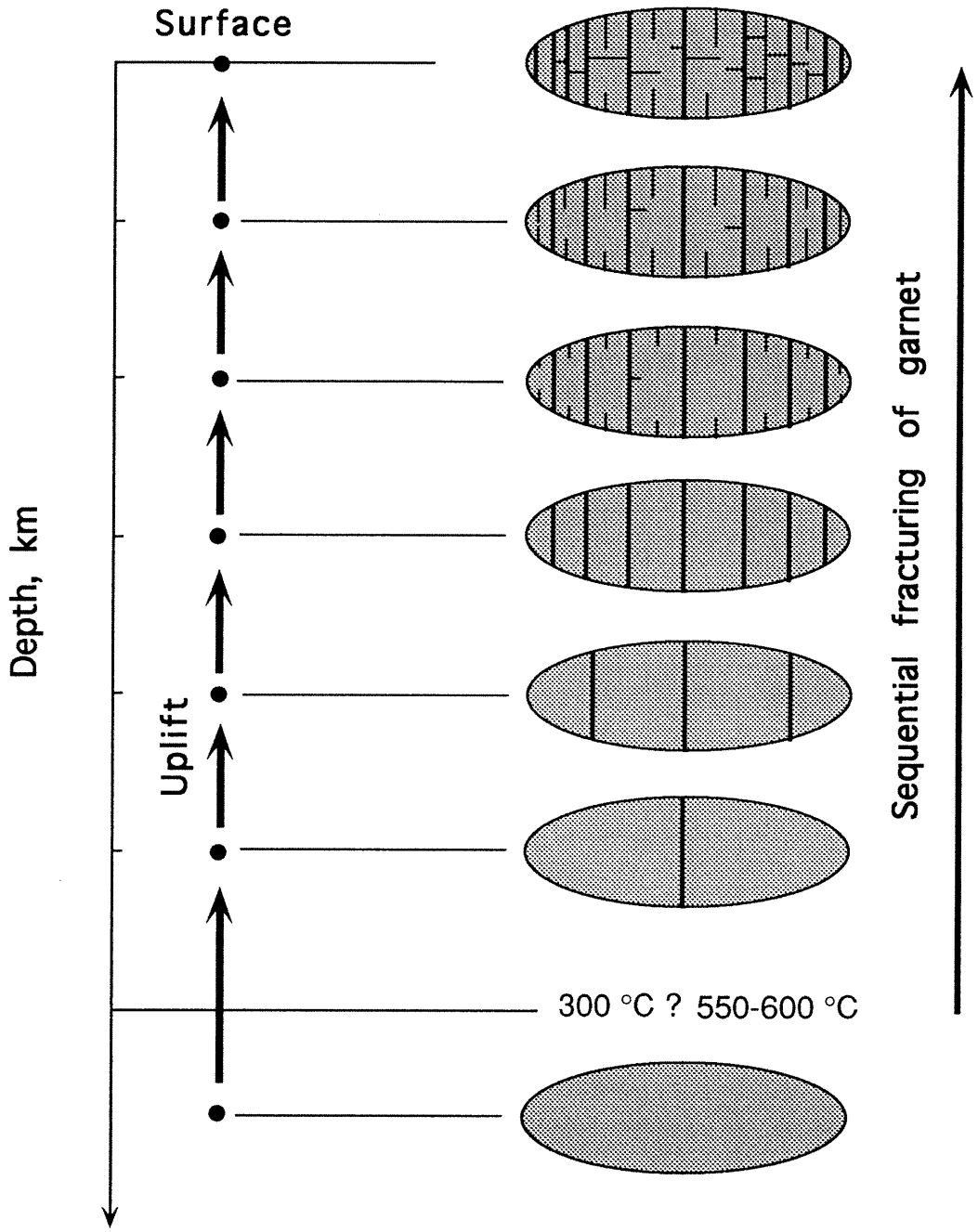

Figure 3.19. Schematic illustration showing growth of two orthogonal sets of tensile fractures in a garnet. The earlier pervasive fractures are perpendicular to the lineation and the later less-pronounced fractures are parallel to the foliation (XY-plane). Formation of these two sets of tensile fractures is attributed to a decrease in the aspect ratio of garnet fragments due to the sequential fracturing process.

3.7.4. Discussion about the shear-lag model

It is necessary to discuss if the fiber/matrix interface strength should be stronger than the fiber strength in order for the fiber to be fractured. For a brittle cylindrical fiber in a weak matrix, the largest tensile stress (σ_{max}) in the fiber occurs at the center while the largest interfacial shear stress (τ_{max}) appears at the ends of the fiber (see Eq. 3.8). If τ_{max} is equal to the shear strength of the interface (τ_0), slip will occur over a certain length at both ends of the fiber. Once the slip takes place, the shear stress along the slipping part of the interface is constant and equal to τ_0. For the central part of the fiber, however, there is no interfacial slip since the interfacial shear stress is still lower than τ_0, and controlled by the shear-lag effect. Thus, the end and the center of the fiber should be treated separately (Piggott, 1980). The mechanical analysis of interfacial slip is very complex (see Ji et al., 1998 for detailed derivations). Moreover, the ratio of σ_{max} to τ_{max} can be calculated using Kelly and Macmillan's (1986) equation (6.50). The value of σ_{max} is always larger and commonly much larger than that of τ_{max}. Thus, it is much easier for σ_{max} to reach the tensile strength of the fiber (C_0) than for τ_{max} to reach τ_0. This explains why the garnet crystals in the studied rocks are pervasively fractured while no interfacial fracture occurs between the garnets and the matrix (Ji et al., 1997). As noted by Jiang (1997), crystals are not be always much stronger than their interfaces with the matrix. The failure strength of polycrystalline aggregates increases considerably with decreasing grain size or increasing density of grain interfaces. This so-called "Hall-Petch relation" implies that the interfaces are stronger than the crystals in a fine-grained aggregate. If crystals were always much stronger than interfaces, one would hardly observe intragranular and transgranular fractures and grain size reduction in metals, ceramics and rocks (Lloyd and Knipe, 1992).

Like most analyses in composite mechanics (Cox, 1952; Kelly and Macmillan, 1986) and structural geology (Hobbs, 1967; Lloyd et al., 1982; Ji and Zhao, 1993), the shear-lag model presented here assumes no slip on phase interfaces. Many observations

support this assumption and it is most likely correct for the rocks studied here. First, microstructural evidence shows no relative motion between garnet and its matrix in the studied rocks. Second, grain-boundary slip is unlikely in solids which have low porosities and deform elastically. Third, although laboratory experiments (e.g. Schmid et al., 1977) have demonstrated that interfacial slip may operate in ultrafine-grained polycrystalline aggregates being deformed at high temperature and low strain rates, unambiguous evidence for the prevalence of this mechanism in natural mylonites is still rare (Fliervoet and White, 1995).

In the following, the reason why the fractures are closely-spaced in the garnet crystals from the MSZ will be discussed. First, according to the shear-lag theory (Lloyd et al., 1982), the fracture spacing (f) is directly proportional to the ratio of the tensile strength of the fiber (C_0) to the shear strength of the interface between the fiber and matrix (τ_0). In a homogeneous, cylindrical fiber, for instance, the fracture spacing (f) ranges between $(C_0 d)/(4\tau_0)$ and $(C_0 d)/(2\tau_0)$, where d is the diameter of the fiber's circular cross-section. The aspect-ratio of the fractured segment (f/d) can be smaller than 0.25 if $C_0 < \tau_0$. Second, the fracture density in a real fiber is significantly larger than that predicted by the shear-lag model from the tensile stress distribution because of the complexities inherent in fracture propagation (e.g., bifurcation, branching and deflection). For example, two cracks can originate simultaneously on opposite sides of a garnet crystal and propagate inward, forming two overlapping cracks rather than a single transgranular crack. These two overlapping cracks would then grow and form two parallel cracks (Ji et al., 1997). Third, if a garnet has a variable cross-sectional area, more closely-spaced fractures form at locations with smaller cross-sectional areas (Ji and Zhao, 1993; Ji et al., 1997). Fourth, in the garnet clusters, which are found in pelitic and mafic gneisses (Figs. 3.4g, k-l), the garnet crystals may be in contact with each other or very close together. Mechanical interactions between these garnets result in local stress concentrations and thus intensive fracturing. Finally, inhomogeneous distribution of pre-

existing microflaws in the garnets results in inhomogeneous distribution of fractures in them. Higher fracture densities are found near interfaces between the garnets and the matrix and near quartz inclusions in the garnets (Figs. 3.4a-l).

It is interesting to compare the shear-lag model with the Eshelby model (Eshelby, 1957, 1959; see Mura, 1987 for a review). Both models predict an increase in internal stresses in a stiff inclusion as a result of strain misfit between the inclusion and the surrounding matrix. Unlike the shear-lag model, however, the Eshelby model predicts that the stresses inside an ellipsoidal inclusion are homogeneous. This conclusion is based on an assumption that the stresses applied to the infinite matrix surrounding the inclusion are homogeneous (Holzhausen and Johnson, 1979). As pointed out by Taya and Arsenault (1989), Eshelby's procedure for obtaining the stress field outside the inclusion is rigorous, but that for the stress field inside the inclusion is simplified. However, the shear-lag model assumes that the inclusion-matrix system is subjected to a longitudinal extension which results in lateral contraction. If the stresses inside the garnets were homogeneous, we would expect a random distribution of the fracture-spacing since pre-existing microflaws in an isotropic material such as garnet are likely to be randomly distributed (Lawn, 1993). Moreover, the results of the Eshelby model are applicable only to dilute composites in which the volume fraction of stiff inclusions is less than a few percent while those of the shear-lag model are applicable to both dilute and non-dilute systems (Clyne and Withers, 1993). Finally, the stresses in a non-ellipsoidal inclusion (e.g. cylinder, lens or truncated ellipsoid) can be calculated much more easily using the shear-lag model than the Eshelby model.

3.8. Fracturing temperature

Based on the fact that the quartz was brittle when fracturing took place in the garnets and the fractures have not been filled by the matrix or retrograde materials, it is concluded that the fractures in the garnet crystals from the Morin Shear Zone formed at

low temperatures (< 300-350 °C) in which plastic flow of quartz and formation of retrograde materials (e.g. amphibole, biotite, muscovite and chlorite) were impossible. This conclusion is based on the assumption that the rocks were deformed at typical geological strain rates (i.e. 10^{-14} /s).

According to the shear-lag theory, in a deforming composite, the stress always tends to be concentrated in the strong inclusions embedded in a weak matrix. Cracks will form in the inclusions at their weak points where the concentrated tensile stresses have reached the tensile strength of the inclusions. The phenomenon occurs regardless of whether the matrix is deforming elastically or plastically. One should also keep in mind that the mechanical behavior of the matrix depends not only on the temperature but also on the strain rate. The matrix can be elastic or even brittle at high temperature if the strain rate is sufficiently high. Such high strain rates may occur temporarily in natural shear zones.

Since the fractured segments tend not to separate in an elastic matrix, the relative timing of the fractures cannot be determined in any given grain. In a flowing matrix, however, the segments can be separated and filled with matrix materials (Ji and Zhao, 1993). Then the cracks serve as paths for fluids and mass transport and/or as privileged locations for the nucleation and growth of retrograde minerals which depend on both the chemical composition of the rock and metamorphic conditions. For example, a finer-grained symplectite of orthopyroxene-plagioclase-spinel developed along the foliation-perpendicular tensile fractures of garnets in the mafic granulites from Sostrene Island, East Antarctica (Thost et al., 1991). Similarly the "elongate" garnets in the anorthosite-charnockite suite of the Adirondacks (New York State) developed two generations of foliation-perpendicular tensile fractures (Ji, unpublished data). The first generation of fractures formed at high temperature, making the garnet crystals boudinaged. The gaps between the boudins are filled first with biotite and then with opaque minerals. The second generation of fractures, which occurs in the garnet boudins, is similar to those in

the Morin shear zone, and is interpreted to have formed at low temperature. Therefore, the shear-lag process is a viable mechanism for the development of tensile fractures in stiff inclusions in a soft matrix under all metamorphic conditions.

3.9. Conclusions

The results of this study are consistent with the following conclusions:

(1) Fractured garnets are an important feature of the well foliated and lineated mylonites and gneisses from the granulite-facies Morin Shear Zone of the Grenville Province (Quebec). They are clearly observed both in outcrop and in thin section. The pervasive, closely spaced, relatively straight fractures in garnet crystals are planar tensile fractures with no displacement parallel to the fracture plane. The fractures are preferentially perpendicular to the mylonitic foliation and lineation.

(2) The intragranular microfractures commonly taper inward from the grain boundary towards the core, suggesting that the fractures initiated at grain boundaries and then propagated inwards. This indicates that the interfaces between different phases are mechanical and structural heterogeneities which control the initiation of fractures.

(3) The fractures developed preferentially in coarse grains with large aspect ratios. Fractures in grains smaller than 0.2 mm with an aspect ratio less than 2 are rare. This is probably because large grains contain more and larger microflaws than small grains (Lloyd 1991) and because the stress transferred from the incompetent matrix to the more competent particle increases with the particle aspect ratio.

(4) Samples with clustered garnet crystals exhibit a greater degree of garnet fracturing than samples in which the local concentration of garnet crystals is more dilute. This is because closely spaced strong particles cause a local stress concentration (Lloyd and Knipe, 1992).

(5) The fractured segments of each garnet crystal have not been separated or filled with matrix minerals such as quartz and feldspar or with retrogressive minerals

such as biotite, muscovite and chlorite. Some garnet fractures extend into the surrounding quartz as healed microcracks marked with fluid inclusions. This suggests that the garnets were fractured at shallow crustal depths (T<300-350 °C, or <15 km for a typical geothermal gradient of 22 °C/km) where the mylonitic matrix was no longer capable of plastic flow at geologically reasonable strain rates (10^{-14} /s). However, both CO_2 and H_2O-rich fluid inclusions are observed in the quartz. The existence of the high-dense CO_2 fluid inclusions suggests that the garnet fracturing might have started at relatively high temperature (500-550 °C). Since the brittle behavior of quartz occurred at such high temperature, an extremely high strain rate ($10^{-9} - 10^{-10}$ /s) should be assumed for the rocks from the MSZ. We are not aware of any geological evidence to support any event with such a high strain rate in the region. Thus, the fracturing temperature of the garnet and quartz is still an open question. One explanation may be that the temperature and pressure of entrapment of the fluid inclusions in the quartz were considerably overestimated by the microthermometrical studies and thus do not give the real conditions for the garnet fracturing.

(6) Laboratory measurements of P-wave velocities show that the mylonites and gneisses containing the fractured garnets are elastically anisotropic; they are more compressible in the direction normal to the foliation than in the direction parallel to the lineation. Based on these results, it is suggested that the fractures observed in the garnets formed by the response of anisotropic metamorphic rocks to horizontal extension during uplift and cooling within the crust.

(7) Based on the fundamental assumptions of the shear-lag theory of Cox (1952) and Kelly and Macmillan (1986), a mechanical model for a particle-matrix system is developed to explain fracturing in garnets. Each particle was assumed to be a rotational body with any given longitudinal section (e.g., a lens, ellipsoid or truncated ellipsoid). This new model explains well why tensile fracturing take place preferentially in stiff garnets rather than in incompetent felsic material, how two sets of tensile fractures can

form in the same garnet grain, and why the fractures are unequally spaced in a lenticular or ellipsoidal garnet grain. We consider that the shear-lag model is a viable model for the tensile fracturing of garnet crystals in the metamorphic rocks from the Morin shear zone.

(8) Electron backscatter diffraction (EBSD) analysis is a new technique which provides the easiest way to determine the lattice preferred orientation (LPO) of garnets in metamorphic rocks. Detailed EBSD measurements show that there is no direct relationship between the orientation of fractures and LPO in garnet. This is different from the case of feldspar because garnet is quasi-isotropic while feldspar is strongly anisotropic in terms of its mechanical properties.

(9) Our results also suggest that the sequential tensile fractures developed in garnet grains record the progressive uplift of metamorphic rocks within the crust.

3.10. Appendix: Mechanical model for an inclusion-matrix system

Consider a basic unit cell consisting of a stiff inclusion embedded completely in a continuous incompetent matrix (Fig. 3.17). This inclusion is represented by a rotational body with a given longitudinal section (lens, ellipsoid or truncated ellipsoid). Both the inclusion and the matrix deform elastically. The inclusion has a long axis length of $2L$ and short axis length of $2r_0$. The rotation axis or the long axis is parallel to the x axis (Fig. 3.17). In order to obtain the relationship between the longitudinal stress in the inclusion and the far-field stress in the matrix, it is necessary to consider the equilibrium of an infinitesimal element such as that shown in Fig. 3.17b. Because the total axial force along the x direction should be equal to zero under equilibrium conditions,

$$\pi[r_0(x)+dr_0(x)]^2[\sigma(x)+d\sigma(x)]-\pi[r_0(x)]^2\sigma(x)+2\pi r_0(x)\tau_0(x)dx$$

$$+2\pi[r_0(x)+dr_0(x)]\sigma_m dx\tan\theta=0 \qquad (x\geq 0) \qquad \text{(A1)},$$

and

$$\pi[r_0(x)+dr_0(x)]^2[\sigma(x)+d\sigma(x)]-\pi[r_0(x)]^2\sigma(x)+2\pi r_0(x)\tau_0(x)dx$$
$$-2\pi[r_0(x)+dr_0(x)]\sigma_m dx\tan\theta=0 \qquad (x<0) \qquad \text{(A2)}$$

where $r_0(x)$ is the radius of the circular cross section of the inclusion at x, $\sigma(x)$ is the axial tensile stress on the circular cross section with a radius of $r_0(x)$, σ_m is the far field stress in the matrix, and θ is the angle between the x-axis and the tangent of the rotational surface at x. All of the terms in equations (A1) and (A2) are also defined in Fig. 3.17a.

In the infinitesimal element shown in Fig. 3.17b,

$$\tan\theta=\begin{cases}-\dfrac{dr_0(x)}{dx} & (x\geq 0)\\[2ex] \dfrac{dr_0(x)}{dx} & (x<0)\end{cases} \qquad \text{(A3).}$$

Ignoring the high order differential terms and considering equation (A3), equations (A1) and (A2) can be combined and rewritten as

$$r_0(x)^2\frac{d\sigma(x)}{dx}+2r_0(x)\sigma(x)\frac{dr_0(x)}{dx}+2r_0(x)\tau_0(x)-2\sigma_m r_0(x)\frac{dr_0(x)}{dx}=0 \qquad \text{(A4).}$$

According to the shear-lag model (Cox, 1952; Kelly and Macmillan, 1986), the shear stress, $\tau(r,x)$, on the circular ring surface in the matrix around the inclusion (Fig. 3.17c) is proportional to the difference between the longitudinal displacement u in the matrix close to the inclusion and the displacement of the matrix (v) at the same point if the inclusion were absent, that is,

$$-2\pi r(x)\tau(r,x) = H(u-v) \qquad \text{(A5)}.$$

If there is no slip at the inclusion/matrix interface (Cox, 1952; Kelly and Macmillan, 1986), then we have $u = w$, where w is the longitudinal displacement in the inclusion, and when $r(x) = r_0(x)$,

$$-2\pi r_o(x)\tau_o(x) = H(w-v) \qquad \text{(A6)}.$$

At a distance from the x-axis of the inclusion equal to half the average spacing (R) between inclusions, $u = v$. The R value depends on the volume fraction (V_f), the shape and size of the inclusion and the length of the unit cell. If we consider the equilibrium of the matrix between r_o and $r(x)$ ($r_0 \le r(x) \le R$) (Fig. 4.17c), we have

$$2\pi r(x)\tau(r,x) = 2\pi r_o(x)\tau_o(x) \qquad \text{(A7)}$$

so the shear strain in the matrix is given by the following equation:

$$\frac{\partial u}{\partial r} = \frac{\tau(r,x)}{G_m} = \frac{\tau_o(x)r_o(x)}{G_m r(x)} \qquad \text{(A8)}$$

where G_m is the shear modulus of the matrix. Integrating equation (A8) from r_o to R,

$$\Delta u = \frac{\tau_o(x)r_o(x)}{G_m}\ln\left(\frac{R(x)}{r_o(x)}\right) \qquad \text{(A9)}.$$

Because $\Delta u = v - w$, from equations (A6) and (A9), we have

$$H(x) = \frac{2\pi G_m}{\ln\left(\frac{R}{r_o(x)}\right)} \qquad \text{(A10).}$$

Substituting equation (A6) into equation (A4), we obtain

$$r_0(x)^2 \frac{d\sigma(x)}{dx} + 2r_0(x)\sigma(x)\frac{dr_0(x)}{dx} - \frac{H}{\pi}(w-v) - 2\sigma_m r_0(x)\frac{dr_0(x)}{dx} = 0 \qquad \text{(A11).}$$

Differentiating equation (A11) and considering

$$\varepsilon = \frac{dv}{dx} \qquad \text{(A12)}$$

and

$$\frac{dw}{dx} = \frac{\sigma(x)}{E_f} \qquad \text{(A13),}$$

the final differential equation for the tensile stress as a function of distance along the x-direction in the inclusion is:

$$\frac{d^2\sigma(x)}{dx^2} + A(x)\frac{d\sigma(x)}{dx} + B(x)\sigma(x) = C(x) \qquad \text{(A14)}$$

where

$$A(x) = \frac{4}{r_0(x)}\frac{dr_0(x)}{dx} - \frac{1}{H(x)}\frac{dH(x)}{dx} \qquad \text{(A15)}$$

$$B(x) = \frac{2}{r_0(x)^2}\left(\left(\frac{dr_0(x)}{dx}\right)^2 + r_0(x)\left(\frac{d^2r_0(x)}{dx^2}\right) - \frac{r_0(x)}{H(x)}\frac{dH(x)}{dx}\frac{dr_0(x)}{dx} - \frac{H(x)}{2\pi E_f}\right)$$

(A16),

and

$$C(x)=\frac{2E_m\varepsilon}{r_0(x)^2}\left(\left(\frac{dr_0(x)}{dx}\right)^2+r_0(x)\left(\frac{d^2r_0(x)}{dx^2}\right)-\frac{r_0(x)}{H(x)}\frac{dH(x)}{dx}\frac{dr_0(x)}{dx}\right)-\frac{H\varepsilon}{\pi r_0(x)^2}$$

(A17).

Chapter 4

Relationship between joint spacing and layer thickness*

温故知新
孔子
(論語-為政)

4.1. Introduction

Hobbs (1967) first introduced the shear-lag model of Cox (1952) to geologists and modified the mathematical derivations of the model to incorporate an elastic layer-matrix system. As described by Gross et al. (1995), Hobbs' paper has been commonly cited as a theoretical explanation for the linear relationship between joint spacing and bed thickness in sedimentary rocks (Price, 1966; McQuillan, 1973; Ladeira and Price, 1981; Huang and Angelier, 1989; Narr and Suppe, 1991; Gross, 1993; Gross et al., 1995; Wu and Pollard, 1995). However, Hobbs' model is based on an assumption that the shear stress in the matrix (bounding non-jointing beds), which is caused by the strain incompatibility between the competent layer and the incompetent matrix, decreases linearly from a maximum value at the layer/matrix interface to zero at a distance exactly equal to the jointing layer thickness from the interface [his equation (9)]. This assumption imposes a condition that must be formally met for Hobbs' model to apply: the incompetent layer thickness should always be larger than the thickness of the jointing competent layer (Narr and Suppe, 1991). In many interbedded sedimentary rocks, however, the bounding non-jointing beds are very thin relative to the jointed layer thickness (Narr and Suppe, 1991;

---

* Published in Journal of Structural Geology, 20, (1998) 1495-1508.

Gross et al., 1995). Moreover, finite-element analyses of Fischer et al. (1995) demonstrate that the shear stress formed by the strain incompatibility decays non-linearly in the matrix with the vertical distance from the layer/matrix interface. Theoretical analysis of composites with an identical arrangement of constituents (Zhao and Ji, 1997) suggests that the shear stress should decrease from a maximum value at the layer/matrix interface to zero at half way between two neighboring competent layers. The reason is simple: the layer-matrix composite is considered as an edifice constructed from identical building blocks which are named "unit-cells". The boundary between two neighboring unit-cells should be a plane over which no shear stress acts because the composite is assumed to be under uniform extension.

As noted by Gross et al. (1995), it is difficult to understand the above problems in Hobbs' paper because it is compact and lacks illustrations. It is the purpose of this paper to provide a straightforward yet rigorous modification of Hobbs' original shear-lag analysis in order to account for the non-linear decay of shear stress in the matrix. Starting from first principles and using equilibrium and continuity conditions, a revised model is provided for the relationship between joint spacing and bed thickness.

4.2. The revised model

Hobbs (1967) treated bedded strata as a lamellar composite containing continuous, aligned competent (higher elastic modulus) and incompetent (lower elastic modulus) layers of equal length (Fig. 4.1a). He assumed that each component layer behaves in a purely linear-elastic manner, that is, no plastic yielding is allowed. Further, in his treatment, residual stress effects are also neglected. If a uniform extensional strain (ε) is applied in the direction parallel to the layers (Fig. 4.1b), the resulting tensile stress will be higher in the competent layer than in the incompetent layers (matrix). Joints will then form in the competent layer at its weak points where the tensile stress has reached its critical tensile

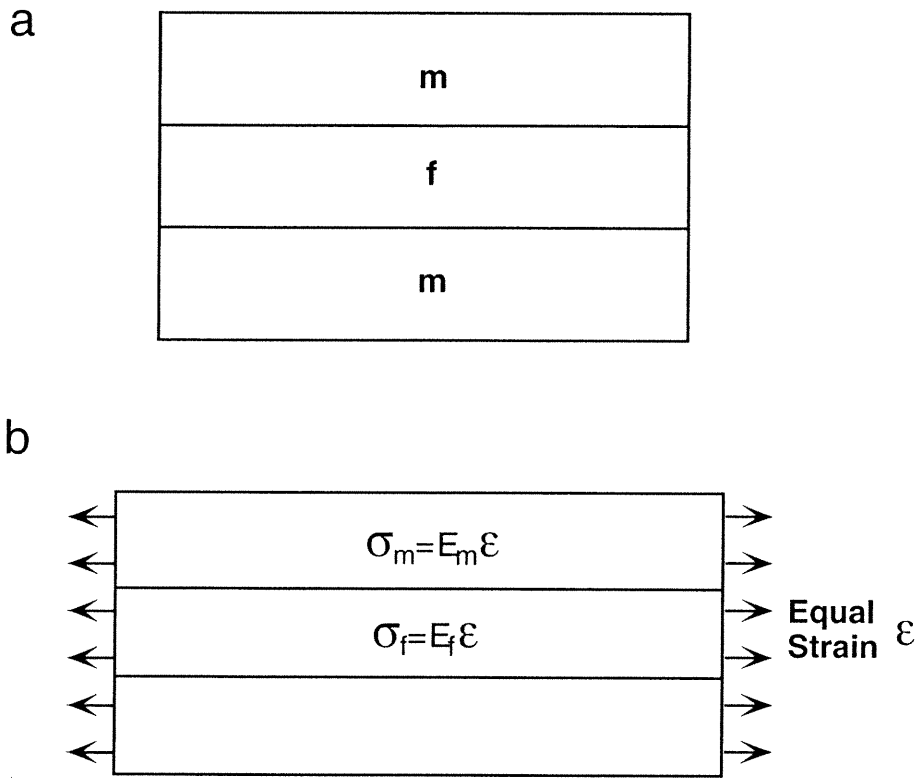

Figure 4.1. Schematic illustrations of a lamellar composite containing continuous, aligned competent (f) and incompetent (m) layers of equal length. (a) The unstrained state. (b) The composite is subject to a uniform, layer-parallel extensional strain (ε). In this case, the competent layer carries a greater stress than the incompetent layer.

strength (C_0). The joints terminate at contacts with adjacent incompetent layers because the competent layer fails at much lower values of extensional strain than the incompetent layers (Garrett and Bailey, 1977).

Because joints are free surfaces across which no stress can be transferred (Lachenbruch, 1961; Pollard and Segall, 1987), the far-field extensional strain cannot be directly applied to a discontinuous, jointed layer segment (ACDB in Fig. 4.2a) from its ends (AB and CD planes in Fig. 4.2a). Thus, the tensile stress built-up in this layer segment is purely due to the stress transfered from the matrix to the competent layer by means of interfacial shear stresses. Because the interfaces between the layers (AC and BD in Fig. 4.2a) are assumed to be welded, the different amounts of layer-parallel displacements between the matrix and the competent layer result in shear strains, and thus shear stresses, parallel to the layers. It is of considerable interest to know how tensile stress is built up in an individual layer segment because the final joint spacing is controlled by the magnitude and distribution of the stress. The stress transfer can be analyzed according to the shear-lag model (Cox, 1952; Holister and Thomas, 1966; Kelly and Macmillan, 1986; Zhao and Ji, 1997). Since the following analysis does not address the problems of joint propagation, the three-dimensional aspects of the phenomenon are ignored.

In order to perform the shear-lag analysis, a unit cell is used. In the unit cell shown in Fig. 4.2a, a jointed competent layer segment (ACDB) lies between two half incompetent beds (EGCA and BDHF), with joints (AB and CD) forming the ends of the competent layer segment. As suggested by Price (1966), a sedimentary bed always contains some randomly positioned pre-existing joints which can result from a Poisson process. The boundary conditions at the ends of the unit cell are critical for the analysis. First, the jointing layer is extended parallel to the X-direction and the tensile stress in this direction should be zero across each joint surface (AB and CD planes). Second, the interfaces between the layers are assumed to be welded and thus there is no interfacial slip. Third,

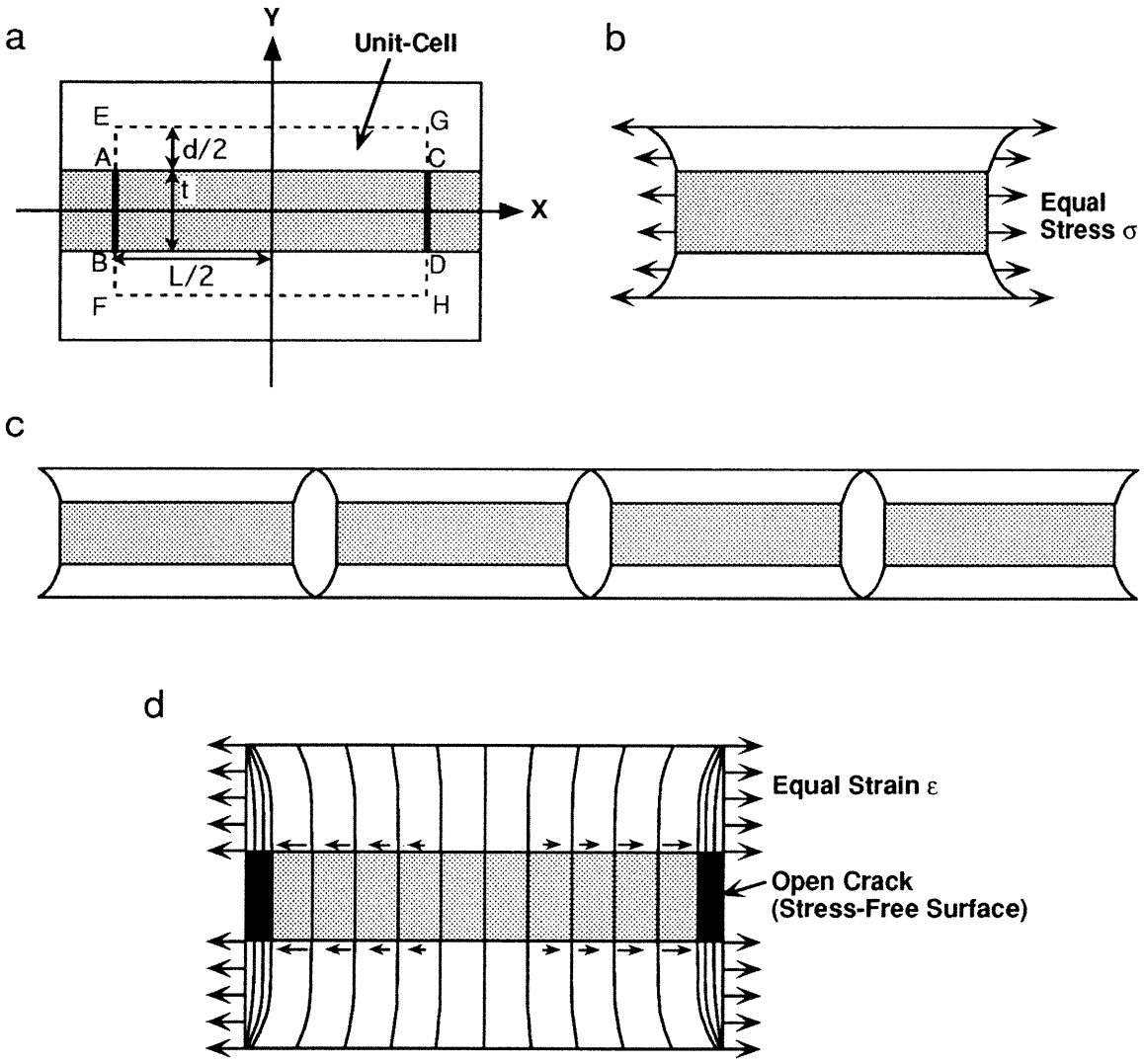

Figure 4.2. Schematic illustration of a unit-cell (a) used in the mechanical equilibrium analysis of the shear-lag model for the layer-matrix system. Variables are defined in text. The coordinate origin is located at the center of the layer segment. The Z-axis is perpendicular to the X- and Y-axes. Under a uniform stress, the two ends of the unit-cell will be bent (b). As a result, a "lens"-shaped void will be formed between two adjacent unit-cells (c). (d) shows the variation of the longitudinal displacements introduced by applying a uniform extensional strain to the ends of the matrix. The openings at joints are exaggerated.

the external loading on the ends of the matrix (EA, BF, GC and DH planes in Fig. 4.2a) cannot be uniform. If the loading is uniform, the edges of the matrix will be bent (Fig. 4.2b) during deformation, and consequently, a "lens"-shaped void will be formed between two adjacent unit-cells (Fig. 4.2c). Such a scenario implies that the joint extends beyond the competent layer into the neighboring incompetent beds a distance equal to half the thickness of the incompetent beds. In nature, however, the joints are restricted to the competent layers (Huang and Angelier, 1989; Narr and Suppe, 1991; Gross et al., 1995). In order to avoid the above problem, it is assumed here that the ends of the matrix experience a uniform extensional strain (ε) and the existing joints at the ends of the competent layer segment are open during the deformation (Fig. 4.2d). This assumption also implies that two adjacent competent layer segments physically separate a finite distance during the extension. However, the exact size of the gaps is not critical to the model. The model shown in Fig. 4.2d is believed to represent the state of affairs around a jointed layer segment with sufficient accuracy for present purposes.

In the following analyses, the shear-lag model developed by Cox (1952) and summarized by Holister and Thomas (1966), Kelly and Macmillan (1986), and Zhao and Ji (1997) is used. This model is elegant in its simplicity and provides accurate estimates of the longitudinal tensile stress in the continuous or discontinuous fibers embedded in a weak matrix. Hence the model has been widely used by geologists to explain the origin of extension fracture boudinage (Lloyd et al., 1982; Masuda and Kuriyama, 1988; Ji and Zhao, 1994; Ji et al., 1997; Ji, 1997). The model is also able to provide the distribution of shear stresses in the weak matrix surrounding strong inclusions and accordingly, to interpret the variations of dislocation density and of recrystallized grain size in composites and polyphase rocks (Dunand and Mortensen, 1991; Zhao and Ji, 1997). Furthermore, the model is widely used to predict the elastic or flow strength of two-phase composites (e.g. Nardone and Prewo, 1986; Zhao and Ji, 1993) and rocks (Ji and Zhao, 1994).

Under the above conditions, as shown in detail in the shear-lag model (Hobbs, 1967; Kelly and Macmillan, 1986; Lloyd et al., 1982), the governing equation for the tensile stress in the competent layer segment, $\sigma_f(x)$, is given by

$$\sigma_f(x) = E_f\varepsilon + \frac{S_1}{A_f}\sinh(\beta x) + \frac{S_2}{A_f}\cosh(\beta x) \qquad (4.1)$$

where ε is the far-field strain, E_f and A_f are the Young's modulus and the cross-sectioned area of the competent layer, respectively. $A_f = bt$, where t and b are the thickness and width of the competent layer in the Y- and Z-directions (Fig. 4.2a), respectively.

$$\beta = \left(\frac{H}{E_f A_f}\right)^{1/2} \qquad (4.2),$$

where H is a constant, which depends on the geometrical arrangement of the layer and the matrix and on their respective elastic moduli.

In equation (4.1), S_1 and S_2 are constants which can be determined for to the following boundary conditions:

$$\sigma_f\left(-\frac{L}{2}\right) = \sigma_f\left(\frac{L}{2}\right) = 0 \qquad (4.3)$$

where L is the length of the layer segment, as shown in Fig. 4.2a. Equation (4.3) is due to the fact that the tensile stress is reduced to zero at the existing joints since they are free surfaces (Lachenbruch, 1961; Pollard and Segall, 1987).

Substituting equation (4.1) into equation (4.3), we obtain

$$S_1 = 0 \qquad (4.4)$$

and

$$S_2 = -\frac{E_f A_f \varepsilon}{\cosh\left(\frac{\beta L}{2}\right)} \qquad (4.5).$$

The distribution of tensile stress in the competent layer segment is then:

$$\sigma_f(x) = E_f \varepsilon \left(1 - \frac{\cosh(\beta x)}{\cosh\left(\frac{\beta L}{2}\right)} \right) \qquad (4.6).$$

where equation (4.6) shows that the tensile stress in a competent layer segment builds up from the ends ($x = -L/2$ and $x = L/2$) and reaches a maximum at the center (Fig. 4.3).

The value of H can be obtained from the following analysis. If $P(x)$ is the load in the competent layer segment at a distance x from the origin of the coordinates (Fig. 4.2a), Cox (1952) assumed that

$$\frac{dP(x)}{dx} = H[u(x) - v(x)] \qquad (4.7)$$

where $u(x)$ is the longitudinal displacement in the competent layer and $v(x)$ is the corresponding displacement the matrix would undergo if the competent layer were absent (Hobbs, 1967; Kelly and Macmillan, 1986; Lloyd et al., 1982)

If $\tau(x,y)$ is the shear stress in the X direction on planes parallel to the XZ plane (Fig. 4.2a), then at the interface between the layer and the matrix, the shear stress is $\tau(x,t/2)$. According to mechanical equilibrium,

$$dP(x) = -2\tau(x,t/2) \cdot (b dx) \qquad (4.8)$$

or

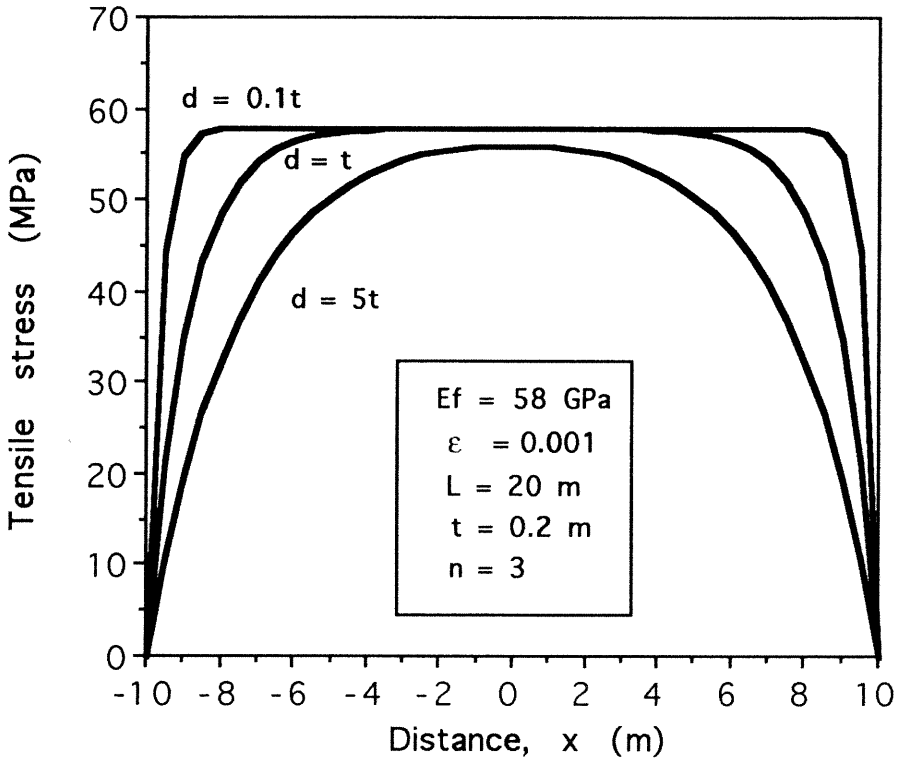

Figure 4.3. Predicted tensile stress variations, as functions of the incompetent layer thickness (d = 0.1t, d = t, and d = 5t), along a competent layer (t = 0.2 m and L = 20 m), using E_f = 58 GPa, E_f/E_m = 3 , ε = 0.1%, ν_m = 0.25 , and n = 3 as input data.

$$\frac{dP(x)}{dx} = -2b\tau(x,t/2) = H[u(x) - v(x)] \qquad (4.9)$$

Therefore,

$$H = -\frac{2b\tau(x,t/2)}{u(x) - v(x)} \qquad (4.10)$$

From the mechanical equilibrium point of view (Zhao and Ji, 1997), the shear stress caused by the strain incompatibility between the competent layer and the matrix should progressively decrease in the Y direction from a maximum value [$\tau(x,t/2)$] at the layer/matrix interface to zero at the middle way between two neighboring competent layers (EG and FH planes in Fig. 4.2a), that is,

$$\tau(x,y) = 0, \text{ when } y = \frac{t+d}{2} \qquad (4.11)$$

and

$$\tau(x,y) = \tau(x,t/2), \text{ when } y = \frac{t}{2} \qquad (4.12)$$

The reason for this is that the boundaries of the unit cell (EG and FH planes in Fig. 4.2a) should have zero shear stress. Lloyd et al. (1982) assumed that shear stress is constant in the X direction on any XZ plane parallel to the layer (their equation 10). However, their assumption cannot satisfy the above mechanical equilibrium conditions (Zhao and Ji, 1997).

Hobbs (1967) proposed that the shear stress decreases in the Y direction in the matrix according to the following equation:

$$\tau(x,y) = \tau(x,y)\Big|_{y=t/2}\left(\frac{t-y}{t}\right) \qquad (4.13a)$$

He located the coordinate origin at the layer/matrix interface [his equation (9)]. If we locate the coordinate origin at the center of the competent layer (Fig. 4.2a), equation (4.13a) becomes

$$\tau(x,y) = \tau(x,y)\Big|_{y=t/2}\left(\frac{\frac{3t}{2}-y}{t}\right) \qquad (4.13b).$$

Unse this assumption, the shear stress in the matrix decreases linearly from a maximum value of $\tau(x,y)\Big|_{y=t/2}$ at the layer-matrix interface to zero at a distance exactly equal to the competent layer thickness (t) from the interface. Such a shear stress distribution does not apply to the case where $d<t$ (Fig. 4.2a) since mechanical equilibrium cannot be attained. In nature, however, many non-jointing incompetent beds are much thinner than jointed beds. This situation is thus precluded by Hobbs' model. These shortcomings in the Hobbs' model were also recognized by Narr and Suppe (1991), Gross et al. (1995) and Fischer et al. (1995).

Tyson and Davies (1965) performed a photoelastic study of the shear stresses in a quasi-infinite matrix (araldite CT 200) around a single cylindrical fiber (dural). They found that the shear stresses in the matrix (τ_m) fall off radially approximately as the inverse of the distance (r) from the fiber axis. Thus, $\tau_m = \tau_i\left(r_f/r\right)$, where τ_i is the interfacial shear stress and r_f is the fiber radius. In composites with large fiber volume fractions, however, the above equation is inappropriate to describe the shear stress distribution in the matrix. The reason is that the shear stress should be equal to zero at the midpoint between two neighboring fibers (Zhao and Ji, 1997).

In contrast to Hobbs' assumption, shown by equation (4.13a or b), two-dimensional finite element numerical simulations by Fischer et al. (1995) demonstrated that the bedding-parallel shear stress decreases non-linearly with increasing the vertical distance from the maximum value at the bedding interface to zero away from the interface.

A simple expression for the non-linear variations of $\tau(x,y)$, which can satisfy the boundary conditions given by equations (4.11)-(4.12), is the following:

$$\tau(x,y) = \tau(x,y)\Big|_{y=t/2}\left(\frac{d+t-2y}{d-t+2y}\right)^n \qquad (4.14)$$

where n is a decay constant larger than or equal to 1. As shown in Fig. 4.4, the shear stress decreases more rapidly with the vertical distance from the interface for larger n values. Although equation (4.14) is certainly not a unique solution to the boundary conditions, we could find no constraints for values of $\tau(x,y)$ from $y=t/2$ to $y=(t+d)/2$ to warrant the use of a more complicated function for $\tau(x,y)$. It should be pointed out that the actual decay model used to calculate the shear stress in the matrix affects the relationship between the joint spacing and bed thickness. It is hoped that this work will encourage experimental studies of the shear stress distribution and magnitude in the matrix. For simplicity, it is assumed in the present study that the shear stress in the matrix can be described by equation (4.14).

Now let w be the displacement in the soft matrix due to extension. If there is no slippage between the competent and incompetent layers, $w=u$. At a distance from the X-axis equal to $(t+d)/2$, we have $w=v$. Considering equation (4.14), the shear strain in the matrix is described by the following equation:

$$\frac{\partial w}{\partial y} = \frac{\tau(x,y)}{G_m} = \frac{\tau(x,t/2)}{G_m}\left(\frac{d+t-2y}{d-t+2y}\right)^n \qquad (4.15)$$

where G_m is the shear modulus of the incompetent matrix. Integrating from $t/2$ to $(t+d)/2$ gives

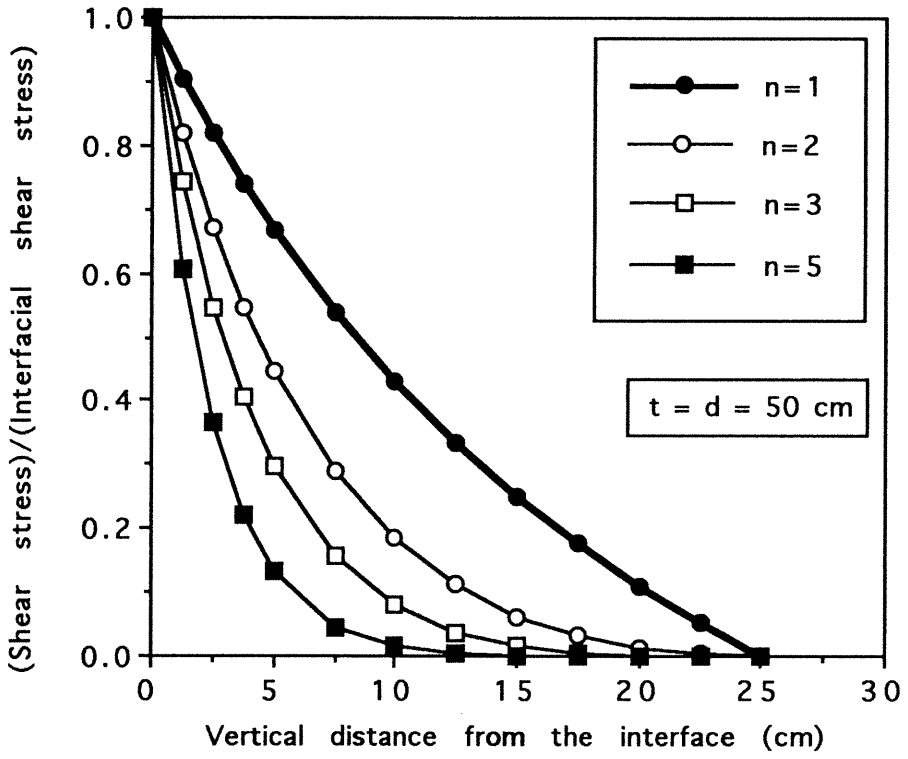

Figure 4.4. Variations in the ratio of the matrix shear stress to the interfacial shear stress as a function of vertical distance from the layer-matrix interface. Calculated according to equation (4.14); t = d = 50 cm and n is the decay constant.

$$v-u=\Delta w=\int_{t/2}^{(t+d)/2}\frac{dw}{dy}dy=\frac{\tau(x,t/2)M}{G_m} \qquad (4.16)$$

where

$$M=\int_{t/2}^{(t+d)/2}\left(\frac{d+t-2y}{d-t+2y}\right)^n dy \qquad (4.17)$$

Equation (4.17) requires numerical methods for its solution. For a given n value, M value increases with the thickness of the incompetent layer (d) in an approximately linear manner (Fig. 4.5a). The M-value is independent of t.

Substituting equation (4.16) into equation (4.10), we have

$$H=\frac{2bG_m}{M} \qquad (4.18).$$

Then, substituting equation (4.18) into equation (4.2), we obtain

$$\beta=\left(\frac{2bG_m}{E_fA_fM}\right)^{1/2}=\left[(1+\upsilon_m)tM\frac{E_f}{E_m}\right]^{-1/2} \qquad (4.19).$$

where υ_m is the Poisson ratio of the incompetent layer, and E_f/E_m is the elastic contrast between the competent and incompetent layers. For a given competent layer, β value decreases non-linearly with increasing d (Fig. 4.5b).

From equations (4.1) and (4.9), we can obtain the shear stress at the layer/matrix interface ($y=t/2$):

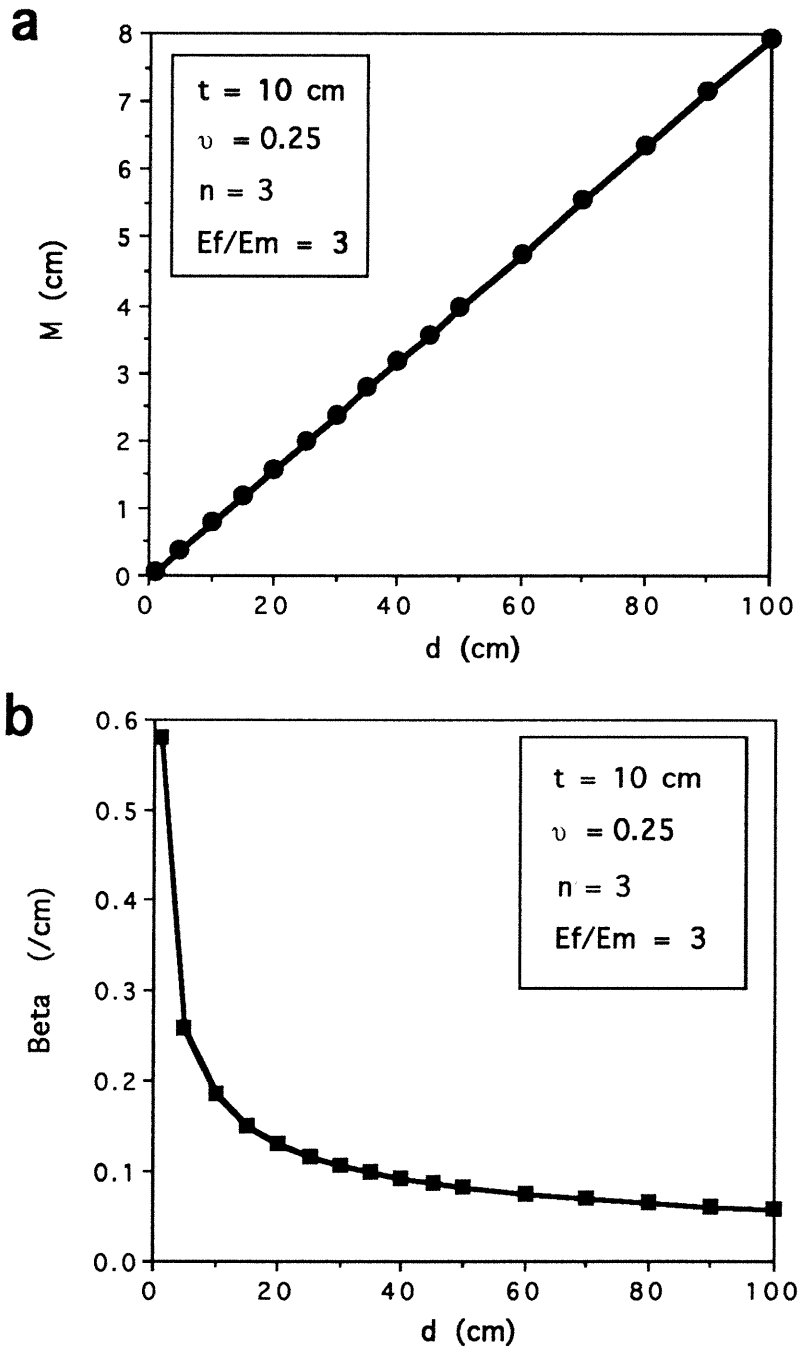

Figure 4.5. (a) Linear variation of M-value and (b) non-linear variation of β–value as a function of d. Calculated using t = 10 cm, $\nu_m = 0.25$, n = 3, and $E_f/E_m = 3$.

$$\tau(x,t/2) = -\frac{1}{2b}\frac{dP(x)}{dx} = -\frac{A_f}{2b}\frac{d\sigma_f(x)}{dx} = \frac{t}{2}E_f\varepsilon\beta\frac{\sinh(\beta x)}{\cosh\left(\frac{\beta L}{2}\right)} \qquad (4.20)$$

The derivative $dP(x)/dx$ at each position along the length of the layer can be derived from the slope of the stress transfer profile of Fig. 4.3. Figure 4.6 shows the variation of the shear stress along the layer/matrix interface $\tau(x,t/2)$. As expected from equation (4.20), the interfacial shear stress takes up maximum values at the ends of the jointed layer and sharply decays to zero at a distance termed the "transfer length" in composite mechanics (Jahankhani and Galiotis, 1991). As shown in Fig. 4.6, the transfer length increases with increasing ratio of *d/t*. The distribution of the interfacial shear stress in fiber composites has been experimentally measured employing Raman spectroscopy (Jahankhani and Galiotis, 1991) and photoelastic techniques (Dow, 1961; Tyson and Davies, 1965). Their measured stress distribution patterns are very similar to the calculated results shown in Fig. 4.6.

According to equation (4.6), the maximum tensile stress in the competent layer occurs midway between two existing joints (i.e., $x = 0$), and is given by

$$\left(\sigma_f\right)_{\max} = E_f\varepsilon\left(1 - \frac{1}{\cosh\left(\frac{\beta L}{2}\right)}\right) \qquad (4.21).$$

The maximum tensile stress decreases with decreasing aspect ratio, L/t, of the fragmented layer and with increasing thickness of the incompetent layers (Fig. 4.3). In other words, the maximum tensile stress in the competent layers increases as their volume fraction increases.

When the magnitude of the tensile stress (σ_f) transferred from the matrix reaches the tensile strength, C_0, of the brittle layer, a new joint forms midway between the existing joints, and the tensile stress goes to zero at this point. As for the garnet fractures

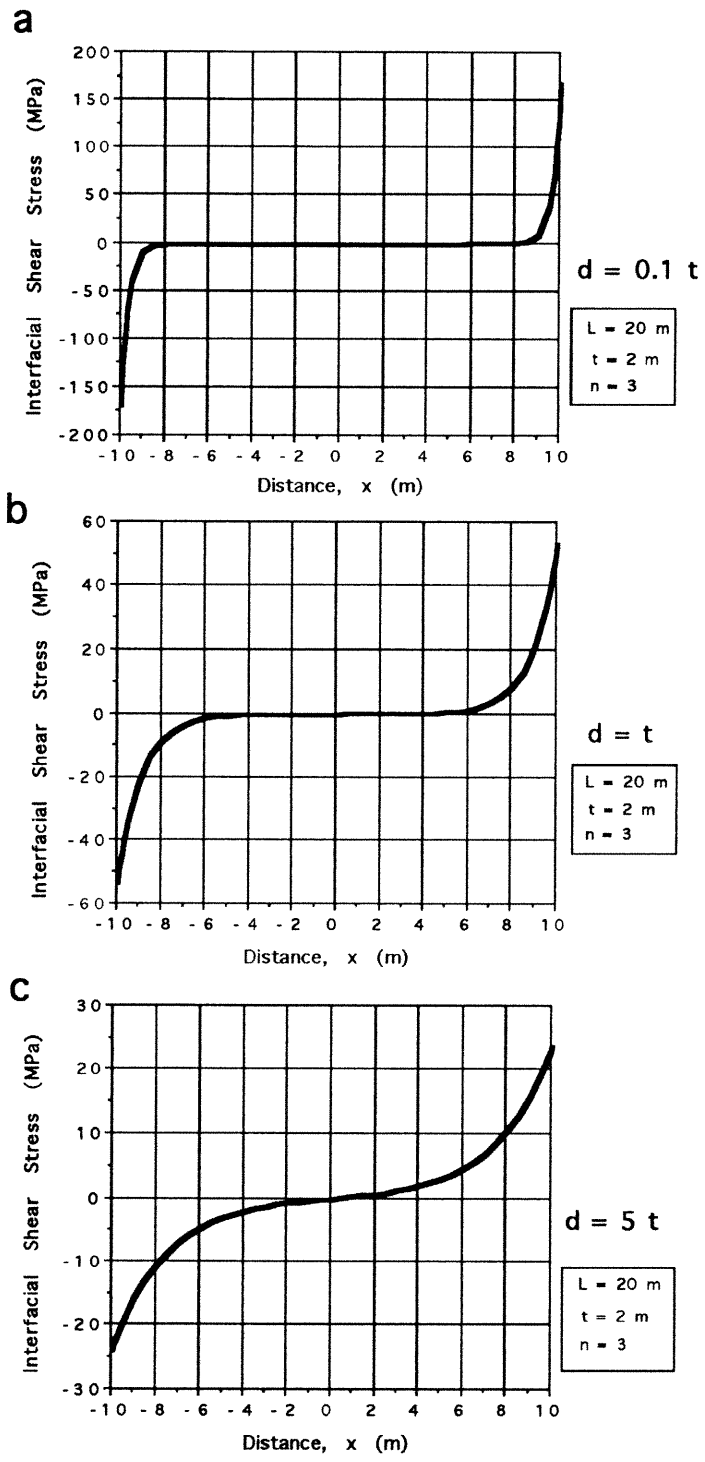

Figure 4.6. Predicted variations along a competent layer (t = 2 m, L = 20 m) of the shear stress at the layer-matrix interface as a function of the bounding bed thickness (d) according to equation (4.20), using $E_f/E_m = 3$, $\nu_m = 0.25$, and $\varepsilon = 0.1\%$. (a) d = 0.1t, (b) d = t, and (c) d = 5t.

discussed in Chapter 3, the joints are formed by a sequential process (Price, 1966; Hobbs, 1967; Narr and Suppe, 1991; Gross, 1993). After a break, the segments are newly loaded in the course of extension and break again. Since the tensile stress in each segment reaches a maximum at only one point along the loading direction, the fractured segment should never be broken along more than one plane at the same time if this segment is mechanically homogeneous. In sedimentary rocks, a number of parallel tensile joints are commonly observed in each single competent layer. These joints belong to different generations which were formed at different times in a successive jointing process.

Equation (4.21) indicates that the magnitude of the maximum tensile stress in a jointed layer segment decreases with decreasing length/thickness ratio (L/t). The sequential jointing process will decrease the aspect ratio and in consequence, will reduce the maximum tensile stress in the subsegment. Thus layer segments which have high aspect ratios break first. Moreover, when a layer segment is jointed during tension, its internal stress is relaxed, and the force carried by this segment may be transferred to the surrounding matrix and beyond, to neighboring layers.

The final joint spacing (s) is thus controlled by a critical length (with respect to the layer thickness) below which the maximum tensile stress cannot exceed the tensile fracture strength of the layer (C_0). This is exactly analogous to the behavior in extension of certain types of fiber-reinforced composites (Klipeel et al., 1990; Melanitis et al., 1992) and rocks (Hobbs, 1967; Lloyd et al., 1982; Ji and Zhao, 1993; Ji et al., 1997). By setting the maximum tensile stress $\left(\sigma_f\right)_{\max}$ equal to C_0, we obtain the critical length of the layer segment (L_c) through the following equation:

$$L_c = \frac{2}{\beta}\cosh^{-1}\left(\frac{E_f\varepsilon}{E_f\varepsilon - C_0}\right) \qquad (4.22).$$

L_c is thus the shortest length of layer segment which can fracture because in shorter segments the tensile stress nowhere exceeds the tensile strength of the layer. Segments longer than L_c, however, will fracture again. The minimum possible length of a layer segment should be equal to $L_c/2$ because segments shorter than L_c cannot fracture further (Lloyd et al., 1982). When all of the layer segments finally have lengths between $L_c/2$ and L_c, jointing stops and the spacing remains constant despite increasing strain. This layer has reached a state of fracture saturation (Cobbold, 1979; Rives et al., 1992; Wu and Pollard, 1995).

At the state of fracture saturation, the layers display a range of layer segment lengths: $L_c/2 \le L_i \le L_c$, where L_i is the length of jointed layer segments. If the frequency distribution of fracture spacing shows a normal distribution in the range from $L_c/2$ to L_c, the mean fracture spacing (equivalent to the median joint spacing in the present case), s, should be:

$$s = \frac{3}{4} L_c \qquad (4.23)$$

(Ohsawa et al., 1978). Substituting equation (4.22) into equation (4.23), we obtain

$$s = \frac{3}{2\beta} \cosh^{-1}\left(\frac{E_f \varepsilon}{E_f \varepsilon - C_0}\right) \qquad (4.24).$$

Then substituting equation (4.19) into equation (4.24), we have

$$s = \frac{3}{2}\left[t(1+\upsilon_m) M \frac{E_f}{E_m}\right]^{\frac{1}{2}} \mathrm{Cosh}^{-1}\left(\frac{E_f \varepsilon}{E_f \varepsilon - C_0}\right) \qquad (4.25)$$

where E_m and υ_m are the Young's modulus and the Poisson's ratio of the matrix, respectively. It is worth mentioning that Hobbs (1967) took L_c as s.

Equation (4.25) shows that the median joint spacing depends on the thickness of the competent layer, the mechanical properties (E_f, E_m, υ_m and C_0) of both the competent and adjacent incompetent layers, and the degree of tectonic deformation (ε). It depends also on the thickness of the incompetent layers (*d*) and the decay constant (n) of the shear stress in the incompetent layers because the M value in equation (4.25) is controlled by these two factors.

It should be pointed out that the applied strain (ε) in equation (4.25) cannot exceed the fracture saturation strain of the jointed layer. As shown by the experiments of Rives et al. (1992) and Wu and Pollard (1992, 1995), when the applied strain reaches a critical value, fracture spacing stops evolving and remains nearly constant. The critical strain is called fracture saturation strain. In other words, joint spacing decreases with increasing strain before the fracture saturation strain has been reached, but continued application of strain beyond the fracture saturation strain will not significantly change the joint spacing (Cobbold, 1979; Narr, 1991; Narr and Suppe, 1991; Rives et al., 1992; Wu and Pollard, 1992 and 1995). By inserting the fracture saturation strain into equation (4.25), one can obtain the relationship between saturated joint spacing and bed thickness.

4.3. Analysis of field data

Field data were collected from the St-Roch Formation of Lower Cambrian age in continuous exposures at Plage Victor along the Saint-Lawrence River near Saint-Jean-Port-Joli (Fig. 4.7) which is located 113 km northeast of Quebec city. Rocks in this area belong to the flysch sequence belt which forms the western front of the Quebec Appalachians. The regional geology and stratigraphy of this area are given in Hubert (1967), St-Julien (1967), Hubert (1969) and Shalaby (1977).

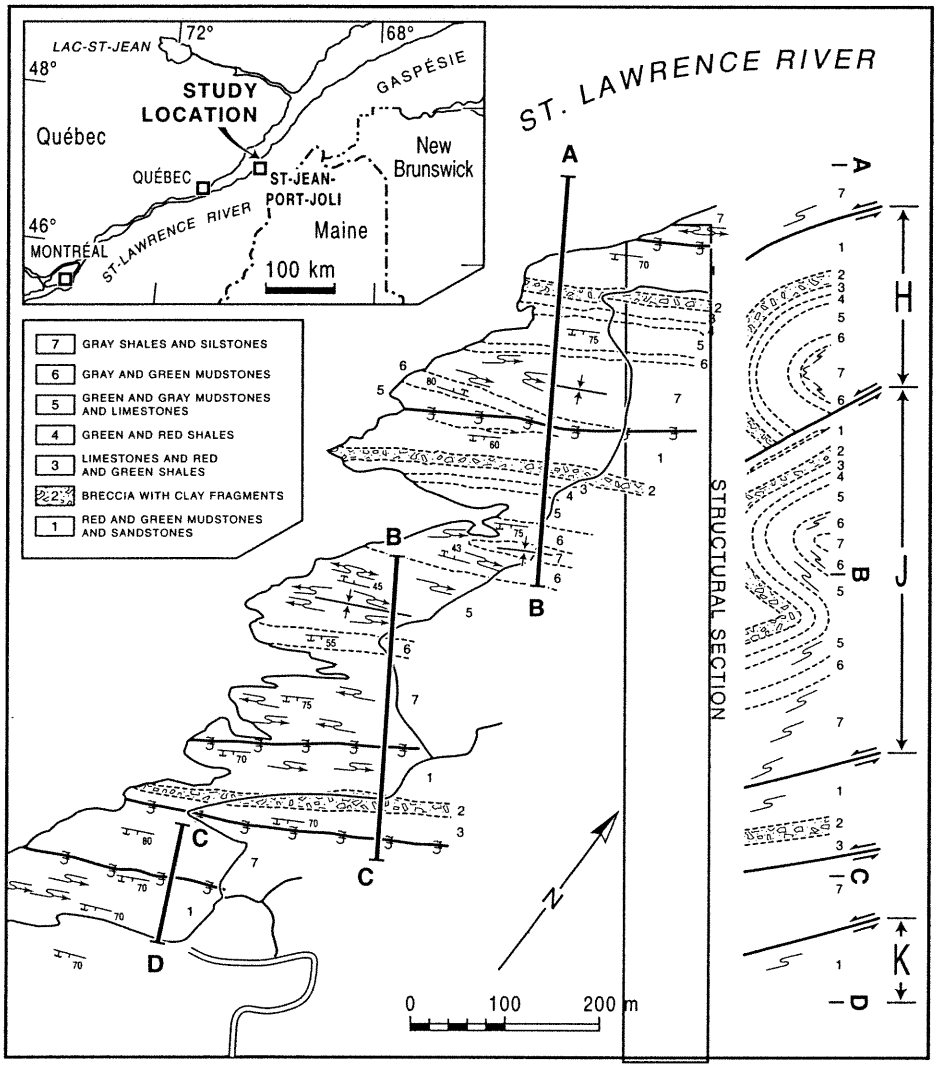

Figure 4.7. Geological map of Plage Victor along the Saint-Lawrence River near Saint-Jean-Port-Joli, Quebec. Modified from Hubert (1969). Seven subunits were identified by Hubert (1969) and Shalaby (1977). Subunit 1 is characterized by interbedded siltstones, sandstones and red and green mudstones. Subunit 2 is a slump deposit with irregular mudstone breccia, flow rolls and irregular fold axes. Subunit 3 consists of limestone conglomerate and red and green shales. Subunit 4 is composed of red and green shales with laminated calcareous siltstones. Subunit 5 is characterized by green and gray mudstones interbedded with thick laminated limestones and siltstones. Subunit 6 consists of interbedded limestones and gray and green mudstones. Subunit 7 consists of red and green mudstones and thin sandstones beds. The lithology and thickness of the sandstone beds persists laterally. The joint data were measured mainly from subunits 1 and 7.

The tectonic structures of the area are characterized by NE-SW-trending folds and reverse faults which formed during the Appalachian compressional orogeny. In the study area (900 x 300 m^2), tectonic strain is fairly homogeneous except near the faults (Fig. 4.7). Joints are confined to the hard sandstone, siltstone and limestone layers while the soft shale and mudstone layers remain non-jointed (Fig. 4.8). The joints are approximately planar fractures with little or no offset parallel to the fracture plane, and are thus extension fractures ("mode I" cracks of fracture mechanics) which formed as the result of extensional strain normal to the plane of fracture (Pollard and Aydin 1988). There are two sets of joints in the studied area, one strikes about 325-340° and dips between 65° and 85°, and the other trends about 140-155° and dips 10-30°. Only the first set of joints was measured in the field because they are nearly perpendicular to the fold axes and likely formed by regional tectonic extension induced by the Appalachian compressional orogeny. The joint spacing of this set is commonly greater in thick beds than in thin beds, as shown in Fig. 4.8. Measurements were performed on jointed layers which were (i) uniform in thickness; (ii) bounded by two incompetent layers nearly identical in thickness; (iii) not disturbed by faults; and (iv) cut by at least 40 parallel joints whose spacing could be measured on continuous outcrop. In total, 42 sandstone layers were measured, among them 30 from area H, 5 from area J and 7 from area K (Fig. 4.7). A small number of measurements from areas J and K make it impossible to investigate the effect of strain on joint spacing.

Plume structures (Fig. 4.8f) and rib marks on joint surfaces in uniform fine-grained siltstones and limestones indicate that the joints initiated and propagated away from point defects such as nodules, pebbles, pores, and minerals (Price, 1966; Syme-Gash, 1971; Bahat and Engelder, 1984). It may be reasonable to assume that such defects are randomly distributed in the rocks.

The joint-spacings belonging to a single joint set along an individual bed with a uniform thickness generally display a normal distribution (Fig. 4.9a, c) but some have a

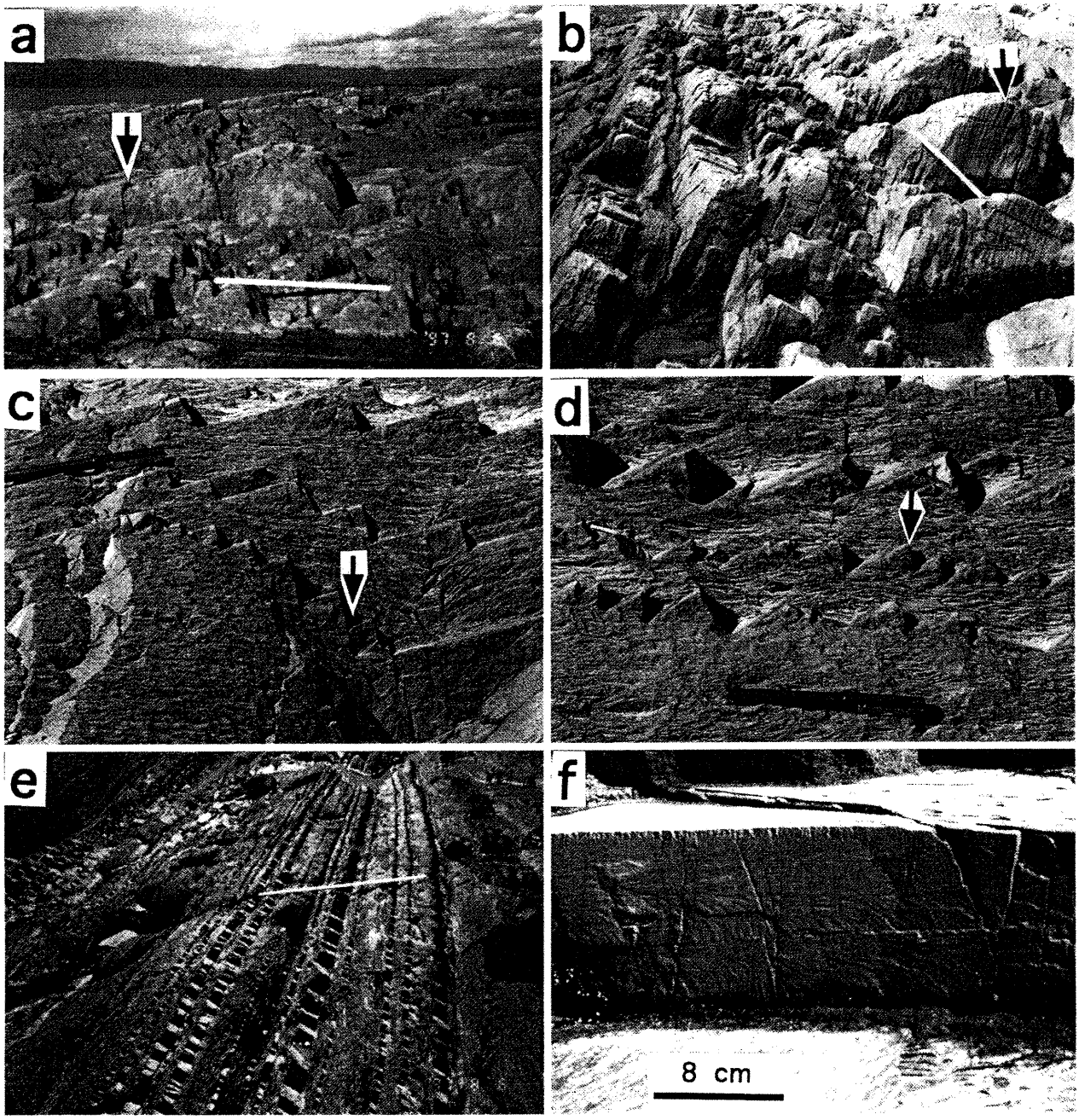

Figure 4.8. Photographs of the interbedded sedimentary rocks at Plage Victor along the Saint-Laurence River near Saint-Jean-Port-Joli, Quebec. Jointing layers are competent sandstone in (a) and (c-f) and limestone in (b) while non-jointing layers are incompetent mudstone or shale. The systematic set of steepy dipping joints (indicated by arrows) was chosen for analysis in the present study. Note that the joint spacing in the thicker sandstone layers is consistently greater than in the thinner beds. (f) Joint plane in fine-grained sandstone showing plumose structure propagating away from a point. Length of ruler in (a, b, e): 1.0 m. Length of pen in (c, d): 0.14 m.

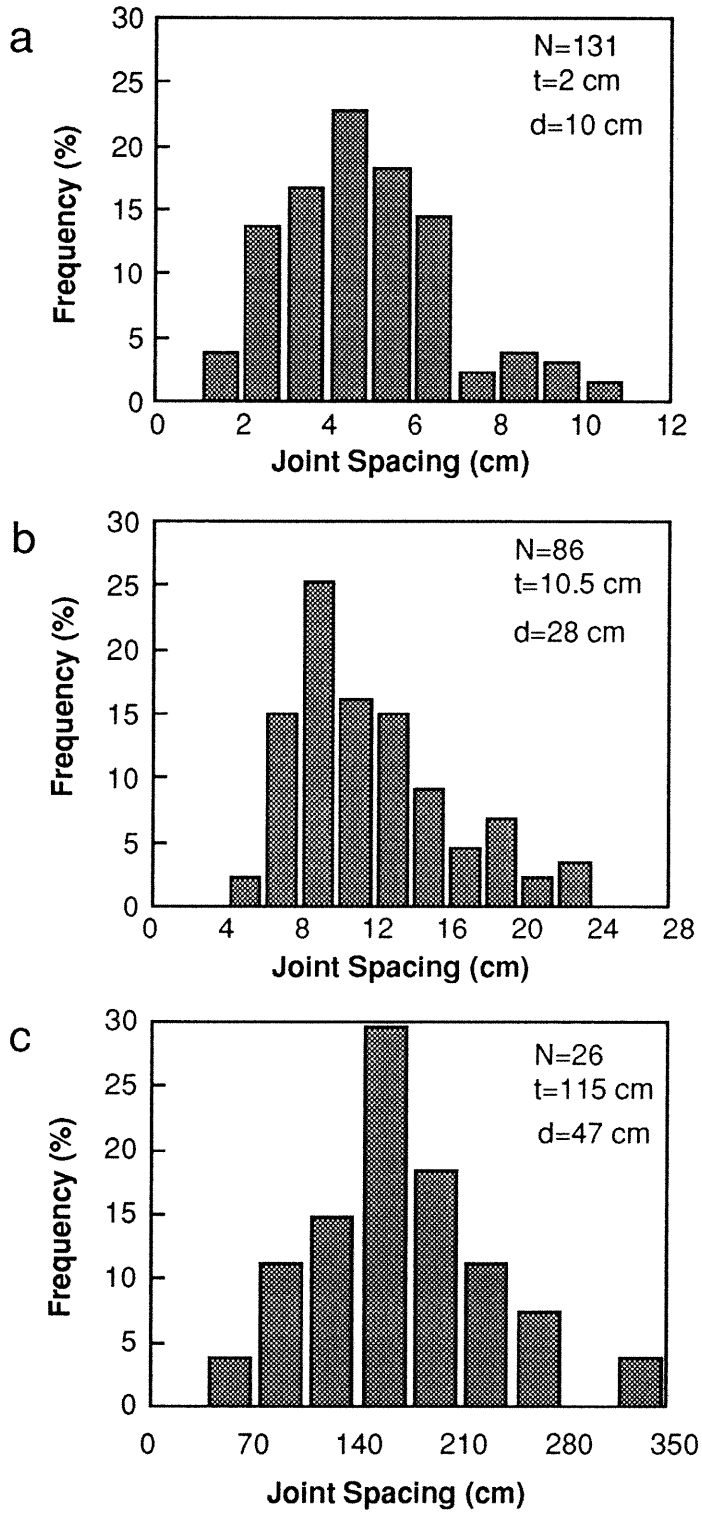

Figure 4.9. Histograms of joint spacing values in three typical sandstone layers at Plage Victor in the Saint-Jean-Port-Joli area of the Quebec Appalachians. N: number of measurements; t: thickness of competent layer; d: thickness of bounding non-jointed layers.

positively skewed frequency distribution (Fig. 4.9b). Similar skewed distributions have been described as gamma distributions (Huang and Angelier, 1989; Gross, 1993; Castaing et al., 1996) or log-normal distributions (Sen and Kazi, 1984; Narr and Suppe, 1991; Rives et al., 1992; Becker and Gross, 1996; Pascal et al., 1997). Huang and Angelier (1989) suggest that the skewed distributions are due to censuring of the minute joints, which do not completely cut the competent layer, during measurements. Their suggestion is based on the fact that there are several different orders of joint-spacings in rocks, of which only the larger orders are visible as joints (e.g., Castaing et al., 1996). Narr and Suppe (1991) and Becker and Gross (1996) propose that such distributions are a direct consequence of stress reduction shadows, which inhibit the formation of new joints in the vicinity of existing joints. Rives et al. (1992) suggest that joint set development is controlled by the spatial distribution of initiation points, the size of the interaction zones, the initiation and propagation criteria of the joint set, and the stage of evolution. The evolution from a negative exponential to a normal distribution through a log-normal distribution corresponds to an increase in the degree of fracture saturation with increasing extension strain. If this is true, the normal distribution of joint spacing observed in this study indicates a state of fracture saturation for the jointed layers. Thus the relationship between joint spacing and bed thickness may provide meaningful insights about the material properties of the rocks because the spacing is not sensitive to the applied strain once fracture saturation has been reached (Wu and Pollard, 1995).

Figure 4.10a shows plots of median joint spacing vs layer thickness for 42 studied sandstone layers. Each point in Fig. 4.10a is the median spacing of 40-250 measurements. The best-fit straight line for these data has a slope equal to 0.83 although there is considerable scatter in the data for beds having a thickness $t > 20$ cm. Such a slope is referred to as the coefficient of joint spacing, K (Ladeira and Price, 1981). Table 4.1 lists the K-values of sandstones reported in the literature (Price, 1966; Angelier et al., 1989; Aydan and Kawamoto, 1990; Narr and Suppe, 1991; Gross, 1993). These K-

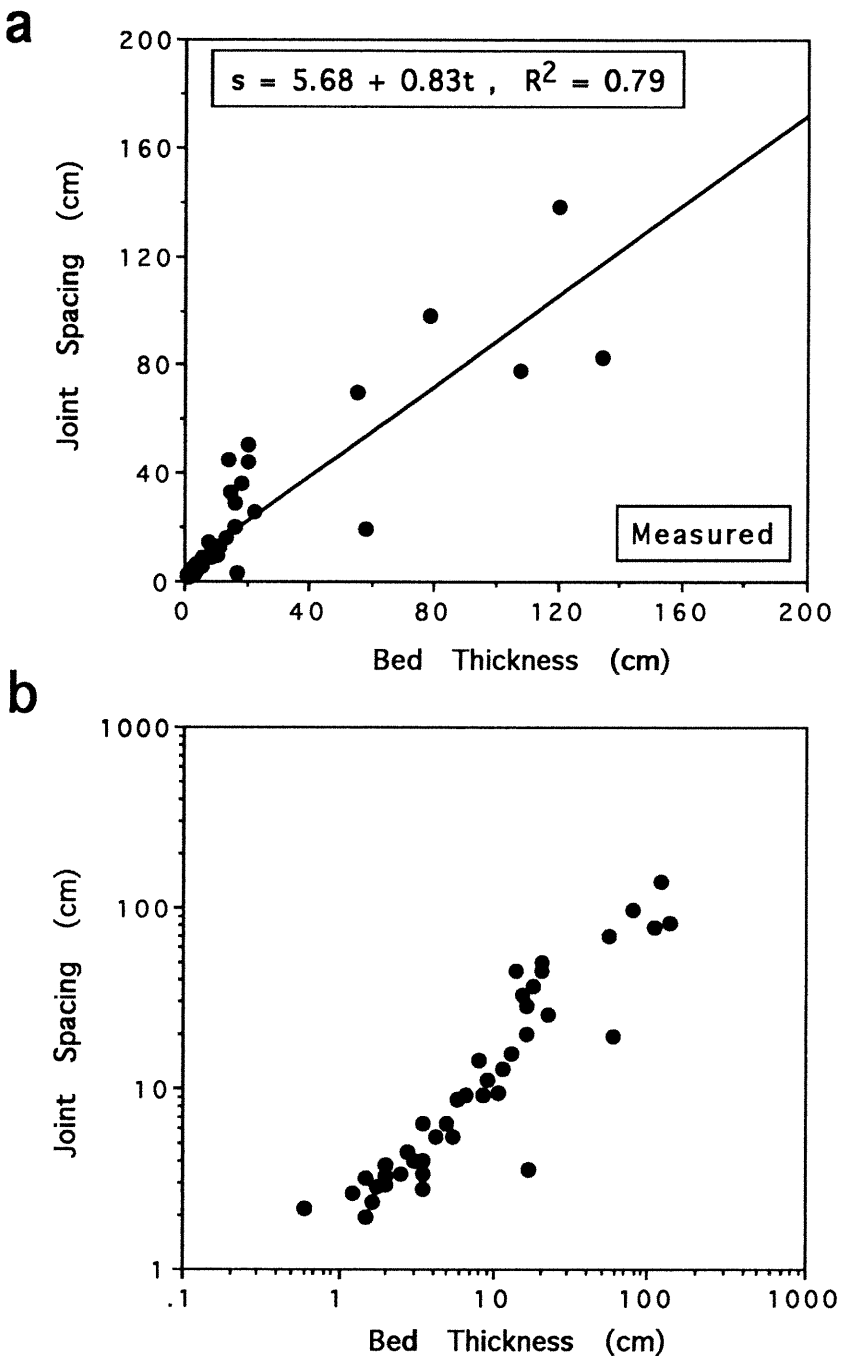

Figure 4.10. Plots of median joint spacing (*s*) vs layer thickness of sandstone, measured at Plage Victor in the Saint-Jean-Port-Joli area of the Quebec Appalachians. (a) The data are represented in a linear scale so that the linear relationship between joint spacing and bed thickness may readily be seen. (b) The data are represented in a logarithmic scale in order to resolve the data near the origin.

Table 4.1. Coefficient of joint spacing (K), defined as the slope of the median joint spacing vs layer thickness regression line, for sandstones.

Lithology	K-value	References
Sandstone	1.27	Aydan and Kawamoto (1990)
Sandstone	1.20	Price (1960)
Porcelanite & Siliceous Shale	0.82	Narr and Suppe (1991)
Sandstone	0.60	Angelier et al. (1989)
Sandstone (Alegria)	0.81	Gross (1993)
Sandstone (Gaviota)	0.79	Gross (1993)
Sandstone	0.83	this study

values vary from 0.60 to 1.27 with a mean value of 0.90. Our measured K-value from Saint-Jean-Port-Joli is close to the mean value for sandstones.

In order to calculate the theoretical joint spacing in the layers from Plage Victor, we need the material constants E_f, E_m, υ_m, and C_0 in addition to the measured t and d values. In the present case, E_f and C_0 are the Young's modulus and tensile fracture strength of sandstone, respectively. For the shale and mudstone, we assume that E_m=16 GPa (Gross et al., 1995) and υ_m=0.25. For sandstone, E_f = 58 GPa, which was obtained by averaging the Young's moduli calculated from P-wave velocity and density measurements on sandstones at 100 MPa reported by Christensen (1989). Because the joints were formed at depth in the crust, the Young's moduli measured at room pressure (Hatheway and Kiersch, 1989) were not used in these calculations. As done by Gross et al. (1995) and Fischer et al. (1995), a fracture saturation strain of 5×10^{-4} was assumed. The decay constant (n) of the shear stress in the matrix is taken to be 3. As shown in Fig. 4.11, a good general similarity between the calculated and measured relationships between s and t is found using C_0 = 20 MPa. If the fracture saturation strain is taken to be 10^{-3}, an unrealistic C_0 value as high as 40 MPa is needed to achieve such a similarity.

4.4. Discussion

As mentioned before, there is a linear relation between M and d, $M = jd$, where j is a constant. Equation (4.25) can be written as

$$s = \eta\sqrt{td} \qquad (4.26)$$

where

$$\eta = \frac{3}{2}\left[j(1+\upsilon_m)\frac{E_f}{E_m}\right]^{1/2} \mathrm{Cosh}^{-1}\left(\frac{E_f\varepsilon}{E_f\varepsilon - C_0}\right) \qquad (4.27).$$

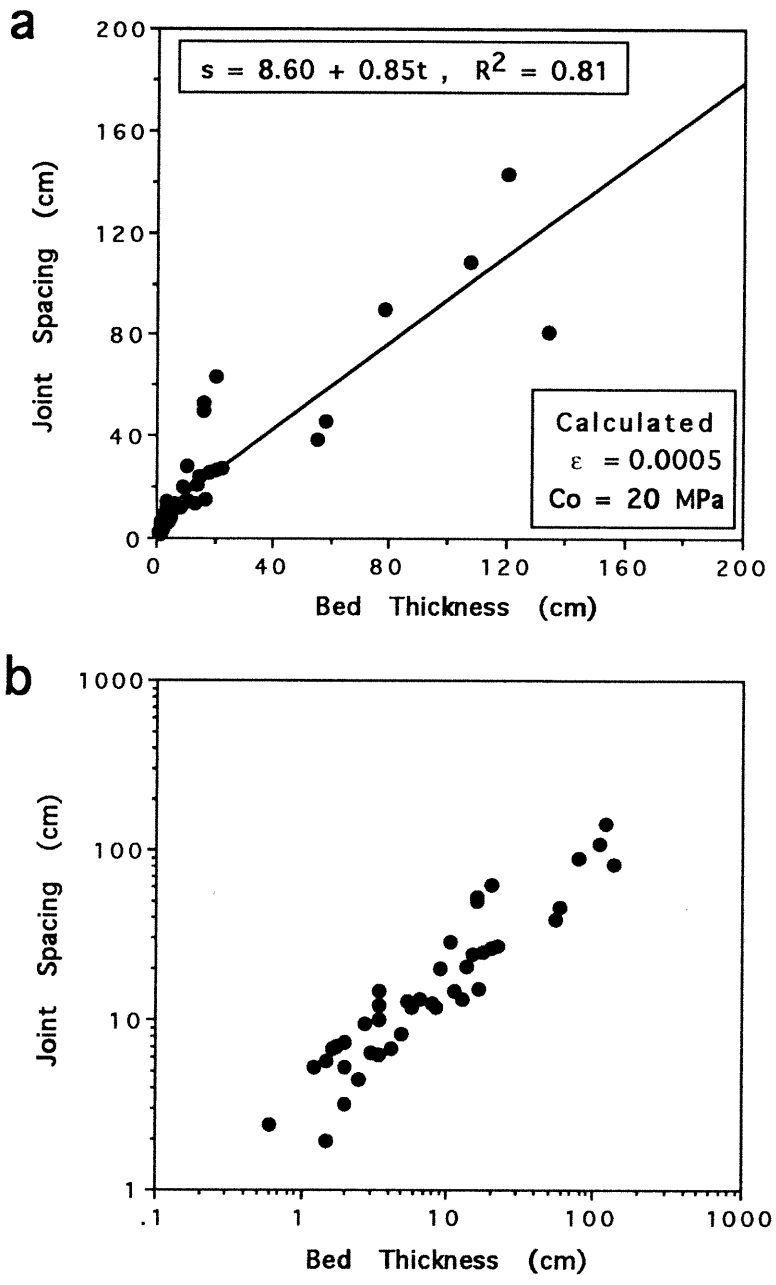

Figure 4.11. Calculated joint spacings according to equation (4.25), using E_f = 58 GPa, E_m = 16 GPa, ν_m = 0.25, $\varepsilon = 5 \times 10^{-4}$, C_0 = 20 MPa, and t-d data from Fig. 4.13. (a) Linear scale. (b) Logarithmic scale.

The constant η depends on both the material properties of rocks and the decay modes of the shear stress in the bounding beds.

Equation (4.26) indicates that the joint spacing depends not only on the jointed layer thickness (t) but also on the non-jointed layer thickness (d). This agrees qualitatively with Ladeira and Price's (1981) field data collected in Carboniferous flysch exposed near Devon and Cornwall (U.K.). They found, for a given thickness of competent layers, that the joint spacing is significantly larger when the adjacent incompetent layers are more than 5 cm thick than when the adjacent layers are thinner than 5 cm (Fig. 4.12). Using finite-element techniques, Fischer et al. (1995) attempted to examine the effects of bounding bed thickness on the size of the stress reduction shadow, and hence joint spacing. They demonstrated that the joint spacing first increases with increasing d/t ratio (from 0.1 to 0.33), but then decreases with increasing d/t ratio (from 0.33 to 0.66). They concluded that the observed variations are nonsystematic and primarily due to inaccuracies in their numerical solution and contouring algorithm.

Equation (4.26) shows that the relationship between joint spacing (s) and bed thickness (t) depends on the relationship between t and d. If the ratio of d to t is constant, the relationship between s and t is linear. That is to say, a linear relationship occurs between s and t when d varies linearly with t. Hobbs (1967) could obtain a linear relationship between s and t simply because he assumed that the shear stress in the matrix extends a distance exactly equal to t in the direction normal to the layer from the interface (i.e. He assumes that $d = 2t$). The well-documented linear relationship between s and t (< 1.0 m) in sedimentary sequences (Price, 1966; McQuillan, 1973; Ladeira and Price, 1981; Aydan and Kawamoto, 1990; Narr and Suppe, 1991) may indicate a statistically linear relationship between the competent bed thickness and the incompetent layer thickness.

In other cases, equation (4.26) predicts a non-linear increase in joint spacing (s) with bed thickness (t). For example, when d is constant or d-t is constant, the joint spacing increases as a function of the square root of the bed thickness, that is, $s \propto \sqrt{t}$.

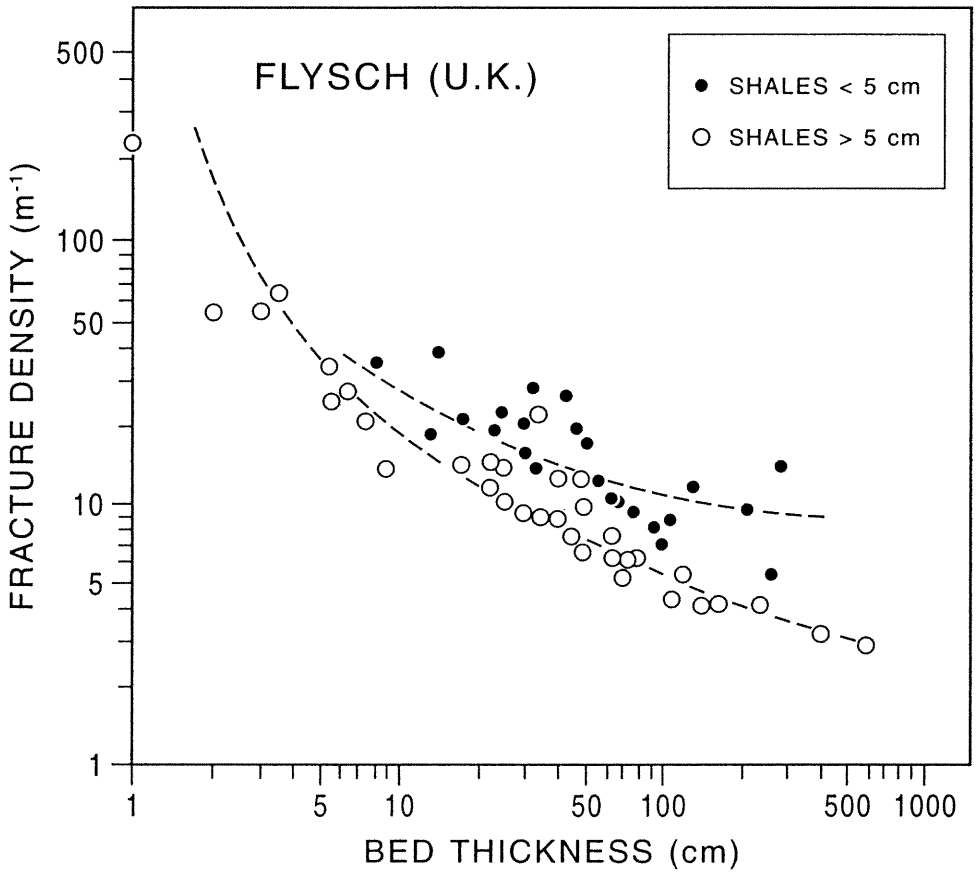

Figure 4.12. Relationship between fracture density and competent bed thickness for different thicknesses of adjacent incompetent layers in the Carboniferous flysch of Devon and Cornwall (U.K.). The fracture density is defined as the number of fractures per meter. The fracture density in the competent layers which adjoin incompetent layers thicker than 5 cm is significantly smaller (for a given thickness of competent layer) than when the adjacent layers are thinner than 5 cm. After Ladeira and Price (1981).

Mandal et al. (1994) carried out a series of experiments using rigid layers of Plaster of Paris with different thicknesses resting on a ductile substratum of pitch with a constant thickness. They observed that the joint spacing is proportional to the square root of the bed thickness. It is noted that there is an important difference between the theoretical model presented above and their experimental model. In the theoretical model, the competent layer is confined and bonded on its top and bottom surfaces to the adjacent incompetent layers. In the model of Mandal et al. (1994), however, the competent layer is bonded only to the incompetent substratum and has a shear-stress-free top surface. In both cases, the competent layer is loaded through shear stresses at the layer-matrix interface. Analysis of equation (4.8) suggests that the different boundary conditions of the two models affect only the η value but the relation $s \propto \sqrt{td}$ is still valid. A doubly-bonded layer should have a smaller η value and accordingly, a smaller joint spacing than a layer with a free top surface. Therefore, the agreement between the theoretical predictions and the experimental results of Mandal et al. (1994) suggests that the non-linear relationship between *s* and *t* documented for beds thicker than 1.0 m (Ladeira and Price, 1981), may be due to the fact that the thickness of the incompetent layers in these sequences does not increase with, and is much less than the thickness of the competent layers.

Similarly, the transition from linear to non-linear relationships with increasing competent bed thickness, reported by Ladeira and Price (1981), may be related to a change in the relationship between *d* and *t* with increasing *t*. Therefore, the relationship between joint spacing and bed thickness cannot be understood without measurements of incompetent layer thickness. Unfortunately, no published field measurement data except those in the present paper are available on *s-t-d* relationships. It is hoped that the present work will encourage systematic measurements of *s*, *t* and *d* in the field.

For the sandstones at Plage Victor, Saint-Jean-Port-Joli, the measured *t-d* relationship is quite complex (Fig. 4.13). Surprisingly, such complex *t-d* variations result in a statistically linear relationship between t and s (Fig. 4.11a).

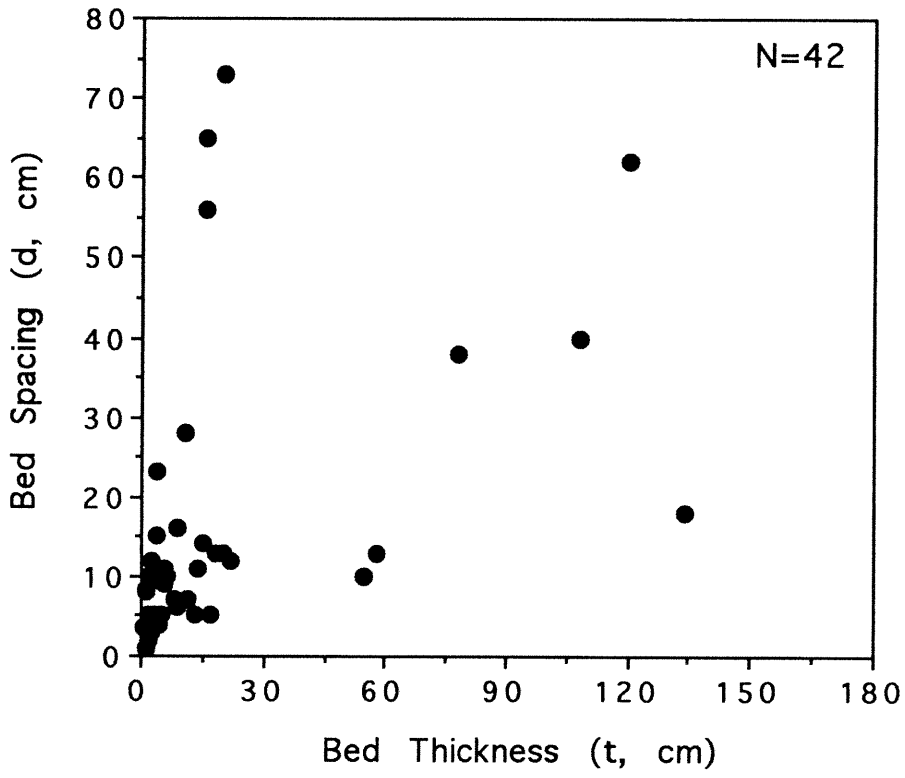

Figure 4.13. Relationship between thicknesses of competent sandstone and of its bounding incompetent shale layers at 42 study sites from Plage Victor in the Saint-Jean-Port-Joli area of the Quebec Appalachians.

It should be kept in mind that the shear-lag model presented above deals with the distribution of joints in sedimentary rocks composed of alternating competent and incompetent beds. Apparently, the model cannot be applied to massive rock units or igneous intrusions where joints were formed by mechanisms which are different from the stress transfer mechanism discussed above. The effects of residual stresses, bending, cooling and unloading should play a major role in building up tensile stresses for the formation of fractures in massive rocks.

It should be noted that there are a number of assumptions in the models presented above, the elimination of which would lead to a better correlation between the model and observation.

(1) Like other previous models (Price, 1966; Hobbs, 1967; Sowers, 1972; Narr and Suppe, 1991; Mandal et al., 1994; Fischer et al., 1995), the mechanical analysis is based on the assumption that there is no slip on the layer/matrix interfaces. Slip between the competent and incompetent layers will take place when the interfacial shear stress reaches the interfacial slip strength (τ_0). As shown by equation (4.20) and Fig. (4.6), the interfacial shear stress varies along the layer length and has a maximum at the ends of the layer and a minimum at the center of the layer. Therefore, the slip will occur over a certain length at each end of the layer. There is no interfacial slip near the center of the layer. The tensile stresses for the slip and non-slip regions should be treated separately (Ji, 1997). The interfacial slip decreases the maximum tensile stress and thus increases the mean joint spacing.

(2) It should also be pointed out that the relationship between joint spacing and bed thickness depends on the actual mode of shear stress decay in the matrix. The actual mode should be studied by well-designed experiments. Moreover, the decay constant (n) in equation (4.14) may also vary with the relative thickness of the bounding layers with respect to the jointed layer.

(3) It has been assumed that the competent layer has a unique tensile strength whereas in a natural sedimentary bed, a fairly wide distribution of strengths is expected (Narr and Suppe, 1991; Rives et al., 1992) along the layer due to the random nature of defects (e.g., nodules, pebbles, pores, minerals and fossils).

(4) The principal limitation to the theory presented in this paper is the assumption that the two incompetent layers bounding the jointed layer are of equal thickness. This arises from the simple form of the equation for mechanical equilibrium [i.e. equation (4.8)]. This assumption is also included in the previous models (Price, 1966; Hobbs, 1967; Narr and Suppe, 1991; Gross et al., 1995; Fischer et al., 1995). In order to remove this limitation, a complex unit-cell must be used but this cannot be treated with the present analytic solution. Nevertheless the present analysis is useful for bedded sedimentary rocks with nearly identical jointed layer spacings. A rigorous elastic analysis is only possible at present using numerical methods, but it may be too tedious to employ for each actual layer measured in the field.

(5) The model is two-dimensional and implicitly assumes that joints are infinite in the third direction. Thus, the interaction between joints in this direction is ignored. The effects of such interactions on the frequency distribution of joint spacing have been discussed in Rives et al. (1992) and Wu and Pollard (1995).

The general trend of the field measurement results can be predicted by the model. It should be emphasized, however, that the prediction is based on the assumptions inherent in the model and on the selection of the material constants (E_f, E_m, υ_m, C_0) and fracture saturation strain (ε) for the rocks. It is believed, however, that the theoretical model presented here will be useful in analyzing the relationship between joint spacing and bed thickness.

4.5. Conclusions

The shear lag model of Hobbs (1967) has been cited as fundamental to the interpretation of the linear relationship between saturated joint spacing (s) and bed thickness (t) in interbedded sedimentary rocks. However, this model is based on an assumption that the shear stress in the bounding non-jointing layers decreases linearly with distance from the interface from a maximum value at the layer/matrix interface to zero at a distance exactly equal to the jointing layer thickness. A revised analytical model is presented which takes into account the non-linear decay of the shear stress and the effects of incompetent bed thickness (d). The model shows that $s = \eta\sqrt{td}$ for competent beds bounded by two incompetent layers nearly identical in thickness. The constant η depends on both the material properties of rocks (i.e. the Young's modulus, tensile strength and fracture saturation strain of the competent bed, and the shear modulus of the incompetent layers) and the decay modes of the shear stress in the bounding layers. If the ratio of d to t is constant, the relationship between s and t is linear. If d is constant, the joint spacing increases as a function of the square root of t. Complex t-d variations observed in Cambrian flysch sediments at Plage Victor in the Saint-Jean-Port-Joli area of the Quebec Appalachians, however, result in a statistically linear relationship between s and t.

REFERENCES

Adams, J., Bell, J.S., 1991. Crustal stressed in Canada, In: Slemmons, D.E., Engdahl, E.R., Zoback, M.D., Blackwell, D.D. (Ed.), Neotectonics of North America, Geological Society of America, Boulder, Colorado, 367-386.

Alexandrov, K.S., Ryzhova, T.V., 1961. The elastic properties of rock-forming minerals II: layered silicates. Izvestiya, Academy of Science, USSR Geophysics Series 9, 1799-1804.

Alexandrov, K.S., Ryzhova, T.V., Belikov, B.P., 1963. The elastic properties of pyroxenes. Soviet Physics Crystallography 8, 738-741.

Alsina, D., Snieder, R., 1994. Small-scale sublithospheric continental mantle deformation: constraints from SKS splitting observations, 2nd International Workshop on Dynamics of the Subcontinental Mantle from Seismic Anisotropy to Mountain Building, La Grande Motte, France.

Ando, M., Ishikawa, Y., Wada, H., 1980. S-wave anisotropy in the upper mantle under a volcanic area in Japan. Nature 268, 43-46.

Ando, M., Ishikawa Y., Yamazaki, F., 1983. Shear wave polarization anisotropy in the upper mantle beneath Honshu, Japan. Journal of Geophysical Research 88, 5850-5864.

Angelier, J., Souffache, B., Barrier, E., Bergerat, F., Bouaziz, S., Bouroz, C., Creuzot, G., Ouali, J., Tricart, P., 1989. Distribution de joints de tension dans un banc rocheux: loi théorique et espacements. Comptes Rendus de l'Academie des Sciences 309, 2119-2125.

Askarpour, V., Manghnani, M.H., Fassbender, S., Yoneda, A., 1993. Elasticity of single-crystal $MgAl_2O_4$ spinel up to 1273 K by Brillouin spectroscopy. Physics and Chemistry of Minerals 19, 511-519.

Ave Lallement, H.G., 1967. Structural and petrofabric analysis of an "Alpine type" peridotite: the lherzolite of the French Pyrenees. Leidse Geol. Meded 42, 1-57.

Aydan, O., Kawamoto, T., 1990. Discontinuities and their effect on rock mass. In: Barton, N., Stephansson, O. (Ed.), Rock Joints, Balkema, Rotterdam, 149-156.

Azor, A., Simancas, J.F., Exposito, I., Lodeiro, F.G., Poyatos, D.J.M., 1997. Deformation of garnets in a low-grade shear zone. Journal of Structural Geology 19, 1137-1148.

Bahat, D., Engelder, T., 1984. Surface morphology on cross-fold joints of the Appalachian plateau, New York and Pennsylvania. Tectonophysics 104, 299-313.

Bakker, R.J., Jansen, J.B.H., 1984. A mechanism for preferential H_2O leakage from fluid inclusions in quartz based on TEM observations. Contributions to Mineralogy and Petrology 116, 7-20.

Bass, J. D., 1995. Elasticity of minerals, glasses, and melts, in Bass, J. D., A.G.U., Washington, 45-63.

Becker, A., Gross, M.R., 1996. Mechanism for joint saturation in mechanically layered rocks - an example from southern Israel. Tectonophysics 257, 223-237.

Bell, T.H., Hickey, K.A., Upton, G.J.G., 1998. Distinguishing and correlating multiple phases of metamorphism across a multiply deformed region using the axes of spiral, staircase and sigmoidal inclusion trails in garnet. Journal of Metamorphic Geology 16, 767-794.

Birch, F., 1960. The velocity of compressional waves in rocks to 10 kilobars. Journal of Geophysical Research 65, 1083-1102.

Bogdonov, A.A., 1947. The intensity of cleavage as related to the thickness of beds. Soviet Geology (in Russian) 16.

Bostock, M.G., Cassidy, J.F., 1995. Variations in SKS splitting across western Canada. Geophysical Research Letters 22, 5-8.

Bostock, M.G., VanDecar, J.C., 1995. Upper mantle structure of the northern Cascadia subduction zone. Canadian Journal of Earth Sciences 32, 1-12.

Boullier, A.-M., 1999. Fluid inclusions: tectonic indicators. Journal of Structural Geology 1229-1235.

Boullier, A.M., Nicolas, A., 1975. Classification of textures and fabrics of peridotite xenoliths from South African kimberlites, Physics and Chemistry of the Earth, 9, 467-475.

Boullier, A.-M., Michot, G., Pecher, A., Barres, O., 1989. Diffusion and/or plastic deformation around fluid inclusions in synthetic quartz: new investigations. In: Bridgwater, D., (Ed.), Fluid Movements - Element Transport and the composition of the Deep Crust, Kluwer Academic Publishers, 345-360.

Boullier, A.-M., France-Lanord, C., Dubessy, J., Adamy, J., Champenois, M., 1991. Linked fluid and tectonic evolution in the High Himalaya mountains (Nepal). Contributions to Mineralogy and Petrology 107, 358-372.

Boullier, A.-M., Firdaous, K., Boudier, F., 1997. Fluid inclusion related to deformation in the Zabargad gneisses (Red Sea rift). Tectonophysics 279, 281-302.

Brace, W.F., Bombolakis, E.G., 1963. A note on brittle crack growth in compression. Journal of Geophysical Research 68, 3709-3713.

Brantley, S.L., 1992. The effect of fluid chemistry on quartz microcrack lifetimes. Earth

and Planetary Science Letters 113, 145-156.

Brearley, M., Scarfe, C.M., Fujii, T., 1984. The petrology of ultramafic xenoliths from Summit Lake, near Prince George, British Columbia. Contributions to Mineralogy and Petrology 88, 53-63.

Brey, G.P., Köhler, T., 1990. Geothermobarometry in four-phase lherzolites II. New thermobarometers, and practical assessment of existing thermobarometers. Journal of Petrology 31, 1353-1378.

Bruner, W. M., 1984. Crack growth during unroofing of crustal rocks: effects on thermoelastic behavior and near-surface stresses. Journal of Geophysical Research 89, 107-118.

Burianyk, M.J.A., Kanasewich, E.R., 1995. Crustal velocity structure of the Omineca and Intermontane Belts, southern Canadian Cordillera. Journal of Geophysical Research 100, 15303-15316.

Burianyk, M.J.A., Kanasewich, E.R., 1997. Upper mantle structure in the southern Canadian Cordillera. Geophysical Research Letters 24, 739-742.

Cameron, M., Sueno, S., Prewitt, C.T., Papike, J.J., 1973. High-temperature crystal chemistry of acmite, diopside, hedenbergite, jadeite, spodumene, and ureyite. American Mineralogist 58, 594-618.

Campbell, R.B., 1978. Quesnel Lake map-area. Geological Survey of Canada O.F., 574.

Caputo, R., 1995. Evolution of orthogonal sets of coeval extension joints. Terra Nova 7, 479-490.

Carlson, W., Denison, C., 1992. Mechanisms of porphyroblast crystallization: results from high-resolution computed X-ray tomography. Science 257, 1236-1239.

Carter, N.L., Ave Lallement, H.G., 1970. High temperature flow of dunite and peridotite. Geological Society of America Bulletin 81, 2181-2202.

Cassidy, J.F., Bostock, M.G., 1996. Shear-wave splitting above the subducting Juan de Fuca plate. Geophysical Research Letters 23, 941-944.

Castaing, C., Halawani, M.A., Gervais, F., Chilès, J.P., Genter, A., Bourgine, B., Ouillon, G., Brosse, J.M., Martin, P., Genna, A., Janjou, D., 1996. Scaling relationships in intraplate fracture systems related to Red Sea rifting. Tectonophysics 261, 291-314.

Chastel, Y.B., Dawson, P.R., Wenk, H.-R., Bennett, K., 1993. Anisotropic convection with implications for the upper mantle. Journal of Geophysical Research 98, 17757-17771.

Chopin, C., 1984. Coesite and pure pyrope in high-grade blueschists of the western

Alps: a first record and some consequences. Contributions to Mineralogy and Petrology 86, 4167-4184.

Christensen, N.I., 1971. Shear wave propagation in rocks. Nature 229, 549-550.

Christensen, N.I., 1989. Seismic velocities. In: Carmichael, R.S. (Ed.), Practical Handbook of Physical Properties of Rocks and Minerals, CRC Press, Boca Raton, Florida, 429-546.

Christensen, N.I., Lundquist, S.M., 1982. Pyroxene orientation within the upper mantle. Geological Society of America Bulletin 93, 279-288.

Christensen, N.I., Salisbury, M.H., 1979. Seismic anisotropy in the oceanic upper mantle: Evidence from the Bay of Islands ophiolite complex. Journal of Geophysical Research 84, 4601-4610.

Christensen, N. I., Shaw, G., 1970. Elasticity of mafic rocks from the middle Atlantic Ridge. Geophysics Journal 20, 271-284.

Cleveland, J.J., Bradt, R.C., 1978. Grain size/microcracking relations for pseudobrookite oxides. Journal of the American Ceramics Society 61, 478-481.

Clowes, R.M., Cook, F.A., Green, A.G., Keen, C.E., Ludden, J.N., Percival, J.A., Quinlan, G.M., West, G.F., 1992. Lithoprobe: New perspectives on crustal evolution. Canadian Journal of Earth Sciences 29, 1813-1864.

Clowes, R.M., Zeit, C.A., Amor, J.R., Ellis, R.M., 1995. Lithospheric structure in the southern Canadian Cordillera from a network of seismic refraction lines. Canadian Journal of Earth Sciences 32, 1485-1513.

Clyne, T.W., Withers, P.J., 1993. An introduction to metal matrix composites, Cambridge University Press, New York.

Cobbold, P.R., 1979. Origin of periodicity: saturation or propagation? Journal of Structural Geology 1, 96.

Cox, H.L., 1952. The elasticity and strength of paper and other fibrous materials. British Journal of Applied Physics 3, 72-79.

Creaser, B., Spence, G., 1999. Crustal seismic velocity structure of the northern Cordillera, southern Yukon Territory - Lithoprobe SNORE line 31. LITHOPROBE Report No. 69, 163-167.

Crosson, R.S., Lin, J.W., 1971. Voigt and Reuss prediction of anisotropic elasticity of olivine. Journal of Geophysical Research 76, 570-578.

Dawson, P.R., Wenk, H.-R., in press. Texturing of the upper mantle during convection. Philosophy Magazine.

DeMets, C., Gordon, R.G., Argus, D.F., Stein, S., 1990. Current plate motions.

Geophysics Journal International 101, 425-478.

Denison, C., Carlson, W.D., Ketcham, R.A., 1997. Three-dimensional quantitative textural analysis of metamorphic rocks using high-resolution computed X-ray tomography: Part I. Methods and techniques. Journal of Metamorphic Geology 15, 29-44.

Doig, R., 1991. U-Pb zircon data of Morin anorthosite suite rocks, Grenville Province, Quebec. Journal of Geology 99, 729-738.

Dow, N.F., 1961. General Electric Co., Space Mechanics Memo No. 102, May, 1961, Philadelphia, Pennsylvania.

Drucker, D.C., 1965. Engineering and continuum aspects of high-strength materials, in Drucker, D. C., Wiley, New York, 795-833.

Duffy, T.S., Vaughan, M.T., 1988. Elasticity of enstatite and its relationship to crystal structure. Journal of Geophysical Research 93, 383-391.

Dunand, D.C., Mortensen, A., 1991. Dislocation emission at fibers I. Theory of longitudinal punching by thermal stresses. Acta Metallurgica et Materialia 39, 1405-1416.

Elvevold, S., Reginiussen, H., Krogh, E.J., Bjorklund, F., 1994. Reworking of deep-seated gabbros and associated contact metamorphosed paragneisses in the south-eastern part of the Seiland Igneous Province, Northern Norway. Journal of Metamorphic Geology 12, 539-556.

Engelder, T., 1993. Stress Regimes in the Lithosphere. Princeton University Press, Princeton, New Jersey.

Eshelby, J.D., 1957. The determination of the elastic field of an ellipsoidal inclusion, and related problems. Proceeding of the Royal Society of London A241, 376-396.

Eshelby, J.D., 1959. The elastic field outside an ellipsoidal inclusion. Proceeding of the Royal Society of London A252, 561-569.

Estey, L., Douglas, B., 1986. Upper mantle anisotropy: a preliminary model. Journal of Geophysical Research 91, 11393-11406.

Evans, A.G., 1978. Microfracture from thermal expansion anisotropy I. Single phase systems. Acta Metallurgica 26, 1845-1853.

Fei, Y., 1995. Thermal expansion, in Fei, Y., American Geophysical Union, Washington D.C., 29-44.

Ferguson, C.C., 1987. Fracture and separation histories of stretched belemnites and other rigid-brittle inclusions in tectonites. Tectonophysics 139, 255-273.

Ferguson, C.C., Lloyd, G.E., 1982. Paleostress and strain estimates from boudinage structure and their bearing on the evolution of a major Variscan fold-thrust complex in southwest England. Tectonophysics 88, 269-289.

Fischer, K.M., Wiens, D.A., 1996. The depth distribution of mantle anisotropy beneath the Tonga subduction zone. Earth and Planetary Science Letters 142, 253-260.

Fischer, M.P., Gross, M.R., Engelder, T., Greenfield, R.J., 1995. Finite-element analysis of the stress distribution around a pressurized crack in a layered elastic medium: implications for the spacing of fluid-driven joints in bedded sedimentary rock. Tectonophysics 247, 49-64.

Fliervoet, T.F., White, S.H., 1995. Quartz deformation in a very fine grained quartzo-feldspathic mylonite: a lack of evidence for dominant grain boundary sliding deformation. Journal of Structural Geology 17, 1095-1109.

Fouch, M.J., Fischer, K.M., 1996. Mantle anisotropy beneath northwest Pacific subduction zones. Journal of Geophysical Research 101, 15987-16002.

Francis, D., 1987. Mantle-melt interaction recorded in spinel lherzolite xenoliths from the Alligator Lake volcanic complex, Yukon, Canada. Journal of Petrology 28, 569-597.

Frederiksen, A.W., Bostock, M.G., VanDecar, J.C., Cassidy, J.F., 1998. Seismic structure of the upper mantle beneath the northern Canadian Cordillera from teleseismic travel-time inversion. Tectonophysics 294, 43-55.

Fredrich, J.T., Wong, T., 1986. Micromechanics of thermally induced cracking in three crustal rocks. Journal of Geophysical Research 91, 12743-12764.

Friedman, M., Logan, J.M., 1970. Microscopic feather fractures. Bulletin of geological Society of America 81, 3417-3420.

Friedman, R.M., Martignole, J., 1995. Mesoproterozoic sedimentation, magmatism and metamorphism in the southern part of the Grenville Province (western Quebec): U-Pb geochronological constraints. Canadian Journal of Earth Sciences 32, 2103-2114.

Frisillo, A.L., Barsch, G.R., 1972. Measurements of single-crystal elastic constants of bronzite as a function of pressure and temperature. Journal of Geophysical Research 77, 6360-6384.

Frisillo, A.L., Buljan, S.T., 1972. Linear thermal expansion coefficients of orthopyroxene to 1000 °C. Journal of Geophysical Research 77, 7115-7117.

Fujii, T., Scarfe, C.M., 1982. Petrology of Ultramafic Nodules from West Kettle River, near Kelowna, Southern British Columbia. Contributions to Mineralogy and Petrology 80, 297-306.

Gabrielse, H., Yorath, C.J., 1989. The Cordilleran Orogen in Canada. Geoscience Canada 16, 67-83.

Gabrielse, H., Monger, J.W.H., Wheeler, J.O., Yorath, C.J., 1991. Tectonic framework. Part A. Morphogeological belts, tectonic assemblages and terranes. In Gabrielse, H., Yorath, C.J. (Ed.), Geology of the Cordilleran Orogen in Canada, Geological Survey of Canada, Geology of Canada, 4, 15-28.

Gabrielse, H., 1991. Structural styles, Chapter 17. In Gabrielse, H., Yorath, C.J. (Ed.), Geology of the Cordilleran Orogen in Canada, Geological Survey of Canada, Geology of Canada, 4, 571-675.

Garrett, K.W. and Bailey, J.E., 1977. Multiple transverse fracture in 90° cross-ply laminates of a glass fiber-reinforced polyester. Journal of Materials Science 12, 157-168.

Geldhill, K., Gubbins, D., 1996. SKS splitting and the seismic anisotropy of the mantle beneath the Hikurangi subduction zone, New Zealand. Physics of the Earth and Planetary Interiors 95, 227-236.

Gillet, P., Ingrin, J., Chopin, C., 1984. Coesite in subducted continental crust: P-T history deduced from an elastic model. Earth and Planetary Science Letters 70, 426-436.

Glassley, W.E., 1983. The role of CO_2 in the chemical modification of deep continental crust. Geochimica et Cosmochimica Acta 47, 597-616.

Gledhill, K., Stuart, G., 1996. Seismic anisotropy in the fore-arc region of the Hikurangi subduction zone, New Zealand. Physics of the Earth and Planetary Interiors 95, 211-225.

Godbout, J., 1967. Salut Galarneau! Edition du Seuil.

Gough, D.I., 1984. Mantle upflow under North America and plate dynamics. Nature 311, 428-433.

Gratier, J.P., Jenatton, L., 1984. Deformation by solution-deposition, and re-equilibration of fluid inclusions in crystal depending on temperature, internal pressure and stress. Journal of Structural Geology 6, 189-200.

Green, D.H., Hibberson, W., 1970. The instability of plagioclase in peridotite at high pressure. Lithos 3, 209-221.

Gross, M.R., 1993. The origin and spacing of cross joints: examples from the Monterey Formation, Santa Barbara Coastline, California. Journal of Structural Geology 15, 737-751.

Gross, M.R., Fischer, M.P., Engelder, T., Greenfield, R.J., 1995. Factors controlling joint spacing in interbedded sedimentary rocks: integrating numerical models with

field observations from the Monterey Formation, USA. In: Ameen, M.S. (Ed.), Fractography: Fracture Topography as a Tool in Fracture Mechanics and Stress Analysis, Geological Society, London, Special Publication 92, 215-253.

Hames, W.E., Menard, T., 1993. Fluid-assisted modification of garnet composition along rims, cracks, and mineral inclusion boundaries in samples of amphibolite facies schists. American Mineralogist 78, 338-344.

Hanmer, S.K., Ciesielski, A., 1984. A structural reconnaissance of the northwest boundary of the central metasedimentary belt, Grenville Province, Ontario and Quebec. Geological Survey of Canada, Ottawa.

Hannula, K.A., Lackey, J.S., Mattox, E., Mcgrath, G., Onasch, E., Wertheim, J., 1999. Syn-tectonic pluton intrusion during contractional deformation: microstructural and metamorphic evidence from the aureole of the Acadian Victory Pluton, north-eastern Vermont, USA. Journal of Metamorphic Geology 17, 271-286.

Hatheway, A.W., Kiersch, G.A., 1989. Engineering properties of Rock. In: Carmichael, R.S. (Ed.), Practical Handbook of Physical Properties of Rocks, CRC Press, Boca Raton, Florida, 671-715.

Haxby, W.F., Turcotte, D.L., 1976. Stresses induced by the addition or removal of overburden and associated thermal effects. Geology 4, 181-184.

Hearmon, R.F.S., 1956. The elastic constants of anisotropic materials II. Advances Physics 5, 323-382.

Hearmon, R.F.S., 1979. The elastic constants of crystals and other anisotropic materials. In: Hellwege, K.H., Hellwege, A.M. (Ed.), Landolt-Börnstein Tables III/11, Springer-Verlag, Berlin, 1-244.

Herms, P., Schenk, V., 1992. Fluid inclusions in granulite-facies metapelites of Hercynian ancient lower crust of the Serre, Calabria, Southern Italy. Contributions to Mineralogy and Petrology 112, 393-404.

Hill, L., 1952. The elastic behavior of a crystalline aggregate. Proceeding Physical Society of London A65, 349-354.

Hippertt, J.F.M., 1993. 'V'-pull-apart microstructures: a new shear sense indicator. Journal of Structural Geology 15, 1393-1403.

Hiramatsu, Y., Ando, M., 1996. Seismic anisotropy near source region in subduction zones around Japan. Physics of the Earth and Planetary Interiors 95, 237-250.

Hobbs, D.W., 1967. The formation of tension joints in sedimentary rocks: an explanation. Geological Magazine 104, 550-556.

Holister, G.S., Thomas, C., 1966. Fiber Reinforced Materials, Elsevier, New York.

Holmes, A., 1965. Principle of Physical Geology, Thomas Nelson and Sons LTD, London.

Holzhausen, G.R., Johnson, A.M., 1979. The concept of residual stress in rock. Tectonophysics 58, 237-267.

Huang, Q., Angelier, J., 1989. Fracture spacing and its relation to be thickness. Geological Magazine 126, 355-362.

Hubert, C., 1967. Tectonics of part of the Sillery Formation in the Chaudiere-Matapedia segment of the Quebec Appalachians. Royal Society of Canada Special Publication 10, 33-41.

Hubert, C., 1969. Guidebook-Flysch Sedimentology in the Appalachians. The Geological Association of Canada and The Mineralogical Association of Canada, Montreal.

Hurai, V., Horn, E.-E., 1992. A boundary layer-induced immiscibility in naturally re-equilibrated H_2O-CO_2-NaCl inclusions from metamorphic quartz (Western Carpathians, Czechoslovakia). Contributions to Mineralogy and Petrology 112, 414-427.

Hyndman, R.D., Lewis, T.J., 1999. Geophysical consequences of the Cordillera-Craton thermal transition in southern Canada. Tectonophysics 306, 397-422.

Hynes, A., 1994. Gravity, flexure, and the deep structure of the Grenville Front, eastern Quebec and Labrado. Canadian Journal of Earth Sciences 31, 1002-1011.

Hynes, A. and Eaton, D., 1998. Lateral ramps as an aid to the unroofing of deep crustal rocks: seismic evidence from the Grenville province. Tectonics 18, 343-360.

Hynes, A., Snyder, D.B., 1995. Deep-crustal mineral assemblages and potential for crustal rocks below the Moho in the Scottish Caledonides. Geophysical Journal International, 123, 923-339.

Iidaka, T., Obara, K., 1995. Shear-wave polarization anisotropy in the mantle wedge above the subducting Pacific plate. Tectonophysics 249, 53-68.

Indares, A.M., Martignole, J., 1990. Metamorphic constraints on the tectonic evolution of the allochthonous monocyclic belt of the Grenville Province, western Quebec. Canadian Journal of Earth Sciences 27, 371-386.

Indares, A., 1995. Metamorphic interpretation of high-pressure-temperature metapelites with preserved growth zoning in garnet, eastern Grenville Province, Canadian Shield. Journal of Metamorphic Geology 13, 475-486.

Ismail, W.B., Mainprice, D., 1998. An olivine fabrics database: an overview of upper mantle fabrics and seismic anisotropy. Tectonophysics 296, 145-157.

Jackson, E.D., 1969. Chemical variation in coexisting chromite and olivine in the chromite zones of the Stillwater Complex. Symposium on Magmatic Ore Deposits, Economic Geology Monograph 4, 41-71.

Jackson, M.D., Ohnenstetter, M., 1981. Peridotite and gabbroic structures in the Monte Maggiore Massif, Alpine Corsica. Journal of Geology 89, 703-719.

Jahankhani, H., Galiotis, C., 1991. Interfacial shear stress distribution in model composites, Part 1: A Kevlar 49 fiber in an epoxy matrix. Journal of Composite Materials 25, 609-631.

Ji, S., 1997. Fracturing of garnet crystals in anisotropic metamorphic rocks during uplifts: Discussion. Journal of Structural Geology 19, 1432-1435.

Ji, S., Martignole, J., 1994. Ductility of garnet as an indicator of extremely high temperature deformation. Journal of Structural Geology 16, 985-996.

Ji, S., Salisbury, M., 1993. Shear-wave velocities, anisotropy and splitting in high-grade mylonites. Tectonophysics 221, 453-473.

Ji, S., Saruwatari, K., 1998. A revised model for the relationship between joint spacing and layer thickness. Journal of Structural Geology 20, 1495-1508.

Ji, S., P. Zhao, 1994. Strength of two-phase rocks: a model based on fiber-loading theory. Journal of Structural Geology 16, 253-262.

Ji, S., P. Zhao, 1993. Location of tensile fracture within rigid-brittle inclusions in ductilely flowing matrix. Tectonophysics 220, 23-31.

Ji, S., M. H. Salisbury and S. Hanmer, 1993. Petrofabric, P-wave anisotropy and seismic reflectivity of high-grade tectonites. Tectonophysics 222, 195-226.

Ji, S., Zhao, X., Francis, D., 1994. Calibration of shear-wave splitting in the subcontinental upper mantle beneath active orogenic belts using ultramafic xenoliths from the Canadian Cordillera and Alaska. Tectonophysics 239, 1-27.

Ji, S., Zhao, P., Saruwatari, K., 1997. Fracturing of garnet crystals in anisotropic metamorphic rocks during uplifts. Journal of Structural Geology 19, 603-620.

Ji, S., Long, C., Martignole, J., Salisbury, M., 1997. Seismic reflectivity of a finely layered, granulite-facies ductile shear zone in the southern Grenville Province (Quebec). Tectonophysics 279, 113-133.

Ji, S., Zhu, Z.M., Wang, Z.C., 1998. Effects of interfacial slip on the relationship between joint spacing and bed thickness. Geological Magazine 135, 637-655.

Jiang, D., 1997. Fracturing of garnet crystals in anisotropic metamorphic rocks during uplifts: Discussion. Journal of Structural Geology 19, 1429-1431.

Kanasewich, E.R., Burianyk, M.J.A., Ellis, R.M., Clowes, R.M., White, D.T., Cote, T.,

Forsyth, D.A. Luetgert, J.H., Spence, G.D., 1994. Crustal velocity structure of the Omineca belt, southern Canadian Cordillera. Journal of Geophysical Research 99, 2653-2670.

Kaneshima, S., 1990. Origin of crustal anisotropy: shear wave splitting studies in Japan. Journal of Geophysical Research 95, 11121-11133.

Kaneshima, S., Silver, P.G., 1995. Anisotropic loci in the mantle beneath central Peru. Physics of the Earth and Planetary Interiors 88, 257-272.

Karato, S.-I., 1992. On the Lehmann discontinuity. Geophysical Research Letters 19, 2255-2258.

Karato, S.-I., Li, P., 1992. Diffusive creep in perovskite: Implications for the rheology of the lower mantle. Science 255, 1238-1240.

Karato, S., Wu, P., 1993. Rheology of the upper mantle: a synthesis. Science 260, 771-778.

Karato, S., Paterson, M.S., FitzGerald, J.D., 1986. Rheology of synthetic olivine aggregates: influence of grain-size and water. Journal of Geophysical Research 91, 8151-8176.

Kelly, A., Street, K.N., 1972. Creep of discontinuous fiber composites: II. Theory for the steady-state. Proceedings of the Royal Society of London A328, 283-293.

Kelly, A., Macmillan, N.H., 1986. Strong Solids, Oxford Science Publications, London.

Kern, H., 1993. P- and S-wave anisotropy and shear-wave splitting at pressure and temperature in possible mantle rocks at their relation to the rock fabric. Physics of the Earth and Planetary Interiors 78, 245-256.

Kern, H. W., H.-R., 1985. Anisotropy in rocks and the geological significance, in Kern, H. W., H.-R., Academic Press, New York, 537-555.

Kern, H., Wenk, H.-R., 1990. Fabric-related velocity anisotropy and shear wave splitting in rocks from Santa Rosa mylonites zone, California. Journal of Geophysical Research 95, 11213-11223.

Kern, H., Burlini, L., Ashchepkov, I.V., 1996. Fabric-related seismic anisotropy in upper-mantle xenoliths: evidence from measurements and calculations. Physics of the Earth and Planetary Interiors 95, 195-209.

Kerrick, D.M., Jacobs, G.K., 1981. A modified Redlich-Kwong equation for H_2O, CO_2 and H_2O-CO_2 mixtures at elevated pressures and temperatures. American Journal of Science 281, 735-767.

Klipeel, Y.L., He, M.Y., McMeeking, R.M., Evans, A.G., Mehrabian, R., 1990. The processing and mechanical behavior of an aluminum matrix composite reinforced with short fibers. Acta Metallurgica et Materialia 38, 1063-1074.

Kowallis, B.J., Wang, H.F., Jang, B., 1987. Healed microcracks orientations in granite from Illinois borehole UHP-3 and their relationship to the rock's stress history. Tectonophysics 135, 297-306.

Krantz, R., 1983. Microcracks in rocks: a review. Tectonophysics 100, 449-480.

Kraus, J., Williams, P.F., 1998. Relationships between foliation development, porpyroblasts growth and large-scale folding in a metaturbidite suite, Snow Lake, Canada. Journal of Structural Geology 20, 61-76.

Kreulen, R., Schuiling, R.D., 1982. N_2-CH_4-CO_2 fluids during formation of the Dome de L'Agout, France. Geochimica et Cosmochimica Acta 46, 193-203.

Kumazawa, M., 1969. The elastic constants of single-crystal orthopyroxene. Journal of Geophysical Research 74, 5973-5980.

Kumazawa, M., Anderson, O.L., 1969. Elastic moduli, pressure derivatives, and temperature derivatives of single-crystal olivine and single-crystal forsterite. Journal of Geophysical Research 74, 5961-5972.

Kushiro, I., Yoder, H.S., Mysen, B.O., 1976. Viscosities of basalt and andesite melts at high pressures. Journal of Geophysical Research 81, 6351-6356.

Lachenbruch, A.H., 1961. Depth and spacing of tension cracks. Journal of Geophysical Research 66, 4273-4292.

Ladeira, F.L., Price, N.J., 1981. Relationship between fracture spacing and bed thickness. Journal of Structural Geology 3, 179-183.

Lamb, W.M., Valley, J.W., Brown, P.E., 1987. Post metamorphic CO_2-rich fluid inclusions in granulites. Contributions to Mineralogy and Petrology 96, 485-495.

Lamb, W.M., Brown, P.E., Valley, J.W., 1991. Fluid inclusions in Adirondack granulites: implications for the retrograde P-T path. Contributions to Mineralogy and Petrology 107, 472-483.

Laubach, S.E., 1989. Paleostress directions from the preferred orientation of closed microfractures (fluid-inclusion planes) in sandstone, East Texas basin, U.S.A. Journal of Structural Geology 11, 603-611.

Lawn, B., 1993. Fracture of Brittle Solids, Cambridge University Press, Cambridge.

Lee, J.K.W., Tromp, J., 1995. Self-induced fracture generation in zircon. Journal of Geophysical Research 100, 17753-17770.

Lespinasse, M., 1999. Are fluid inclusion planes useful in structural geology? Journal of Structural Geology 21, 1237-1243.

Lespinasse, M., Pecher, A., 1986. Microfracturing and regional stress field: a study of the preferred orientations of fluid-inclusion planes in a granite from the Massif

Central, France. Journal of Structural Geology 8, 169-180.

Levien, L., Weidner, D.J., Prewitt, C.T., 1979. Elasticity of diopside. Physics and Chemistry of Minerals 4, 105-113.

Lewis, T.J., Bentkowski, W.H., Davis, E.E., Hyndman, R.D., Souther, J.G., Wright, J.A., 1988. Subduction of the Juan de Fuca plate: thermal consequences. Journal of Geophysical Research 93, 15207-15225.

Lewis, T.J., 1991. Heat flux in the Canadian Cordillera. In: Slemmons, D.B., Engdahl, E.R., Zoback, M.D., Blackwell, D.D. (Ed.), Neotectonics of North America, Geological Society of America, Boulder, 445-456.

Lewis, T.J., Bentkowski, W.H., Hyndman, R.D., 1992. Crustal temperatures near the Lithoprobe Southern Canadian Cordillera Transect. Canadian Journal of Earth Sciences 29, 1197-1214.

Li, C., Ellyin, F., 1995. Short crack growth behavior in a particulate-reinforced aluminum alloy composite. Metallugical and Materials Transactions A26, 3177-3182.

Littlejohn, A.L., Greenwood, H.J., 1974. Lherzolite nodules in basalts from British Columbia, Canada. Canadian Journal of Earth Sciences 11, 1288-1308.

Lloyd, D., 1991. Aspects of particle fracture in particulate reinforced MMCs. Acta Metallurgica et Materialia 39, 59-72.

Lloyd, G.E., Knipe, R.J., 1992. Deformation mechanisms accommodating faulting of quartzite under upper crustal conditions. Journal of Structural Geology 14, 127-143.

Lloyd, G.E., Ferguson, C.C., Reading, K., 1982. A stress-transfer model for the development of extension fracture boudinage. Journal of Structural Geology 4, 355-372.

Long, C., Christensen, N.I., in press. Seismic anisotropy of South African upper mantle xenoliths. Earth and Planetary Science Letters.

Lowe, C., Cassidy, J.F., 1995. Geophysical evidence for crustal thickness variations between the Denali and Tintina Fault Systems in west-central Yukon. Tectonics 14, 909-917.

Mainprice, D., 1990. A FORTRAN program to calculate seismic anisotropy from the lattice preferred orientation of minerals. Computer Geosciences 16, 385-393.

Mainprice, D., Silver, P.G., 1993. Interpretation of SKS-waves using samples from the subcontinental lithosphere. Physics of the Earth and Planetary Interiors 78, 257-280.

Mandal, N., Deb, S.K., Khan, D., 1994. Evidence for a non-linear relationship between fracture spacing and layer thickness. Journal of Structural Geology 16, 1275-1281.

Mareschal, J.C., Pinet, C., Gariépy, C., Jaupart, C., Bienfait, G., Dalla Colletta, G., Jolivet, J., Lapointe, R., 1989. New heat flow density and radiogenic heat production data in the Canadian Shield and the Quebec Appalachians. Canadian Journal of Earth Sciences 26, 845-852.

Mareschal, J.C., Jaupart, C., Gariépy, C., Cheng, L.Z., Guillou-Frottier, L., Bienfait, G., Lapointe, R., 2000. Heat flow and deep thermal structure near the edge of the Canadian Shield. Canadian Journal of Earth Sciences, in press.

Mareschal, J.C., Jaupart, C., Cheng, L.Z., Rolandone, F., Gariépy, C., Bienfait, G., Guillou-Frottier, L., Lapointe, R., 2000. Heat flow in the Trans-Hudson Orogen of the Canadian Shield: implications for Proterozoic continental growth. Journal of Geophysical Research, in press.

Martignole, J, 1975. Le Precambrien dans le sud de la Province tectonique de Grenville, Ph.D. thesis, Université de Toulouse (France).

Martignole, J., Schrijver, K., 1970. Tectonic setting and evolution of the Morin Anorthosite, Grenville Province, Quebec. Bulletin of the Geological Society of Finland 42, 165-209.

Martignole, J., Ji, S., Zhao, X., 1995. High temperature mylonites of the Morin shear zone (Grenville Province, Quebec). Canadian Tectonic Group Meeting, Montreal.

Martignole, J., Calvert, A.J., 1996. Crustal scale shortening and extension across the Grenville Province of western Quebec. Tectonics 15, 376-386.

Masuda, T., Kuriyama, M., 1988. Successive 'mid-point' fracturing during microboudinage: an estimate of the stress-strain relation during a natural deformation. Tectonophysics 147, 171-177.

Matsui, M., Busing, W., 1984. Calculation of the elastic constants and high-pressure properties of diopside, $CaMgSi_2O_6$. American Mineralogist 69, 1090-1095.

McLean, D., 1972. Viscous flow of aligned composites. Journal of Material Science 7, 98-104.

McQuillan, H., 1973. Small-scale fracture density in Asmari formation of southwest Iran and its relation to bed thickness and structural setting. The American Association of Petroleum Geologist Bulletin 57, 2367-2385.

Meade, C., Silver, P.G., Kaneshima, S., 1995. Laboratory and seismological observations of lower mantle isotropy. Geophysical Research Letters 22, 1293-1296.

Melanitis, N., Galiotis, C., Tetlow, P.L., Davies, C.K.L., 1992. Interfacial shear stress

distribution in model composites Part 2: Fragmentation studies on carbon fiber/epoxy systems. Journal of Composite Material 26, 574-610.

Mercier, J.-C.C., Nicolas, A., 1975. Texture and fabrics of upper-mantle peridotites as illustrated by xenoliths from basalts. Journal of Petrology 16, 454-487.

Michibayashi, K., 1996. The role of intragranular fracturing on grain size reduction in feldspar during mylonitization. Journal of Structural Geology 18, 17-25.

Mitchell, R.H., 1987. Mantle-derived xenoliths in Canada, In: Nixson, P.H. (Ed.), Mantle Xenoliths, John Wiley & Sons, New York, 33-40.

Mockel, J.R., 1969. Structural petrology of the garnet peridotite of Alpe Arami (Ticino, Switzerland). Leide Geol. Medelelingen 42, 61-130.

Moecher, D.P., Wintsch, R.P., 1994. Deformation-induced reconstitution and local resetting of mineral equilibrium in polymetamorphic gneisses: tectonic and metamorphic implications. Journal of Metamorphic Geology 12, 523-538.

Monger, J., Clowes, R., Cowan, D., Potter, C., Price, R., Yorath, C., 1994. Continent-ocean transitions western North America between latitudes 46 and 56 degrees: Transects B1, B2, B3, In: Speed, R.C. (Ed.), Decade of North American Geology Continent-Ocean Transect Volume, Geological Society of America, Boulder, Colorado, 357-397.

Montagner, J.-P., Tanimoto, T., 1991. Global upper mantle tomography of seismic velocities and anisotropy. Journal of Geophysical Research 96, 20337-20351.

Mura, T., 1982. Micromechanics of defects in solids, Martinus Nijhoff, Boston.

Nardone, V.C., Prewo, K.M., 1986. On the strength of discontinuous silicon carbide reinforced aluminum composites. Scripta Metallurgica et Materialia 20, 43-48.

Narr, W., 1991. Fracture density in the deep subsurface: techniques with application to Point Arguello oil field. The American Association of Petroleum Geologists Bulletin 75, 1300-1323.

Narr, W., Suppe, J., 1991. Joint spacing in sedimentary rocks. Journal of Structural Geology 13, 1037-1048.

Newton, R.C., Smith, J.V., Windley, B.F., 1980. Carbonic metamorphism, granulites and crustal growth. Nature 288, 45-50.

Nichols, T.C., 1980. Rebound, its nature and effect on engineering works. Quarterly Journal of Engineering Geology 13, 133-152.

Nickelsen, R.P., Hough, V.N.D., 1967. Jointing in the Appalachian plateau of Pennsylvania. Bulletin of the Geological Survey of America 78, 609-629.

Nicolas, A., Poirier, J. P., 1976. Crystalline Plasticity and Solid State Flow in

Metamorphic Rocks, John Wiley, New York.

Nicolas, A., Prinzhofer, A., 1983. Cumulative or residual origin for the transition zone in ophiolites: structural evidence. Journal of Petrology 24, 188-206.

Nur, A., Simmons, G., 1969. Stress induced anisotropy in rocks: an experimental study. Journal of Geophysical Research 74, 6667-6674.

Ohsawa, T., Nakayana, A., Miwa, M., Hasegawa, A., 1978. Temperature dependence of critical fiber length for glass fiber reinforced thermosetting resins. Journal of Applied Polymer Science 22, 3203-3212.

Oliver, N.H.S., 1996. Review and classification of structural controls on fluid flow during regional metamorphism. Journal of Metamorphic Geology 14, 477-492.

Olsen, K.I., 1978. Metamorphic petrology and fluid inclusion studies of granulites and amphibolite facies gneisses on Langoy and W-Hinnoy, Vesteralen North Norway. Ph.D. thesis, Oslo (Norway).

O'Neil, H.S.C., 1981. The transition between spinel lherzolite and garnet lherzolite, and its use as a geobarometer. Contributions to Mineralogy and Petrology 77, 185-194.

Okada, T., Matsuzawa, T., Hasegawa, A., 1995. Shear-wave polarization anisotropy beneath the north-eastern part of Honshu, Japan. Geophysical Journal of Interior 123, 781-797.

Pascal, C., Angelier, J., Cacas, M.-C., Hancock, P.L., 1997. Distribution of joints: probabilistic modeling and case study near Cardiff (Wales, U.K.). Journal of Structural Geology 19, 1273-1284.

Passchier, C.W. and Trouw, R.A.J., 1995. Microtectonics, Springer, Berlin.

Pecher, A., 1981. Experimental decrepitation and re-equilibration of fluid inclusions in synthetic quartz. Tectonophysics 78, 567-584.

Pecher, A., Boullier, A.-M., 1984. Evolution a pression et temperature elevées d'inclusions fluids dans un quartz synthetique. Bulltein des Mineralogie 107, 139-153.

Pecher, A., Lespinasse, M., Leroy, J., 1985. Relations between fluid inclusion trails and regional stress field: a tool for fluid chronology - An example of an intragranitic uranium ore deposit (northern Massif Central, France). Lithos 18, 229-237.

Pennacchioni, G., Cesare, B., 1997. Ductile-brittle transition in pre-Alpine amphibolite facies mylonites during evolution from water-present to water-deficient conditions (Mont Mary nappe, Italian Western Alps). Journal of Metamorphic Geology 14, 477-492.

Peng, S.S., Johnson, A.M., 1972. Cracks growth and faulting in cylindrical specimens of Chelmsford granite. International Journal of Rock Mechanics and Mineral Science 9, 37-86.

Peselnick, L., Nicolas, A., Stevenson, P.R., 1974. Velocity anisotropy in a mantle peridotite from the Ivrea Zone: Application to upper mantle anisotropy. Journal of Geophysical Research 79, 1175-1182.

Peslier, A., 1999. Petrologie et geochimie isotopique de xenolithes mantelliques de la Cordillere Canadienne, Ph.D. thèsis, Université de Montréal (Canada).

Petrakakis, K., 1986. Metamorphism of high-grade gneisses from the Moldanubian zone, Austria, with particular reference to the garnets. Journal of Metamorphic Geology 4, 323-344.

Piggott, M.R., 1980. Loading-Bearing Fiber Composites, Pergamon Press, Toronto.

Pollard, D.D. and Aydin, A., 1988. Progress in understanding jointing over the past century. Geological Society of America Bulletin 100, 1181-1204.

Pollard, D.D., Segall, P., 1987. Theoretical displacements and stresses near fractures in rocks, with applications to faults, joints, veins, dikes, and solution surfaces. In: Atkinson, B.K. (Ed.), Fracture Mechanics of Rock, Academic Press, London, 277-349.

Price, N.J., 1966. Fault and joint development in brittle and semi-brittle rocks, Pergamon Press, Oxford.

Price, N.J., Cosgrove, J.W., 1990. Analysis of Geological Structures, Cambridge University Press, Cambridge.

Prior, D.J., Behrmann, J.H., 1990. Thrust-related mudstone fabrics from the Barbados forearc: A backscattered scanning electron microscope study. Journal of Geophysical Research 113, 545-556.

Prior, D.J., 1993. Sub-critical fracture and associated retrogression of garnet during mylonitic deformation. Contributions to Mineralogy and Petrology 113, 545-556.

Raith, J.G., Harley, S.L., 1998. Low-P/high-T metamorphism in the Okeip Copper District, western Namaqualand, South Africa. Journal of Metamorphic Geology 16, 281-305.

Ranalli, G., 1980. Rheological properties of the upper mantle in Canada from olivine microrheology. Canadian Journal of Earth Sciences 17, 1499-1505.

Randle, V., 1992. Microtexture determination and its applications, The Institute of Materials.

Randle, V., 1993. The measurement of grain boundary geometry (Electron Microscopy

in Materials Science Series). Institute of Physics Publishing, Bristol.

Rawnsley, K.D., Rives, T., Petit, J.-P., Hencher, S.R., Lumsden, A.C., 1992. Joint development in perturbed stress fields near faults. Journal of Structural Geology 14, 939-951.

Ren, X., Kowallis, B.J., Best, M.G., 1989. Paleostress history of the Basin and Range province in western Utah and eastern Nevada from healed microfracture orientations in granites. Geology 17, 487-490.

Reuss, A., 1929. Berechnung der Fliessgrenze von Mischkristallen auf Grund der Plastizitatsbedingung fur Einkristalle. Z. Angew. Math. Mech 9, 49-58.

Reynolds, S.J., Lister, G.S., 1987. Structural aspects of fluid-rock interactions in detachment zones. Geology 15, 362-366.

Ribe, N.M., 1989. Seismic anisotropy and mantle flow. Journal of Geophysical Research 94, 4213-4223.

Ribe, N.M., 1992. On the relation between seismic anisotropy and finite strain. Journal of Geophysical Research 97, 8737-8747.

Ribe, N.M., Yu, Y., 1991. A theory for plastic deformation and textural evolution of olivine polycrystals. Journal of Geophysical Research 96, 8325-8335.

Rice, R.W., Pohanka, R.C., 1979. Grain-size dependence of spontaneous cracking in ceramics. Journal of the American Ceramics Society 62, 559-563.

Rivers, T., Martignole, J., Gower, C.F., Davidson, A., 1989. New tectonic divisions of Grenville Province. Tectonics 8, 63-84.

Rives, T., Razack, M., Petit, J.-P., Rawnsley, K.D., 1992. Joint spacing: analogue and numerical simulations. Journal of Structural Geology 14, 925-937.

Roedder, E., 1984. Fluid inclusions, Mineralogical Society of America, Washington.

Roedder, E., Skinner, B.J., 1968. Experimental evidences that fluid inclusions do not leak. Economic Geology 63, 715-730.

Roedder, E., Kopp, O.C., 1975. A check on the validity of the pressure correction in inclusion geothermometry, using hydrothermally grown quartz. Fortschr Mineral 52, 431-446.

Ross, J.V., 1983. The nature and rheology of the cordilleran upper mantle of British Columbia: inferences from peridotite xenoliths. Tectonophysics 100, 321-357.

Rudnick, R.L., Ashwal, L.D., Henry, D.J., 1984. Fluid inclusions in high-grade gneisses of the Kapuskasing structural zone, Ontario: metamorphic fluids and uplift/erosion path. Contributions to Mineralogy and Petrology 87, 399-406.

Russo, R.M., Silver, P.G., 1993. Shear-wave splitting in the Andean and Western Pacific Subduction zones. Eos, American Geophysical Union Transaction 74(43), 96.

Russo, R.M., Silver, P.G., 1994. Trench-parallel flow beneath the Nazca Plate from Seismic anisotropy. Science 263, 1105-1111.

Russo, R.M., Silver, P.G., Franke, M., Ambeh, W.B., James, D.E., 1996. Shear-wave splitting in northeast Venezuela, Trinidad, and the eastern Caribbean. Physics of the Earth and Planetary Interiors 95, 251-275.

Ryzhova, T.V., 1964. Elastic properties of plagioclases. Izvestiya, Academy of Science, USSR Geophysics Series 7, 1049-1051.

Ryzhova, T.V., Aleksandrov, K.S., 1965. The elastic properties of rock-forming minerals, IV: nepheline. Izvestiya, Academy of Science, USSR Geophysics Series 12, 1799-1801.

Salisbury, M.H., Fountain, D.M., 1994. The seismic velocity and Poisson's ratio structure of Kapuskasing uplift from laboratory measurements. Canadian Journal of Earth Sciences 31, 1052-1063.

Salisbury, M.H., Iuliucci, R., Long, C., 1994. Velocity and reflection structure of the Sudbury structure from laboratory measurements. Geophysical Research Letters 21, 923-926.

Salisbury, M.H., Milkereit, B., Bleeker, W., 1996. Seismic imaging of massive sulfide deposits, Part 1: Rock properties. Economic geology 91, 821-828.

Saruwatari, K., Ji, S., Salisbury, M.H., 1998. Seismic properties of the upper mantle beneath the Canadian Cordillera - a study of mantle xenoliths. LITHOPROBE Report No. 64 307-311.

Savage, M.K., 1999. Seismic anisotropy and mantle deformation: What have we learned from shear wave splitting? Review of Geophysics 37, 65-106.

Savage, M.K., Silver, P.G., 1993. Mantle deformation and tectonics: constraints from seismic anisotropy in the western United States. Physics of the Earth and Planetary Interiors 78, 207-227.

Schmid, S., Boland, J.N., Paterson, M., 1977. Superplastic flow in fine-grained limestone. Tectonophysics 43, 257-291.

Schmidt, N.H., Olesen, N.O., 1989. Computer-aided determination of crystal lattice orientation from electron channeling patterns in the SEM. Canadian Mineralogist 27, 15-22.

Scholz, C.H., 1990. The Mechanics of Earthquakes and Faulting, Cambridge University Press, Cambridge.

Sen, Z., Kazi, A., 1984. Discontinuity spacing and RQD estimates from finite length scanlines. International Journal of Rock Mechanics and Mining Sciences and

Geomechanics Abstracts 21, 203-212.

Shalaby, H., 1977. Analyse des Structures Geométriques et Interprétation Rhéologique d'un Slump Cambrien dans le Flysch de Saint-Jean-Port-Joli, Appalaches du Québec. M.Sc. thèsis, Université de Montréal (Canada).

Shelton, K.L., Orville, P.M., 1980. Formation of synthetic fluid inclusions in natural quartz. American Mineralogist 65, 1233-1236.

Shi, L., Francis, D., Ludden, J., Frederiksen, A., Bostock, M.G., 1998. Xenoliths evidence for lithospheric melting above anomalously hot mantle under the northern Canadian Cordillera. Contributions to Mineralogy and Petrology 131, 39-53.

Shih, X.R., Meyer, R.P., Schneider, J.F., 1991. Seismic anisotropy above a subducting plate. Geology 19, 807-810.

Silver, P.G., 1996. Seismic anisotropy beneath the continents: Probing the depths of geology. Annual Review of Earth Planetary Science 24, 385-432.

Silver, P.G., Chan, W.W., 1988. Implications for continental structure and evolution from seismic anisotropy. Nature 335, 34-39.

Silver, P.G., Chan, W.W., 1991. Shear wave splitting and subcontinental mantle deformation. Journal of Geophysical Research 96, 16429-16454.

Silver, P., Mainprice, D., Ismail, W.B., Tommasi, A., Barruol, G., 1999. Mantle structural geology from seismic anisotropy. In: Fei, Y. (Ed.), Mantle Petrology: Field Observations and High Pressure Experimentation: A Tribute to Francis, R., The Geochemical Society Special Publication 6, 1-25.

Smith, G.P., Ekstrom, G., 1999. A global study of Pn anisotropy beneath continents. Journal of Geophysical Research 104, 963-980.

Smith, D.L., Evans, B., 1984. Diffusional crack healing in quartz. Journal of Geophysical Research 89, 4125-4135.

Sowers, G.M., 1972. Theory of spacing of extension fracture. Engineering Geology Case Histories 9, 27-53.

Sterner, S.M., Bodnar, R.J., 1989. Synthetic fluid inclusions - VII. Re-equilibration of fluid inclusions in quartz during laboratory-simulated metamorphic burial and uplift. Journal of Metamorphic Geology 7, 243-260.

St-Julien, P., 1967. Tectonics of part of the Appalachian region of southeastern Quebec. Royal Society of Canada Special Publications 10, 41-47.

Suhr, G., 1993. Evaluation of upper mantle microstructures in the Table Mountain massif (Bay of Islands ophiolite). Journal of Structural Geology 15, 1273-1292.

Suppe, J., 1985. Principals of Structural Geology, Prentice-Hall, Englewood Cliffs, New Jersey.

Swanenberg, H.E.C., 1980. Fluid inclusions in high-grade metamorphic rocks from SW Norway, Ph. D. thesis, Utrecht University.

Sweeney, J.F., Stephenson, R.A., Currie, R.G., DeLaurier, J.M., 1991. Part C. Crustal Geophysics in Chapter 2. In: Sweeney, J. F., Stephenson, R.A., Currie, R.G., DeLaurier, J.M. (Ed.), Geology of the Cordilleran Orogen in Canada, Geological Survey of Canada, Geology of Canada, 39-53.

Syme-Gash, P. J., 1971. A study of surface features relating to brittle and semibrittle fracture. Tectonophysics 12, 349-391.

Tapponnier, P., Brace, W.F., 1976. Development of stress-induced microcracks in Westerly granite. International Journal of Rock Mechanics and Mineral Science 13, 103-112.

Taya, M., Arsenault, R.J., 1989. Metal Matrix Composites, Pergamon Press, New York.

Thost, D.E., Hensen, B.J., Motoyoshi, Y., 1991. Two-stage decompression in garnet-bearing mafic granulites from Sostrene Island, Prydz Bay, East Antarctica. Journal of Metamorphic Geology 9, 245-256.

Tommasi, A., 1998. Forward modeling of the development of seismic anisotropy in the upper mantle. Earth and Planetary Science Letters 160, 1-13.

Toriumi, M., 1984. Preferred orientation of olivine in mantle-derived peridotites and stress in the lithosphere. Journal of physics of the earth 32, 259-271.

Touret, J., 1981. Fluid inclusions in high grade metamorphic rocks. In: Hollister, L.S., Crawford, M.L. (Ed.), Mineralogical Association of Canada, Short Course in Fluid inclusions: Applications to Petrology, Calgary, 182-208.

Touret, J.L.R., Dietvort, P., 1983. Fluid inclusions in high-grade anatectic metamorphites. Journal of Geological Society of London 140, 635-649.

Turcotte, D.L., Schubert, G., 1982. Geodynamics, Wiley, New York.

Tuttle, O.F., 1949. Structural petrology of planes of liquids inclusions. Journal of Geology 57, 331-356.

Tvergaard, V., Hutchinson, J.W., 1988. Microcracking ceramics induced by thermal expansion or elastic anisotropy. Journal of the American Ceramics Society 71, 157-166.

Tyson, W.R., Davies, G.J., 1965. A photoelastic study of the shear stresses associated with the transfer of stress during fiber reinforcement. British Journal of Applied Physics 16, 199-205.

Underwood, E.E., 1970. Quantitative Stereology, Addison-Wesley, Reading,

Massachusetts.

Valentino, A.J., Sclar, C.B., 1981. Parting in giant garnets as an indicator of late brittle deformation at Gore Mountain, Warren Country, N.Y. Geophysical Research Letters 8, 883-885.

van der Molen, I., 1981. The shift of A-B transition temperature of quartz associated with the thermal expansion of granite at high pressure. Tectonophysics 73, 323-342.

Vinnik, L.P., Makeyeva, L.I., Milev, A., Usenko, A.Y., 1992. Global patterns of azimuthal anisotropy and deformations in the continental mantle. Geophysics Journal International 111, 433-447.

Vinnik, L.P., Green, R.W.E., Nicolaysen, L.O., 1995. Recent deformations of the deep continental root beneath southern Africa. Nature 375, 50-52.

Vityk, M.O., Bodnar, R.J., 1995. Textural evolution of synthetic fluid inclusion in quartz during reequilibration, with applications to tectonic reconstruction. Contributions to Mineralogy and Petrology 121, 309-323.

Vityk, M.O., Bodnar, R.J., Schmidt, C.S., 1994. Fluid inclusions as tectonothermobarometers: Relation between pressure-temperature history and re-equilibration morphology during crustal thickening. Geology 22, 731-734.

Voigt, W., 1928. Lehrbuch der Kristallphysik, B.G. Tubner, Leipzig.

Vollbrecht, A., Rust, S., Weber, K., 1991. Developments of microcracks in granites during cooling and uplift: examples from the Variscan basement in NE Bavaria, Germany. Journal of Structural Geology 13, 787-799.

Vollbrecht, A., Durrast, H., Kraus, J., Weber, K., 1994. Paleostress directions deduced from microcrack fabrics in KTB core samples and granites from the surrounding area. Scientific Drilling 4, 233-241.

Vollbrecht, A., Stipp, M., Olesen, N.O., 1999. Crystallographic orientation of microcracks in quartz and inferred deformation processes: a study on gneisses from the German Continental Deep Drilling Project (KTB). Tectonophysics 303, 279-297.

Walther, J.V., Orville, P.M., 1983. The extraction-quench technique for determination of the thermodynamic properties of solute complexes: application to quartz solubility in fluid mixtures. American Mineralogist 68, 731-741.

Wang, C.-Y., Sun, Y., 1990. Oriented microfractures in Cajon Pass Drill Cores: stress field near the San Andreas Faults. Journal of Geophysical Research 95, 11135-

11142.

Watson, E.B., Brenan, J.M., 1987. Fluids in the lithosphere, 1. Experimentally-determined wetting characteristics of CO_2-H_2O fluids and their implications for fluid transport, host-rock physical properties and fluid inclusion formation. Earth and Planetary Science Letters 85, 497-515.

Watt, D.F., Xu, X.Q., Lloyd, D.J., 1996. Effects of particle morphology and spacing on the strain fields in a plastically deforming matrix. Acta Materialia 44, 789-799.

Wells, P.R.A., 1977. Pyroxene thermometry in simple and complex systems. Contributions to Mineralogy and Petrology 62, 129-139.

Wendt, A.S., D'Arco, P., Goffe, B., Oberhansli, R., 1993. Radial cracks around a-quartz inclusions in almandine: constraints on the metamorphic history in the Oman mountains. Earth and Planetary Science Letters 114, 449-461.

Wheeler, J.O., Brookfield, A.J., Gabrielse, H., Monger, J.W.H., Tipper, H.W., Woodsworth, G.J., 1991. Terrane map of the Canadian Cordillera. Geological Survey of Canada Map 1713A.

White, S.H., Burrows, S.E., Carreras, J., Shaw, N.D., Humphreys, F.J., 1980. On mylonites in ductile shear zones. Journal of Structural Geology 2, 175-187.

Whiteny, D.L., 1996. Garnets as open systems during regional metamorphism. Geology 24, 147-150.

Wickens, A.J., 1977. The upper mantle of southern British Columbia. Canadian Journal of Earth Sciences 14, 1100-1115.

Wilshire, H.G., Shervais, J.W., 1975. Al-augite and Cr-diopside ultramafic xenoliths in basaltic rocks from western United States. Physics and Chemistry of the Earth 9, 257-272.

Wise, D.U., 1964. Microjointing in Basement, Middle Rocky Mountains of Montana and Wyoming. Geological Society of America Bulletin 75, 287-306.

Wu, H., Pollard, D.D., 1992. Propagation of a set of opening-mode fractures in layered brittle materials under uniaxial strain cycling. Journal of Geophysical Research 97, 3381-3396.

Wu, H., Pollard, D.D., 1995. An experimental study of the relationship between joint spacing and layer thickness. Journal of Structural Geology 17, 887-905.

Xie, J., 1992. Shear-wave splitting near Guam. Physics of the Earth and Planetary Interiors 72, 211-219.

Yang, X., Fischer, K.M., 1995. Seismic anisotropy beneath the Shumagin Islands

segment of the Aleutian-Alaska subduction zone. Journal of Geophysical Research 100, 18165-18177.

Yardley, B.W.D., 1977. An empirical study of diffusion in garnet. American Mineralogist 62, 793-800.

Yoneda, A., 1990. Pressure derivatives of elastic constants of single crystal MgO and $MgAl_2O_4$. Journal of physics of the earth 38, 19-55.

Zhang, R., Hirajima, T., Banno, S., Cong, B., Liou, J.G., 1995. Petrology of ultrahigh-pressure rocks from the southern Su-Lu region, eastern China. Journal of Metamorphic Geology 13, 659-675.

Zhang, R., Karato, S., 1993. Simple shear deformation of olivine aggregates. EOS, American Geophysical Union Transactions 74(43), 610.

Zhang, R.Y., Liou, J.G., 1998. Partial transformation of gabbro to coesite-bearing eclogite from Yangkou, the Sulu terrane, eastern China. Journal of Metamorphic Geology 15, 183-202.

Zhang, S., Karato, S.-I., 1995. Lattice preferred orientation of olivine aggregates deformed in simple shear. Nature 375, 774-777.

Zhang, S., Karato, S.-I., FitzGerald, J., Faul, U.H., Zhou, Y., 2000. Simple shear deformation of olivine aggregates. Tectonophysics 316, 133-152.

Zhao, X., 1997. Microstructure et petrofabrique des mineraux a haute temperature: example du Terrain de Morin, Province de Grenville, Quebec, Université de Montréal, Thèse de doctorat.

Zhao, X., Ji, S., Martignole, J., 1997. Quartz microstructures and c-axis preferred orientation in high-grade gneisses and mylonites around the Morin anorthosite (Grenville Province). Canadian Journal of Earth Sciences 34, 819-832.

Zhao, P., Ji, S., 1993. Comment on "Strengthening behavior of particulate reinforced MMCs" by Y. Wu and E. J. Lavernia, and "On the strength of discontinuous silicon carbide reinforced aluminum composites" by V. C. Nardone & K. M. Prewo. Scripta Metallurgica et Materialia 27, 1443.

Zhao, P., Ji, S., 1997. Refinements of shear-lag model and its applications. Tectonophysics 279, 37-53.

Zoback, M.D., Zoback, M.L., 1991. Tectonic stress field of North America and relative plate motions, In: Slemmons, D.E., Engdahl, E.R., Zoback, M.D., Blackwell, D.D. (Ed.), Neotectonics of North America, Geological Society of America, Boulder, Colorado, 339-366.

Appendix 1

Olivine (Kumazawa &Anderson, 1967)

Average thermal expansion coefficient (1/K) $\alpha = 0.00002465$

Adiabatic bulk modulus (Mbar) K = 1.294

Density (g/cm^3) (P_0, T_0) = (0.000001 , 25°C) $\rho_0 = 3.3111$

C_0 (i, j)

3.237	0.664	0.716	0	0	0
0.664	1.976	0.756	0	0	0
0.716	0.756	2.351	0	0	0
0	0	0	0.6462	0	0
0	0	0	0	0.7805	0
0	0	0	0	0	0.7904

dC_{ij}/dP

7.98	4.74	4.48	0	0	0
4.74	6.37	3.76	0	0	0
4.48	3.76	6.38	0	0	0
0	0	0	2.17	0	0
0	0	0	0	1.64	0
0	0	0	0	0	2.31

dC_{ij}/dT

-0.00034	-0.000105	-0.000094	0	0	0
-0.000105	-0.000285	-0.000051	0	0	0
-0.000094	-0.000051	-0.000286	0	0	0
0	0	0	-0.000128	0	0
0	0	0	0	-0.00013	0
0	0	0	0	0	-0.000157

ρ (0.015 Mbar, 1000 °C) = 3.2699

C_{ij} (0.015 Mbar, 1000 °C)

3.025192	0.632720	0.691545	0	0	0
0.632720	1.793668	0.762671	0	0	0
0.691545	0.762671	2.167843	0	0	0
0	0	0	0.553947	0	0
0	0	0	0	0.678348	0
0	0	0	0	0	0.671972

Opx (enstatite)

Average thermal expansion coefficient (1/K) α = 0.0000477 (Frisillo & Buljan, 1972)
Adiabatic bulk modulus (Mbar) K = 1.023 (Duffy & Vaughan, 1988)
Density (g/cm^3) (P_0, T_0) = (0.000001 , 25°C) ρ_0 = 3.272 (Duffy & Vaughan, 1988)

C_0 (i, j) (Duffy & Vaughan, 1988)

2.293	0.736	0.498	0	0	0
0.736	1.67	0.466	0	0	0
0.498	0.466	1.939	0	0	0
0	0	0	0.797	0	0
0	0	0	0	0.761	0
0	0	0	0	0	0.771

dC_{ij}/dP (Frisillo &Barsch, 1972)

11.04	6.97	9.09	0	0	0
6.97	9.19	8.73	0	0	0
9.09	8.73	16.42	0	0	0
0	0	0	2.38	0	0
0	0	0	0	2.92	0
0	0	0	0	0	2.75

dC_{ij}/dT (Frisillo &Barsch, 1972)

-0.000352	-0.000212	-0.000318	0	0	0
-0.000212	-0.000328	-0.000107	0	0	0
-0.000318	-0.000107	-0.000516	0	0	0
0	0	0	-0.000131	0	0
0	0	0	0	-0.000138	0
0	0	0	0	0	-0.000145

ρ (0.015 Mbar, 1000 °C) = 3.1678
C_{ij} (0.015 Mbar, 1000 °C)

2.115388	0.633843	0.324290	0	0	0
0.633843	1.488040	0.492616	0	0	0
0.324290	0.492616	1.682183	0	0	0
0	0	0	0.704972	0	0
0	0	0	0	0.670247	0
0	0	0	0	0	0.670872

Cpx (diopside)

Average thermal expansion coefficient (1/K) $\alpha = 0.0000333$ (Cameron et al., 1973)
Adiabatic bulk modulus (Mbar) K = 1.13 (Levien et al., 1979)
Density (g/cm^3) (P_0, T_0) = (0.000001 , 25°C) $\rho_0 = 3.277$ (Levien et al., 1979)

C_0 (i, j) (Levien et al., 1979)

2.23	0.77	0.81	0	0.17	0
0.77	1.71	0.57	0	0.07	0
0.81	0.57	2.35	0	0.43	0
0	0	0	0.74	0	0.073
0.17	0.07	0.43	0	0.67	0
0	0	0	0.073	0	0.66

dC_{ij}/dP (Estey & Douglas, 1986, << Frisillo & Barsch, 1972 + Bass et al., 1981)

9.09	5.74	7.49	0	0	0
5.74	7.57	7.19	0	0	0
7.49	7.19	13.53	0	0	0
0	0	0	2.38	0	0
0	0	0	0	2.92	0
0	0	0	0	0	2.75

dC_{ij}/dT (Estey & Douglas, 1986, << Frisillo & Barsch, 1972 + Bass et al., 1981)

-0.000352	-0.000212	-0.000318	0	0	0
-0.000212	-0.000328	-0.000107	0	0	0
-0.000318	-0.000107	-0.000516	0	0	0
0	0	0	-0.000131	0	0
0	0	0	0	-0.000138	0
0	0	0	0	0	-0.000145

ρ (0.015 Mbar, 1000 °C) = 3.2141
C_{ij} (0.015 Mbar, 1000 °C)

2.023140	0.649394	0.612292	0	0.17	0
0.649394	1.503742	0.573517	0	0.07	0
0.612292	0.573517	2.049836	0	0.43	0
0	0	0	0.647972	0	0.073
0.17	0.07	0.43	0	0.579247	0
0	0	0	0.073	0	0.559872

Spinel (Yoneda, 1990)

Average thermal expansion coefficient (1/K) $\alpha = 0.0000249$ (Yamanaka & Takeuchi, 1983)
Adiabatic bulk modulus (Mbar) $K_S = 1.979$
Density (g/cm^3) (P_0, T_0) = (0.000001 , 25°C) $\rho_0 = 3.578$

C_0 (i, j)

2.829	1.554	1.554	0	0	0
1.554	2.829	1.554	0	0	0
1.554	1.554	2.829	0	0	0
0	0	0	1.548	0	0
0	0	0	0	1.548	0
0	0	0	0	0	1.548

dC_{ij}/dP

5.59	5.69	5.69	0	0	0
5.69	5.59	5.69	0	0	0
5.69	5.69	5.59	0	0	0
0	0	0	1.44	0	0
0	0	0	0	1.44	0
0	0	0	0	0	1.44

dC_{ij}/dT (Askarpour et al. 1993)

-0.000232	-0.000129	-0.000129	0	0	0
-0.000129	-0.000232	-0.000129	0	0	0
-0.000129	-0.000129	-0.000232	0	0	0
0	0	0	-0.000114	0	0
0	0	0	0	-0.000114	0
0	0	0	0	0	-0.000114

ρ (0.015 Mbar, 1000 °C) = 3.5182
C_{ij} (0.015 Mbar, 1000 °C)

2.686644	1.513569	1.513569	0	0	0
1.513569	2.686644	1.513569	0	0	0
1.513569	1.513569	2.686644	0	0	0
0	0	0	1.458448	0	0
0	0	0	0	1.458448	0
0	0	0	0	0	1.458448